

**Fabrication and Transport Properties of Carbon Nanotube
Quantum Dots with Ferromagnetic and Superconducting
Leads**

by

Nikolaus Hartman

A dissertation submitted to The Johns Hopkins University in conformity with the
requirements for the degree of Doctor of Philosophy.

Baltimore, Maryland

August, 2015

© Nikolaus Hartman 2015

All rights reserved

Abstract

Carbon nanotube quantum dots are an attractive platform in which to measure quantum transport phenomena. Low-energy transport properties of one dimensional nanotubes are easily understood and the devices are simple to fabricate with a wide range of metal contact materials. Quantum transport in a zero dimensional carbon nanotube quantum dot is dominated by the device length, choice of contact material, and symmetries inherent in the nanotube. By fabricating carbon nanotube quantum dots with ferromagnetic and superconducting contacts, it becomes possible to measure a wide variety of spin transport phenomena at low temperatures. In this thesis, I have studied the fabrication and low-temperature transport properties of carbon nanotube quantum dots with normal metal, ferromagnetic, and superconducting contacts. A wide range of fabrication techniques were tested and optimized, along with improvements to image processing and contact fabrication. F-CNT-F devices show a range of spin dependent physics, including tunneling magnetoresistance and suppression of conductance peaks due to spin selection rules. These results demonstrate a new probe into the collective spin states in a CNTQD. F-CNT-S devices show evidence

ABSTRACT

of proximity induced superconductivity and magnetic field dependent switching of the conductance. The measurements are the first attempt at analyzing conductance through a F-CNT-S quantum dot. The results presented in this thesis represent a step in improving device fabrication through statistical analysis and improved methods, as well as a look at spin dependent transport through a variety of carbon nanotube quantum dot structures.

Primary Reader: Nina Markovic

Secondary Reader: N. Peter Armitage

Acknowledgments

Over the past seven years, whenever I have been asked why I chose to do my PhD work at Johns Hopkins I have had the same answer; the people here were by far the nicest and most helpful scientists I spoke with in making my decision. That has remained true throughout my time at Johns Hopkins. With that, the biggest thanks goes to my advisor, Nina Marković. She has consistently brought in big ideas for each of the graduate students in her lab and given us the freedom to run wild with them. I could not have had an advisor with a personality I related to more than Nina. She always encouraged me to keep pushing through the moment I wanted to slow down and complain. That alone has gone a long way to making me a better scientist. Along with Nina, I owe thanks to Dan Reich, Peter Armitage, and Oleg Tchernyshyov for making sure I was alive, paid, and stocked with equipment in my last year.

During the time I spent in the Marković lab I learned a great deal from my lab-mates. Soo Hyung Lee was here at the beginning to help me navigate the unfamiliar lab. Janice Guikema, throughout my time here, was always willing to help me think about a problem or correct a sloppy technique. Similarly, our post doc Atikur Rah-

ACKNOWLEDGMENTS

man provided huge amounts of measurement advice. I would not be able to cool down a single sample without what I learned from Atikur. Tyler Morgan-Wall has worked with me since nearly my first day in the lab. Rewiring cryostats, troubleshooting fabrication, and cooling a sample down until 2am would not have been half as much fun without him. JT Mlack, despite abandoning us for Copenhagen for a year, has been a great labmate to spend two years sitting uncomfortably close to in the basement. He was always on hand to listen to a rant about fabrication problems, or, just as likely, whatever science fiction we were into at the time. Finally, I have to acknowledge the hard work of all of the undergraduate and high school students who have worked with me over the years; Steph Blease, Joe Schwartz, Ben Hartman, Paul Bewak, Alec Jordan, and Streit Cunningham. They all deserve a lot of credit for carrying the team through long hours in the cleanroom, in front of the AFM, and watching over the tube furnace. This thesis would not have been possible without their dedication and insights.

In addition to my labmates, there are too many other physicists and Baltimoreans to thank. I owe so much to Dan Allan, Nuala McCullagh, and Dan Richmond for being here throughout my whole career to celebrate success, work through failure, and have a beer pretty much any time anything happened. To all of you who spent time with me at the Meat Castle, Countdown, and New Years cabins, it was phenomenal and I hope to see you all for years to come. Finally, thanks to every other physicist I've spent time with in Bloomberg. You've all done a great job at maintaining the

ACKNOWLEDGMENTS

spirit that brought me here in the first place.

Thanks to my family, my parents Ann and George, and my sister Erika, who were unfailingly supportive of my work on this PhD. Finally, thanks to Stephanie, who, to put it briefly, is the reason I made it to my defense with my sanity (along with Herman, of course).

Contents

Abstract	ii
Acknowledgments	iv
List of Tables	xiv
List of Figures	xv
1 Introduction	1
1.1 Transport Spectroscopy in Quantum Dots	3
1.2 Working with Carbon Nanotubes	5
1.3 Current Work	6
2 Electronic Properties of Carbon Nanotubes	8
2.1 Electronic Bandstructure of Graphene	8
2.1.1 Graphene Lattice	9
2.1.2 Tight Binding Model	12

CONTENTS

2.1.3	Low Energy Bandstructure of Graphene	17
2.2	Electronic Bandstructure of Carbon Nanotubes	19
2.2.1	Types of Carbon Nanotubes	23
2.2.2	Low Energy Bandstructure of Carbon Nanotubes	24
2.3	Carbon Nanotube Field Effect Transistors	26
2.4	Carbon Nanotube Quantum Dots	29
3	Carbon Nanotube Growth and Placement	37
3.1	Random Dispersion	38
3.1.1	Catalyst	38
3.1.2	Growth	39
3.1.3	Nanotube Placement	41
3.1.4	Advantages and Disadvantages	43
3.2	Catalyst Island Growth	44
3.2.1	Catalyst	44
3.2.2	Growth	47
3.2.3	Advantages and Disadvantages	49
3.3	Imaging Nanotubes	49
3.3.1	Atomic Force Microscopy	50
3.3.2	Electric Force Microscopy	51
3.3.3	EFM Through PMMA	53
3.3.4	Scanning Electron Microscopy	54

CONTENTS

3.4	Image Filtering	56
3.4.1	Histogram Equalization	57
3.4.2	Matched Filter Bank	59
3.4.2.1	Nanotube Profile Model	59
3.4.2.2	Filter Kernel	61
3.4.2.3	Filter Bank	63
4	Metallic Contacts to Carbon Nanotubes	68
4.1	Statistics of Carbon Nanotube Contacts	70
4.1.1	Ferromagnetic Contacts	73
4.1.2	Superconducting Contacts	74
4.1.3	Normal Metal Contacts	75
4.1.4	Additional Comments	77
4.2	Reducing Contamination	78
4.2.1	Choice of Developer	78
4.2.2	Dose Scaling	80
4.2.3	Annealing	82
4.3	Electrical Noise in CNT Contacts	84
4.3.1	Random Telegraph Noise	85
4.3.2	$1/f$ Noise	88
5	Low Temperature Transport Measurements	94

CONTENTS

5.1	Transport Measurements	94
5.1.1	DC Current Measurements	95
5.1.2	AC Conductance Measurements	96
5.1.3	Custom Electronics	98
5.2	Cryogenics	101
5.2.1	Cryostat Wiring	102
5.2.2	Dunker	103
5.2.3	3He Cryostats	104
5.2.4	Dilution Refrigerator	106
5.2.5	Superconducting Magnets	108
6	Quantum Dots with Ferromagnetic Leads	110
6.1	Tunneling Magnetoresistance	112
6.1.1	Results	115
6.2	Negative Differential Conductance in Coulomb Blockade Regime . . .	118
6.2.1	Spin Blockade in a Double Quantum Dot	119
6.2.2	NDC from Spin Selection Rules	122
6.3	Spin Selection Rules with Applied Magnetic Field	125
6.3.1	Results and Discussion	127
6.4	Spectroscopy of a Magnetic Impurity	127
6.4.1	Characteristic Size and Level Spacing	128
6.4.2	Effects on CNT Quantum Dot Levels	131

CONTENTS

7 Spin Transport in Tunable Ferromagnet/Superconductor Junction	133
7.1 Background	134
7.2 Characteristics of Samples	138
7.3 Zeeman Splitting of Differential Conductance Peaks	144
7.4 Hysteretic Switching of Quantum Dot Conductance in an External Field	148
7.4.1 Discussion	153
8 Additional Carbon Nanotube Devices	157
8.1 NM-CNT-NM Quantum Dots	157
8.2 Locally Gated Quantum Dots	158
8.3 CNT Tunnel Probe into Aluminum Nanowires	162
8.3.1 Background	162
8.3.2 Device and Measurement	164
8.4 Majorana Fermions in CNTs	167
8.4.1 Background	167
8.4.2 Device and Measurement	169
9 Conclusion	172
9.1 Fabrication of Nanotube Devices	173
9.2 Ferromagnetic and Superconducting Device Measurements	175
9.3 Future Work on Other Devices	176
A Fabrication Details	177

CONTENTS

A.1 Wafer Preparation	178
A.1.1 Selection and Cleaning	178
A.1.2 Optical Lithography	179
A.1.2.1 Projection Lithography	180
A.1.2.2 Mask Aligner	181
A.2 Device Design	183
A.3 Electron Beam Lithography	184
A.3.1 Standard Recipe	185
A.3.2 Cold Development	186
A.4 Thin Film Deposition	187
A.4.1 Thermal Evaporation	187
A.4.2 Electron Beam Evaporation	188
A.4.3 Sputtering	189
A.4.4 Atomic Layer Deposition	190
A.4.5 Lift-off	192
A.5 Room Temperature Testing	193
A.5.1 Probe Station	193
A.5.2 Wire Bonding	194
B Details of Cryostat Operation	197
B.1 Oxford Kelvinox Dilution Refrigerator	197
B.2 RMC 3He Cryostat	205

CONTENTS

Bibliography	208
Vita	231

List of Tables

3.1	Powder Catalyst	38
3.2	Patterned Catalysts	45
3.3	Matched Filter Bank Parameters	66
4.1	Summary of all materials and deposition methods tested for nanotube contacts.	72
4.2	Surface roughness after development of PMMA films.	80
6.1	Details of measured F-CNT-F devices	111
6.2	Low temperature characteristics of F-CNT-F quantum dots	111
A.1	Standard PMMA/MIBK recipe	185
A.2	Cold developer recipe	186
A.3	Thermal evaporation materials	188

List of Figures

2.1	The real-space structure of the graphene lattice. Vectors \vec{a}_1 and \vec{a}_2 define the unit cell, which contains two atoms, highlighted in red and blue.	10
2.2	The reciprocal lattice of graphene. Vectors \vec{b}_1 and \vec{b}_2 define the Brillouin zone. The high symmetry points Γ , K , K' , and M are labeled..	11
2.3	(a) The π -bands of graphene calculated using a nearest neighbor tight binding model. (b) A contour plot of the upper band with the first Brillouin zone drawn. The bands meet at the three K and three K' points at the vertices of the Brillouin zone.	17
2.4	The real-space structure of a carbon nanotube. The nanotube unit cell is defined by the vectors \vec{C}_h and \vec{T}	20
2.5	The reciprocal lattice of a carbon nanotube, defined by the vectors K_1 and K_2	22
2.6	Two types of carbon nanotube bandstructure. The left plot shows a metallic (5,5) armchair nanotube. The right plot shows a semiconducting (4,2) chiral nanotube.	24
2.7	Schematic of a carbon nanotube field effect transistor.	27
2.8	Current versus gate voltage characteristics for three typs of CNTFET.	27
2.9	IV characteristics of a typical small band gap semiconducting CNT-FET. The current saturates at higher bias voltage, but is not typically measured due to avalanche breakdown of the devices. Inset: Current versus gate at a fixed bias for the same device.	28
2.10	R-T curve of a CNTFET cooled to 4 K	29
2.11	Quantum dot energy diagram.	30
2.12	Left: A quantum dot level resonant with the source/drain chemical potential. Right: The same device in the blockaded region.	32
2.13	Conductance as a function of applied gate voltage in a cobalt contacted nanotube quantum dot. Inset: A close up showing a region with clear 4 fold symmetry.	33

LIST OF FIGURES

2.14 Left: A quantum dot level resonant with the drain chemical potential. Right: The same device in the blockaded region.	34
2.15 Left: An IV curve at fixed gate voltage Right: Differential conductance measured at fixed gate voltage.	34
2.16 Conductance of a cobalt contacted nanotube quantum dot at 4K as a function of bias and gate voltages.	35
3.1 The tube furnace fitted with a 1" diameter quartz tube. The tube is sealed at both ends using 1" rubber tubing, cable clamps, and KF25 fittings. Gas flows from left to right in the picture. The gas flows out of the furnace into a mineral oil bubbler to keep hot hydrogen from reaching the air in the room. Gas then flows from the bubbler into the building exhaust.	39
3.2 The gas handling panel for our Lindberg tube furnace. Gas flow is from left to right.	40
3.3 A Si/SiO ₂ substrate with 1 μm Au markers. Left scale bar: 100 μm. Right scale bar: 20 μm	43
3.4 A Si/SiO ₂ substrate with 3 μm catalyst islands and Mo leads. Left scale bar: 100 μm. Right scale bar: 20 μm	46
3.5 AFM height and amplitude scans of nanotubes dispersed over a substrate with 1.5 μm gold markers. The scale bar is 10 μm.	50
3.6 An EFM image of nanotubes dispersed over a substrate with 1.5 μm gold markers. The markers have been automatically located using the height data and highlighted in blue on the EFM image. The scale bar is 10 μm.	52
3.7 (a) Frequency data collected from an EFM scan of a catalyst island sample after nanotube growth. (b) Frequency data collected from an EFM scan of a similar sample. Prior to the scan this sample was coated with a 250 nm PMMA layer. Both scale bars are 10 μm.	54
3.8 A scanning electron micrograph of a catalyst island sample after nanotube growth. The scale bar is 10 μm.	55
3.9 An illustration of the histogram equalization process.	57
3.10 Top image is the original SEM image after a plane fit. Middle image shows the SEM image after histogram equalization. Bottom image shows the final result after gaussian smoothing. Plots on the right show the histogram of brightness values and cumulative distribution function at each step.	58
3.11 a) The original data set of SEM nanotube images used to create and optimize the matched filter bank. b) The same data set rotated and overlaid with extracted nanotube profiles.	60

LIST OF FIGURES

3.12 a) Extracted nanotube profiles with linear background removed (blue). Fits to 3.1 (red). b) Distribution of k values extracted from profile fits. c) Distribution of straight nanotube section lengths.	62
3.13 (a) Original image. (b) Final filtered image, which is the sum of the binary images in (d). (c) The rotated kernels that form the full matched filter bank. d) Each rotated kernel applied to an image in (a).	64
3.14 Optimization of the matched filter bank threshold value.	65
3.15 Two examples applying the matched filter bank to full SEM images of as-grown carbon nanotubes.	67
4.1 Pie charts showing the percentage of quantum dots with measured resistances below $1\text{ G}\Omega$. Data includes all metals and deposition methods.	70
4.2 Histograms showing distribution of devices resistances. Only measured resistances below $1\text{ G}\Omega$ are plotted. Data includes all metals and de- position methods.	71
4.3 Histograms showing distribution of ferromagnetic metal contact resis- tances. Insets show the yield of devices with resistance below $1\text{ G}\Omega$. . .	73
4.4 Histograms showing distribution of superconducting metal contact re- sistances. Insets show the yield of devices with resistance below $1\text{ G}\Omega$. . .	75
4.5 Histograms showing distribution of normal metal contact resistances. Insets show the yield of devices with resistance below $1\text{ G}\Omega$	76
4.6 Histograms showing contact resistance as a function of developer choice. Data include all metals and deposition methods. Insets show the yield of devices with resistance below $1\text{ G}\Omega$	79
4.7 Surface roughness after development of PMMA film using 0°C IPA:water in 7:3 mixture.	79
4.8 An example of a lithography pattern with dose scaling based on poly- gon geometry. Inset shows a close up of the nanotube contacts.	82
4.9 A typical current anneal trace. Initially, the resistance was seen to decrease. After sometime the device abruptly died.	84
4.10 Noise power spectra from a nanotube device at 4 K. V_{gate} is fixed. Each curve is taken at a different V_{bias}	86
4.11 Hysteresis in a CNTFET I - V_{gate} curve.	87
4.12 Left: Measured current as a function of V_{bias} at $V_{gate} = 0.304\text{V}$. Right: Time series at fixed V_{bias} and V_{gate} . Colors for each individual time series correspond to those in the bias sweep.	88
4.13 Simulated noise power spectrum for a CNTFET.	89
4.14 Noise power spectra from a nanotube device at 4 K. V_{gate} is fixed. Each curve is taken at a different V_{bias}	90
4.15 Left: $S_I \cdot f$ plotted against measured current with $V_{bias} > 0$ at a range of V_{gate} . Right: The same data plotted against conductance.	91

LIST OF FIGURES

4.16 Conductance (Top) and $\log_{10} S_I \cdot f$ (Bottom) as a function of V_{bias} and V_{gate}	92
5.1 Diagram of typical DC measurement setup.	96
5.2 Diagram of typical DC measurement setup.	97
5.3 Circuit diagram and photo of the current-to-voltage amplifier. The amplifier has a fixed gain of $1V/10^7A$. Each power line is filtered with a $0.47\mu F$ capacitor. The $5pF$ capacitor in the feedback loop forms a low pass filter with the $10M\Omega$ resistor, with a cutoff frequency of about $3kHz$	99
5.4 Circuit diagram and photo of the active subtractor/adder circuit. The DPDT switch is used to change between adder/subtractor circuits. The output state also features an antialiasing filter with $10kHz$ cutoff not drawn here.	100
5.5 Circuit diagram and photo of the AC-DC adder. The voltage is added in the first stage, while the second stage consists of a two-pole RC low pass filter with a cutoff frequency of $1kHz$ to suppress any switching noise from the voltage sources.	101
5.6 (a) Parallel magnetic field sample holder. (b) 24-pin BNC breakout box for Fischer connectors.	102
5.7 Liquid helium dunker with parallel field sample holder (far right).	103
5.8 Oxford Heliox with the sample holder removed from helium 3 pot (far left).	104
5.9 Photo of the RMC 3He cryostat with the sample holder removed from the 3He pot.	105
5.10 Oxford Kelvinox dilution refrigerator with custom built three sample holder (far right).	107
6.1 Conductance as a function of V_{bias} and V_{gate} for all measured ferromagnetic quantum dots.	112
6.2 Calculating the lever arm using Coulomb diamond geometry.	113
6.3 Top: A diagram of the magnetization of the ferromagnetic nanotube contacts corresponding to the data shown in the lower plot. Bottom: TMR signal measured through a carbon nanotube quantum dot.	114
6.4 Tunneling magnetoresistance measurements taken on device SCF72 (17-19) at $V_{gate} = 0V$. The plots show data for $V_{bias} = 5mV$ (left) and $V_{bias} = 10mV$ (right).	115
6.5 Conductance as a function of V_{gate} for sample SCF72. Note the conductance peak at $V_{gate} = 0V$	118
6.6 Conductance as a function of V_{bias} and V_{gate} in samples SCF75 (left) and SCF96 (right). Note the differential conductance peaks in dark blue running parallel to the diamond edges in each sample.	119

LIST OF FIGURES

6.7	Current as a function of V_{gate} in samples SCF75 (top) and SCF96 (bottom). No clear periodicity is visible in either measurement implying disorder along the nanotube.	121
6.8	Figure adapted from [1]. (a) Double quantum dot levels. Numbering refers to the occupation of (QDA,QDB). $\delta\epsilon$ is the splitting between single particle energy levels. U and U' are the charging energies. (b) With strong coupling the (1,1) and (0,2) states hybridize to form bonding and anti-bonding orbitals S_1 and S_2 different from the triplet state T . (c) At negative bias the (1,1) to (0,2) transition is forbidden by spin blockade as the (0,2) must be a spin singlet. (d) The transition is allowed in the reverse bias situation.	121
6.9	A comparison of the SCF75 negative differential conductance data (a) with double quantum dot data (b) and simulations (c) from Reference [1].	122
6.10	Table tabulating possible occupation numbers, spin states, and relevant energy level splittings for low occupation number quantum dots as calculated by Weinmann et al. [2].	123
6.11	A comparison between simulated transport through a quantum dot with spin selection rules and data from SCF75. The simulation is taken from Weinmann et al. [3]. Simulation data shows regions of negative differential conductance as bright white lines. Data on the right shows regions of negative differential conductance in dark blue.	124
6.12	(a) Energy level diagram for an F-CNT-F quantum dot. The two barrier colors represent the two spin dependent tunnel barrier heights for spin up and spin down electrons. Blue and red arrows illustrate the different tunneling rates for up and down spins. (b) SCF72 conductance at $B = 0$. (c) SCF72 conductance at $B = 4T$	125
6.13	Conductance as a function of V_{gate} and V_{bias} for sample SCF72 at $B = 0T$ (a) and -4T (b). Solid lines trace conductance peaks. Dashed lines trace suppressed peaks. (c) Schematic of energies on the dot. (d) Sketch of energy levels as seen in the Coulomb diamond plots.	126
6.14	Top: Conductance as a function of V_{bias} and V_{gate} in zero field. Bottom: Conductance measured over the same portion of the quantum dot spectrum in a 2T magnetic field.	129
6.15	Top: Conductance as a function of V_{bias} and V_{gate} in zero field. Bottom: Conductance measured over the same portion of the quantum dot spectrum in a 2T magnetic field.	130
6.16	Conductance as a function of V_{bias} and V_{gate} at $B = 2T$ in sample SCF96. Note the difference in slope in the excited states of the two Coulomb diamonds seen at negative bias and the strong negative differential conductance.	132

LIST OF FIGURES

7.1 (a) Energy diagram showing the density of states of each material in the F-I-S junction. Figure adapted from [4]. (b) Superconducting density of states with Zeeman splitting. (c) Spin-dependent kernel used to calculate the tunneling current. (d) Differential conductance as measured through the junction. Different spin-resolved peaks are labeled σ_{1-4} . Figures (b)-(d) are adapted from [5].	135
7.2 Energy diagram showing the density of states and energy levels in a F-QD-S junction. Figure adapted from [4].	137
7.3 Scanning electron microscope image of sample MT7. The leads are alternating Co and Nb, starting with Co at the top. Each section of nanotube between two adjacent leads forms a 300nm long quantum dot. The nanotube is not visible because of the 30kV accelerating potential used to make the image.	139
7.4 Conductance as a function of V_{gate} in MT7. The inset shows a region with clear two-fold symmetry in the addition energy.	140
7.5 Conductance as a function of V_{bias} and V_{gate} in 0T (top) and 1T (bottom) magnetic field parallel to the leads.	141
7.6 Scanning electron microscope image of sample scfmh8. The three wide leads are Nb, while the three narrow leads are Py. These leads are connected to bonding pads made with electron beam lithography and thermally evaporated Cr/Au layers.	142
7.7 Current (left) and conductance (right) as a function of V_{bias} in sample SCFMH8.	143
7.8 Top left: Coulomb diamonds in 0T. The white dashed line marks the gate voltage where the field sweep was taken. Top right: Coulomb diamonds in 2T parallel field. Bottom: Conductance as a function of V_{bias} and parallel magnetic field. Here V_{bias} was the fast sweep axis. Dashed lines represent approximate peak positions.	145
7.9 Conductance as a function of V_{bias} and parallel magnetic field in SCFMH8. V_{bias} was the fast sweep axis. Dashed lines represent approximate peak positions. Magnetic field sweep direction is from left to right.	146
7.10 Conductance as a function of V_{bias} and parallel magnetic field in samples MT7 (left) and SCFMH8 (right). Conductance curves have been offset for clarity.	146
7.11 Current as a function of field measured at V_{bias} between -2.5 and 2.5mV. The same measurement was made from 0 to -3T with similar results. See Figure 7.17 for a summary of the switching behaviors at both field polarities.	149
7.12 A comparison of the current versus field data with fast and slow sweep axes reversed.	150

LIST OF FIGURES

7.13 Left column shows current as a function of magnetic field for the Py-CNT-Nb quantum dot. Right column shows the same data for a Nb-CNT-Nb quantum dot on the same nanotube. Note the appearance of a conductance change at 0.5T in some of the Nb-CNT-Nb data with no hysteresis.	151
7.14 Current as a function of field measured at V_{bias} between -2.5 and 2.5mV for a Nb-CNT-Nb quantum dot.	152
7.15 (a) A schematic of sample SCFMH8. Purple leads are Py, blue are Nb. The two quantum dots measured for Figure 7.11 and 7.14 are circled in red. (b) An energy level diagram representing the tunneling at $V_{bias} = 0.153$	
7.16 (a) An energy level diagram in zero field. (b) The same diagram with Zeeman splitting of the quantum dot levels and the superconducting density of states.	154
7.17 Position of the hysteretic switching events as a function of V_{bias} at positive and negative magnetic field values. Note, the field was not swept through 0. Positive field data was taken for all bias voltages, then negative field data. This is done to separate the feature at 0.5T from any effects related to the switching magnetization of the leads, as discussed in Section 6.1	155
8.1 (a) Room temperature gate sweep of a palladium contacted quantum dot at positive bias voltage. (b) Resistances versus temperature curve for the same device. Coulomb blockade effects begin to dominate the transport below 10 K.	158
8.2 (a) Conductance as a function of V_{gate} in a Pd contacted nanotube quantum dot at 4K. (b) Conductance as a function of V_{bias} and V_{gate} taken in the region marked by dashed lines in (a).	159
8.3 Two local gating techniques. Left: A top gated devices with a low temperature ALD grown Al_2O_3 layer separating the top gate from the underlaying nanotube. Right: a side gated devices with narrow Cr/Au leads positioned between the Co leads 200 nm from the nanotube. . .	159
8.4 Left: Current as a function of V_{BG} . Right: Current as a function of V_{TG} . Even in this simple example it is clear that the local gates are much more effective at tuning the Fermi level on the carbon nanotube.	160
8.5 Top: Current as a function of V_{TG} and V_{BG} . Bottom: A cut across the plot demonstrating how both gates can be used together to keep the tunnel barrier height fixed while varying the Fermi level on the quantum dot.	161
8.6 Schematic of a CNT tunnel probe under two narrow aluminum wires.	162

LIST OF FIGURES

8.7	Figure taken from Ref [6]. (a) Potential seen by vortices along width of the aluminum nanowire as a function of applied perpendicular magnetic field. (b) Potential seen by vortices along width of the aluminum nanowire as a function of applied current. (c) Critical current as a function of applied perpendicular magnetic field. The Weber blockade region can be seen clearly in Region III.	163
8.8	Figure taken from Ref [6]. (a) IV curves as a function of applied magnetic field. The Weber blockade region can be clearly seen around 100mT. (b) Close up of the Weber blockade region. (c) Weber blockade effect with superconducting regions containing a fixed number of vortices seen in blue.	165
8.9	(a) SEM image of a typical aluminum wire tunnel probe device. The Pd leads connected to the nanotube form a quantum dot under the device. (b) Conductance through the nanotube quantum dot with aluminum nanowire on top. (c) Conductance as a function of back gate voltage through the same devices.	166
8.10	(a) Approximate band structure of a semiconductor. (b) Band splitting along the k-axis due to spin-orbit coupling. (c) Additional Zeeman splitting along the E-axis leads to individual, helical conduction bands.	170
8.11	Left: A typical tunnel probe device with aluminum leads and a Cr/Au tunnel probe. Right: Data taken from a similar device with Niobium leads at 250mK.	171
A.1	Custom projection lithography setup in the JHU physics department cleanroom. (a) The arrows from left to right show the UV lamp, sliding UV filter, and mask holder. (b) A projection lithography mask and holder. The arrow shows the mask itself.	180
A.2	OAI mask aligner in the JHU physics department cleanroom. (a) The mask aligner. (b) A typical 3" chromium on glass mask.	182
A.3	Adobe Illustrator designs used for optical and electron beam lithography masks. (a) The pink outlines show the large molybdenum leads patterned with the mask aligner. Inside that pattern are the four $3\text{ }\mu\text{m}$ catalyst islands patterned with electron beam lithography. (b) An SEM micrograph of a sample after CVD growth fitted into the pattern. (c) A complete circuit design. In this case, the layers are normal metal (green), ferromagnet (purple), and superconductor (blue).	183
A.4	Zeiss EVO50 SEM with Raith control computer and external beam blanker.	184
A.5	The Markovic lab ALD reactor. Gas flow is from right to left.	190

LIST OF FIGURES

A.6 (a) A substrate with catalyst islands and a few long nanotubes before patterning. (b) The same substrate after patterning and liftoff. Comparing the two images, it is clear that the use of sonication during liftoff has broken many of the nanotubes.	193
A.7 The Markovic lab probe station. Four sharp probes are located under an optical microscope. Each can be connected to external sources and measurements using BNC connectors.	194
A.8 (a) Kulicke and Soffa wire bonder. (b) An optical image of a completed device mounted in a chip carrier. (c) An SEM image detailing aluminum wires bonded to large gold leads.	195
B.1 3He pot temperature versus time for the RMC 3He cryostat.	207

Chapter 1

Introduction

A quantum dot is a metal or semiconductor structure in which electron levels are quantized due to confinement in all three dimensions. Confinement of electrons in a potential well is one of the first problems taught in introductory quantum mechanics. Like most introductory level problems, at first glance it appears to be an unrealistically simple model. Contrary to that first impression, potential wells can be simple to fabricate and show a remarkable array of physical phenomena. In the simplest picture, electrons confined to the potential well can be thought of as an artificial atom, with each additional electron added filling the lowest unoccupied energy level and subject to spin and orbital degeneracies.

Fabricating a potential well requires confining electrons within a physical constriction with tunnel barriers. This is clear from the results of the infinite well problem, where the energy levels are proportional to $1/L^2$. As long as the electron temperatures

CHAPTER 1. INTRODUCTION

are lower than the energy level spacing, the quantum level spacing can be observed by measuring electrons hopping into and out of the constriction. The important question in fabrication becomes, what sizes are small enough? The simplest cold temperature to reach in a modern laboratory is 4K, the temperature of a liquid helium bath. $k_B T$ provides a sensible energy scale from which to derive typical quantum dot sizes.

Three dimensional nanoparticles must be grown or patterned down to dimensions of approximately 10nm and become very difficult contact electrically [7,8]. In two dimensions, defining a quantum dot requires complex gate structures on top of two dimensional conductors constricting electrons to areas with dimensions less than 100nm [9,10]. Carbon nanotubes, however, are intrinsically one dimensional conductors with diameters of approximately one nanometer. In this case, only the length along the tube axis must be constricted to a few hundred nanometers to observe quantum levels at 4K. Making this constriction can be as simple as fabricating two metal contacts to the nanotube, where the metal/nanotube interface provides the confinement potential. The same metal contacts that define the quantum dot make it possible to perform electronic transport measurements through the quantum dot. In this way the quantum mechanical structure is revealed by observing the tunneling of electrons through the dot. All of this, combined with simple carbon nanotube growth techniques, make nanotubes an ideal platform for studying quantum dot physics.

This thesis work focuses on fabrication techniques and electronic transport measurements on this specific type of mesoscopic device, carbon nanotube quantum dots.

CHAPTER 1. INTRODUCTION

In this introduction, the motivations behind this work will be explained along with an outline of what is to be discussed.

1.1 Transport Spectroscopy in Quantum Dots

Using transport spectroscopy to probe low energy density of states can yield a great deal of insight into the nature of the materials being probed. A simple conductance measurement through two materials and a tunnel barrier measures a convolution of the density of states for each of the materials, $N_1(E)$ and $N_2(E)$.

$$G \sim \int N_1(E)N_2(E) \frac{df(E + eV)}{dV} dE \quad (1.1)$$

At low temperatures, the derivative of the Fermi function is approximated by a delta function and provides a sharp kernel for this convolution. By measuring the conductance across the junction, much can be learned about the nature of the materials, such as in the work of Tedrow and Meservey on measuring the polarization of magnetic materials [11]

By using making a two junction device, and introducing a constriction in the intermediate material, either through local gating or by using low dimensional materials, an interesting situation is created. At low temperatures, the confinement of

CHAPTER 1. INTRODUCTION

electrons in the constriction will dominate the transport. Consider an electron confined within a one dimensional length, L . The electron has energies on the order of $E \sim \hbar^2 k \pi^2 / 2mL^2$. For length scales smaller than 100nm and $k_B T < E$, the quantum mechanical levels in the constriction dominate the electron transport through the device. The measured conductance will show discrete levels corresponding to the filling of the quantum levels in the constriction.

Calculating the electron transport properties through a quantum dot is considerably more complicated than the application of Equation 1.1. At small sizes and low temperatures, not only is the filling of the quantum levels in the dot important, but the electron-electron interactions on the dot must be considered, as well as the interactions between the dot, the two materials connected to it through tunnel barriers, and any electrostatic gates. The Hamiltonian for such a quantum dot with N electrons looks like [12]:

$$H_N = \sum_{n=1}^N \left(\frac{\mathbf{p}_n^2}{2m^*} - e \int_V dV \rho_{ion}(\mathbf{r}) G(\mathbf{r}_n, \mathbf{r}) + \frac{e^2}{2} G(\mathbf{r}_n, \mathbf{r}) - e \sum_i \phi_i \alpha_i(\mathbf{r}_n) + e^2 \sum_{m=1}^{n-1} G(\mathbf{r}_m, \mathbf{r}_n) \right) \quad (1.2)$$

In order, these terms describe the kinetic energy of the electrons, the energy of interactions with fixed ions in the system, image charge potential for an individual electron, changes in potential energy from interaction with i gate electrodes, and a self-energy term that should be renormalized away. Obviously, comparing every experiment to this model is impractical and unnecessary. Section 2.4 will introduce the

CHAPTER 1. INTRODUCTION

simplest model for capturing quantum dot behavior, called the constant interaction model. In the CI model, the Hamiltonian above is simplified such that conductance through the dot only depends on the energy levels on the dot and the total capacitance of the device, which takes the place of all the electrostatic terms in Equation 1.2. Chapter 2 will discuss the basic behavior, at room temperature and low temperatures, of carbon nanotube quantum dot devices in terms of the constant interaction model.

The constant interaction model can be expanded by adding asymmetric, spin dependent tunnel barriers, and spin interactions between electrons in different energy levels confined to the same dot. This is the case when quantum dots are formed using ferromagnetic and superconducting materials. The interplay between magnetism, superconductivity, and transport through a quantum dot is the focus of much of this thesis.

1.2 Working with Carbon Nanotubes

Carbon nanotube quantum dots are an ideal platform for making the type of transport measurements described above. They are inherently one dimensional conductors with diameters on the order of 1nm. The large aspect ratio of carbon nanotubes ($>1000:1$) leaves plenty of room to fabricate the metallic contacts needed for transport measurements along the nanotube length.

CHAPTER 1. INTRODUCTION

Building carbon nanotube quantum dot devices tends to be a very personal experience. Each young scientist has a list of recipes, opinions, and techniques both scientific and quasi-religious motivations. Occasionally, this effort results in gorgeous datasets and rich physics. Once this happens, the hundreds of devices built, and subtle techniques tested that lead to the publication are quickly cast aside. The lack of transparency hinders reproducibility and progress in the field. An effort has been made in this thesis to detail all of the techniques used in fabrication and comment on their reproducibility.

1.3 Current Work

Chapters 3 and 4 document a variety of nanotube growth and contact fabrication techniques tested in this work. Chapter 3 discusses efforts made in our lab to replicate a number of nanotube growth recipes. In Chapter 4, statistics on the devices made, their fabrication steps, and resulting measurements are discussed. The large volume of devices fabricated allows for a meaningful comparison of fabrication techniques that has not previously been seen. Improved imaging and sample processing techniques are also developed in this chapter. Additionally, a discussion of noise sources in the resulting devices is presented. Recommendations for fabrication are made based on the data analysis.

Chapters 6 and 7 discuss spin-dependent, low-temperature, transport measure-

CHAPTER 1. INTRODUCTION

ments on carbon nanotube quantum dot devices with ferromagnetic and superconducting contacts. These devices allow for the possibility of using applied fields to manipulate quantum states in the device in ways not previously observed. In ferromagnetic devices, we were able to test a number models proposed in previous work and observe, for the first time in F-CNT-F devices, the appearance of conductance suppression and negative differential conductance based on spin selection rules. The F-CNT-S devices show evidence for proximity induced superconductivity as well as spin non-degenerate quantum dot levels in the same device. A measurement of hysteretic conductance switching provides evidence for new transport phenomena in the same devices. These measurements are the first attempt to analyze conductance through such a device.

Chapter 2

Electronic Properties of Carbon

Nanotubes

Carbon nanotubes exhibit a variety of interesting material and electrical properties. Nanotubes can be used as mechanical oscillators, one dimensional conductors, and quantum dots, among many other applications. The work in this thesis takes advantage of the unique electronic and spin transport properties of carbon nanotubes. By starting with the graphene lattice, these properties are easily derived.

2.1 Electronic Bandstructure of Graphene

The electronic bandstructure of graphene was first calculated in 1947 by P.R. Wallace [13]. This was done as part of an effort to understand the electronic structure

CHAPTER 2. PROPERTIES OF CNTS

of bulk graphite. In this paper, there is mention of the two lowest energy bands and the half filling of a single layer of carbon atoms. It was not until 1984 that Semenoff discussed the existence of a linear dispersion relation for low energy electronic excitations in single layers of carbon atoms [14]. This was done by looking at a generic honeycomb lattice as an analogue of 2+1 dimensional electrodynamics. Semenoff found the low energy electronic band structure of the monoatomic honeycomb lattice matched that of Dirac fermions.

Graphene was first isolated on silicon wafers through mechanical exfoliation in 2004. The semimetallic characteristics were confirmed through measuring transistor curves and the charge carrier sign change through the Hall effect [15]. Shortly after, the same research group confirmed the existance of low energy Dirac fermions in graphene [16].

Beginning with the structure of the monoatomic honeycomb lattice, and following the original work of Wallace, the electronic band structure of graphene will be derived below.

2.1.1 Graphene Lattice

As mentioned above, single layers of carbon atoms, graphene, form a honeycomb lattice. This lattice can be seen in Figure 2.1.

The unit cell is in Figure 2.1 is defined by the two lattice vectors \vec{a}_1 and \vec{a}_2 . Each unit cell is comprised of two atoms. The honeycomb lattice can be thought of as two

CHAPTER 2. PROPERTIES OF CNTS

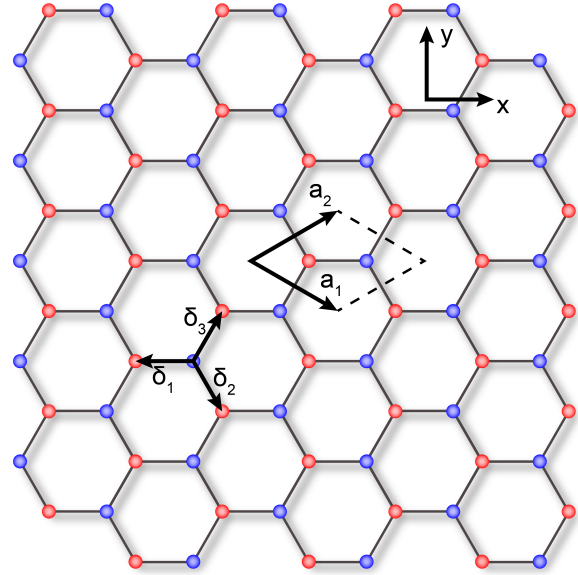


Figure 2.1: The real-space structure of the graphene lattice. Vectors \vec{a}_1 and \vec{a}_2 define the unit cell, which contains two atoms, highlighted in red and blue.

interpenetrating triangular sublattices. With that picture, the honeycomb unit cell contains one atom from each of the two sublattices, highlighted in Figure 2.1 as red (A) and blue (B). Each atom on the lattice contributes one conduction electron.

Using the coordinates defined in Figure 2.1, the lattice vectors are defined, from the center of a honeycomb.

$$\vec{a}_1 = \frac{3a}{2}\hat{i} + \frac{\sqrt{3}a}{2}\hat{j} \quad (2.1)$$

$$\vec{a}_2 = \frac{3a}{2}\hat{i} - \frac{\sqrt{3}a}{2}\hat{j} \quad (2.2)$$

Here a is the carbon-carbon bond distance, 1.42 Å [17].

The reciprocal lattice vectors, \vec{b}_1 and \vec{b}_2 can now be found in the usual way.

CHAPTER 2. PROPERTIES OF CNTS

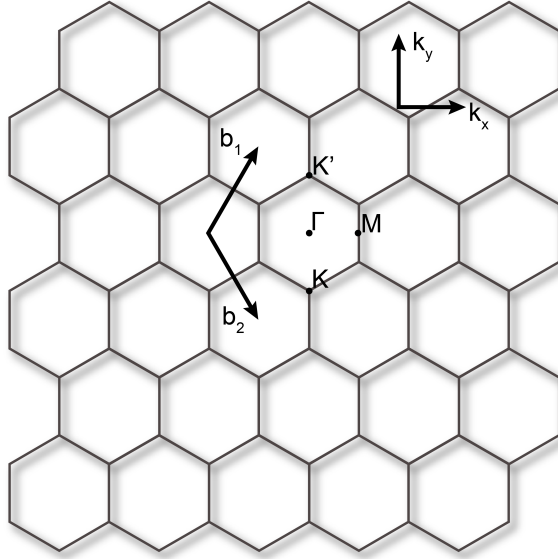


Figure 2.2: The reciprocal lattice of graphene. Vectors \vec{b}_1 and \vec{b}_2 define the Brillouin zone. The high symmetry points Γ , K , K' , and M are labeled.

$$a_i \cdot b_j = 2\pi\delta_{ij} \quad (2.3)$$

Here δ_{ij} is the Kronecker delta. The reciprocal lattice defined by \vec{b}_1 and \vec{b}_2 can be seen in Figure 2.2.

$$\vec{b}_1 = \frac{2\pi}{3a}\hat{i} + \frac{2\sqrt{3}\pi}{3a}\hat{j} \quad (2.4)$$

$$\vec{b}_2 = \frac{2\pi}{3a}\hat{i} - \frac{2\sqrt{3}\pi}{3a}\hat{j} \quad (2.5)$$

The reciprocal lattice is also a honeycomb lattice, rotated 90 degrees from the real space lattice. The size of each Brillouin zone is defined by the reciprocal lattice vectors above. A few high symmetry points have been labelled in the figure. Of particular note are the three K and three K' points. As will be seen in the band

CHAPTER 2. PROPERTIES OF CNTS

structure calculation, these are the points at which the conduction and valence bands will meet to form the Dirac cones that give rise to graphene's interesting low energy conduction properties.

2.1.2 Tight Binding Model

The simplest way to calculate the low energy electronic band structure for graphene is using a nearest neighbor tight binding model, also known as a linear combination of atomic orbitals [18, 19]. In this model, each conduction electron is tightly bound to a lattice site with a small probability of hopping only to a nearest neighbor site. With this simple picture for electron conduction, one can find the lowest energy bands in graphene.

Given that the model deals with the motion of individual electrons and their wavefunctions at each atomic site, the goal will be to solve the time independent Schrödinger equation.

$$\hat{H}\Psi = \varepsilon\Psi \quad (2.6)$$

Ψ is a single particle wavefunction over the whole graphene lattice. As such, it can be written as a linear combination of Bloch wavefunctions.

CHAPTER 2. PROPERTIES OF CNTS

$$u_A(\vec{r}) = \frac{1}{\sqrt{N}} \sum_{\vec{r}_A} e^{i\vec{k}\cdot\vec{r}_A} \phi_{2p_z}(\vec{r} - \vec{r}_A) \quad (2.7)$$

$$u_B(\vec{r}) = \frac{1}{\sqrt{N}} \sum_{\vec{r}_B} e^{i\vec{k}\cdot\vec{r}_B} \phi_{2p_z}(\vec{r} - \vec{r}_B) \quad (2.8)$$

These two functions represent Bloch waves localized on the A and B sublattices, respectively. With these definitions the full single-particle wavefunction can be rewritten as follows:

$$\Psi = C_A u_A + C_B u_B \quad (2.9)$$

$C_{A(B)}$ represents the amplitude of the wavefunction on the A(B) sublattice. With all of the above definitions the time independent Schrödinger equation can be rewritten in a matrix form:

$$\begin{pmatrix} H_{AA} & H_{AB} \\ H_{BA} & H_{BB} \end{pmatrix} \begin{pmatrix} C_A \\ C_B \end{pmatrix} = \varepsilon \begin{pmatrix} S_{AA} & S_{AB} \\ S_{BA} & S_{BB} \end{pmatrix} \begin{pmatrix} C_A \\ C_B \end{pmatrix} \quad (2.10)$$

Where:

$$H_{ij} = \langle u_i | H | u_j \rangle \quad (2.11)$$

$$S_{ij} = \langle u_i | u_j \rangle \quad (2.12)$$

Where H_{ij} and S_{ij} are the hopping integral and wavefunction overlap for electrons on nearest neighbor sites. For simplicity, the rest of this calculation will assume

CHAPTER 2. PROPERTIES OF CNTS

$\langle u_i | u_j \rangle = \delta_{ij}$. Meaning, there is no overlap of the two Bloch wavefunctions and that each of the wave functions is already properly normalized. Rewriting Equation 2.10 yields:

$$\begin{pmatrix} H_{AA} - \varepsilon & H_{AB} \\ H_{BA} & H_{BB} - \varepsilon \end{pmatrix} \begin{pmatrix} C_A \\ C_B \end{pmatrix} = 0 \quad (2.13)$$

Non-trivial solutions to Equation 2.13 exist when:

$$\begin{vmatrix} H_{AA} - \varepsilon & H_{AB} \\ H_{BA} & H_{BB} - \varepsilon \end{vmatrix} = 0 \quad (2.14)$$

Solving equation 2.14 gives the energy eigenvalues in terms of the matrix elements defined in equation 2.11.

$$\varepsilon = H_{AA} \pm |H_{AB}| \quad (2.15)$$

Where the relations $H_{AA} = H_{BB}$ and $H_{AB} = H_{BA}^*$ were used.

In order to obtain a useful expression for the energy bands in terms of the electron momentum \vec{k} , Equation 2.15 must be simplified using the expressions for the Bloch wavefunctions.

$$H_{AA} = \frac{1}{N} \sum_{\vec{r}_A} \sum_{\vec{r}'_A} e^{i\vec{k} \cdot (\vec{r}_A - \vec{r}'_A)} \int \phi_{2p_z}^*(\vec{r} - \vec{r}_A) \hat{H} \phi_{2p_z}(\vec{r} - \vec{r}'_A) d^3\vec{r} \quad (2.16)$$

$$H_{AB} = \frac{1}{N} \sum_{\vec{r}_A} \sum_{\vec{r}_B} e^{i\vec{k} \cdot (\vec{r}_A - \vec{r}_B)} \int \phi_{2p_z}^*(\vec{r} - \vec{r}_A) \hat{H} \phi_{2p_z}(\vec{r} - \vec{r}_B) d^3\vec{r} \quad (2.17)$$

CHAPTER 2. PROPERTIES OF CNTS

The summation in Equation 2.16 can be evaluated to yield:

$$H_{AA} = \int \phi_{2p_z}^*(\vec{r} - \vec{r}_A) \hat{H} \phi_{2p_z}(\vec{r} - \vec{r}_A) d^3\vec{r} = \varepsilon_{p_z} \quad (2.18)$$

Where ε_{p_z} is the energy of a single electron on a p_z orbital. For the sake of simplicity, the rest of this chapter will assume $\varepsilon_{p_z} = 0$.

In order to simplify Equation 2.17 it is useful to define the vectors pointing from an atom on the B sublattice to its three nearest neighbors on the A sublattice.

$$\begin{aligned} \vec{\delta}_1 &= -a\hat{i} \\ \vec{\delta}_2 &= \frac{a}{2}\hat{i} - \frac{\sqrt{3}}{2}a\hat{j} \\ \vec{\delta}_3 &= \frac{a}{2}\hat{i} + \frac{\sqrt{3}}{2}a\hat{j} \end{aligned} \quad (2.19)$$

With these definitions Equation 2.17 can be rewritten as:

$$\hat{H}_{AB} = \sum_{i=1}^3 e^{i\vec{k}\cdot\vec{\delta}_i} \int \phi_{2p_z}^*(\vec{r}) \hat{H} \phi_{2p_z}(\vec{r} - \vec{\delta}_i) d^3\vec{r} \quad (2.20)$$

Since the exact form of the Hamiltonian is not known, the integral in Equation 2.20 cannot be evaluated. However, the integral clearly represents the overlap between the wavefunction of an electron in a p_z orbital on the A lattice and its nearest neighbor on the B lattice. With that in mind, the hopping amplitude t is defined:

$$t = \int \phi_{2p_z}^*(\vec{r}) \hat{H} \phi_{2p_z}(\vec{r} - \vec{\delta}_i) d^3\vec{r} \quad (2.21)$$

CHAPTER 2. PROPERTIES OF CNTS

Note, there is only one hopping amplitude, independent of the index i , since the distance between all nearest neighbors, $|\delta_i|$, is the same. With this definition, the overlap integral can be rewritten once more.

$$H_{AB} = t \sum_{i=1}^3 e^{i\vec{k} \cdot \vec{\delta}_i} \quad (2.22)$$

Equation 2.22 can be combined with the assumption that the onsite energy can be set to zero, $\varepsilon_{p_z} = 0$ to give the final effective Hamiltonian.

$$\hat{H} = \begin{pmatrix} 0 & t \sum_i e^{i\vec{k} \cdot \vec{\delta}_i} \\ t \sum_i e^{-i\vec{k} \cdot \vec{\delta}_i} & 0 \end{pmatrix} \quad (2.23)$$

Using these same results in Equation 2.15 gives the two lowest energy bands in terms of the hopping amplitude, t .

$$\varepsilon(\vec{k}) = \pm t \left| \sum_i e^{i\vec{k} \cdot \vec{\delta}_i} \right| \quad (2.24)$$

$$\varepsilon(\vec{k}) = \pm t \sqrt{1 + 4 \cos\left(\frac{3a}{2}k_x\right) \cos\left(\frac{\sqrt{3}a}{2}k_y\right) + 4 \cos^2\left(\frac{\sqrt{3}a}{2}k_y\right)} \quad (2.25)$$

These two bands can be seen in Figure 2.3. Note that the plot does not assume $S_{ij} = \langle u_i | u_j \rangle = \delta_{ij}$, which introduces some asymmetry in the valence and conduction bands.

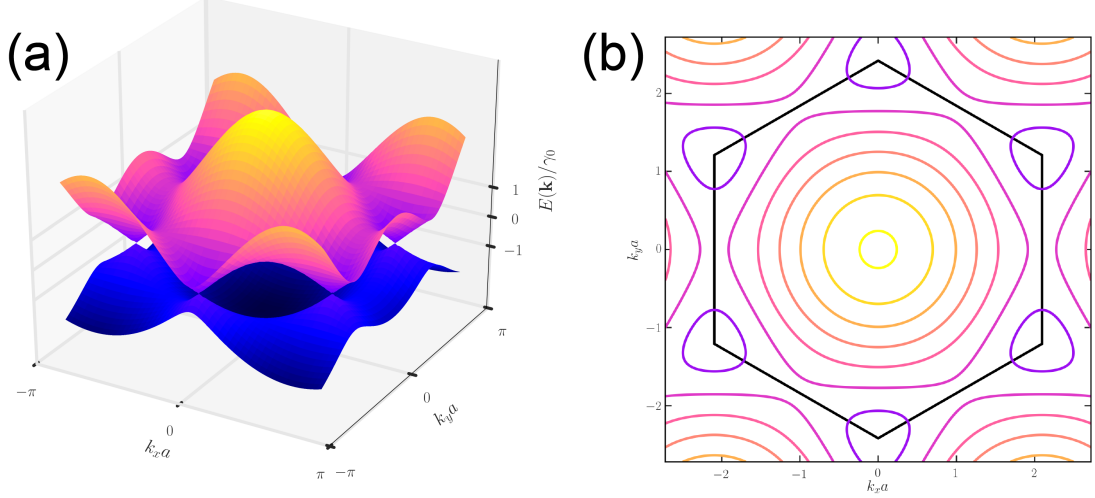


Figure 2.3: (a) The π -bands of graphene calculated using a nearest neighbor tight binding model. (b) A contour plot of the upper band with the first Brillouin zone drawn. The bands meet at the three K and three K' points at the vertices of the Brillouin zone.

2.1.3 Low Energy Bandstructure of Graphene

For low energy electronic excitations, conduction will be dominated by the band-structure near the K and K' points. There are only two inequivalent points, since the other 4 are equivalent by the symmetry of the honeycomb lattice. Consider the two points located at:

$$\vec{K} = 0\hat{i} - \frac{4\pi}{3\sqrt{3}a}\hat{j} \quad (2.26)$$

$$\vec{K}' = -\vec{K} = 0\hat{i} + \frac{4\pi}{3\sqrt{3}a}\hat{j} \quad (2.27)$$

To get the low-energy dispersion relation, expand the Hamiltonian in Equation 2.23 around the K point.

$$\vec{k} = \vec{K} + \vec{q} \quad (2.28)$$

$$\hat{H} \approx -i\frac{3at}{2} \begin{pmatrix} 0 & q_x + iq_y \\ -(q_x - iq_y) & 0 \end{pmatrix} \quad (2.29)$$

Similarly, expanding around the K' point yields:

$$\hat{H} \approx -i\frac{3at}{2} \begin{pmatrix} 0 & q_x - iq_y \\ -(q_x + iq_y) & 0 \end{pmatrix} \quad (2.30)$$

By defining $v_f \equiv 3at/2\hbar$, using the standard Pauli matrices, and rotating the phase, Equations 2.29 and 2.30 can be written in a more suggestive form.

$$\hat{H}_K = \hbar v_f \vec{\sigma} \cdot \vec{q} \quad (2.31)$$

$$\hat{H}_{K'} = \hbar v_f \vec{\sigma}^* \cdot \vec{q}$$

These Hamiltonians describe massless Dirac fermions in 2D. Meaning, low-energy conduction electrons are fermions with dispersion relations like that of a massless photon. This is clear in the low-energy dispersion relation.

$$\varepsilon(\vec{q}) = \pm \hbar v_f q \quad (2.32)$$

It is also important to note, in Equation 2.31, that the sublattice structure has lead to a spin-1/2 degree of freedom. This degree of freedom is known as the valley

CHAPTER 2. PROPERTIES OF CNTS

degeneracy or pseudospin.

A useful consequence of the pseudospin is the reduction in scattering in graphene and carbon nanotubes. The reduced backscattering is a result of the introduction of an additional symmetry to the system. This reduction in scattering leads to unusually high mobilities and long spin coherence lengths in both materials. The increased spin coherence length make carbon nanotubes suitable for spin-based devices.

2.2 Electronic Bandstructure of Carbon Nanotubes

Now that the bandstructure a graphene sheet has been calculated, finding the electronic bandstructure of various carbon nanotubes is as simple as applying a few boundary conditions [17, 18, 20, 21].

The structure of a carbon nanotube can be completely described by its chiral vector.

$$\vec{C}_h = m\vec{a}_1 + n\vec{a}_2 \quad (2.33)$$

$$\vec{C}_h = \frac{3}{2}(n+m)a\hat{i} + \frac{\sqrt{3}}{2}(n-m)a\hat{j}$$

This vector describes how to roll a graphene sheet to form the nanotube. The tube is formed by rolling the graphene sheet such that the tip and tail of \vec{C}_h meet. The

CHAPTER 2. PROPERTIES OF CNTS

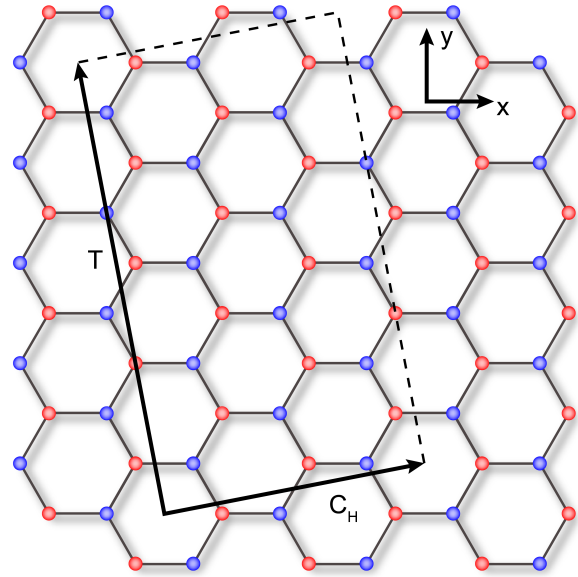


Figure 2.4: The real-space structure of a carbon nanotube. The nanotube unit cell is defined by the vectors \vec{C}_h and \vec{T}

indices (n, m) describe the type of nanotube that is formed. A tube where $0 < m < n$ is known as chiral, $m = n$ is an armchair nanotube, and $m = 0$ is a zig-zag nanotube. Armchair and zig-zag tubes get their names from the shape of the carbon bonds on the edge of the unit cell.

An example of a chiral $(2,1)$ nanotube unit cell can be seen in Figure 2.4. The unit cell is defined by the chiral vector \vec{C}_h and the translation vector \vec{T} , which is defined as:

$$\vec{T} = t_1 \vec{a}_1 + t_2 \vec{a}_2 \quad (2.34)$$

where $t_1 = (2m + n)/d_R$, $t_2 = (2n - m)/d_R$ and $d_R = \gcd(2n + m, 2m + n)$. These two vectors can be used to calculate a few basic properties of the nanotube. The

CHAPTER 2. PROPERTIES OF CNTS

diameter of the nanotube is found from the chiral vector:

$$d = \left| \vec{C}_h \right| / \pi = \frac{\sqrt{3}a}{\pi} \sqrt{n^2 + nm + m^2} \quad (2.35)$$

The number of graphene unit cells contained in the nanotube unit cell is also easily calculated:

$$N = \frac{\left| \vec{C}_h \times \vec{T} \right|}{\left| \vec{a}_1 \times \vec{a}_2 \right|} = \frac{2}{d_R} \sqrt{n^2 + nm + m^2} \quad (2.36)$$

Knowing the number of graphene unit cells contained in the nanotube unit cell yields a lot of useful information about the band structure. There are $2N$ carbon atoms in the nanotube unit cell and N conduction electrons. There will be $2N$ bands (one for each carbon atom) that will be half-filled, just like the graphene bandstructure.

The reciprocal lattice vectors for the carbon nanotube defined by (n, m) can be found in the usual way.

$$\begin{aligned} \vec{C}_h \cdot \vec{K}_1 &= \vec{T} \cdot \vec{K}_2 = 2\pi \\ \vec{C}_h \cdot \vec{K}_2 &= \vec{T} \cdot \vec{K}_1 = 0 \end{aligned} \quad (2.37)$$

$$\begin{aligned} \vec{K}_1 &= -\frac{(t_2 \vec{b}_1 - t_1 \vec{b}_2)}{N} \\ \vec{K}_2 &= \frac{(m \vec{b}_1 - n \vec{b}_2)}{N} \end{aligned} \quad (2.38)$$

CHAPTER 2. PROPERTIES OF CNTS

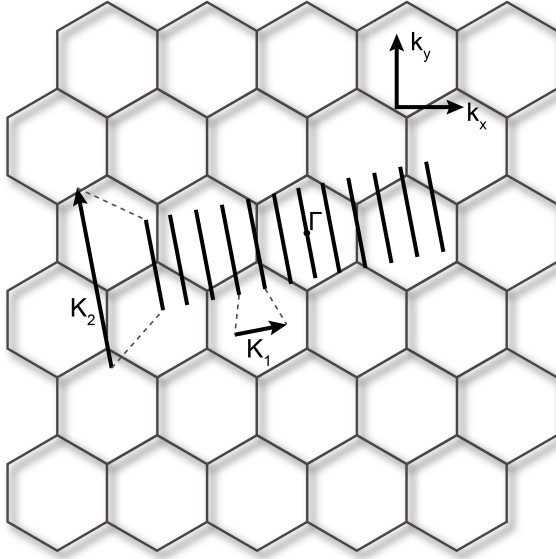


Figure 2.5: The reciprocal lattice of a carbon nanotube, defined by the vectors K_1 and K_2

The reciprocal space of the unrolled nanotube is quantized along \vec{K}_1 and continuous along \vec{K}_2 . This means the electron momentum k in the nanotube is quantized along the direction of C_h . These quantized 'cutting lines' define the electronic bands in the carbon nanotube:

$$\vec{k} \cdot \vec{C}_h = 2\pi\mu \quad (2.39)$$

Where μ is an integer from $1 - N/2$ to $N/2$ and $\mu = 0$ cuts through the Γ point at the center of the graphene Brillouin zone. The structure of the nanotube reciprocal lattice, defined by K_1 and K_2 can be seen in Figure 2.5.

With all of these definitions, the electron momentum in the carbon nanotube can be rewritten.

$$\vec{k} = \mu \vec{K}_1 + k_{\parallel} \frac{\vec{K}_2}{|\vec{K}_2|} \quad (2.40)$$

The bands for a generic nanotube can be found by simply inserting this definition for the momentum into the graphene bands derived in Equation 2.25.

2.2.1 Types of Carbon Nanotubes

The electronic properties of a carbon nanotube are determined by its chirality, (n, m) . If one of the cutting lines, as seen in Figure 2.5, passes through a K or K' point, the nanotube will have a metallic band structure. Like in graphene, two of the valence and conduction bands will meet at discrete points at the Fermi energy. If this is not the case, and none of the cutting lines pass through a K or K' point, the nanotube will be semiconducting with a bandgap determined by the chirality.

To determine if a nanotube is semiconducting or metallic, one can look at the projection of \vec{K} , the vector pointing to a K point in the graphene Brillouin zone, and \vec{K}_1 , the nanotube reciprocal lattice vector.

$$\frac{\vec{K} \cdot \vec{K}_1}{\vec{K}_1 \vec{K}_1} = \frac{(2n + m)}{3} \quad (2.41)$$

From Equation 2.41, it is clear that a nanotube is metallic if $(n - m) \bmod 3 = 0$. There are two other cases, where $(n - m) \bmod 3 = 1$ or $(n - m) \bmod 3 = 2$. Each of these results in a semiconducting nanotube. Based on these results, in a collection of

CHAPTER 2. PROPERTIES OF CNTS

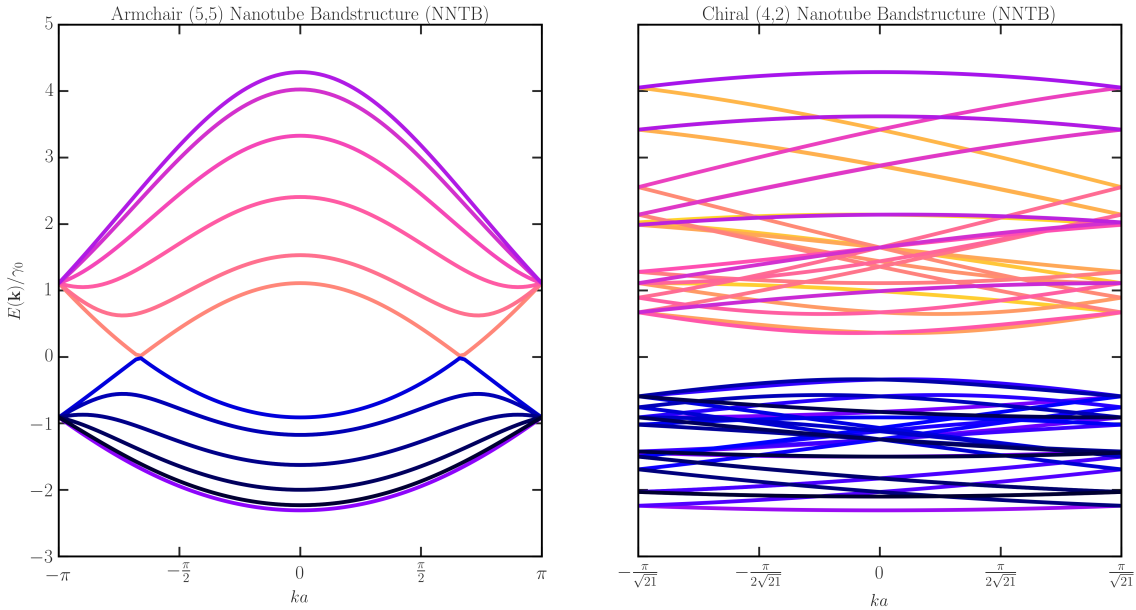


Figure 2.6: Two types of carbon nanotube bandstructure. The left plot shows a metallic $(5, 5)$ armchair nanotube. The right plot shows a semiconducting $(4, 2)$ chiral nanotube.

nanotubes with random chirality, (n, m) , there will be roughly $1/3$ metallic and $2/3$ semiconducting nanotubes.

Figure 2.6 shows the full bandstructure of a metallic $(5, 5)$ armchair nanotube and a semiconducting $(4, 2)$ chiral nanotube. These have 20 and 56 bands, respectively.

2.2.2 Low Energy Bandstructure of Carbon Nanotubes

To calculate the full set of bands for a generic nanotube (n, m) is cumbersome. The basic properties for a generic nanotube can be more easily calculated by first

CHAPTER 2. PROPERTIES OF CNTS

expanding the graphene bands about the K and K' points as in Equation 2.32, then using the quantized momentum derived in Equation 2.40. Doing this yields the low energy dispersion relation for a generic carbon nanotube:

$$\varepsilon_\mu(k) = \pm \frac{2\hbar v_f}{d} \sqrt{\left(\frac{m-n}{3} - \mu\right)^2 + \left(\frac{kd}{2}\right)^2} \quad (2.42)$$

Where μ is the band index, d is the nanotube diameter, and k is the electron momentum along the nanotube axis. Looking at the first term in parentheses, it is clear that the nanotube will be metallic if $(m - n)/3$ is an integer. In that case, there will be some integer μ for which the valence and conduction bands meet at the Fermi energy. This is consistent with the condition derived previously for metallic and semiconducting chiral vectors. Using that information, the low energy bandstructure can be written as:

$$\varepsilon(k) = \pm \left(\frac{1}{2} E_g(n, m) + \frac{\hbar^2}{2m^*} k^2 \right) \quad (2.43)$$

$$\varepsilon(k) = \pm \hbar v_f k \quad (2.44)$$

These are the approximate bandstructures at low energy. Semiconducting nanotubes have a bandgap, $E_g(n, m)$ dependent on the chirality, and an effective mass m^* dependent on the lowest band curvature. Metallic nanotubes maintain the massless Dirac fermion properties found in graphene at low energies. This calculation has ignored spin-orbit coupling that can be derived from the curvature of the graphene

lattice to form the nanotube, and curvature along the nanotube length [22]

2.3 Carbon Nanotube Field Effect Transistors

The simplest device that one can make with a carbon nanotube is a field effect transistor. A nanotube is placed, or grown, on a silicon substrate capped with an insulating silicon dioxide layer. Source and drain contacts are then made to the nanotube. The completed three terminal device consists of the source, drain, and a doped silicon substrate serves as the gate, with a silicon dioxide layer acting as the gate dielectric. A schematic of such a device is seen in Figure 2.7

Measurements on carbon nanotube field effect transistors (CNTFETs) depend on the type of carbon nanotube that has been contacted.

Metallic source/drain contacts typically form Schottky barriers with carbon nanotubes. The polarity of the resulting CNTFET is thus determined by the relation between the work function of the contact material and nanotube. For metals with a relatively high work function, such as Pd, Ti, Cr, and Co, the devices are expected to be p-type. Metals with a lower work function, such as Al, Mg, and Sc, can produce n-type transistors. However, many of these low work function metals also happen to have a very poor wettability on the nanotube surface, which leads to large contact resistances, making the devices difficult to fabricate and measure.

CHAPTER 2. PROPERTIES OF CNTS

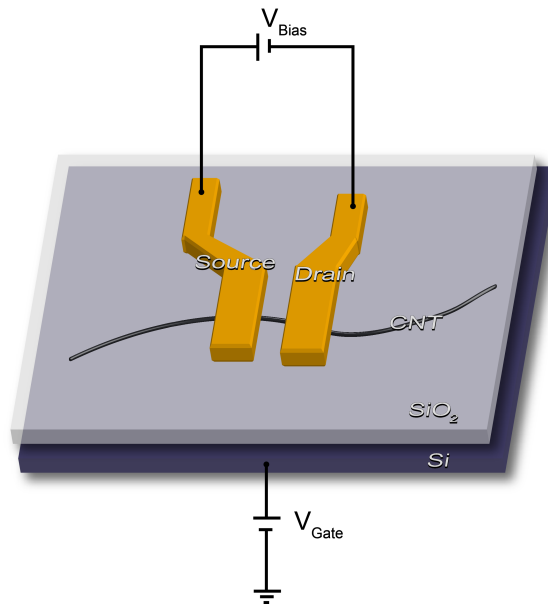


Figure 2.7: Schematic of a carbon nanotube field effect transistor.

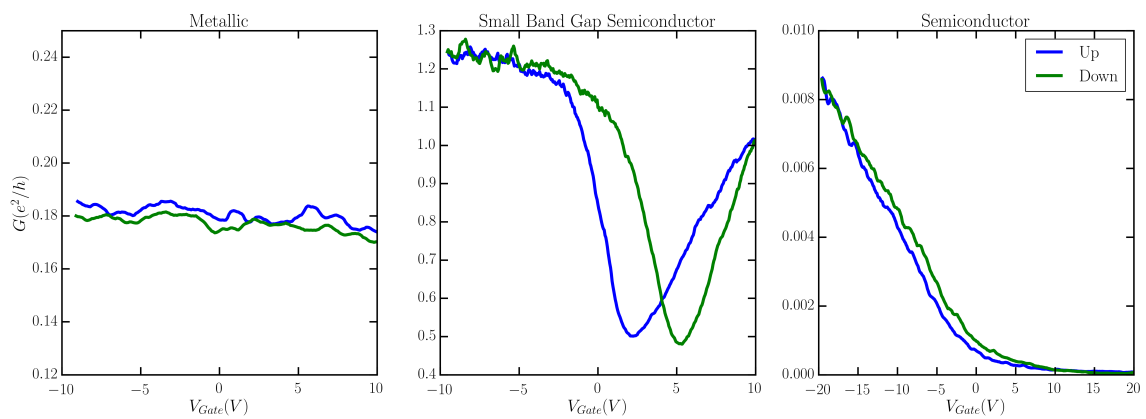


Figure 2.8: Current versus gate voltage characteristics for three types of CNTFET.

CHAPTER 2. PROPERTIES OF CNTS

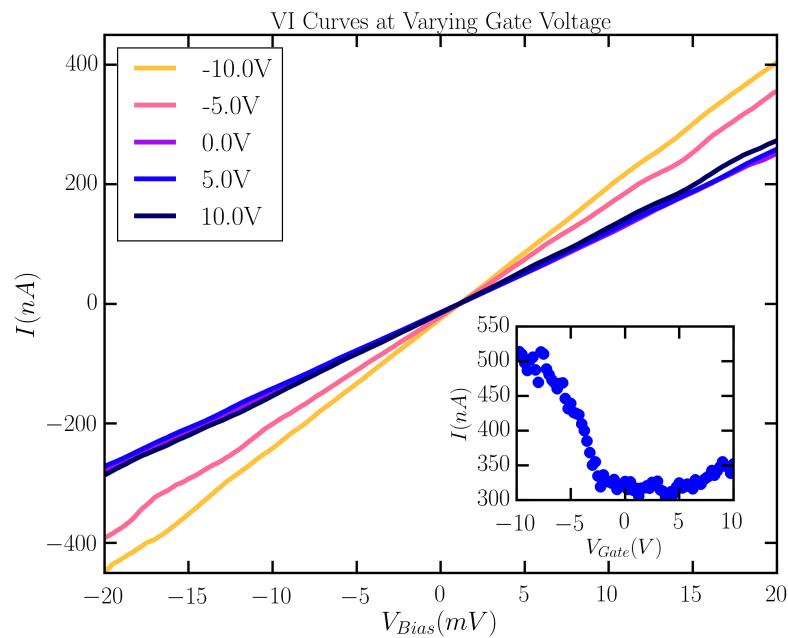


Figure 2.9: IV characteristics of a typical small band gap semiconducting CNTFET. The current saturates at higher bias voltage, but is not typically measured due to avalanche breakdown of the devices. Inset: Current versus gate at a fixed bias for the same device.

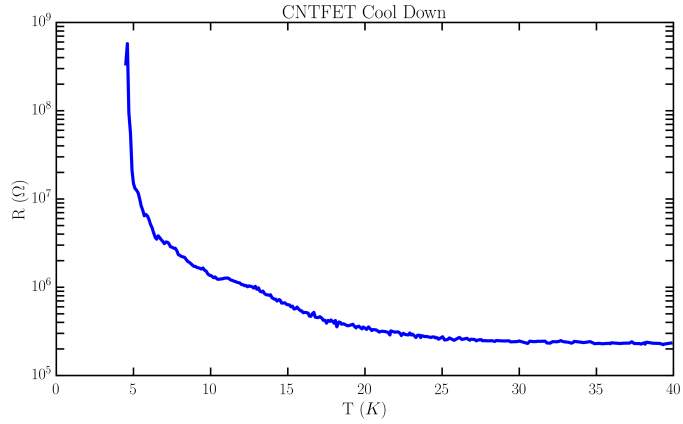


Figure 2.10: R-T curve of a CNTFET cooled to 4 K

2.4 Carbon Nanotube Quantum Dots

When cooled to low temperatures ($\lesssim 10$ K), the device drawn in Figure 2.7 exhibits quantum mechanical behavior. For a sufficiently short channel length ($L \lesssim 500$ nm), electrons become confined within the carbon nanotube and behave like quantum mechanical particles in a box. This device is called a quantum dot. The resistance versus temperature plot in Figure 2.10 shows the sharp increase in resistance as the tunneling through the device is suppressed at low temperatures.

Once the device is cold, the filling of electrons can be controlled by varying the bias and gate voltages. A schematic of the relevant energies is seen in Figure 2.11. The bias voltage can be used to change the relative chemical potential of the source and drain metals. The gate voltage is then used to change the chemical potential on the quantum dot relative to the source/drain.

The model we will use to discuss this device is called the constant interaction

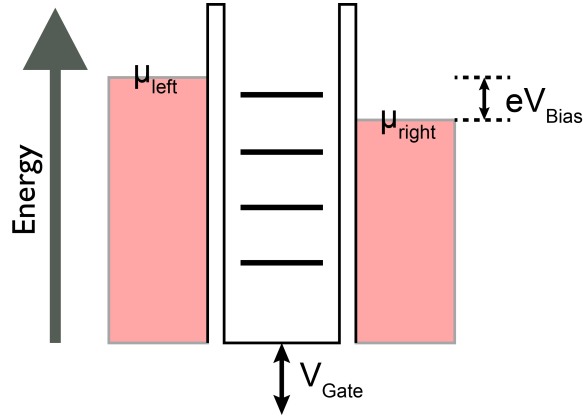


Figure 2.11: Quantum dot energy diagram.

model. Tunnel barriers naturally form at the interface between the metal contacts and the nanotube. At low temperatures, this leads to weak tunneling on/off the nanotube (quantum dot). Because of this, the number of electrons confined on the dot at any given time is an integer, N . Adding an additional electron to the dot requires overcoming the Coulomb repulsion between the additional electron and those already confined on the dot. The constant interaction model treats this charging energy as a constant, regardless of the number of electrons confined on the dot. The model also assumes that the states on the quantum dot are not affected by the electron-electron interactions [23].

With these assumptions, it is simple to find the energy required to add an electron to the dot. To begin, the total energy on the dot can be approximated.

$$U(N) = \frac{[e(N - N_0) - C_g V_g]^2}{2C} + \sum_N E_n \quad (2.45)$$

CHAPTER 2. PROPERTIES OF CNTS

Here N_0 is the charge on the dot at zero gate voltage, C_g is the gate capacitance, and $C = C_{source} + C_{drain} + C_{gate}$. The summation represents the sum over all of the filled quantum dot levels, denoted by E_n . The chemical potential is defined as $\mu(N) = U(N) - U(N+1)$.

$$\mu(N) = (N - N_0 - \frac{1}{2}) \frac{e^2}{2C} - \frac{eC_g V_g}{C} + E_N \quad (2.46)$$

Finally, the addition energy is given by the change in chemical potential from the N to $N+1$ levels.

$$\begin{aligned} \Delta\mu(N) &= \frac{e^2}{2C} + (E_{N+1} - E_N) \\ \Delta\mu(N) &= \frac{e^2}{2C} + \Delta E \end{aligned} \quad (2.47)$$

Equation 2.47 gives the amount of energy required to add the N th electron to the quantum dot. Note that the first term in this energy is the constant interaction term representing the Coulomb repulsion, $E_{charging} = \frac{e^2}{2C}$.

The simplest measurement to make on a quantum dot like the one described here, is to measure the conductance as a function of the gate voltage. Figure 2.12 shows diagrammatically how the process works. At very small bias ($\mu_{left} \sim \mu_{right}$), the gate voltage is varied. When the chemical potential on the source/drain are resonant with a level on the quantum dot, a peak is observed in the conductance. Otherwise, conductance across the dot is suppressed. Spacing between conductance peaks should

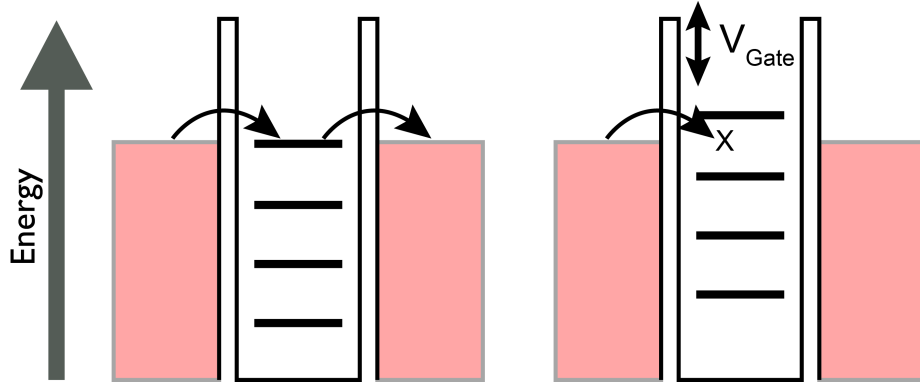


Figure 2.12: Left: A quantum dot level resonant with the source/drain chemical potential. Right: The same device in the blockaded region.

follow Equation 2.47.

Figure 2.13 shows conductance as a function of gate voltage through an actual carbon nanotube quantum dot device. The inset reveals some hints of four-fold symmetry that is an important part of the structure of the nanotube quantum dot [24]. Adding the first electron to the dot costs an energy $\Delta\mu(N) = \frac{e^2}{2C} + \Delta E$. However, the electron spin and valley degeneracy combine to give each level in the quantum potential well a degeneracy of four. The next three electrons added move into the same energy level, which only requires an energy of $\Delta\mu(N) = \frac{e^2}{2C}$ for each electron. This pattern continues for each level on the dot, such that the energy required to add the N electron is always larger than the energy required to add the $N+1$, $N+2$, and $N+3$ electrons.

Varying the bias voltage also changes the relative alignment of the energy levels on the dot and the chemical potentials of the source and drain electrodes,, as illustrated in Figure 2.14. If a level on the quantum dot lies between the chemical potentials

CHAPTER 2. PROPERTIES OF CNTS

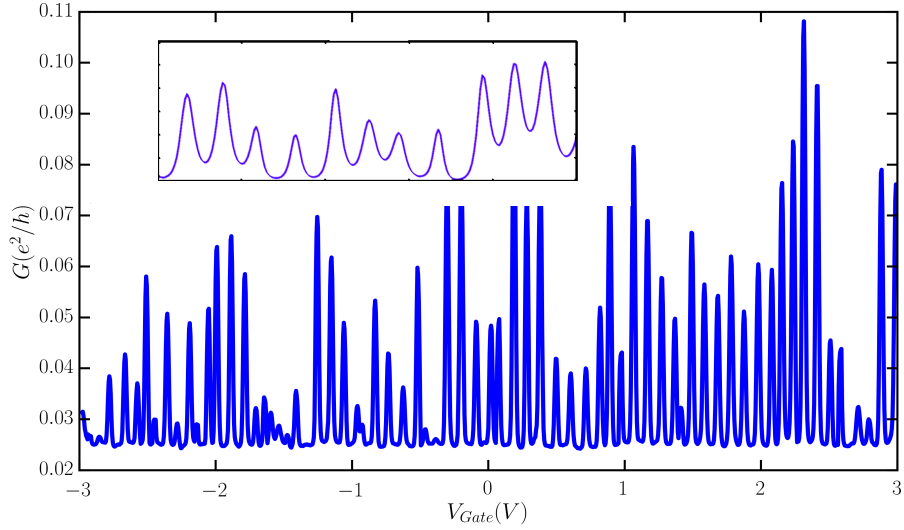


Figure 2.13: Conductance as a function of applied gate voltage in a cobalt contacted nanotube quantum dot. Inset: A close up showing a region with clear 4 fold symmetry.

of the source and the drain (the bias window), conductance is possible. Otherwise, if there are no energy levels in the bias window, the conductance through the device is suppressed. With further increases of the bias voltage, higher order conductance processes are possible.

Figure 2.15 shows current and conductance as a function of applied bias voltage in the blockaded regime. The differential conductance is suppressed across the dot at low bias voltage. At higher bias, the bias window increases, eventually encompassing an energy level on the dot, which causes the conductance to increase. A further increase of the bias voltage allows for transport through excited states and higher order processes, which will be discussed in later chapters.

Finally, measuring conductance as a function of both the bias and gate produces a stability diagram of the quantum dot. An example of this can be seen in Figure 2.16.

CHAPTER 2. PROPERTIES OF CNTS

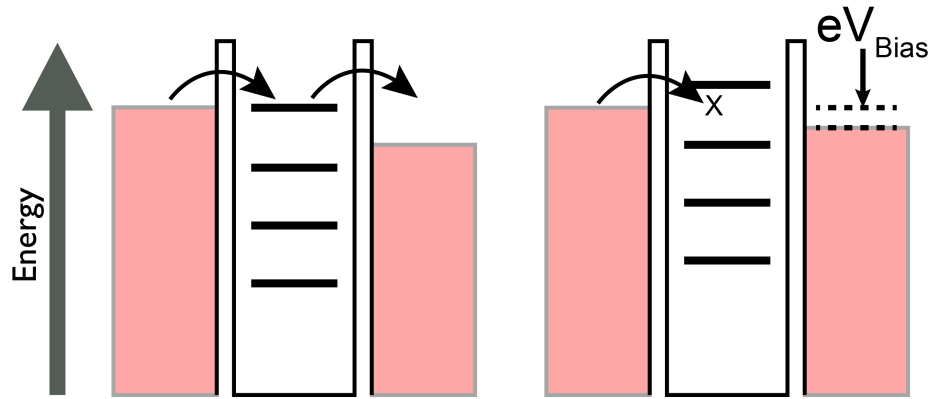


Figure 2.14: Left: A quantum dot level resonant with the drain chemical potential. Right: The same device in the blockaded region.

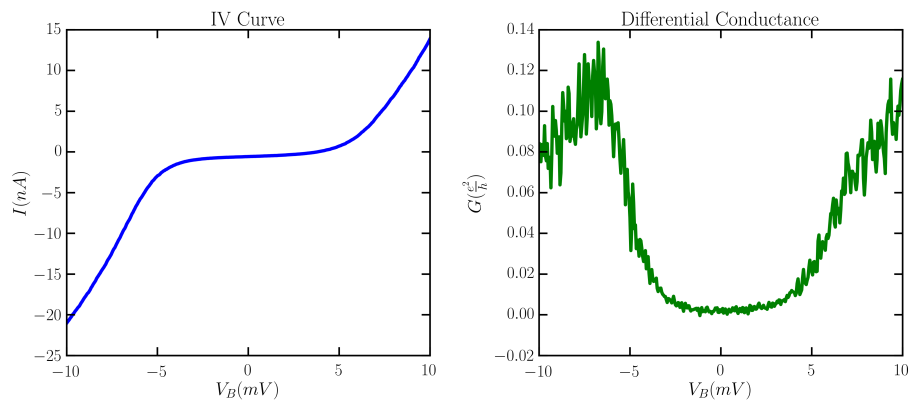


Figure 2.15: Left: An IV curve at fixed gate voltage Right: Differential conductance measured at fixed gate voltage.

CHAPTER 2. PROPERTIES OF CNTS

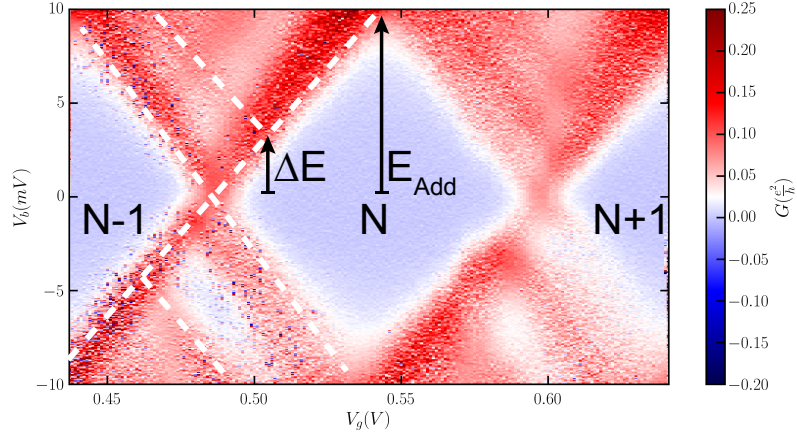


Figure 2.16: Conductance of a cobalt contacted nanotube quantum dot at 4K as a function of bias and gate voltages.

Looking at a cut of this plot at constant bias reproduces Figure 2.13. Similarly, a cut at constant gate voltage reproduces Figure 2.15. Putting both together produces diamond-shaped regions in which the charge on the quantum dot is constant, denoted by $N - 1$, N , and $N + 1$ in the figure. The white dashed lines serve as a guide to the eye. The two black arrows mark the level spacing, ΔE , and addition energy E_{Add} (or $\Delta\mu$). By measuring both of these quantities it is possible to know the level spacing on the quantum dot and the capacitance of the device. By observing changes in the conductance peaks at different fillings and applied fields, much can be learned about the energy levels, interactions, and transport across the quantum dot.

As an illustrative example the properties of the device measured in Figure 2.16 can be calculated. Here the level spacing on the dot is measured to be $\Delta E = 4meV$ and the addition energy $E_{Add} = 9meV$. At low energies the dispersion relation of the nanotube can be assumed to be roughly linear $\varepsilon(k) = \hbar v_f k$. k is quantized because of

CHAPTER 2. PROPERTIES OF CNTS

the confinement potential created by the leads $k = \frac{n\pi}{L}$. The level splitting can then be written as $\Delta E = \frac{\hbar v_f \pi}{L}$, where $v_f = c/300$. Using the measured value of ΔE gives an estimate of $L = 520\text{nm}$, which is consistent with the device design of 500 nm. This result can now be used, along with the addition energy, to find the total capacitance of the quantum dot. Starting with $E_{Add} = \frac{e^2}{2C} + \Delta E$ gives an estimate of $C = 10^{-17}\text{F}$, which is consistent with typical carbon nanotube quantum dot measurements.

Chapter 3

Carbon Nanotube Growth and Placement

In the years since their discovery, many methods of producing electronic devices from carbon nanotubes have been developed. These include random dispersion (Section 3.1), on-substrate catalyst island growth (Section 3.2) and stamping [25, 26]. For this work, the first two methods were successfully used to produce carbon nanotube quantum dots. It was found that the catalyst island growth was much easier to implement and required much less processing time per device at the cost of increased disorder in resulting devices.

Table 3.1: Powder Catalyst

$\text{Fe}(\text{NO}_3)_3 \cdot 9 \text{H}_2\text{O}$	20 mg
$\text{MoO}_2(\text{acac})_2$	5 mg
Al_2O_3	15 mg

3.1 Random Dispersion

The first successful method of nanotube device fabrication was what will be referred to here as random dispersion. First, nanotubes are grown in bulk through chemical vapor deposition (or other preferred method). Then, the nanotubes are suspended in a solution. Finally, the nanotubes are cast onto a substrate. Nanotubes can then be located relative to predefined markers on the substrate.

3.1.1 Catalyst

All of the devices discussed in this thesis have utilized the same, iron-based catalyst [27, 28]. The simplest way to create this catalyst is to combine the ingredients in Table 3.1 in a mortar and pestle and grind until it turns a uniform dark orange color. Adding some additional alumina seems to promote growth of longer tubes, possibly by lowering the density of tubes grown from each alumina/iron/molybdenum cluster.

CHAPTER 3. GROWTH AND PLACEMENT

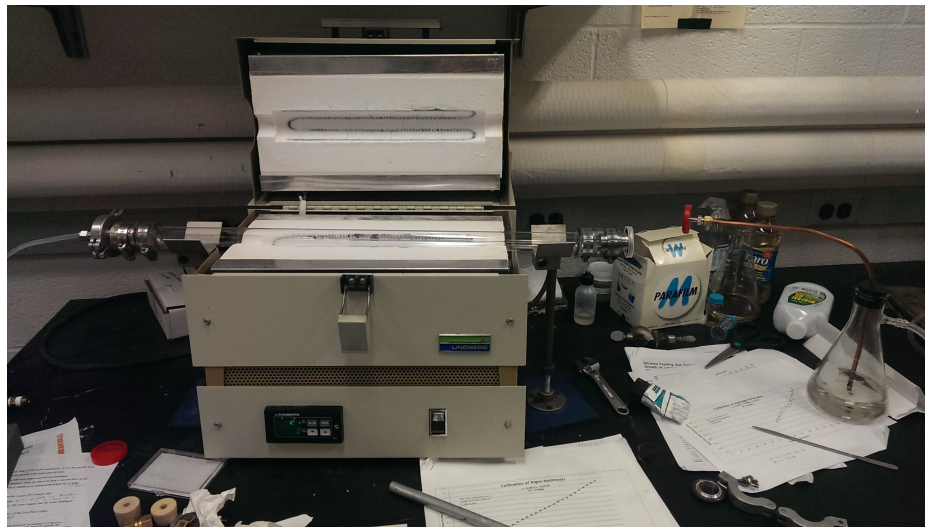


Figure 3.1: The tube furnace fitted with a 1" diameter quartz tube. The tube is sealed at both ends using 1" rubber tubing, cable clamps, and KF25 fittings. Gas flows from left to right in the picture. The gas flows out of the furnace into a mineral oil bubbler to keep hot hydrogen from reaching the air in the room. Gas then flows from the bubbler into the building exhaust.

3.1.2 Growth

Of the many possible techniques for nanotube growth, we choose chemical vapor deposition for its simple implementation. The process is carried out in a Lindberg Blue tube furnace using a 1 inch diameter quartz tube. The furnace, quartz tube, and exhaust filtering are seen in Figure 3.1. This setup has been repeatedly, and successfully, leak checked. Oxygen leaks can be detrimental to the nanotube growth process by forming CO and CO₂ with any free carbon, and potentially causing a fiery reaction with free hydrogen from the methane decomposition.

The gases used in the CVD process, argon, hydrogen, and methane, are fed into the furnace using a custom-made gas handling panel. The panel has three gas channels,

CHAPTER 3. GROWTH AND PLACEMENT

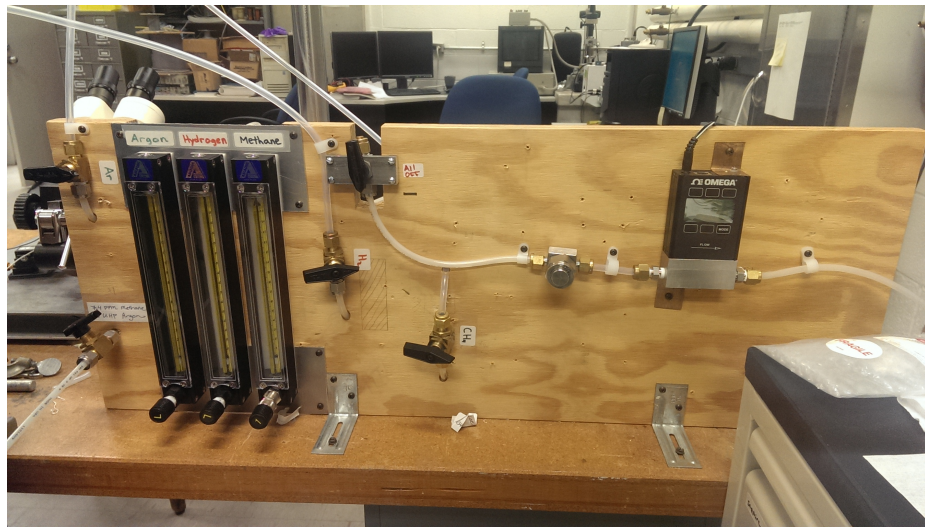


Figure 3.2: The gas handling panel for our Lindberg tube furnace. Gas flow is from left to right.

each with its own analog flowmeter, needle valve, and on/off valve. A digital flowmeter placed at the right side of the panel reads the total flow of combined gas exiting the panel to the furnace. The gas handling panel can be seen in Figure 3.2

The growth procedure begins with filling a ceramic crucible with the iron catalyst described in 3.1.1. The catalyst should be spread in a thin layer across the bottom of the crucible, which is then loaded into the center of a 2-4 foot long quartz tube. The tube is sealed at each end, one side connected to the gas handling panel, and the other connected to the mineral oil filter and building exhaust. Our standard nanotube growth recipe is as follows:

1. Purge the tube by flowing 2000 sccm of Ar for 20 minutes
2. Heat tube to 1000 °C while flowing 1000 sccm Ar and 200 sccm H₂

CHAPTER 3. GROWTH AND PLACEMENT

3. Flow 2000 sccm CH₄ and 200 sccm H₂ for 10 minutes.
4. Set temperature to 0 °C and let the furnace cool while flowing 1000 sccm Ar and 200 sccm H₂

The actual nanotube growth occurs during the methane flow step. The 200 sccm H₂ flow can be omitted, but it does seem to help promote nanotube growth. The flow rates do not need to be precise. Most nanotubes grow in the first few seconds of methane flow regardless of the flow rate. The Ar and H₂ are simply to keep O₂ and H₂O out of the tube.

3.1.3 Nanotube Placement

After the CVD process, the nanotubes remain attached to the iron/alumina/molybdenum catalyst particles, which must be removed before depositing onto a silicon substrate. The nanotube/catalyst powder is first scraped from the ceramic crucible used in the tube furnace. The powder is then mixed with either dichloroethane or dichlorobenzene in a 1 mg to 10 mL ratio. Dichlorobenzene has been found to leave less residue after deposition, but may promote more damage to nanotubes during sonication. This was noted by Justin Silverman, an undergraduate working with our lab on functionalizing short carbon nanotubes. Some attempts were made to use water along with the surfactant SDS. However, SDS turned out to be difficult to remove and no devices were made in this way.

CHAPTER 3. GROWTH AND PLACEMENT

To remove the catalyst particles from the nanotubes, the solution described above must be placed in an ultrasonic bath for 1-60 minutes. The amount of time needed varied a great deal depending on the equipment and solvent used. The goal of this step is to break up large pieces of catalyst, separate nanotube bundles, and break individual nanotubes away from their catalyst particles. Sonication can be stopped when no large pieces of catalyst/nanotube material are visible and the solution has a uniform black color. Leaving the solution in the sonicator for too much time will begin to break long nanotubes. This may be somewhat beneficial in breaking nanotubes at defects that might otherwise affect transport measurements.

When sonication is complete, the solution is transferred to a centrifuge. This step is intended to precipitate the loose catalyst particles from the solution, while leaving the much lighter nanotubes suspended. The centrifuge used in our lab runs at 2200 rpm and nanotube solutions are left inside for 5-10 minutes. Once the centrifuge stops, the precipitate is discarded and the supernatant, containing the suspended nanotubes, is reserved. We also tested using a high-speed, air-powered centrifuge running at 100 000 rpm to separate nanotubes and catalyst. This did lead to much better catalyst separation and cleaner results.,

Now the solution is ready for deposition on a silicon substrate. The substrates are typically pre-patterned with a set of reference markers placed by optical (A.1.2) or electron beam lithography (A.3). An example of a patterned substrate can be seen in Figure 3.3

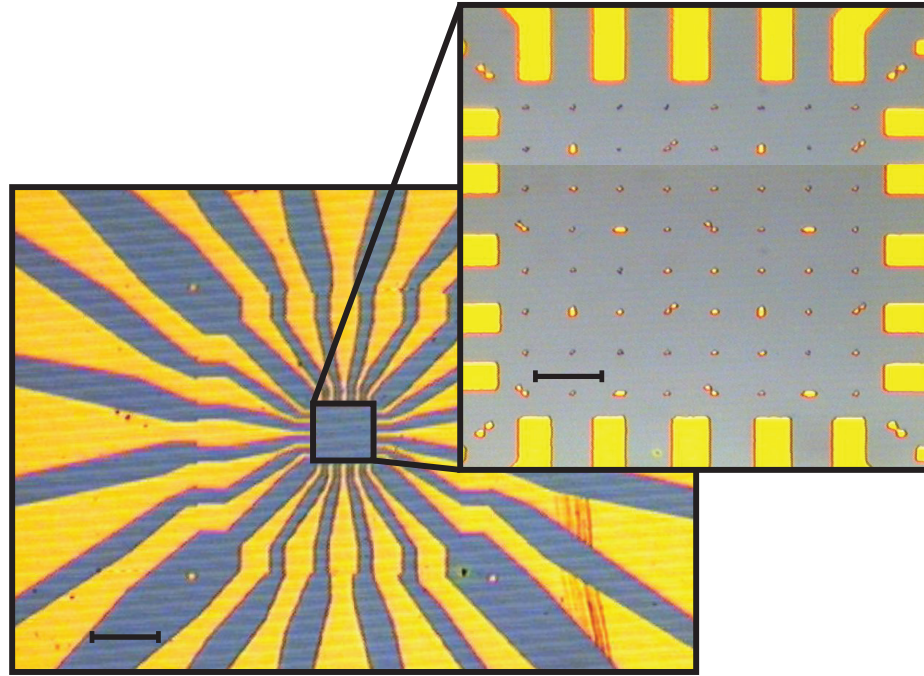


Figure 3.3: A Si/SiO₂ substrate with 1 μm Au markers. Left scale bar: 100 μm. Right scale bar: 20 μm

3.1.4 Advantages and Disadvantages

Despite having some success fabricating devices using randomly dispersed nanotubes and electric force microscopy scans (Section 3.3.2), the process was found to be too time consuming for frequent use. The main failure point was the preparation of nanotube solutions after growth. The concentrations varied significantly, often producing samples with dense nanotube coverage or no nanotubes found in the regions imaged. Additionally, the process of making a suspended nanotube solution is time consuming. Even those solutions with a useful concentration of nanotubes only remain fully suspended for less than 1 hour; meaning the process must be repeated frequently.

3.2 Catalyst Island Growth

In 1998 [28], it was discovered that the same type of catalyst used to grow nanotubes in powder form (Section 3.1.1), could be suspended in solution, patterned, and used to grow nanotubes directly on silicon substrates. When paired with high melting point metals and optical lithography, nanotubes can be grown directly on patterned substrates in known locations. Devices prepared this way take just a fraction of the time to produce. However, these devices were found to be much more prone to other modes of failure, such as leaks in the gate oxide, amorphous carbon contamination on the substrate from the CVD growth process, and defects along the nanotube length.

3.2.1 Catalyst

Many different types of catalyst particles can be used in the growth of carbon nanotubes. The ideal catalyst for patterned growth must be compatible with electron beam or optical lithography. Table 3.2 lists most of the catalysts tested in the Markovic lab. To test each catalyst, sputtered molybdenum markers were patterned using the mask aligner and Futurex NR9 resist. Catalyst islands were then patterned using electron beam lithography. Figure 3.4 shows an example of a substrate with Mo markers/leads and catalyst islands.

All but one of the devices discussed in this thesis were produced using the Fe/Mo/alumina catalyst suspended in water. The islands were patterned using electron

CHAPTER 3. GROWTH AND PLACEMENT

Table 3.2: Patterned Catalysts

Catalyst	Suspended In	Results
Fe/Mo/alumina [27]	Methanol	Easy to pattern. Liftoff difficult. Slowly attacks PMMA mask. Appeared to promote gate leaks through the SiO ₂ layer.
Fe/Mo/alumina [29]	IPA	Poor adhesion to substrate.
Fe/Mo/alumina [30]	DI water	Easy to pattern. Excellent adhesion. No gate leak problems.
FeCl ₃ [31]	DI water	Excellent adhesion to substrate. Not compatible with PMMA mask. Left substrate entirely covered in catalyst. May work well with PDMS stamp.
thermally evaporated Fe [32, 33]	None	Very easy to pattern. Liftoff is clean. Difficult to control the thickness below 1 nm as required.

CHAPTER 3. GROWTH AND PLACEMENT

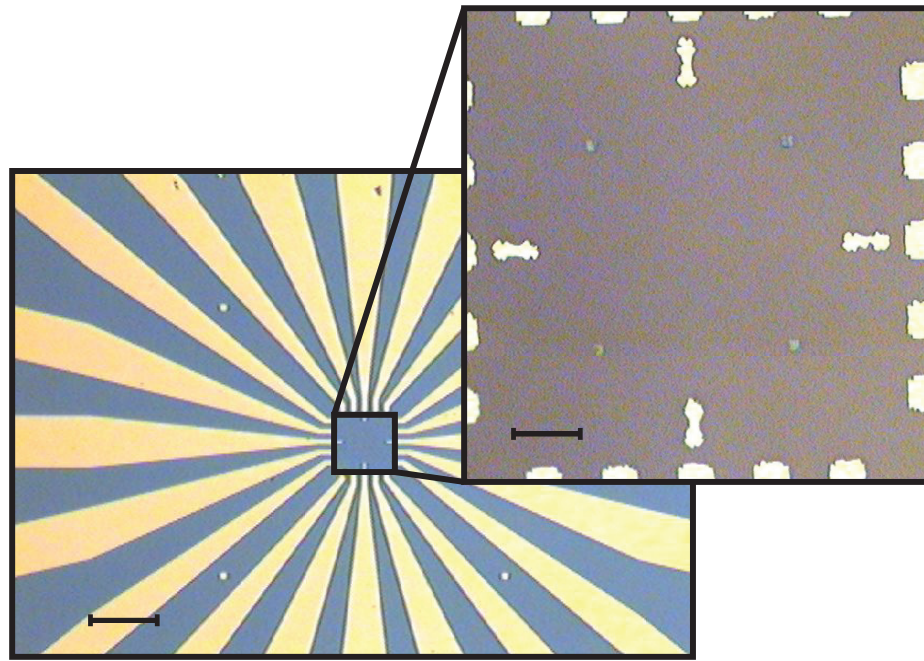


Figure 3.4: A Si/SiO₂ substrate with 3 μm catalyst islands and Mo leads. Left scale bar: 100 μm. Right scale bar: 20 μm

beam lithography. Catalyst is deposited in the following way:

1. Add the powder catalyst from Table 3.1 to 15 mL of DI water and stir for 12 hours
2. Sonicate the solution for 30 minutes
3. Cover the sample in catalyst solution for 30 minutes
4. Dry with N₂ gun
5. Liftoff by sonicating in acetone for 5 minutes, soaking in a clean acetone for 5 minutes, followed by an isopropanol rinse for 1 minute and a DI water rinse for 1 minute

CHAPTER 3. GROWTH AND PLACEMENT

Obtaining reproducible results in the catalyst deposition was the source of much difficulty. The recipe provided here can be repeated before liftoff shows insufficient catalyst coverage on the substrate. Additionally, it is suspected that baking the catalyst on a hot plate to dry the solution leads directly to gate leaks in the SiO₂ layers and later device failure. Thus, there is no baking step in the deposition of our catalyst islands.

3.2.2 Growth

The recipe for on-substrate growth of nanotubes used in this thesis is very similar to the growth recipe for powder catalyst discussed in Section 3.1.2. This recipe was developed over the course of several years from many points of reference [27, 28, 31, 34–37] and my own notes. The recipe is optimized for the 1 inch Lindberg tube furnace as seen in Figures 3.1 and 3.2. Most samples are placed in a smaller 1 cm diameter, 1 foot long quartz tube, then placed in the larger 1 inch diameter quartz tube. This was done to make the samples easier to load into the 1" tube, as well as to reduce turbulence in the gas flow across the sample [31].

The standard nanotube growth recipe used in this work is below:

1. Purge the tube by flowing 2000 sccm of Ar for 20 minutes
2. Heat the tube to 250 °C while flowing 300 sccm Ar and 150 sccm H₂
3. Wait for at least 1 hour

CHAPTER 3. GROWTH AND PLACEMENT

4. Heat the tube to 700 °C while flowing 300 sccm Ar and 150 sccm H₂
5. Wait for 10 minutes
6. Heat tube to 950 °C while flowing 300 sccm Ar and 150 sccm H₂
7. Wait for the temperature to stabilize
8. Flow 700 sccm CH₄ and 150 sccm H₂ for 10-15 minutes
9. Set temperature to 0 °C and let the furnace cool while flowing 300 sccm Ar and 150 sccm H₂

In almost every test, this recipe has grown nanotubes successfully. Steps 2 and 3 are included to remove water vapor from the air that might have collected inside the quartz tube on humid days [34]. Steps 4 and 5 are meant to remove iron oxide from the iron nanoparticles that make up the catalyst.

The most common point of failure in growth has been related to the patterned molybdenum leads/markers on the substrate. Molybdenum oxidizes rapidly at high temperatures. Therefore, any oxygen contamination in the tube during the growth process will form a MoO layer that is then quickly removed by reacting with the high temperature H₂ flow. This process repeats and can lead to the Mo leads being entirely etched away. Additionally, it has been found that opening the furnace too soon during cooling can lead to the Mo leads peeling off of the substrate. This appears to be caused by some super-heating due to IR radiation reflecting off of the surfaces of

CHAPTER 3. GROWTH AND PLACEMENT

the sample and quartz tube. It is a strange phenomenon that is avoided by allowing the furnace to cool to less than 300 °C before opening the lid. These problems could also be solved by using a different high temperature metal such as a W/Pt bilayer, common in many other nanotube projects. Molybdenum was chosen for this work because it is easy to sputter and much more affordable.

3.2.3 Advantages and Disadvantages

Growing nanotubes from catalyst islands near predefined leads and markers offers a large improvement in processing time over the method of random dispersion. Nanotubes produced with this method are longer, cleaner, and easier to locate. These improvements made this method the obvious choice for device fabrication. The main disadvantage found in this technique is the introduction of defects along the nanotube length due to growth along the substrate. Because of this, a large number of devices must be fabricated in order to find one with clean transport properties at low temperature. It is also helpful to limit device lengths to less than 200nm to reduce the chances of a defect being included in the resulting device.

3.3 Imaging Nanotubes

Nanotubes on a SiO₂ surface can be located in a number of ways. This section will review a several different methods, focusing on improvements made in the course

CHAPTER 3. GROWTH AND PLACEMENT

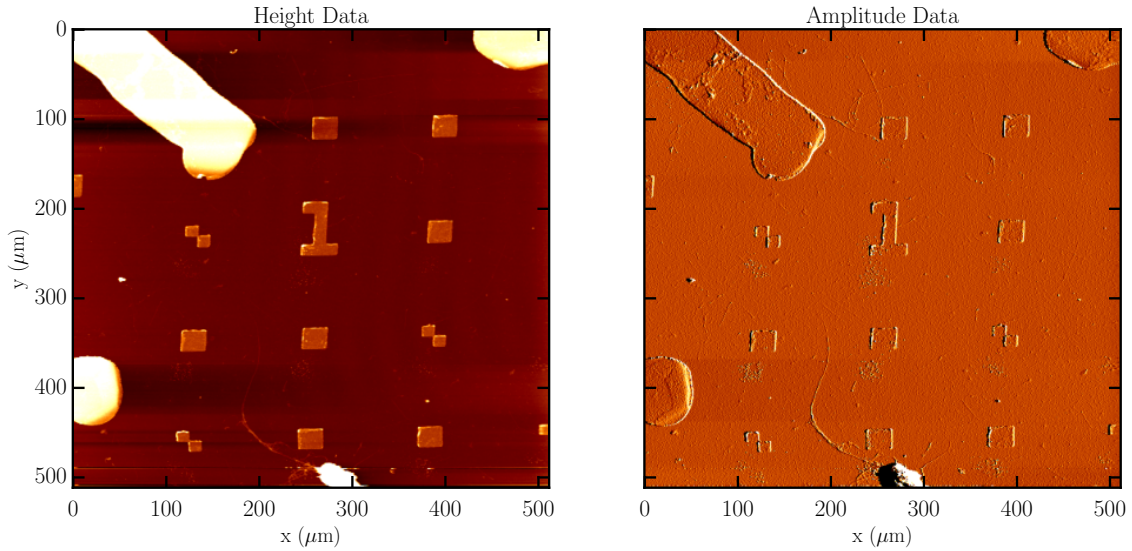


Figure 3.5: AFM height and amplitude scans of nanotubes dispersed over a substrate with $1.5\text{ }\mu\text{m}$ gold markers. The scale bar is $10\text{ }\mu\text{m}$.

of this thesis work.

3.3.1 Atomic Force Microscopy

With nanotubes that have been drop cast onto the surface, the standard method is to locate the tubes relative to the predefined markers using a tapping mode atomic force microscope (AFM). An example of an image created this way is seen in Figure 3.5.

This method is very reliable, but extremely time consuming. In order to resolve nanotubes, as well as the predefined markers in the image, AFM scan sizes must be limited to $25\times 25\mu\text{m}$. Each of these scans takes 30 minutes and many scans are needed to fully image one patterned substrate. Looking closely at Figure 3.5, there are 12

CHAPTER 3. GROWTH AND PLACEMENT

scans covering less than half the substrate. Due to vibrational noise and piezo limits, some images are slightly warped. Stitching the images together is time consuming and inaccurate. One major advantage to AFM imaging is that it is easy to distinguish single tubes from bundles and multiwalled nanotubes, as well as measure nanotube diameter.

3.3.2 Electric Force Microscopy

The Digital Instruments Nanoscope 3 used in our lab is also capable of making electric force microscope (EFM) measurements. An EFM image is made by first measuring the height across the sample in standard tapping mode, then using that height data to run a second ‘interleave’ scan at a fixed height with a bias voltage applied between the tip and sample. By holding the tip at a fixed height, van der Waals interactions between the tip and sample are constant and the only force measured is the electrostatic force from the applied bias voltage. Contrast in the resulting images is related to the different conductivities of the objects on the sample [38]. Thus, conducting (and semiconducting) nanotubes have a high contrast against the insulating SiO_2 substrate. An example of this type of image is shown in Figure 3.6

An entire patterned substrate can be scanned using this method in about 1 hour. The scan size can be increased up to $75 \times 75 \mu\text{m}$ due to the false contrast provided by the large electrostatic forces between the nanotubes and the tip. Rather than appearing as 1 nm in diameter, the tubes appear in the EFM image to be about 100

CHAPTER 3. GROWTH AND PLACEMENT

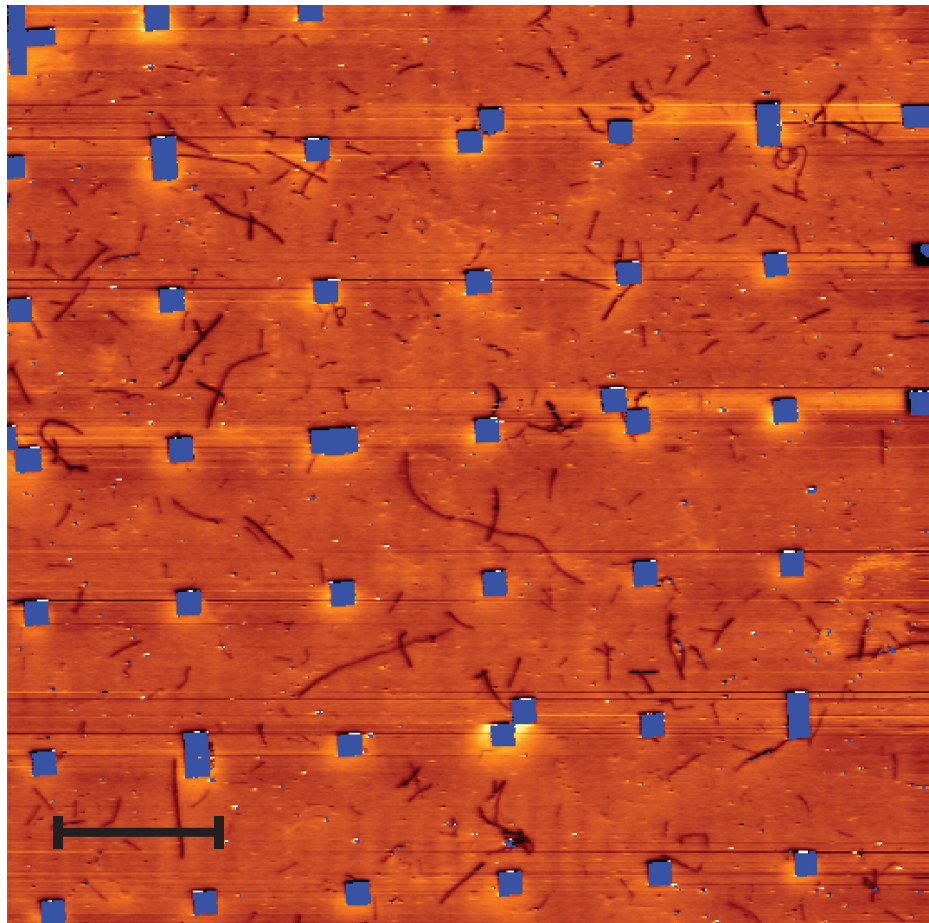


Figure 3.6: An EFM image of nanotubes dispersed over a substrate with $1.5\text{ }\mu\text{m}$ gold markers. The markers have been automatically located using the height data and highlighted in blue on the EFM image. The scale bar is $10\text{ }\mu\text{m}$.

CHAPTER 3. GROWTH AND PLACEMENT

times their real diameter. This was a notable improvement over locating nanotubes using AFM height scans alone. Comparing Figure 3.5 and Figure 3.6, it is clear the EFM image is far more useful in locating nanotubes.

3.3.3 EFM Through PMMA

All of the same techniques from Section 3.3 can be applied to imaging nanotubes grown from patterned catalyst islands. However, because the substrates are not covered in closely spaced markers, it was found that tapping mode AFM height scans were not useful. Scans could only cover a small part of the sample and the resulting images were difficult to orient.

Using electric force microscopy (EFM) made it possible to scan the entire region of interest on the sample in one measurement. An example of this type of scan is shown in Figure 3.7(a). As can be seen in that figure, it was difficult for the AFM tip to avoid crashing into the catalyst islands during the EFM sweep. The catalyst islands are several hundred nanometers in height while the other features on the substrate are less than 10 nm. Such height differences make large area scans difficult in tapping mode. This problem can be avoided by coating the sample in PMMA before scanning with the EFM, as seen in Figure 3.7(b.) The PMMA coating smooths the height differences between the substrate and catalyst islands, without compromising the contrast between the insulating substrate and conducting nanotubes. The idea was adopted from a 2007 paper in which the authors attempted to locate nanotubes

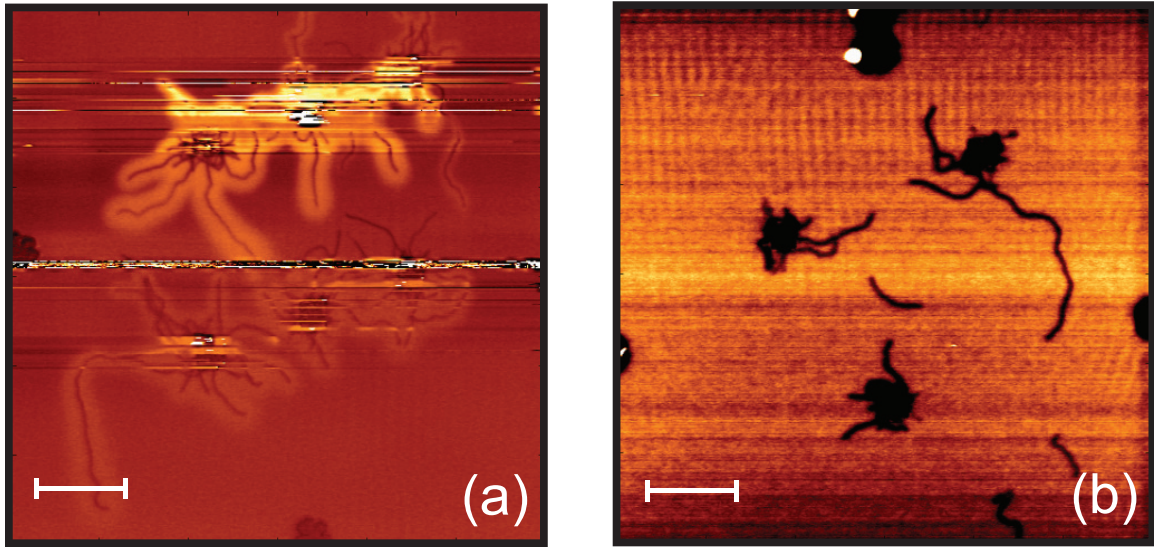


Figure 3.7: (a) Frequency data collected from an EFM scan of a catalyst island sample after nanotube growth. (b) Frequency data collected from an EFM scan of a similar sample. Prior to the scan this sample was coated with a 250 nm PMMA layer. Both scale bars are 10 μm .

suspended in a PMMA layer in three dimensions [39].

3.3.4 Scanning Electron Microscopy

In 2002, a paper [40] was published illustrating that a scanning electron microscope (SEM), operating at a low accelerating potential could provide a similar type of false contrast image as produced by the EFM. The insulating substrate tends to collect charge from the electron beam, while the conducting nanotubes do not. This produces an image in which the nanotubes appear as bright lines about 100 times their actual diameter. An example of this is seen in Figure 3.8.

Typically, an EFM scan of a sample will take 45 minutes. A SEM image of the

CHAPTER 3. GROWTH AND PLACEMENT

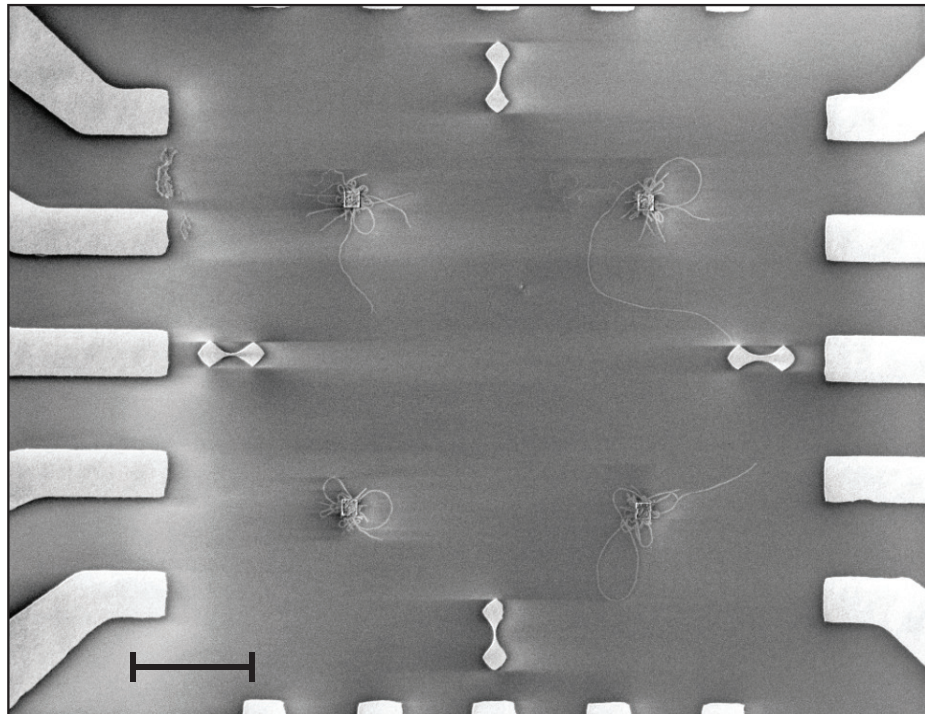


Figure 3.8: A scanning electron micrograph of a catalyst island sample after nanotube growth. The scale bar is 10 μm .

CHAPTER 3. GROWTH AND PLACEMENT

same sample takes less than 2 minutes. However, the SEM can introduce carbon contamination from the high energy electrons passing through small amounts of oil mist back-streaming into the vacuum chamber from the mechanical roughing pump. Due to the large number of samples that were produced to obtain the data in this thesis, it was decided that contamination from the SEM was an acceptable risk, given the immense time savings. No clear effect from carbon contamination was ever observed in the results. Devices made using EFM imaging showed similar disorder and measurement noise.

3.4 Image Filtering

Once it became clear that the scanning electron microscope was by far the most efficient and reliable way to locate carbon nanotubes on a substrate, it also became important to optimize those images to reveal the most information possible. The resolution and contrast in the SEM images produced in our lab are limited by the use of a thermionic LaB₆ filament. Unlike field emission scanning electron microscopes, which are more common in nanofabrication, the thermionic scanning electron microscope has a large initial crossover size, requiring more electromagnetic lens focusing to produce a sufficiently small beam size for imaging. This problem is exasperated when using low accelerating potentials (500-3000 V), which are crucial to achieving good contrast of carbon nanotubes on a silicon substrate.

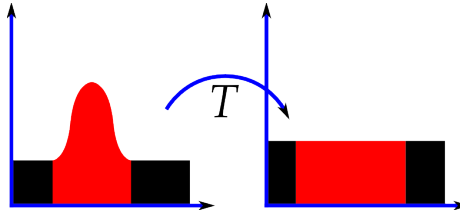


Figure 3.9: An illustration of the histogram equalization process.

3.4.1 Histogram Equalization

This method was based on two corrections. First, a plane fit to correct for the position of the secondary electron detector. Second, calculating the histogram of pixel brightness then transforming it such that there are equal numbers of pixels at each brightness level. An illustration of this can be seen in Figure 3.9

Figure 3.10 shows the process of filtering an SEM image using histogram equalization. At the top of figure is the original image after a plane fit (to correct changes in brightness across the substrate). To the right of the image, the histogram of brightness values and the cumulative distribution function are plotted. The center image is after the histogram equalization. Contrast is now dramatically increased in the image, the histogram is nearly flat, and the cumulative distribution function is linear. Finally, the image is Gaussian filtered using a 3×3 kernel to reduce the high frequency noise, which has been exaggerated by the histogram equalization. The final histogram is not flat quite flat and the cumulative distribution function is not quite linear. However, the contrast in the image has been enhanced significantly

While this filter does succeed in increasing contrast in the image, which was the

CHAPTER 3. GROWTH AND PLACEMENT

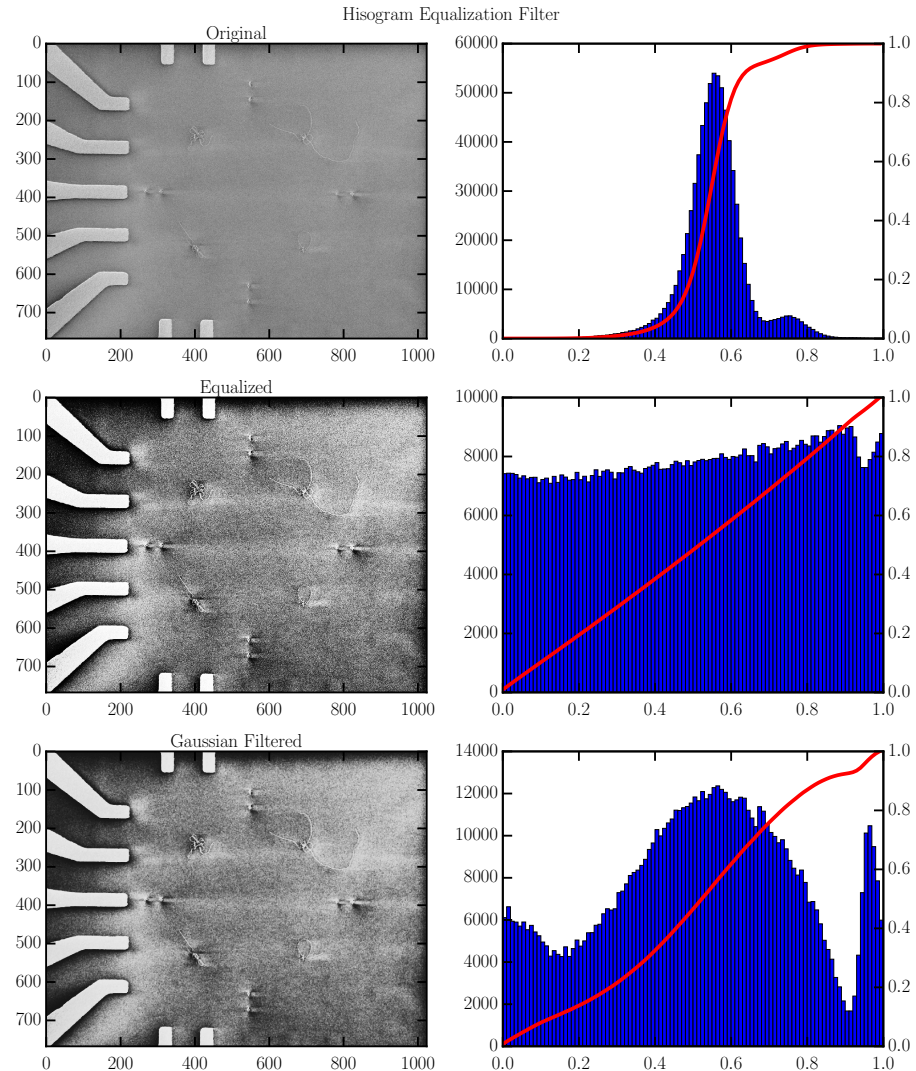


Figure 3.10: Top image is the original SEM image after a plane fit. Middle image shows the SEM image after histogram equalization. Bottom image shows the final result after gaussian smoothing. Plots on the right show the histogram of brightness values and cumulative distribution function at each step.

CHAPTER 3. GROWTH AND PLACEMENT

main problem associated with our SEM, it also increases the background noise to often unacceptable levels. Histogram equalization does not use any specific information about the carbon nanotubes and substrates being imaged. A better filter should be possible by taking advantage of the fact that the features of interest can be well characterized in a sample set of images.

3.4.2 Matched Filter Bank

Matched filter banks are a well known technique that have been used very successfully to filter retinal images in medicine [41]. This technique has previously been adapted to high resolution SEM images of carbon nanotube bundles [42]. The following section describes the implementation of this method to filter images of single walled carbon nanotubes grown on insulating substrates.

3.4.2.1 Nanotube Profile Model

To begin building the matched filter bank, the profile shape of a single nanotube from the SEM image must be determined. To find this shape, a random set of 25 SEM images was selected (similar to those in Figure 3.8). From each of these images, images of two nanotubes were cropped. Those nanotubes can be seen in Figure 3.11a. Each of these images was then rotated such that the longest straight portion (that could be identified by eye) was oriented vertically. The profile of the nanotube was averaged over that long straight section. These results are plotted in Figure 3.11b.

CHAPTER 3. GROWTH AND PLACEMENT

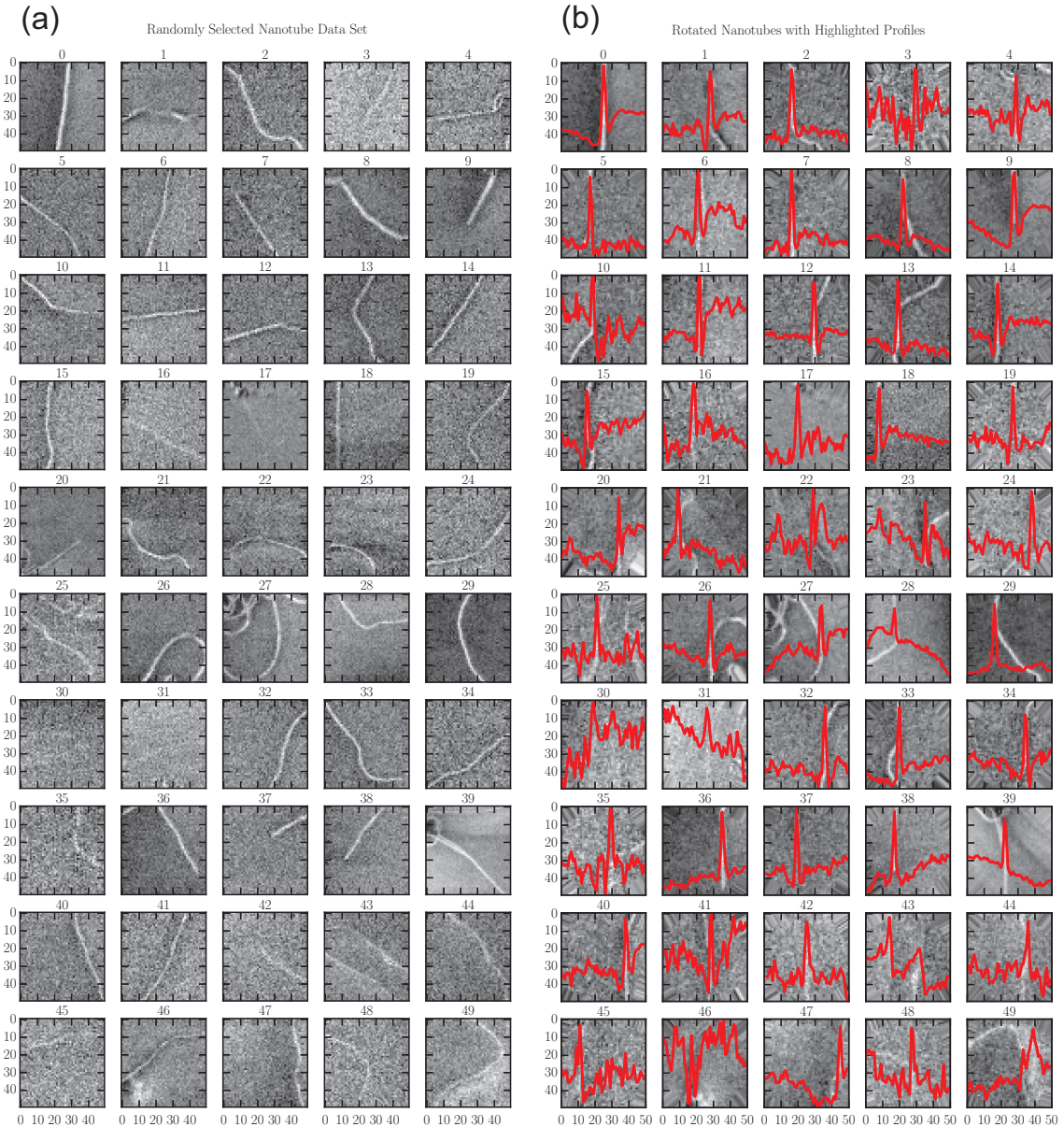


Figure 3.11: a) The original data set of SEM nanotube images used to create and optimize the matched filter bank. b) The same data set rotated and overlaid with extracted nanotube profiles.

CHAPTER 3. GROWTH AND PLACEMENT

Based on the shape of these profiles a truncated *sinc* function, Equation 3.1, was chosen to fit the nanotube profile.

$$f(x) = \begin{cases} \frac{A \sin kx}{kx} & |x| < \frac{2\pi}{k} \\ 0 & |x| > \frac{2\pi}{k} \end{cases} \quad (3.1)$$

This function was chosen because it captures the bright nanotube peak and dark regions beside the nanotube while still only requiring one fit parameter. To determine the fit parameters the linear background was subtracted from each profile in Figure 3.11b and the profiles were fit using 3.1. The results of this fitting can be seen in Figures 3.12a and b.

3.4.2.2 Filter Kernel

The filter kernel is built starting with the median k value found from the profile fits. To extract each profile, horizontal cuts of the nanotube image were averaged over a straight segment of the nanotube that was identified and labelled by hand. The distribution of these straight segment lengths can be seen in Figure 3.12c. Again, to proceed with building the filter we use the median value of L from that distribution. The kernel is built in an $N \times N$ matrix with $(x, y) = (0, 0)$ at the center of the matrix. The full kernel, $K(x, y)$ is defined by Equation 3.2.

CHAPTER 3. GROWTH AND PLACEMENT

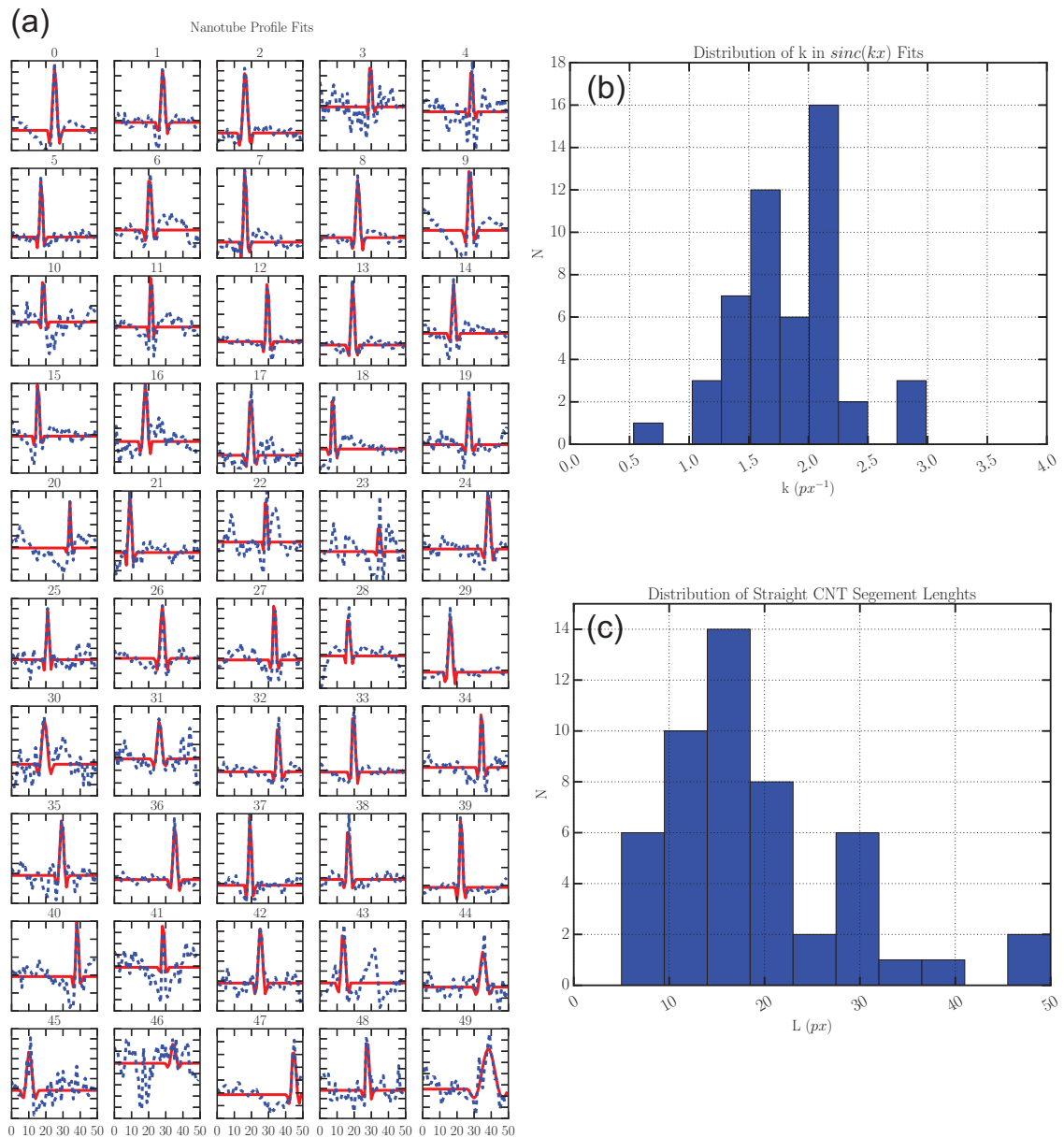


Figure 3.12: a) Extracted nanotube profiles with linear background removed (blue). Fits to 3.1 (red). b) Distribution of k values extracted from profile fits. c) Distribution of straight nanotube section lengths.

$$K(x, y) = \begin{cases} \frac{A \sin kx}{kx} & |x| < \frac{2\pi}{k}, |y| < \frac{L}{2} \\ 0 & |x| > \frac{2\pi}{k}, |y| > \frac{L}{2} \end{cases} \quad (3.2)$$

Once the kernel is defined on the $N \times N$ matrix, the kernel is normalized such that the sum over all of the matrix elements is equal to zero. By convolving this kernel with the SEM image, portions of the image with a shape matching the fit profile and a length L will highlighted in the output. This results in significant background subtraction and accurate nanotube enhancement.

3.4.2.3 Filter Bank

To build the full filter bank, the kernel, built using Equation 3.2, is rotated by a set of angles between 0 and π . Each of these filters is then convolved with the image separately. By doing this, it is possible to identify nanotube sections lying along any direction on the substrate. A binary result is created by thresholding the convolved image. The filter bank and resulting binary images can be seen in Figures 3.13(c) and (d).

After each kernel has been separately convolved with the original image, and the threshold applied, those binary images are added together to produce the final filtered image. Figures 3.13a and b show the original and filtered nanotube images.

In building this filter, many parameters had to be optimized simultaneously and compared by eye. Due to the large parameter space, the matched filters were opti-

CHAPTER 3. GROWTH AND PLACEMENT

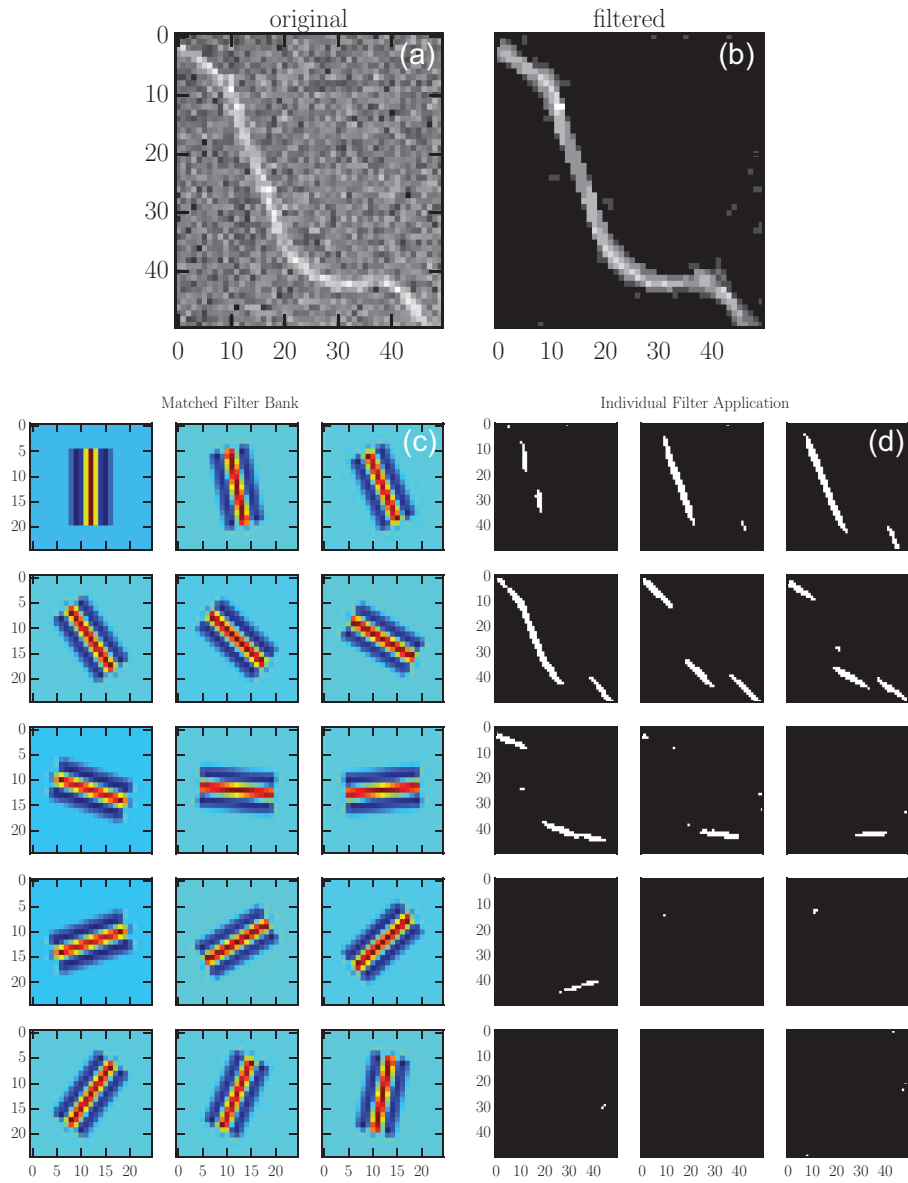


Figure 3.13: (a) Original image. (b) Final filtered image, which is the sum of the binary images in (d). (c) The rotated kernels that form the full matched filter bank. d) Each rotated kernel applied to an image in (a).

CHAPTER 3. GROWTH AND PLACEMENT

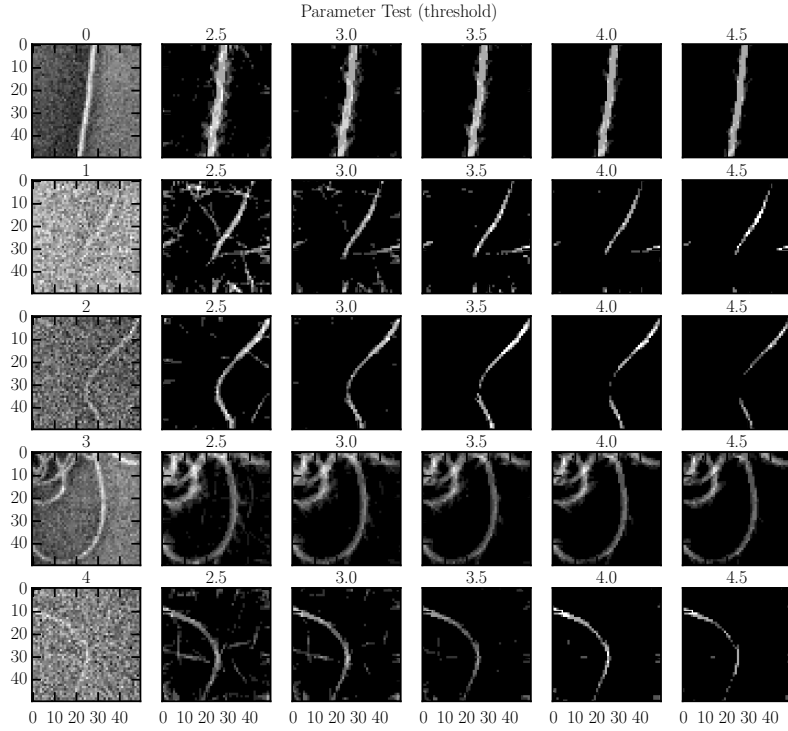


Figure 3.14: Optimization of the matched filter bank threshold value.

mized by iteratively varying a single parameter and choosing the best result. This process is illustrated in Figure 3.14.

The results of this optimization are seen in Table 3.3. The optimized values for k and L were very close to those obtained from the original analysis of extracted nanotube profiles. Note that A and *threshold* are not independent values and A remained fixed for this optimization procedure.

It is also important to note that the length scale for these parameters is in pixels (px). The randomly selected SEM images that were used for this analysis were not all taken at the same magnification level. However, the average magnification was

CHAPTER 3. GROWTH AND PLACEMENT

Table 3.3: Matched Filter Bank Parameters

Parameter	Description	Optimized Value
k	inverse length scale for <i>sinc</i> fit	$1.75px^{-1}$
A	height of <i>sinc</i> function in $K(x, y)$	10
L	length of straight nanotube sections to search for	$16px$
N	size of the kernel matrix	25
R	number of kernels in the filter	15
threshold	cutoff value for thresholding images convolved with filter kernels	3.6

850× giving a pixel size of ∼140 nm

Finally, the filter was tested with the original set of full device SEM images. A selection of the results can be seen in Figure 3.15. It is clear from this set of images that the filter has the desired result. Nanotubes are much more clearly visible and the background is almost completely removed. Because the filter is very similar in its construction to common edge detection algorithms, it also leaves features at the edges of the optical lithography leads and markers defined on the substrate before nanotube growth. This actually works well, since those features are used to align the SEM images for additional electron beam lithography steps.

CHAPTER 3. GROWTH AND PLACEMENT

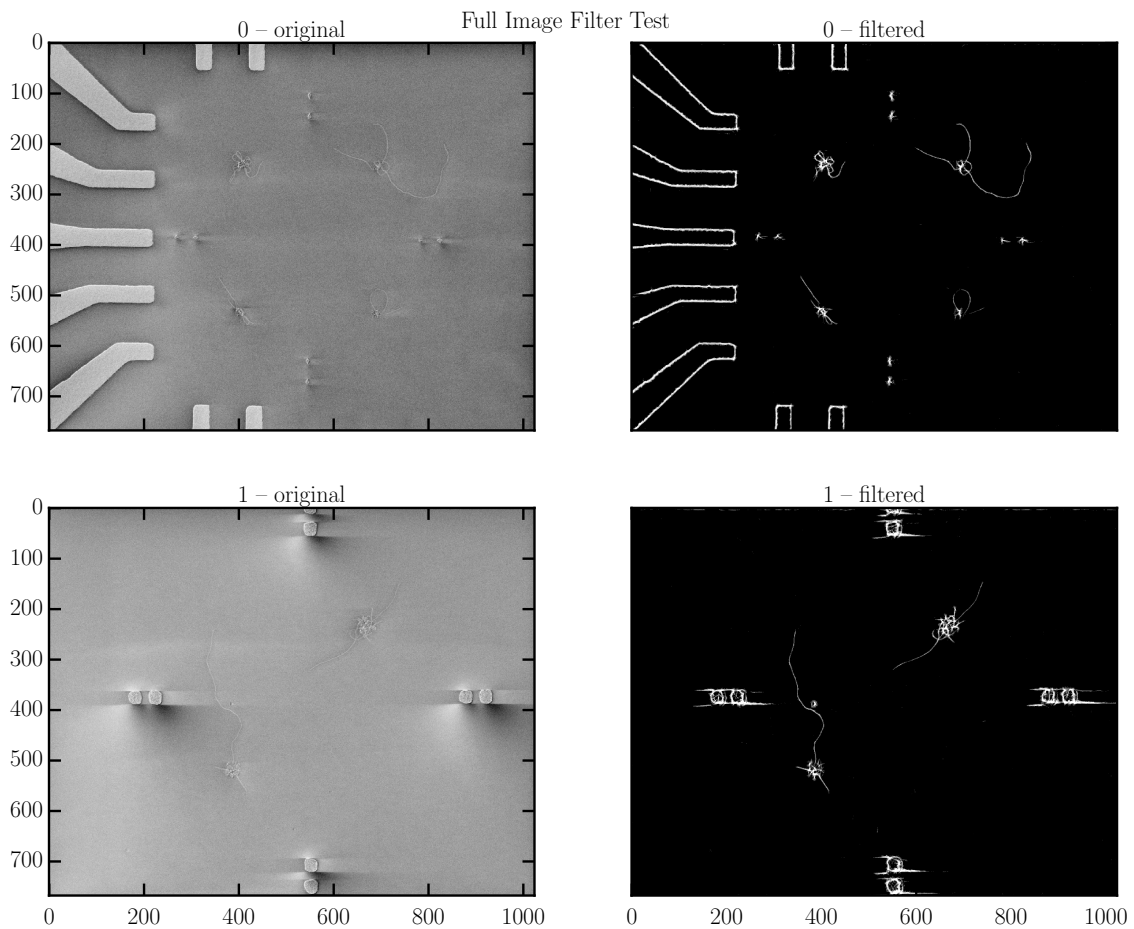


Figure 3.15: Two examples applying the matched filter bank to full SEM images of as-grown carbon nanotubes.

Chapter 4

Metallic Contacts to Carbon Nanotubes

In the course of making the devices measured in later chapters of this thesis, hundreds of carbon nanotube quantum dots were tested in our room temperature probe station. It became clear that there were problems with producing devices with consistent two-probe resistances. The only two possible sources for the anomalously large resistances ($>100\text{ M}\Omega$) are poor quality nanotubes and large contact resistances between thin films deposited for source and drain contacts.

All devices measured for this chapter were created by growing nanotubes directly on silicon substrates using the methods discussed in Section 3.2. The quality of these nanotube was tested with several measurements. Atomic force microscope measurements of the tube diameter confirmed nanotubes were individual, single-walled

CHAPTER 4. CONTACTS TO CNTS

nanotubes with typical diameters around 2 nm. Scanning electron microscope measurements checked the nanotube lengths and density. Finally, electrical measurements of three-terminal devices with low contact resistances showed the expected gate dependence, as seen in Figure 2.8.

While the nanotubes often show defects along their length that affect low temperature transport, these do not have a significant effect when testing devices at room temperature. Metal/nanotube interfaces are the most obvious source of the high resistances measured in many two-probe devices. More importantly, devices on the same chip did not show a broad distribution of contact resistances. Rather, when a silicon chip had working devices, it tended to have many, low resistance ($<10\text{ M}\Omega$) devices. This suggests that some step in the fabrication on a chip wide scale was responsible for the large metal/nanotube contact resistances. Additional evidence for contamination and impurities, as seen in transport measurements, is discussed at the end of this chapter.

To determine the source of the large contact resistances, detailed notes were kept on the fabrication methods and resulting probe station measurements for over 300 silicon chips (one chip typically contains tens of possible quantum dot devices). The first few sections of this chapter discuss the results of several fabrication methods. Recommendations are made for producing more reliable carbon nanotube quantum dots on the basis of these results.

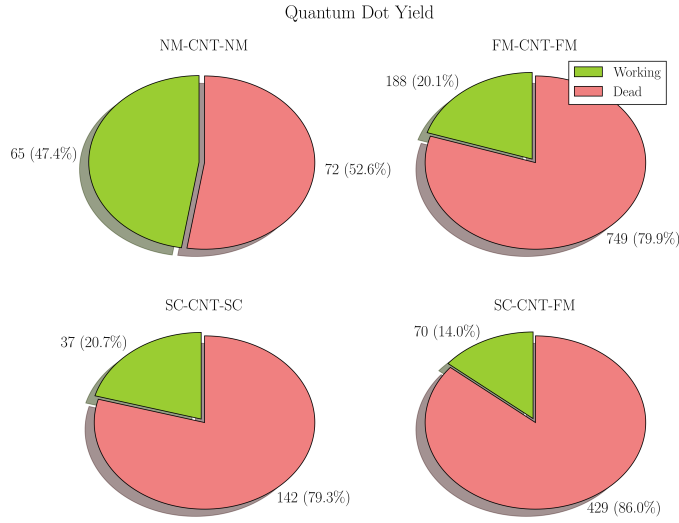


Figure 4.1: Pie charts showing the percentage of quantum dots with measured resistances below $1\text{ G}\Omega$. Data includes all metals and deposition methods.

4.1 Statistics of Carbon Nanotube Contacts

The clearest evidence for chip-wide contamination was in the almost binary nature of the two probe nanotube resistances measured in our probe station. If a chip showed low resistances on one device, that typically held for all devices on the chip, even those built on different nanotubes. Based on this observation, the first statistic checked was the total yield of devices with resistances less than $1\text{ G}\Omega$. Figure 4.1 shows that data, separated by the type of metals used to create the two terminal nanotube device measured. Data includes all metals, all lithography methods, and all substrate preparations.

Figure 4.2 shows the distribution of all devices with resistances less than $1\text{ G}\Omega$ from the same data set as Figure 4.1. Normal metals are most reliable contact materials,

CHAPTER 4. CONTACTS TO CNTS

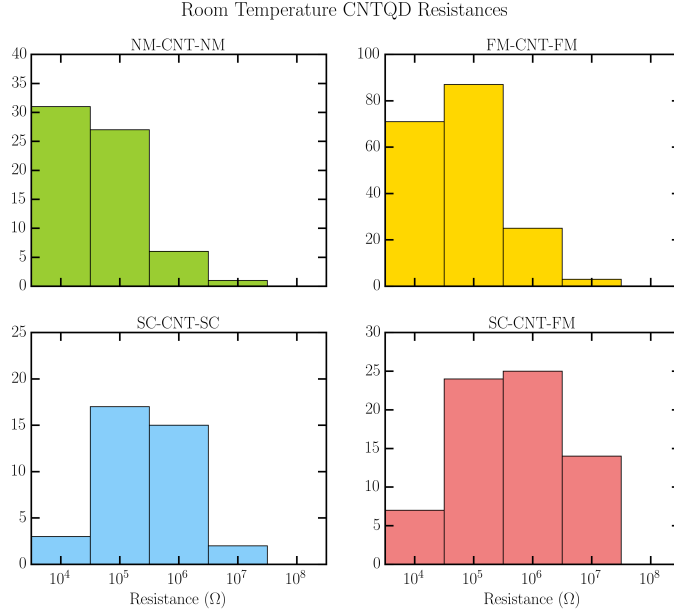


Figure 4.2: Histograms showing distribution of devices resistances. Only measured resistances below $1\text{ G}\Omega$ are plotted. Data includes all metals and deposition methods.

this is likely because the best choice of normal metal is a well researched problem [43–45]. As will be seen later, sputtered palladium was consistently the best contact material tested. Ferromagnetic materials were the most frequently tested in this work. When the devices did work, they show a distribution of contact resistances that skews lower than the superconducting metals. Superconductor-ferromagnet junctions suffer from higher resistance superconducting contacts and an additional fabrication step, both of which contribute to the lower yield and higher average resistances for those devices.

Table 4.1 summarizes all of the materials and deposition methods tested. Many of these materials and methods were also tested with a range of lithography parameters as discussed in Section 4.2.1.

CHAPTER 4. CONTACTS TO CNTS

Table 4.1: Summary of all materials and deposition methods tested for nanotube contacts.

Material	Method	Yield	Total Number Produced
Cobalt	Thermal	19.6%	392
Cobalt	Electron Beam	33.9%	109
Cobalt	Sputtered	24.7%	223
Permalloy	Thermal	54.5%	11
Permalloy	Sputtered	13.0%	23
Aluminum	Thermal	19.2%	167
Niobium	Sputtered	62.5%	8
Gold	Thermal	48.2%	56
Palladium	Sputtered	56.7%	67

CHAPTER 4. CONTACTS TO CNTS

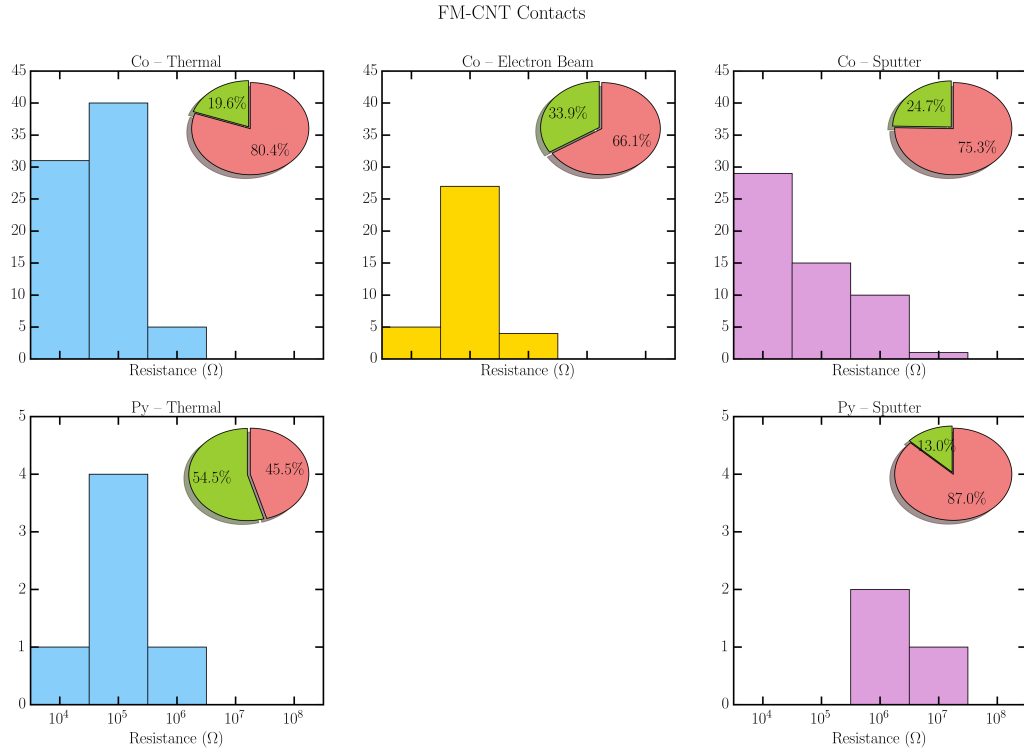


Figure 4.3: Histograms showing distribution of ferromagnetic metal contact resistances. Insets show the yield of devices with resistance below $1\text{ G}\Omega$

4.1.1 Ferromagnetic Contacts

Ferromagnetic materials comprise the largest portion of the dataset collected for this analysis. They were the first materials tested and the widest variety of materials was available. No sticking layers were used in any of the depositions discussed here for fear of ruining the spin transport properties of the metal/nanotube interface, which are discussed in Chapter 6.

Two claims are made based on the results summarized in Figure 4.3. First, sputtered cobalt consistently makes good contact to nanotubes. Second, electron beam evaporation produces lower resistance devices, which is supported by previous

CHAPTER 4. CONTACTS TO CNTS

work [46]. Only a small number of electron beam evaporated devices were tested due to limited access to the evaporator.

The permalloy plots are hiding an important detail. Most thermally evaporated permalloy devices did not have a measurable resistance until after they were annealed at 325 °C for 3 hours in an Ar/H₂ atmosphere. This lowered the resistances to the values recorded in this dataset. However, annealing under these conditions often introduced gate leaks in the devices, making the method useless for later measurements. See Section 4.2.3 for further discussion on attempts to anneal nanotube devices.

4.1.2 Superconducting Contacts

Superconducting contacts were first measured on carbon nanotubes in 1999 [47]. In that work Re/Au and Ta/Au was used as the superconducting layer, but the fabrication involved some unusual processing. In 2006, Ti/Al was used to make a similar measurement using the same process described here [48]. Aluminum is a cheap superconducting material with a relatively long coherence length, making it useful in proximity effect devices, such as nanotube quantum dots. The other commonly used superconductor in nanotube devices is niobium or a Ti/Nb bilayer. Niobium has the advantage of having a transition temperature above 4K, making it possible to measure superconductivity in a simple liquid helium dunker. The Ti layers, in each case, are added because titanium is thought to make good contact with carbon nanotubes by wetting and forming titanium carbide compounds on the nanotube

CHAPTER 4. CONTACTS TO CNTS

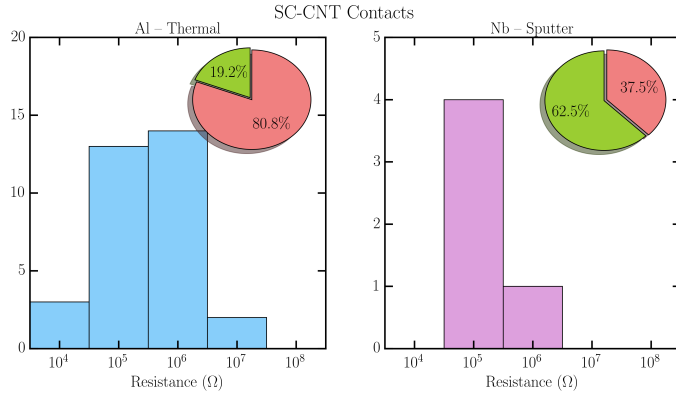


Figure 4.4: Histograms showing distribution of superconducting metal contact resistances. Insets show the yield of devices with resistance below $1\text{ G}\Omega$

surface. Ti/Al and Ti/Nb bilayers were tested for this work. The titanium layer was deposited, without breaking vacuum, in the same way as the superconductor. Despite the difficulty in thermally evaporating titanium, it was necessary here because chromium introduces some trace magnetic contamination to the superconducting material that was deemed unacceptable.

The results in Figure 4.4 are difficult to interpret. The Ti/Al layers have much better statistics, but the Ti/Nb results seem to suggest a better device yield. It is suspected that this is due to difficulty in thermal evaporation of the titanium sticking layer, which is discussed more in the next section.

4.1.3 Normal Metal Contacts

Thanks to their application in CNTFET technologies, normal metal contacts to carbon nanotubes are the best researched of all of the materials discussed here. There

CHAPTER 4. CONTACTS TO CNTS

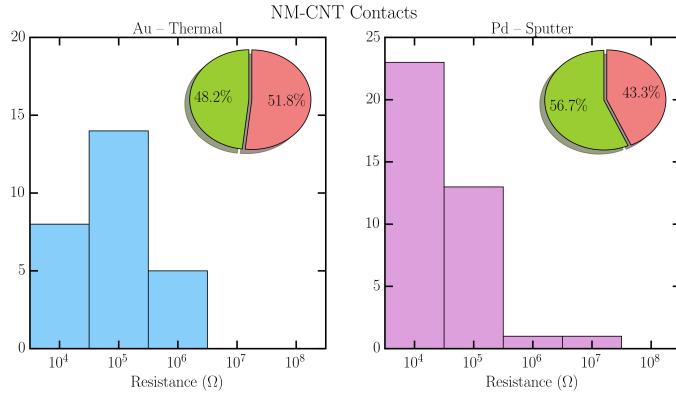


Figure 4.5: Histograms showing distribution of normal metal contact resistances. Insets show the yield of devices with resistance below $1\text{ G}\Omega$

are three popular choices for normal metal contacts to nanotubes. The first is palladium, which was first tested because its work function is very close to that of a typical single-walled nanotube [43, 49]. The second and third are Ti/Au and Cr/Au. These are common evaporated materials and, like palladium, gold is thought to make good contact by wetting carbon nanotubes. The Ti and Cr layers are necessary for sticking layers. Titanium was not used because it is difficult to thermally evaporate and has a tendency to overheat samples and melt the PMMA layer while under vacuum.

Figure 4.5 shows the results for the different normal metal deposition methods tested. Palladium appears to give more reliable and lower resistance contacts than Cr/Au. This is consistent with other work on the subject [43].

CHAPTER 4. CONTACTS TO CNTS

4.1.4 Additional Comments

Contrary to popular opinions, this work suggests that sputtering produces the most consistent, low resistance metallic contacts to carbon nanotubes. Many factors could contribute to this, such as materials choice, different energy scales required for deposition methods, substrate temperatures during deposition, and contamination in the vacuum chambers. A wide range of materials were tested showing that when a device had a measurable resistance, it was consistent with existing literature.

The results of depositions done in the sputtering chamber were relatively consistent across the different materials tested. Additionally, the rate of deposition and partial pressure in the sputtering chamber did not seem to have a noticeable effect on the resulting devices over the ranges tested. More information is available in Appendix A.4.3.

Faster deposition rates in the thermal evaporator did show a connection to lower device resistances. This suggests that there may have been some contamination introduced in the thermal evaporation that was lessened by shortening the evaporation time. Similarly, the thermal anchoring of samples in the thermal evaporator had a marked effect on the measured resistances. Overheating of the sample in the chamber during some longer titanium evaporation was enough to warp the PMMA mask. A temperature controlled stage could eliminate this problem. Electron beam evaporation showed many of the same sample temperature control problems which were part of the reason this method was not tested further.

4.2 Reducing Contamination

4.2.1 Choice of Developer

Recent research has shown that the choice of developer and developer temperature can have a large effect on the resolution of and residue left by electron beam lithography [29, 50, 51]. All electron beam lithography in this thesis used PMMA as the copolymer resist. Two different developers and two different temperatures were tested. More details on recipes and developer choice are available in Appendix A

Figure 4.6 shows the distribution of carbon nanotube devices resistances obtained using each developer. Again, data includes all materials and deposition methods.

Room temperature development using a 1:3 mixture of MIBK:IPA is the most common recipe and appears to yield the most working devices. However, low temperature development with 7:3 IPA:water appears to result in lower resistances for working devices. Since these data do not control for other variables, it is difficult to say which is the better choice. Development in low temperature IPA:water does give considerably better resolution.

In addition to the nanotube device measurements, AFM measurements were used to investigate the amount of residue left behind by different developers. An example of this can be seen in Figure 4.7. These roughness measurements were motivated by the inconclusive results in Figure 4.6.

The roughness results for all developers tested are summarized in Table 4.2 Room

CHAPTER 4. CONTACTS TO CNTS

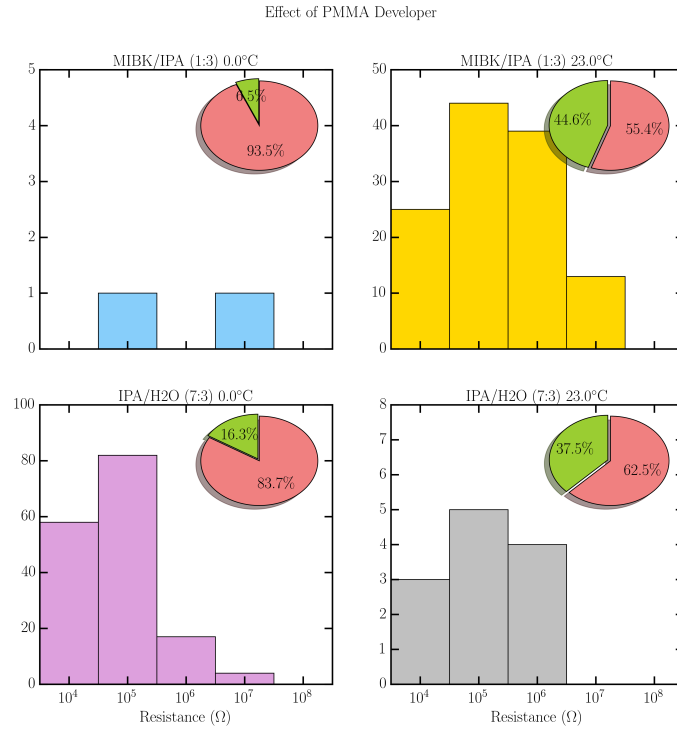


Figure 4.6: Histograms showing contact resistance as a function of developer choice. Data include all metals and deposition methods. Insets show the yield of devices with resistance below 1 GΩ

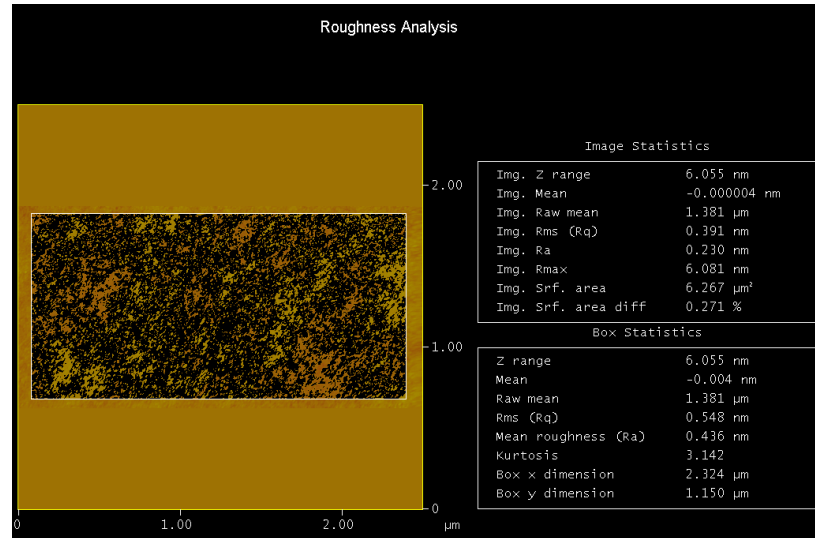


Figure 4.7: Surface roughness after development of PMMA film using 0 °C IPA:water in 7:3 mixture.

Table 4.2: Surface roughness after development of PMMA films.

Developer	Temperature (°C)	RMS Roughness (nm)	Mean Roughness (nm)
7:3 IPA:water	0 °C	0.548	0.436
1:3 MIBK:IPA	0 °C	4.231	1.985
1:3 MIBK:IPA	23 °C	10.871	8.081

temperature IPA:water roughness was not measured, but the data suggests it should be similar to room temperature MIBK:IPA.

Based on the roughness measurements, IPA:water seems to be the clear choice of developer to minimize PMMA residue after development. To determine the reason for the poor device yield in Figure 4.6, more tests should be done with strict control over other variables.

4.2.2 Dose Scaling

Previous work has shown that overexposing PMMA films can lower the roughness of the surface after development [29, 51]. Looking at Table 4.2, the height of the PMMA residue left behind can be on the order of the nanotube diameter. In order to limit the effect this residue has on the resulting metal/nanotube contacts, it is important to reduce the amount of PMMA residue as much as possible.

There are many computationally intensive algorithms for scaling the electron beam dose to a PMMA film based on the pattern geometry [52–55]. Because of the

CHAPTER 4. CONTACTS TO CNTS

high throughput of samples and limits of our lithography software, a much simpler algorithm was developed for this work. The most important parameter in determining the dose is the smallest width of the polygon being written. This is difficult to determine because polygons in the lithography pattern are not always rectangular or aligned with the coordinate axes. A simple proxy for the smallest width across a polygon is $2 \times (Area/Perimeter)$. This is easily seen for a rectangle with a high aspect ratio, $a \ll b$:

$$2 \frac{Area}{Perimeter} = 2 \frac{ab}{2a + 2b} = \frac{1}{\frac{1}{a} + \frac{1}{b}} \sim a \quad (4.1)$$

The dose must be scaled by the inverse of this, $\frac{1}{2} \times (Perimeter/Area)$ such that narrow features receive a higher dose. Once this factor is determined, empirical scaling and dose limits are needed to produce the actual dose values for the lithography pattern. An example of the results of this dose scaling can be seen in Figure 4.8.

Scaling the doses in this way allows for the nanotube contacts to be overexposed, reducing the PMMA residue in those areas, without overexposing the larger features connecting to bonding pads. Overexposing the larger features can lead to degradation of the developed pattern and shorts in the final device.

Implementing this geometry based dose scaling was seen to improve the yield of low resistance nanotube contacts. It also lowered the failure rate of electron beam lithography and metal liftoff by preventing shorts caused by overexposure in large features. The lowest resistance contacts with the best lithography resolution and device

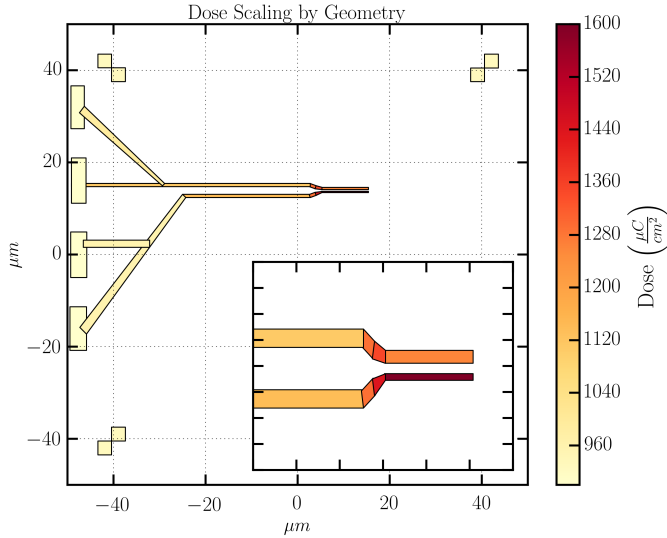


Figure 4.8: An example of a lithography pattern with dose scaling based on polygon geometry. Inset shows a close up of the nanotube contacts.

yield were made with a combination of cold IPA:water developer and the dose scaling described here.

4.2.3 Annealing

Three types of annealing were tested to improve contact resistances in carbon nanotubes. The first is high temperature annealing in an Ar/H₂ atmosphere [45, 56–59] designed to remove residue from polymer resists. Similarly, vacuum annealing at slightly higher temperatures was tested to remove water contamination and polymer resist residue [60–64]. Finally, current annealing was tested on a several devices [25, 65].

High temperature annealing in an Ar/H₂ atmosphere was the most successful

CHAPTER 4. CONTACTS TO CNTS

method tested. Samples were loaded into the same tube furnace used in CVD growth and heated to 325 °C while flowing 500 sccm Ar and 500 sccm H₂ for 3 hours. In cobalt and permalloy contacts this method was found to improve contact resistances by a factor of 2-10x. While annealing did improve room temperature resistances, it did not lower noise levels, which is supported by previous work [66]. For metals requiring a titanium or chromium sticking layer, such as Nb, Al, and Au, this method did not noticeably improve contact resistances and often destroyed the contacts completely. Based on the data collected, it appears the high temperature annealing either caused, or worsened, gate leaks in the devices. Determining the exact cause of the gate leaks is difficult without further experiments.

Vacuum annealing was tested on only a small number of devices. The method was adopted from similar work done on graphene in our lab. Samples were loaded into the tube furnace, which was evacuated to 1×10^{-6} Torr and heated to 500 °C. In the few experiments done, vacuum annealing was not seen to improve the contact resistances in any metals tested.

Current annealing was tested on a number of devices as a last effort to get the sample working. Samples were placed in the probe station and the two contacts of interest were probed. A voltage bias was ramped repeatedly from 0 to a few volts, with a safety resistor preventing the current from exceeding 25 µA. This method was seen to lower contact resistances after 5-10 sweeps. This is either due to dielectric breakdown in the contacts or high temperature annealing due to Joule heating [67–69]. Despite

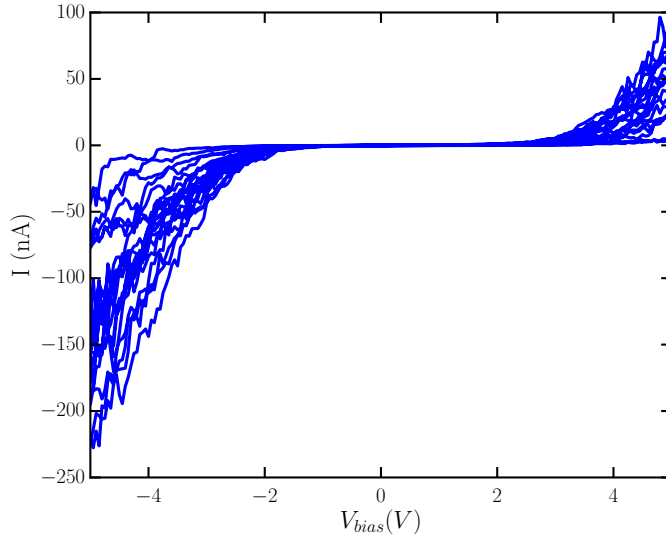


Figure 4.9: A typical current anneal trace. Initially, the resistance was seen to decrease. After sometime the device abruptly died.

some success the method was extremely difficult to control. Most samples were destroyed in the process. A typical trace is seen in Figure 4.9. Contact resistances were never successfully lowered to a useful value before the device died.

4.3 Electrical Noise in CNT Contacts

Electronic noise in the measured current can be used as a measure of the amount of contamination in the metal/nanotube interfaces and on the substrate. The primary sources of contamination on the devices are polymer residues left by the lithography process, organic contamination from thin film deposition, and amorphous carbon deposited during the CVD growth of carbon nanotubes. Each of these contaminants affects the transport properties of the completed device.

CHAPTER 4. CONTACTS TO CNTS

All of the measurements discussed in this thesis were voltage biased, DC current measurements. For each data point, the applied voltages (V_{gate} , V_{bias}) were set, and the current sampled at a fixed rate for a specified amount of time. Typically, data was taken at 3-40 kHz for 0.1-0.5 s. In many cases, the entire time series at each point was dumped into a binary data file for later analysis. These current versus time measurements at fixed gate and bias voltages provide the data used in the following noise analysis.

4.3.1 Random Telegraph Noise

Random telegraph noise in electronic transport measurements is caused by the hopping of charge on and off of impurity charge traps capacitively coupled to the device. In a nanotube quantum dot, these impurities are most likely in one of three places; at the nanotube-metal interface [70], at the nanotube-substrate interface [70, 71], or located at defects in the nanotube itself [59].

Random telegraph noise manifests in the time series data as square pulses in the measured current with random durations. The height of each pulse can be used to identify the pulses as being caused by one or more impurities with different charging energies.

Looking at the conductance as a function of V_{bias} and V_{gate} voltage in Figure 4.10, two types of random telegraph signal are present, with distinctly different time scales. Consider first the switching behavior seen as a function of the gate voltage near

CHAPTER 4. CONTACTS TO CNTS

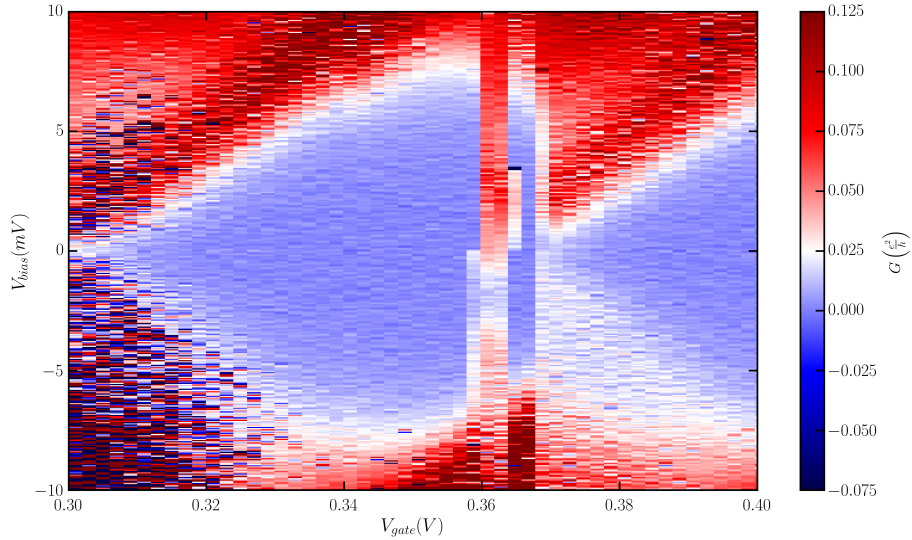


Figure 4.10: Noise power spectra from a nanotube device at 4K. V_{gate} is fixed. Each curve is taken at a different V_{bias} ..

$V_{gate} = 0.36V$ in Figure 4.10. This behavior can be explained by charge trapping in impurities at the gate oxide/nanotube interface. As the gate voltage is swept charge can be trapped and released from impurities capacitively coupled to the nanotube. These impurity charge traps act as local gates which shift the Coulomb diamond plot abruptly to the left or right. This can be thought of as a random telegraph signal with a long time constant, on the order of tens of minutes at low temperatures. At room temperature these trapping events are much more frequent leading to a hysteresis behavior in the gate sweep rather than a discrete charging/discharging event. Figure 4.11 shows an example of this gate hysteresis caused by impurities capacitively coupling to the nanotube.

Near $V_{gate} = 0.3V$ in Figure 4.10, random telegraph noise with much shorter characteristic time scales is observed. This becomes more clear by plotting several

CHAPTER 4. CONTACTS TO CNTS

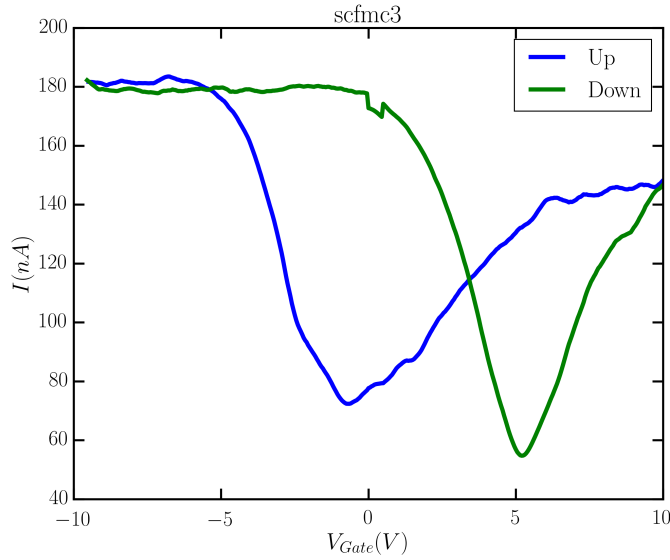


Figure 4.11: Hysteresis in a CNTFET $I-V_{gate}$ curve.

time series as a function of V_{bias} at a fixed V_{gate} , as seen in Figure 4.12.

The time series data in the right panel of Figure 4.12 clearly shows the random telegraph noise in the current measurement. The distribution of switching times has not been carefully measured, but appears to range from about 10-1000 ms. Because the current is only sampled for 0.1-0.5s in a typical measurement (0.4s in the sample being discussed here), it is difficult to get accurate distributions of switching times. Some useful information can be gathered from the fact that there appears to be only two levels in the system. That means the random telegraph noise signal originates from charge tunneling to and from a single impurity, most likely at one of the metal/CNT contacts or along the nanotube itself.

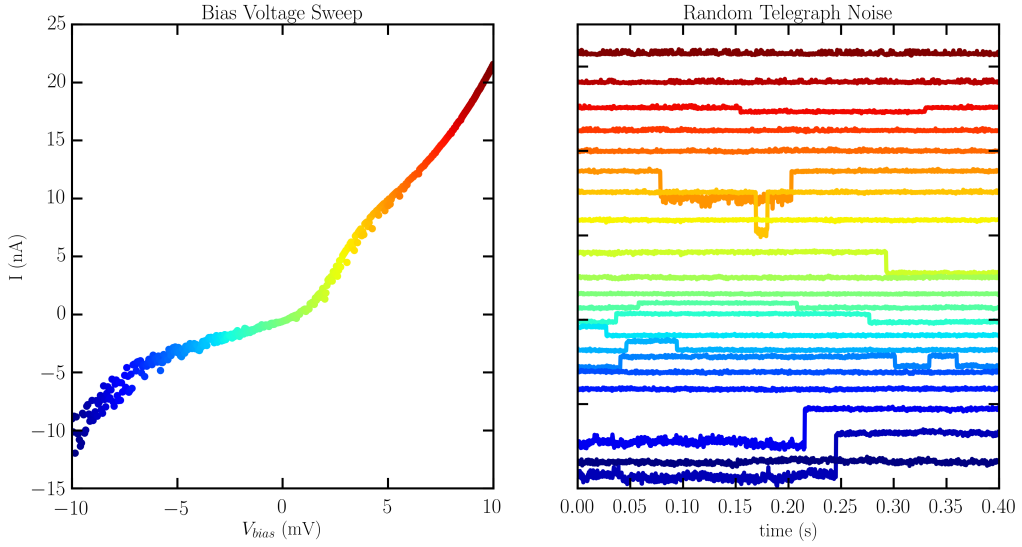


Figure 4.12: Left: Measured current as a function of V_{bias} at $V_{gate} = 0.304V$. Right: Time series at fixed V_{bias} and V_{gate} . Colors for each individual time series correspond to those in the bias sweep.

4.3.2 $1/f$ Noise

$1/f$ noise, or pink noise, is the dominant noise source in nearly every electronic device at low frequencies. Measurements of $1/f$ noise amplitude and how it scales with applied bias and fields can offer insight into the origins of noise and disorder in a semiconductor device. Because the devices made for this thesis had such persistent problems with noise and contamination, it was thought that investigating the $1/f$ noise data could illuminate the source of some of the noise.

A simulated current noise power spectrum is plotted in Figure 4.13. At low frequencies, the noise is dominated by the $1/f$ contribution. At higher frequencies the $1/f$ becomes insignificant and the noise level is dominated by shot noise, which is attributable to the discrete nature of charge moving through the device. Over all

CHAPTER 4. CONTACTS TO CNTS

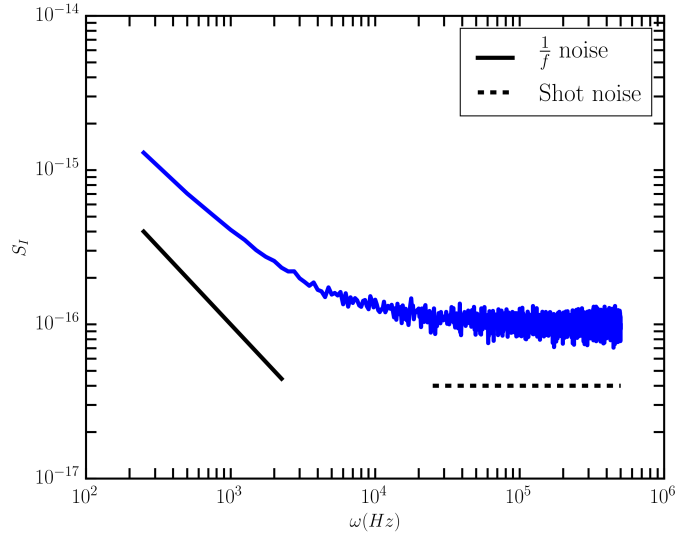


Figure 4.13: Simulated noise power spectrum for a CNTFET.

frequency ranges, there is a constant contribution from Johnson thermal noise.

The first work on $1/f$ noise in nanotubes was published in 2000 [72]. This, and additional work in 2006 [73], confirmed that carbon nanotube field effect transistors operating at room temperature have a $1/f$ noise amplitude that follows the empirical model proposed by Hooge in 1969 [74]. This model predicts that the noise amplitude in a semiconductor device should be proportional to I^2 and inversely proportional to f :

$$S_I = A \frac{I^2}{f} \quad (4.2)$$

Later results [75] showed that this model holds down to $1.2K$ for relatively long channel lengths, $L = 3\mu m$. Only a small amount of research exists on the behavior of

CHAPTER 4. CONTACTS TO CNTS

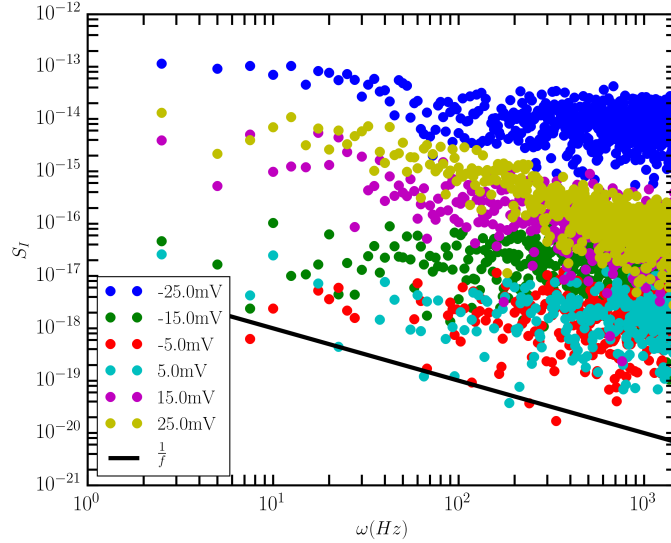


Figure 4.14: Noise power spectra from a nanotube device at 4 K. V_{gate} is fixed. Each curve is taken at a different V_{bias} .

$1/f$ noise when electron confinement becomes important at low temperatures. The most significant work was done on GaAs quantum dots [76] and later repeated for suspended graphene quantum dots [77]. Similar to those two works, all data presented here was taken at 4 K at a range of bias and gate voltages in the Coulomb blockade regime. A sample of the raw data can be seen in Figure 4.14.

The data in Figure 4.14 does fit the $1/f$ dependence well. To test if the data fit Hooge's law, the left side of Figure 4.15 shows the average value of $S_I \cdot f$ plotted against the measured current (each measured current corresponds to a single applied bias voltage) for a range of gate voltage values annotated in the plot legend. It is immediately clear from this plot that the noise amplitude does not scale with I^2 . Most curves show plateaus in $S_I \cdot f$ near resonances in the Coulomb diamond diagram, and an abrupt drop in noise off-resonance. The fact that the noise amplitude does not

CHAPTER 4. CONTACTS TO CNTS

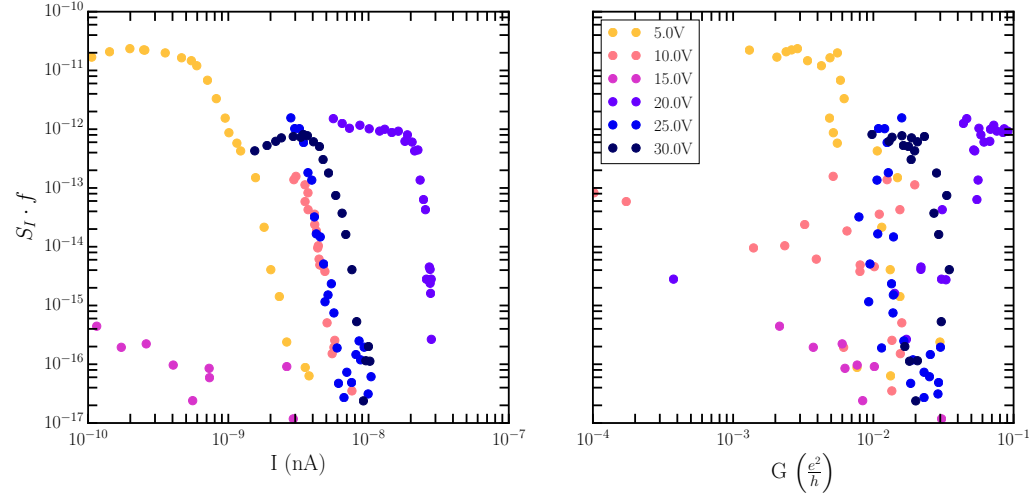


Figure 4.15: Left: $S_I \cdot f$ plotted against measured current with $V_{bias} > 0$ at a range of V_{gate} . Right: The same data plotted against conductance.

follow Hooge's law suggests that the $1/f$ noise is not dominated by noise from the carbon nanotube itself. Instead, the noise must come from another source, most likely from charge trapping in impurity and quantum dot levels. Additional experiments might check the temperature and frequency dependence of this behavior to determine the exact mechanism.

The plot on the right in Figure 4.15 shows $S_I \cdot f$ as a function of the measured conductance. These data do not show any obvious relation between the two quantities.

In order to get a better idea of this noise plateau near resonances in the Coulomb diamond conductance plot, the two are compared in Figure 4.16. The noise amplitude plot at the bottom of Figure 4.16 confirms that there are maxima in the $S_I \cdot f$ data that correspond to maxima in the conductance data, seen in the top plot. Additionally, the noise amplitude plot shows increases in $1/f$ noise in places where there is a lot of

CHAPTER 4. CONTACTS TO CNTS

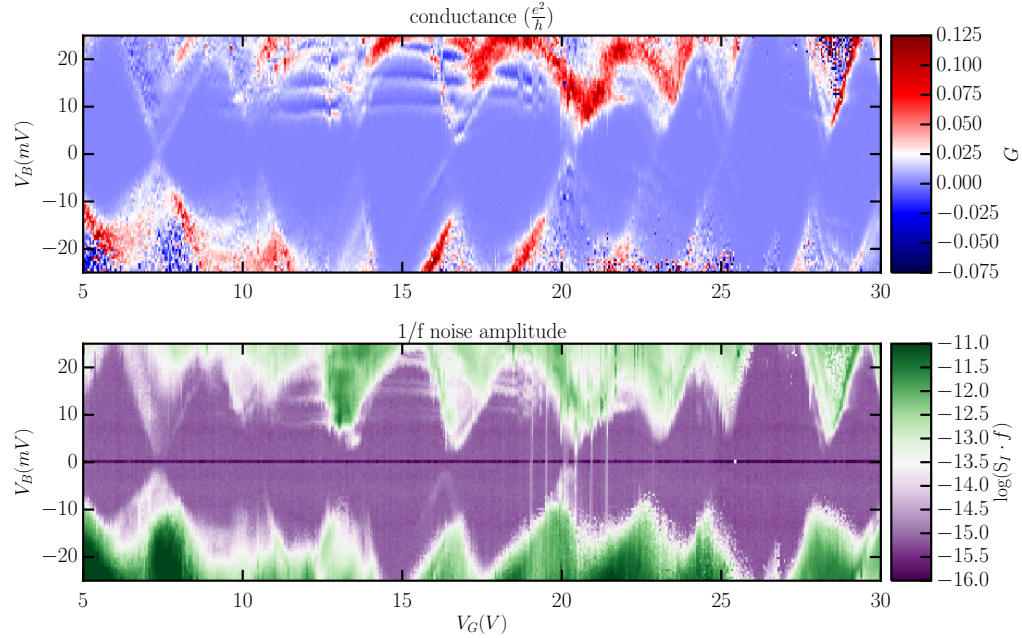


Figure 4.16: Conductance (Top) and $\log_{10} S_I \cdot f$ (Bottom) as a function of V_{bias} and V_{gate} .

random telegraph noise, such as near $V_{gate} = -7V$ and $V_{bias} < 0$. This increased $1/f$ noise near regions with excess random telegraph noise may suggest an explanation of the overall behavior.

The $1/f$ noise increases when there are impurity charge traps that can be accessed by the electrons on or near the quantum dot. For these low dot fillings and low temperatures, the quantum dot itself behaves like a charge trap, where the $1/f$ noise is increased when the Fermi energy on the source/drain are near a resonant level because of discrete tunneling events on and off the quantum dot. Thus, in this regime the $1/f$ noise amplitude can be used as a spectroscopic probe into the energy levels on the quantum dot.

CHAPTER 4. CONTACTS TO CNTS

In Section 4.3.1, the characteristic times for charge hopping onto impurities was found to be on the order of 10-1000 ms. This corresponds to a frequency range of 1-100 Hz. Those frequencies are well within the range considered in calculating the $1/f$ noise amplitude. Therefore, it should be no surprise that the noise amplitude increases in regions showing excess random telegraph noise. This also suggests that the characteristic times for electrons tunneling onto the quantum dot levels fall into a similar range of 0.1-1000 ms. This range of characteristic tunneling times is consistent with previous measurements of the tunneling rate onto a nanotube quantum dot [78].

In previous measurements, the tunneling rates were tuned by varying the barrier heights with local gating. Here, the fluctuations in barrier height are not controlled, the quantum dot is in a static configuration. Therefore, the fluctuations in potential are related to impurity charge trapping. This conclusion is supported by previous research into barrier height fluctuations [76] and dependence of $1/f$ noise on charge trapping in different gate oxide materials [71]. It was suggested in Reference [71] that gamma irradiation of quantum dot samples may eliminate some of these charge trapping problems, which may be an interesting avenue for future work.

Chapter 5

Low Temperature Transport

Measurements

In this thesis work, a variety of low temperature and low noise measurement techniques have been used. This chapter will summarize these techniques with a focus on my own work and making the measurements reproducible by future lab members.

5.1 Transport Measurements

All of the devices measurements carried out for this work have been two-probe, voltage-biased measurements. The majority of measurements were DC, based on the fact that problems like gate leakage current and sources of electronic noise are much

CHAPTER 5. MEASUREMENTS

more easily identified in a DC measurement. A few AC measurements were made, especially in the beginning of this work. Each measurement setup will be reviewed here.

5.1.1 DC Current Measurements

Figure 5.1 shows a typical DC measurement setup. The sample is loaded into a cryostat and accessed through a 24 channel BNC breakout box. The bias voltage is typically supplied by a National Instruments Digital Acquisition (DAQ) board. In some cases, old Kepco programmable voltage supplies were used. The Kepco supplies were found to be much lower noise, due to the opto-couplers used, but the DAQ board were preferred for their speed and ease of programming. Both the Kepco and DAQ boards have output ranges of $\pm 10V$. To utilize the full dynamic range of the voltage sources, a 100:1 voltage divider is used at the output of the bias voltage source. Additionally, a 1kHz, two-pole, RC low pass filter is used to prevent voltage spikes that occur while ramping the output voltage from reaching the sample.

Current through the nanotube is measured by a current-to-voltage converter with an output of $1V/10^7A$. For this work two different amplifiers have been used, an Ithaco 1211, and a battery-powered homemade amplifier, which are discussed further in Section 5.1.3. The output of the current-to-voltage amplifier is measured either by the NI DAQ board or a Keithley 2182A nanovoltmeter. Most measurements were made using the NI DAQ board for its speed and ability to save time series data for

CHAPTER 5. MEASUREMENTS

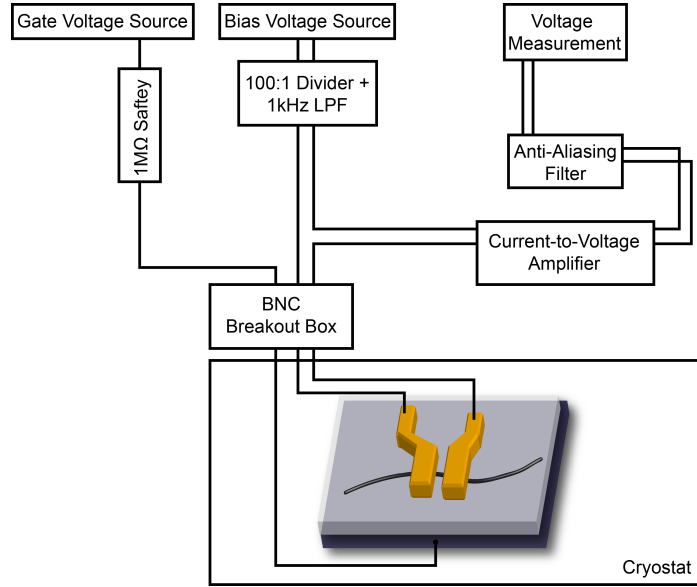


Figure 5.1: Diagram of typical DC measurement setup.

every measurement. To eliminate aliasing effects in the DAQ measurements a 10kHz RC filter was used for anti-aliasing. Measurements were taken at 21.6kHz. To sample the current, data was collected at 21.6kHz for up to one second. The time series data was dumped to a binary file and the current value was calculated from the mean of the acquired data. Saving all the time series data allows for further analysis, such as 1/f and shot noise, to be done later. For differential conductance measurements, the DC current data were numerically differentiated.

5.1.2 AC Conductance Measurements

AC measurements take advantage of lock-in amplifiers to eliminate noise and make direct measurements of differential conductance. Two lock-in amplifiers were used for

CHAPTER 5. MEASUREMENTS

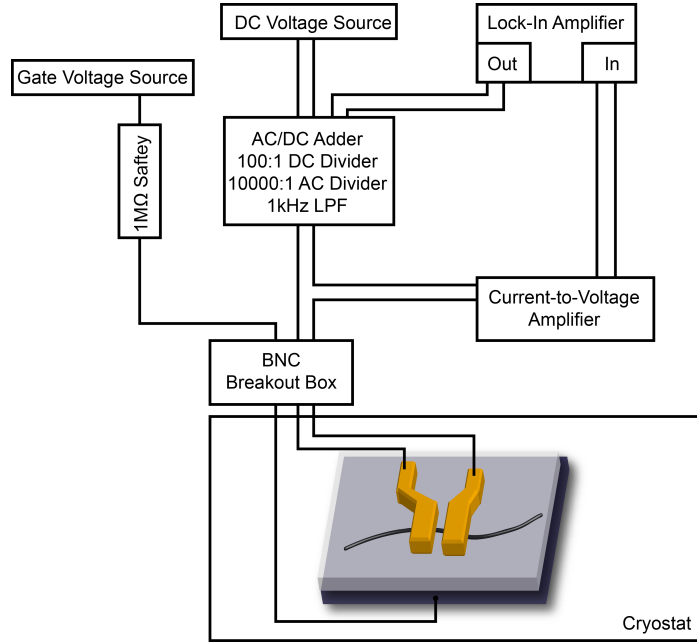


Figure 5.2: Diagram of typical DC measurement setup.

this work, an analog Princeton Applied Research 124A and a digital SRS830. The SRS830 is a standard choice because of its easy setup and remote programming. The 124A, however, has much less output noise and was used for most of this work. The output of the 124A was read by an NI DAQ board in the same way as described in Section 5.1.1.

Samples are biased in the same way as the DC measurement with addition of an AC signal taken from the output of the lock-in amplifier. The AD and DC bias voltages are added together using a passive AC-DC adder, described in Section 5.1.3.

Because the lock-in amplifier can only be used to measure voltage signals, the current-to-voltage amplifier is still needed. The output of the current-to-voltage am-

CHAPTER 5. MEASUREMENTS

plifier is sent to the input of the lock-in. Using this setup, the differential conductance can be directly measured.

Some care must be taken to ensure the lock-in signal is not being attenuated by any of the filtering in the AC-DC adder, cryostat, or current-to-voltage amplifier. In this work, lock-in signals of 27Hz were used, which was well below the cutoff frequency of any filtering in the experiment.

5.1.3 Custom Electronics

Current Amplification

The primary sources of noise in making low current DC measurements come from the 60Hz AC power lines and operational amplifiers in the current-to-voltage amplifier. The first source of noise can be largely eliminated by using an amplifier with battery power. While it is not possible to completely eliminate op amp noise, it can be reduced by choosing designing circuits using low noise amplifiers, metal film resistors, and appropriate filtering.

A custom made current-to-voltage amplifier was designed for our lab by Chris Merchant. It uses two OPA27GP op amps in series before and after the sample. The design is two simple transimpedance amplifiers in series with the sample. For this work, the design was expanded upon by adding power line filtering, a low pass filter on each amplifier, and a simplified output configuration. The design can be seen in

CHAPTER 5. MEASUREMENTS

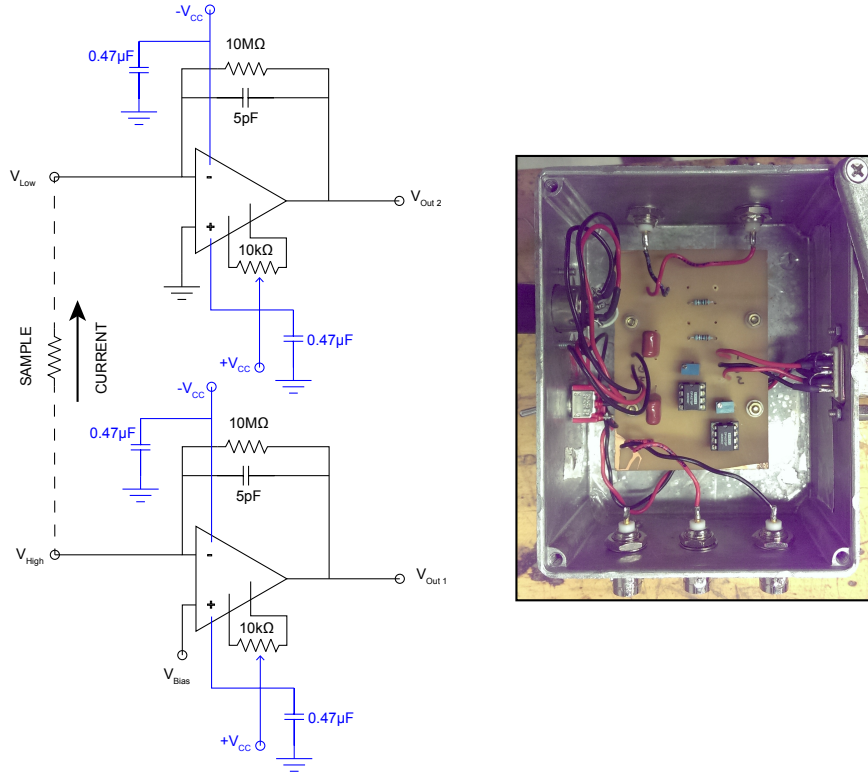


Figure 5.3: Circuit diagram and photo of the current-to-voltage amplifier. The amplifier has a fixed gain of $1V/10^7A$. Each power line is filtered with a $0.47\mu F$ capacitor. The $5pF$ capacitor in the feedback loop forms a low pass filter with the $10M\Omega$ resistor, with a cutoff frequency of about 3kHz.

Figure 5.3. With this amplifier, the sample is symmetrically biased by having the same amplifier impedance on each side.

The output of each amplifier (one measuring I and the other $-I$) goes to a 9-pin Dsub connector along with the $\pm 12V$ power supply lines with the remaining pins grounded. From this cable the signal is sent to the NI DAQ for measurement. This configuration provides some interesting flexibility. In the simplest case, each output is sent to an antialiasing filter and measured separately. Measuring each amplifier separately allows noise measurements to be made by looking at the cross correlation

CHAPTER 5. MEASUREMENTS

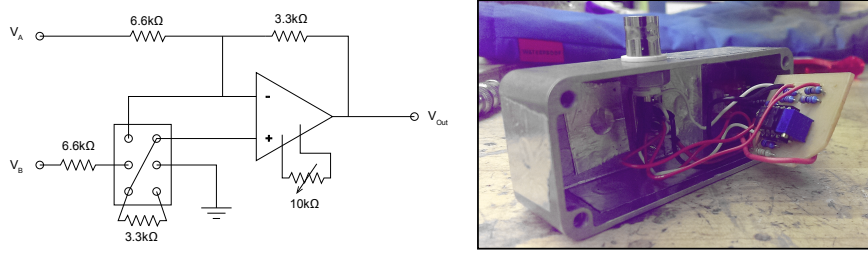


Figure 5.4: Circuit diagram and photo of the active subtractor/adder circuit. The DPDT switch is used to change between adder/subtractor circuits. The output state also features an antialiasing filter with 10kHz cutoff not drawn here.

of the two signals [79]. By measuring the current at with two separate amplifier circuits, the amplifier and environmental noise from each is cancelled, leaving only noise from the sample.

When not making noise measurements, it is simpler to measure just one signal for the current. To do this, while still taking advantage of the noise canceling, an active subtractor circuit was constructed. The subtractor circuit can be seen in Figure 5.4.

Both the amplifier and subtractor are run using the same $\pm 12V$ battery power supply, which is housed in a separate aluminum enclosure and connected with a 5-pin cable. Two identical battery sources were constructed so that one could charge while the other is in use. Measurements can be paused in the software control during battery changes. Most data in this thesis was taken using this setup.

AC-DC Adder

When making AC measurements that incorporate a DC bias voltage, some care must be taken to add the two voltage biases together in the correct way. Several

CHAPTER 5. MEASUREMENTS

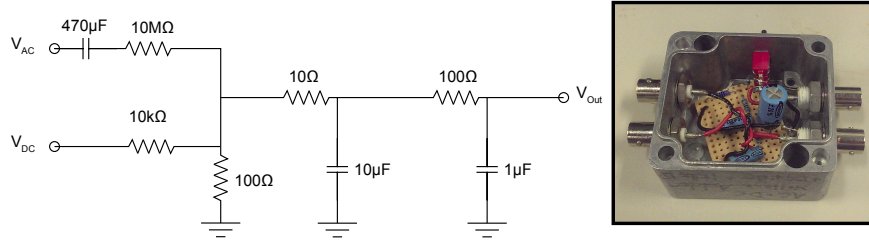


Figure 5.5: Circuit diagram and photo of the AC-DC adder. The voltage is added in the first stage, while the second state consists of a two-pole RC low pass filter with a cutoff frequency of 1kHz to suppress any switching noise from the voltage sources.

circuits were tested to do this, from a simple BNC tee, to an active adder circuit like the one seen in Figure 5.4. The design that yielded the least noise, most accurate output, and shortest decay times is seen in Figure 5.5.

The $470\mu\text{F}$ capacitor on the AC input prevents any DC bias from the lock-in amplifier from affecting the measurements. The second stage is a two voltage dividers (100:1 AC and 100000:1) DC which also serves as the adder circuit by adding the two currents through the 100Ω resistor to ground. The last stage is a two-pole low pass filter. This circuit works well with AC signals up to 100Hz, but is best used with signals of 10-20Hz.

5.2 Cryogenics

A number of cryostats and superconducting magnets were used in this work. This section will briefly review the various components used.

CHAPTER 5. MEASUREMENTS

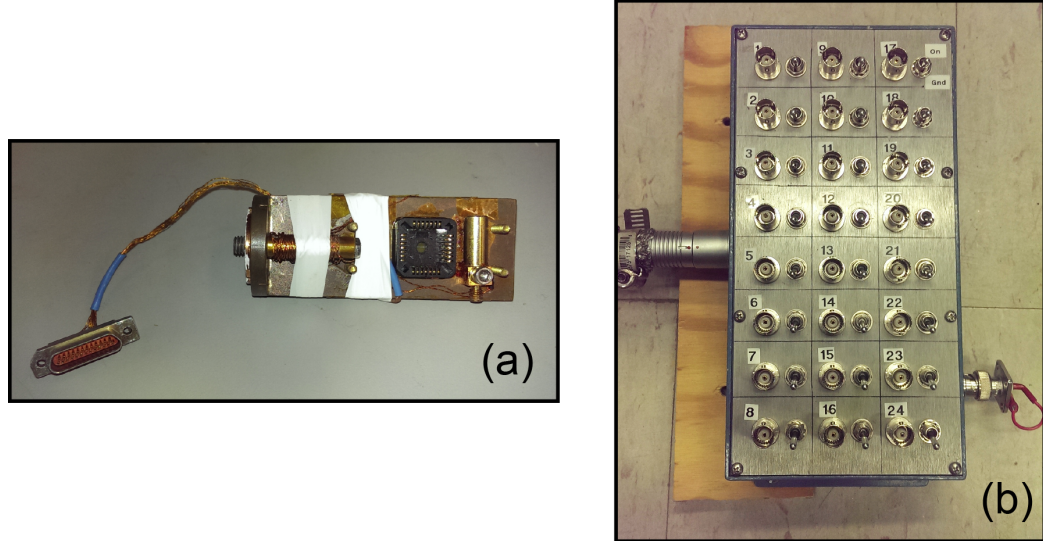


Figure 5.6: (a) Parallel magnetic field sample holder. (b) 24-pin BNC breakout box for Fischer connectors.

5.2.1 Cryostat Wiring

All the cryostats discussed below are wired in the same way. Samples are mounted on 28-pin chip carriers, which are placed in custom built sample holders with custom circuit board designed by our lab. The sample holders, seen in Figure 5.6(a), can be attached to the cryostat at the coldest point. Each sample holder has a mount for a chip carrier, as well as a RuOx or Pt temperature sensor and heater. Lines from the sample are connected using 25 pin Dsub connectors mounted on the sample holder and at the coldest point on the cryostat. From the Dsub connectors, the signal moves through twisted pair ribbon cables to a Fisher connector mounted on the cryostat at room temperature. A 24-lead cable connects the cryostat to a BNC breakout box, seen in Figure 5.6(b). None of the cryostats discussed here have low temperature filtering other than that formed by the impedance of the ribbon cable. Typical cutoff

CHAPTER 5. MEASUREMENTS



Figure 5.7: Liquid helium dunker with parallel field sample holder (far right).

frequencies for this setup are around 10kHz, which dictates the choice of measurement frequency in DC measurements. Adding additional high frequency filtering would certainly improve the noise in our measurements by lowering the electron temperature in the samples and should be implemented in future work.

5.2.2 Dunker

A simple 4He dunker was built for our lab several years ago by Chris Merchant. The dunker, seen in Figure 5.7 consists mainly of a vacuum can, sample holder, and ribbon cable connected to a 24-pin Fischer connector at room temperature. The dunker is very useful for quick measurements, and is extremely reliable for reaching 4K. It is small enough to fit in just about any magnet or transfer dewar and can be loaded and cooled down in about an hour. This dunker was used for many of the measurements in this thesis.

CHAPTER 5. MEASUREMENTS



Figure 5.8: Oxford Heliox with the sample holder removed from helium 3 pot (far left).

5.2.3 3He Cryostats

The primary cooling in 3He cryostat is from evaporative cooling of 3He liquid by cryopumping with a charcoal sorb. Before this is possible the 3He must be liquified. This is done by first pumping on a small volume of 4He known as the 1K pot. This pot will typically reach temperatures between 1.2 and 1.8K. The 3He gas, stored in a charcoal sorb in a separate volume, is released from the charcoal by heating the sorb to about 30K. The 3He gas then passes through the 1K pot, which is cold enough to condense the 3He gas into a liquid. The 3He liquid collects in a 3He pot, to which the sample has been thermally anchored. Once all the gas is released from the sorb, the sorb is cooled to 4K. The cold sorb the acts as a cryopump on the liquid 3He. This cryopumping cools the 3He pot to its base temperature of 250mK [80].

Oxford Heliox

The Oxford 3He cryostat was used in this work for some very early measurements. After that it developed a leak in the 1K pot pumping line that made it very inconve-

CHAPTER 5. MEASUREMENTS

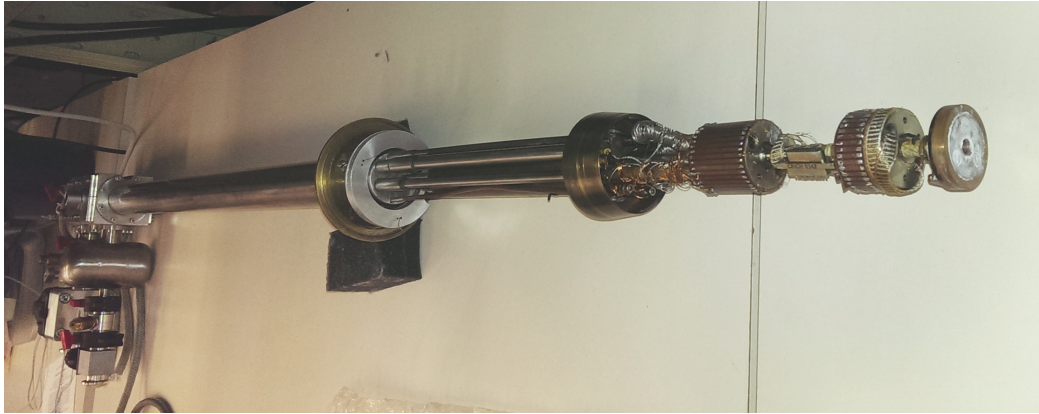


Figure 5.9: Photo of the RMC 3He cryostat with the sample holder removed from the 3He pot.

nient for this work. The typical hold times were about 24 hours, 12 hours on a bad day.

The operation of these Oxford cryostats is well-documented elsewhere. Temperature control is mainly done with an ITC503 temperature controller which monitors the temperature sensors and adjusts needle valve on the 1K pot line to keep the pot at the proper temperature during operation.

RMC 3He Cryostat

After both of our Oxford cryostats were found to have leaks, we obtained this cryostat on loan from a colleague. This cryostat had not been used for a decade before our lab adopted it. In order to make it compatible with our sample holders and breakout boxes, we rewired the cryostat with a 24-pin Fischer connector at room temperature and a 25-pin miniature D-sub connector anchored to the 3He pot. The

CHAPTER 5. MEASUREMENTS

original temperature control wiring was left in place, connected to a separate 19-pin connector which was then connected to a custom breakout box. Heater power was supplied with $\pm 12V$ power supplies on the breakout box. The RuOx and Pt 3He pot temperature sensors were read with a Neocera LTC21 temperature controller.

Instructions for cooling down the RMC 3He cryostat can be found in Appendix B.2

5.2.4 Dilution Refrigerator

Dilution refrigerators rely on a mixture of 3He and 4He to achieve temperatures as low as 5mK. Our Kelvinox system is said to be capable of 7mK base temperatures, although, due to various problems with the IVC vacuum I have been unable to cool it below 70mK.

The process by which the dilution fridge achieves its based temperature is easiest to understand by following the path of the gas mixture through the system. The mixture is cooled from room temperature to 4K by traveling in the condenser line through the LHe bath in the magnet dewar. The mixture then passes through the 1K pot where 3He is condensed. The condensed mixture then passes through the primary impedance, designed to control the flow rate to the mixing chamber. After the primary impedance is a series of heat exchangers, which use outgoing cold gas to cool the incoming mixture to 50mK. From there, the mixture moves into the mixing chamber. The mixing chamber contains two phases of the 3He/4He mixture, a dilute phase and

CHAPTER 5. MEASUREMENTS

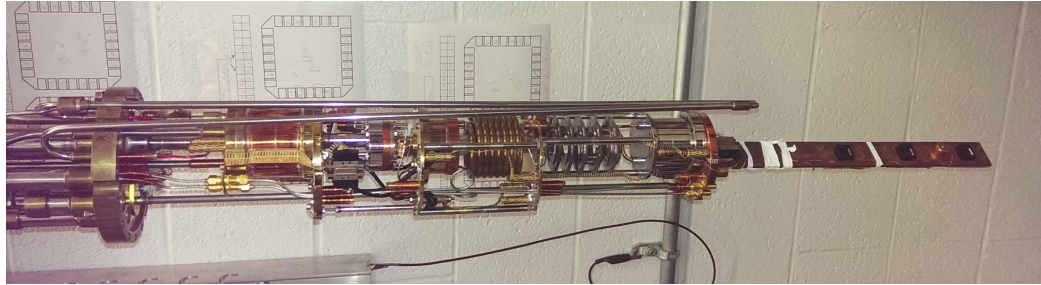


Figure 5.10: Oxford Kelvinox dilution refrigerator with custom built three sample holder (far right).

a concentrated phase. The most important cooling stage of the dilution fridge is the evaporating of ^3He from the concentrated phase into the dilute phase in the mixing chamber. ^3He moves from the dilute phase in the mixing chamber into the still, which is held at about 600mK. Osmotic pressure from the lower ^3He concentration in the still drives this movement. Finally, the mixture is pumped through the heat exchangers and out of the fridge through the still pumping line. It then passes through cold traps to remove any impurities before reentering the condenser line [80].

Oxford Kelvinox

The Oxford Kelvinox used in our lab is pictured in Figure 5.10. This system was not used for about 5 years before I cooled it down in 2014. It required several repairs to the temperature control wiring and pump power supplies, but the gas handling systems were found to be in very good condition. After several cool downs, it became apparent that the system had a leak into the IVC from the top plate.

Instructions on cooling down the Kelvinox dilution refrigerator can be found in

CHAPTER 5. MEASUREMENTS

Appendix B.1.

5.2.5 Superconducting Magnets

Oxford Magnet

This magnet was purchased along with the Oxford Heliox and Kelvinox cryostats. Those two cryostats are designed to fit easily into the magnet bore with the samples sitting at the center of the field as calibrated by the manufacturer. It is an 8T superconducting magnet mounted in an Oxford liquid helium dewar with a liquid nitrogen jacket. Current to the magnet is supplied by a matching Oxford IPS120 magnet power supply. This magnet was used for all of the measurements in Chapter 6.

BTI Magnet

This magnet was taken from a discarded BTI SQUID system. Similar to the Oxford magnet, it is a 9T superconducting magnet mounted in a liquid helium dewar with a liquid nitrogen jacket. This setup was assembled by, and borrowed from, Dan Reich's lab along with the RMC cryostat. Since the magnet could not be used with its original controller, a custom controller was assembled using an AMI controller with a HP power supply and custom made energy absorber/polarity switch. Upon receiving this system, it was tested and wired to a new BNC interface box to be controlled by

CHAPTER 5. MEASUREMENTS

a NI DAQ board along with transport measurements described above. This magnet was used for the data presented in Section 7.4.

Chapter 6

Quantum Dots with Ferromagnetic Leads

Of the many samples discussed in Chapter 4, seven F-CNT-F devices were measured at low temperatures. Details, including room temperature resistance, can be seen in Table 6.

Each of these samples was measured at 4K, with the exception of SCF98 (11-12) which was measured at 150mK. Figure 6.1 shows Coulomb diamond plots for each of the samples. These plots were used to calculate the quantum dot properties seen in Table 6

The lever arm, α_G , defined as $\alpha_G = C_G/C_\Sigma$ and is used to convert gate voltages to energies, $U_{gate} = \alpha_G e V_{gate}$ [12]. It is calculated based on the geometry of the Coulomb diamonds, as illustrated in Figure 6.2 and characterizes the coupling regime for each

CHAPTER 6. FERROMAGNETIC CNTQD

Sample	Leads	Material	Deposition Method	R($T = 300K$)
SCF72	17-19	Co	sputter	65 k Ω
SCF72	21-23	Co	sputter	76 k Ω
SCF75	21-23	Co	sputter	280 k Ω
SCF75	15-16	Co	sputter	30 k Ω
SCF96	9-12	Co	electron beam evaporation	200 k Ω
SCF96	16-17	Co	electron beam evaporation	400 k Ω
SCF98	11-12	Co	electron beam evaporation	120 k Ω

Table 6.1: Details of measured F-CNT-F devices

Sample	Leads	$\Delta\mu(meV)$	$\Delta E(meV)$	$\frac{e^2}{2C}(meV)$	$L_{measured}(nm)$	L_{design} (nm)	$C_\Sigma(aF)$	α_G
SCF72	23-21	8	x	x	175	300	x	0.080
SCF72	17-19	8	1.8	6.2	280	300	13	0.072
SCF75	21-23	15	4.5	11.5	110	300	7	0.075
SCF75	15-16	12	3.5	8.5	140	300	9	0.110
SCF96	9-12	30	4.0	26.0	125	300	3	0.011
SCF96	16-17	22	2.0	20.0	250	300	4	0.006
SCF98	11-12	7	1.8	5.2	280	300	15	0.005

Table 6.2: Low temperature characteristics of F-CNT-F quantum dots

CHAPTER 6. FERROMAGNETIC CNTQD

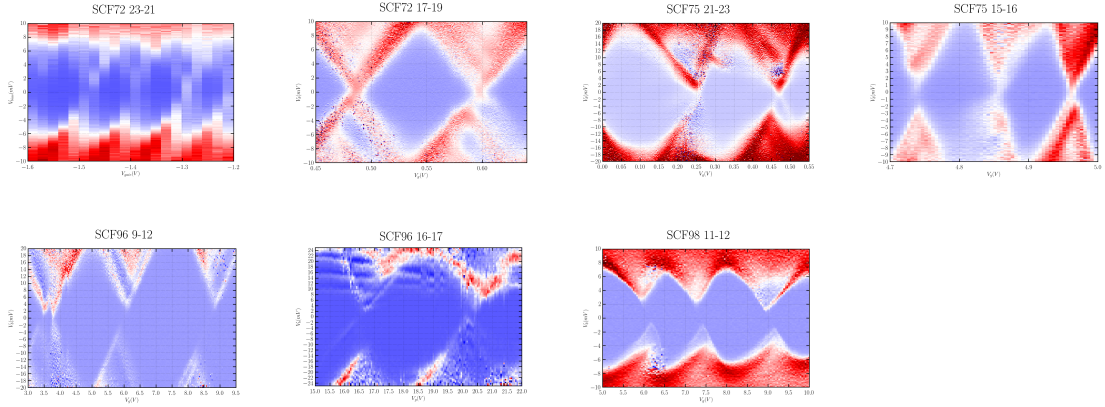


Figure 6.1: Conductance as a function of V_{bias} and V_{gate} for all measured ferromagnetic quantum dots.

device. The electron beam evaporated samples are in a much weaker coupling regime than the sputtered samples. All other aspects of the fabrication were the same over all four chips.

6.1 Tunneling Magnetoresistance

Tunneling magnetoresistance is a change in resistance measured across a ferromagnet/insulator/ferromagnet structure as a function of magnetic field [81]. The spin transport through such an interface can be made tunable by replacing the insulator with a tunable quantum dot. Carbon nanotubes quantum dots are an attractive choice due to their well-understood spin and orbital filling. Exchange coupling with the ferromagnetic leads will split the spin degeneracy of the quantum dot, making it possible to tune the magnitude and even the sign of the tunneling magnetoresis-

CHAPTER 6. FERROMAGNETIC CNTQD

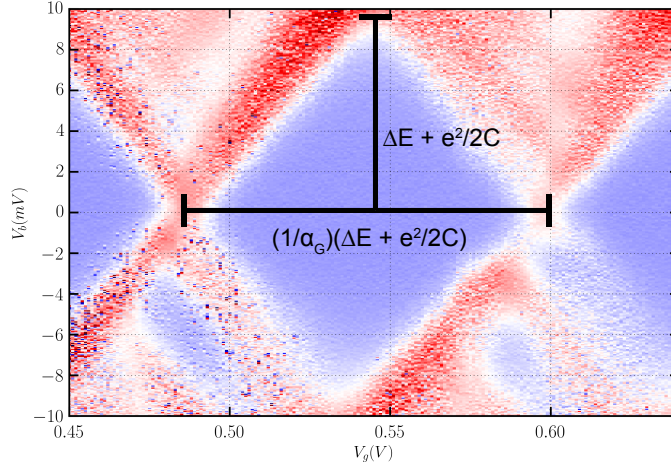


Figure 6.2: Calculating the lever arm using Coulomb diamond geometry.

tance [82–84].

The magnetization of the carbon nanotube contacts is dominated by their shape anisotropy [85]. This is typical for polycrystalline sputtered and electron beam evaporated films, such as the ones used in these samples [86]. For long, narrow, rectangular ferromagnet films, the shape anisotropy depends primarily on the width of the film. Wider films have slightly lower coercive fields at which the magnetization will be flipped as an external, parallel magnetic field is varied. By patterning two ferromagnetic contacts of different widths on a carbon nanotube, tunneling magnetoresistance can be measured through the nanotube quantum dot. A schematic of the situation can be seen in Figure 6.3.

CHAPTER 6. FERROMAGNETIC CNTQD

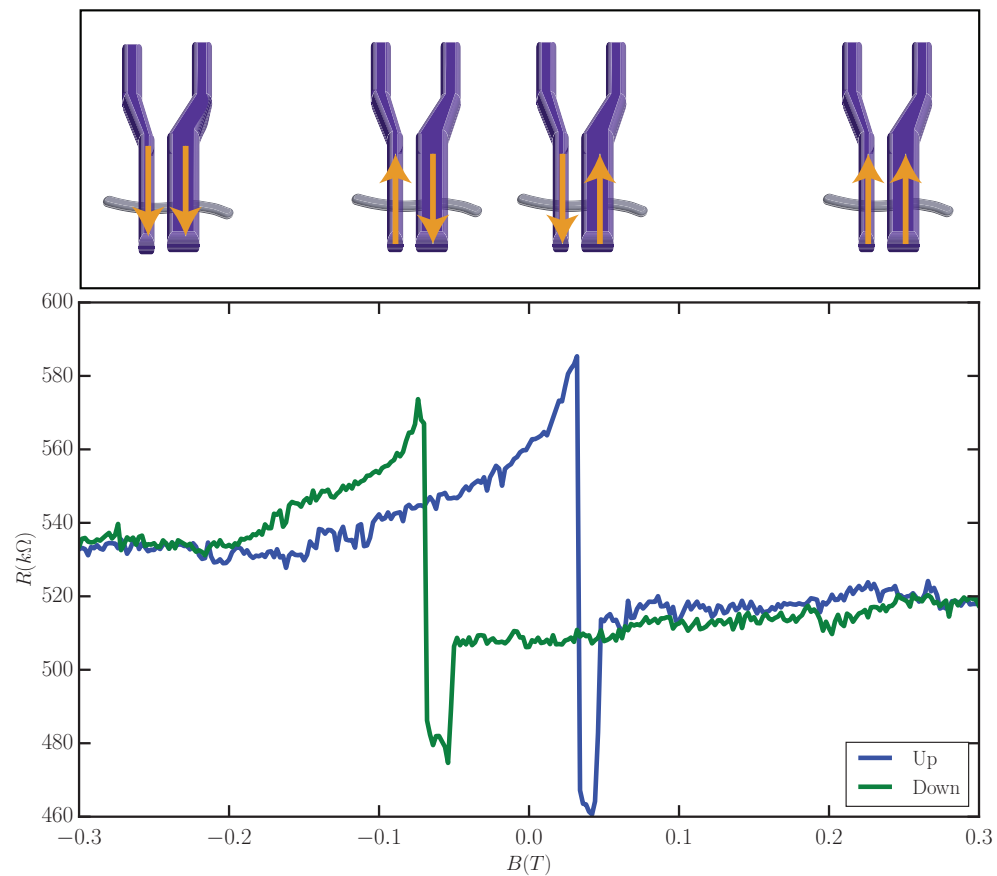


Figure 6.3: Top: A diagram of the magnetization of the ferromagnetic nanotube contacts corresponding to the data shown in the lower plot. Bottom: TMR signal measured through a carbon nanotube quantum dot.

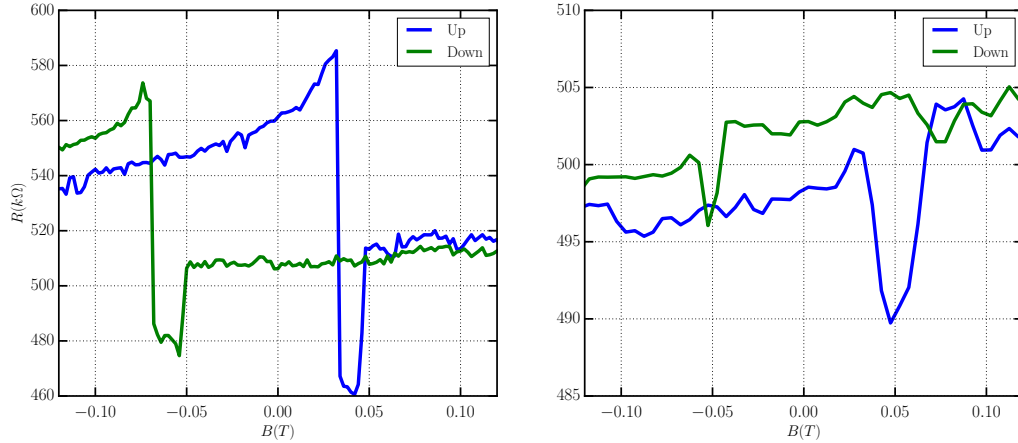


Figure 6.4: Tunneling magnetoresistance measurements taken on device SCF72 (17-19) at $V_{gate} = 0V$. The plots show data for $V_{bias} = 5mV$ (left) and $V_{bias} = 10mV$ (right).

6.1.1 Results

Of the ferromagnetic devices measured, only sample SCF72 showed clear tunneling magnetoresistance behavior. In the other devices the effect was overwhelmed by random telegraph noise in the data, which can look like false TMR signals, or metal/nanotube barriers with impurities causing spin-flip events that destroyed the TMR effect.

In the simplest model, tunneling magnetoresistance is defined as:

$$TMR \equiv \frac{G_P - G_{AP}}{G_P + G_{AP}} = \frac{R_{AP} - R_P}{R_P + R_{AP}} \quad (6.1)$$

$$TMR = P_L P_R \quad (6.2)$$

Where $P_{L(R)}$ are the spin polarizations at the Fermi level for the left and right nanotube contacts [87]. This polarization is defined as:

CHAPTER 6. FERROMAGNETIC CNTQD

$$P_{L(R)} = \frac{\rho_+^{L(R)} - \rho_-^{L(R)}}{\rho_+^{L(R)} + \rho_-^{L(R)}} \quad (6.3)$$

Where $\rho_{+(-)}^{L(R)}$ are the tunneling density of states for the majority (minority) spins at the Fermi level. In this picture, $P_{L(R)}$ will be positive, thus the TMR signal will be positive.

In the data shown in Figure 6.4, the TMR signal is measured to be about -6.0% and -0.8% in the left and right plots, respectively. Additionally, the coercive fields for the two cobalt contacts are 40mT and 60mT. These coercive field measurements are consistent with the predicted values for narrow cobalt wires.

The TMR signal has a magnitude consistent with the predicted values [87], but with the opposite sign. This change in sign of the TMR signal has previously been explained by a resonant tunneling model with asymmetric coupling of the left and right contacts to the nanotube. The model as described here is taken from [82].

First the conductance through the quantum dot can be written as:

$$G(E) = \frac{4e^2}{h} \frac{\Gamma_L \Gamma_R}{(E - E_i)^2 + (\Gamma_L + \Gamma_R)^2} \quad (6.4)$$

Here, $\Gamma_{L(R)}$ are the tunneling rates on/off the quantum dot from the left(right) ferromagnetic contacts. These tunneling rates can be thought of as being proportional to the density of states of the on the leads. E_i is the energy of the quantum dot level nearest to the Fermi level of the leads, E .

When the quantum dot is tuned off resonance, $|E - E_i| \gg \Gamma_L + \Gamma_R$, the TMR

CHAPTER 6. FERROMAGNETIC CNTQD

signal is predicted by Equation 6.2. Near a resonant level, $E \sim E_i$ the situation is quite different. Considering the limit where $\Gamma_L \gg \Gamma_R$, Equation 6.4 simplifies to $G \sim \frac{\Gamma_R}{\Gamma_L}$. The conductance is now inversely proportional to the density of states on one of the leads, which leads to a sign inversion of the TMR signal.

$$TMR = -P_L P_R \quad (6.5)$$

By using a carbon nanotube quantum dot, the TMR signal can be modulated by tuning the resonant energy level E_i with the gate voltage. Additionally, the magnitude can be modulated because the levels on the quantum dot are spin non-degenerate due to the exchange coupling field introduced by the magnetic leads. This effect has been observed previously in carbon nanotube quantum dots [83, 84].

In sample SCF72, the TMR signal was only significant in a narrow range of gate voltages near $V_{gate} = 0V$, as shown in Figure 6.4. Looking at the conductance data as a function of the gate voltage in Figure 6.5, it is clear that at $V_{gate} = 0V$ there is a quantum dot level E_i resonant with the Fermi level on the leads. This TMR measurement is used in Section 6.3 to establish that tunneling onto the dot conserves spin, and tunnel rates from the source and drain are asymmetric.

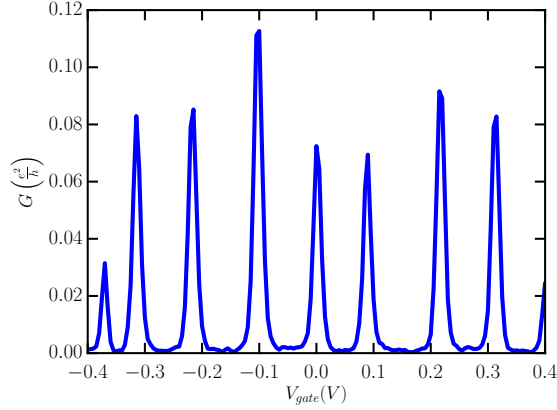


Figure 6.5: Conductance as a function of V_{gate} for sample SCF72. Note the conductance peak at $V_{gate} = 0V$.

6.2 Negative Differential Conductance in Coulomb Blockade Regime

Negative differential conductance resulting from spin blockade has been observed in two devices measured, seen in Figure 6.6. These measurements will be compared to a previous measurement of a carbon nanotube double quantum dot [1] as well as a theoretical model predicting spin suppression in single quantum dots [2]. This work is the first instance of these effects being observed in a F-CNT-F device. Neither device showed clear TMR measurements, but we assume there is some spin transport through the tunnel barriers, as well as asymmetry in the source/drain tunneling rates based on the contact widths.

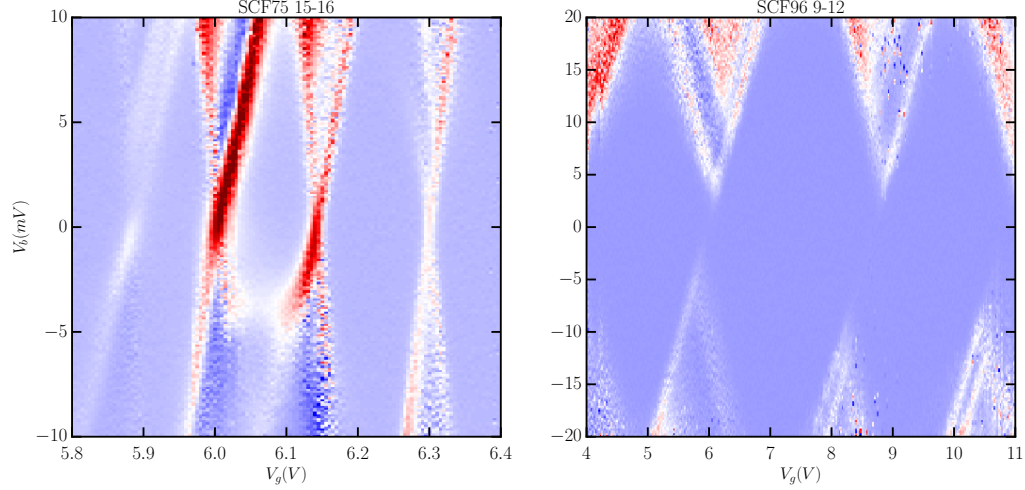


Figure 6.6: Conductance as a function of V_{bias} and V_{gate} in samples SCF75 (left) and SCF96 (right). Note the differential conductance peaks in dark blue running parallel to the diamond edges in each sample.

6.2.1 Spin Blockade in a Double Quantum Dot

Defects or impurities along the length of a nanotube quantum dot can form small tunnel barriers that interrupt electron transport through the dot [88,89]. These tunnel barriers define multiple quantum dots between the fabricated leads on the sample. This is a commonly observed problem in substrate grown carbon nanotubes. Other work has exploited similar defects to form tunable double quantum dots [90,91].

With careful analysis, the formation of multiple quantum dots in series can lead to interesting physical situations not observed in single quantum dot devices. Two quantum dots formed in series by a defect or impurity have much lower tunnel barriers and stronger coupling than double quantum dots formed by the patterning of local gates. Thanks to this strong coupling between dots, spin interactions can be observed

CHAPTER 6. FERROMAGNETIC CNTQD

that are not seen in as-fabricated double quantum dot structures. In 2008, Buitelaar et al. used this idea to measure Pauli spin blockade in a carbon nanotube double quantum dot [1]. The model relies on the formation of a double quantum dot by an impurity.

Table 6 shows samples SCF75 (15-16) and SCF96 (9-12) have calculated lengths of 140nm and 110nm, respectively. Comparing this to the 300nm spacing between cobalt leads suggests that the quantum dot being measured in each case is defined by defects along the nanotube. This is supported by the gate measurements that show no clear periodicity in Figure 6.7. One final piece of evidence for a double quantum dot is the suppressed conductance in the SCF75 levels around $V_{gate} = 5.9V$, this can be attributed to one dot being off resonance while the other is not. This feature also suggests the back gate coupling for each quantum dot is quite different, thus the gate dependent features are dominated by a single dot in the series.

Figure 6.8 illustrates the basic principles of the proposed model. It based on a hybridization between levels in the two strongly coupled quantum dots. Spin blockade then comes from a forbidden transition between the (1,1) spin triplet state and the (0,2) spin singlet state.

Figure 6.9 shows the data from SCF75 alongside the simulation from Buitelaar et al. Note the similarities in the negative differential conductance peak in the data and simulation. The simulation was run for a device 300nm in length with a defect in the center, giving two dots of size 150nm, consistent with Table 6. Using $\alpha_G = 0.11$, gives

CHAPTER 6. FERROMAGNETIC CNTQD

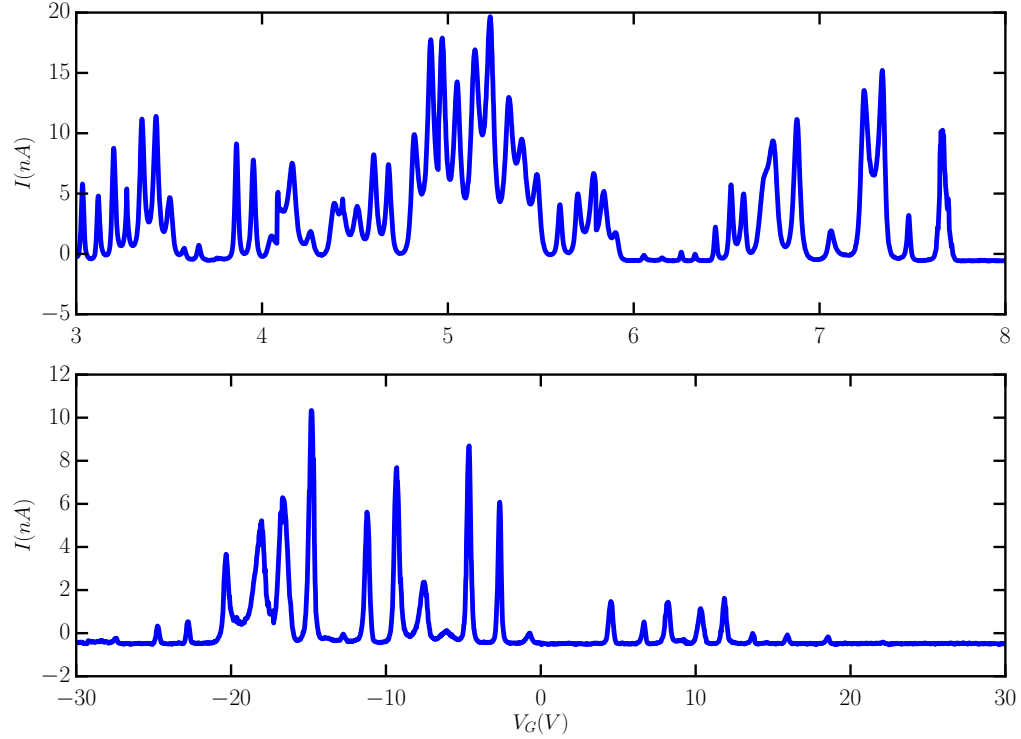


Figure 6.7: Current as a function of V_{gate} in samples SCF75 (top) and SCF96 (bottom). No clear periodicity is visible in either measurement implying disorder along the nanotube.

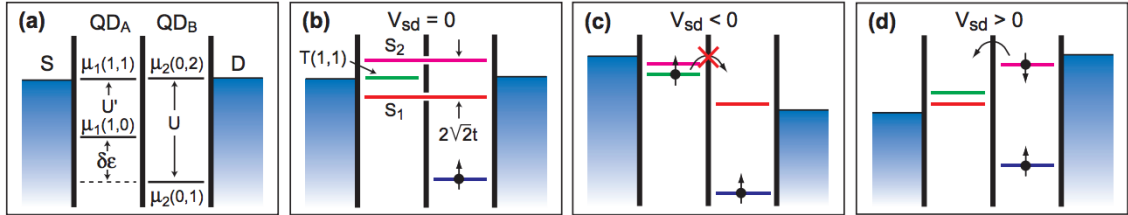


Figure 6.8: Figure adapted from [1]. (a) Double quantum dot levels. Numbering refers to the occupation of (QDA,QDB). $\delta\epsilon$ is the splitting between single particle energy levels. U and U' are the charging energies. (b) With strong coupling the $(1,1)$ and $(0,2)$ states hybridize to form bonding and anti-bonding orbitals S_1 and S_2 different from the triplet state T . (c) At negative bias the $(1,1)$ to $(0,2)$ transition is forbidden by spin blockade as the $(0,2)$ must be a spin singlet. (d) The transition is allowed in the reverse bias situation.

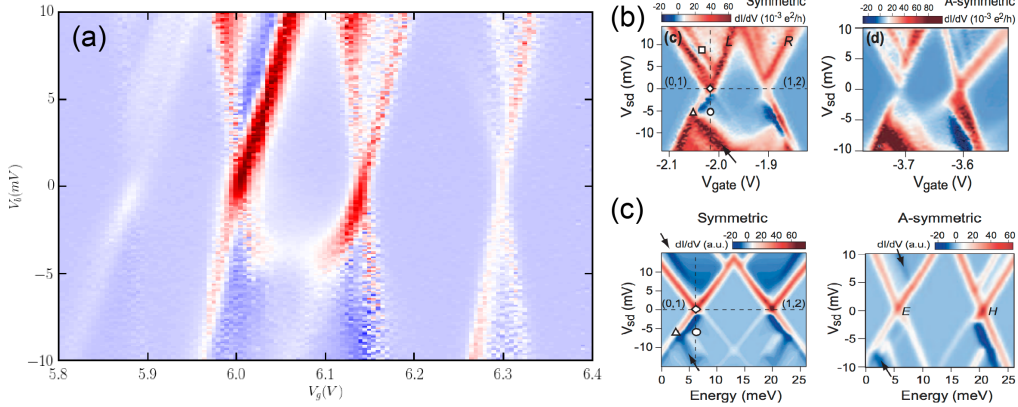


Figure 6.9: A comparison of the SCF75 negative differential conductance data (a) with double quantum dot data (b) and simulations (c) from Reference [1].

an energy spacing between the two zero bias conductance peaks of 15.4 meV, which agrees well with the simulation parameters. The situation is identical for SCF96, with the exception of the gate coupling.

6.2.2 NDC from Spin Selection Rules

The negative differential conductance peaks seen in Figure 6.6 may be explained by a simpler, single dot model, but not necessarily captured by the constant interaction model discussed in Section 2.4. As electrons fill the quantum dot, they are not only subject to charge interactions, but also spin interactions. Each quantum dot occupation number has many possible collective spin states. Figure 6.10 tabulates some of these states for low occupation numbers, calculated from Clebsch-Gordan coefficients [2].

This means that there are spin selection rules that can determine the lifetime of a

CHAPTER 6. FERROMAGNETIC CNTQD

TABLE I. – *Spin and energies of low-lying excitations of the correlated electron model at sufficiently large electron distances $r_s \equiv L/(n-1) \gg a_B$. The tunnelling integrals t_n decrease exponentially with r_s .*

n	S	$E_v - E_0(n)$
2	0	0
2	1	$2t_2$
3	$1/2$	0
3	$1/2$	$2t_3$
3	$3/2$	$3t_3$
4	0	0
4	1	$(1 - \sqrt{2} + \sqrt{3})t_4$
4	1	$(1 + \sqrt{3})t_4$
4	0	$(2\sqrt{3})t_4$
4	1	$(1 + \sqrt{2} + \sqrt{3})t_4$
4	2	$(3 + \sqrt{3})t_4$

Figure 6.10: Table tabulating possible occupation numbers, spin states, and relevant energy level splittings for low occupation number quantum dots as calculated by Weinmann et al. [2].

given quantum dot state. Consider, for example, a state with occupation number n and maximal spin, $S = n/2$. This is possible when transport occurs through excited states in a 1D quantum dot. The $S = n/2$ state must transition to a nearby state ($n - 1$, $S' = (n - 1)/2$). Since the spin can only change by $-1/2$, not $\pm 1/2$, $S = n/2$ is a relatively long lived state. When this state is brought into resonance with the Fermi level on the leads, the current through the dot is reduced, leading to a negative differential conductance peak. Figure 6.11 compares qualitatively a simulation of this effect with the data from SCF96 [3].

A similar effect can explain the missing ground state transitions seen in the data for SCF96. If the spin ground states for two adjacent quantum dot occupation numbers differ by more than $1/2$ the conductance peak is missing from the stability diagram. These calculations assume spin degenerate levels and symmetric coupling to nor-

CHAPTER 6. FERROMAGNETIC CNTQD

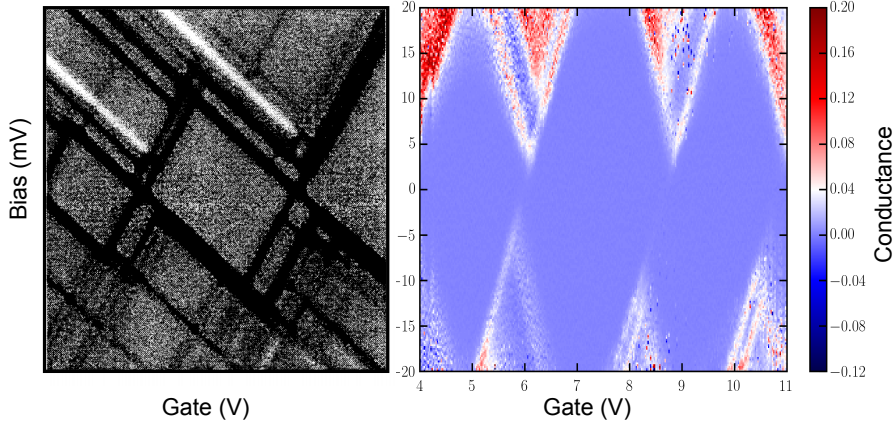


Figure 6.11: A comparison between simulated transport through a quantum dot with spin selection rules and data from SCF75. The simulation is taken from Weinmann et al. [3]. Simulation data shows regions of negative differential conductance as bright white lines. Data on the right shows regions of negative differential conductance in dark blue.

mal metal leads. Without a direct measure of the exchange coupling in ferromagnetically contacted nanotubes, it is unclear if the first criterion is met. The second condition is clearly not met, but it is not required, just a simplification. It is easy to imagine that these types of spin selection rules will be exaggerated further by reducing one spin population and introducing spin dependent tunnel barriers. See Figure 6.12(a) for a model of such a quantum dot.

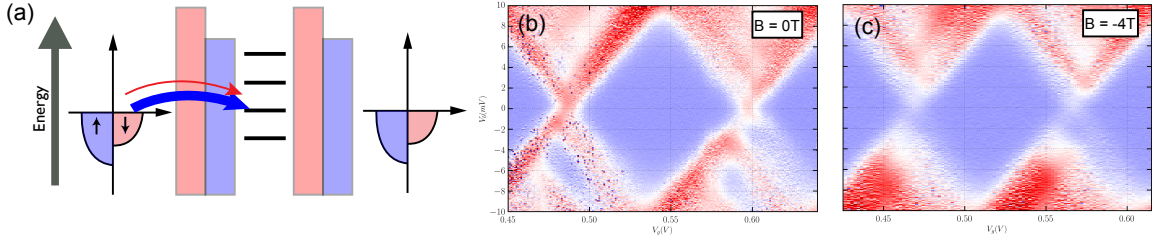


Figure 6.12: (a) Energy level diagram for an F-CNT-F quantum dot. The two barrier colors represent the two spin dependent tunnel barrier heights for spin up and spin down electrons. Blue and red arrows illustrate the different tunneling rates for up and down spins. (b) SCF72 conductance at $B = 0$. (c) SCF72 conductance at $B = 4T$.

6.3 Spin Selection Rules with Applied Magnetic Field

Additional data supporting the suppression of conductance peaks in ferromagnetic quantum dots due to spin selection rules is observed in sample SCF72. This dot has been used throughout this thesis as the canonical example of a Coulomb blockade measurement. It shows regular oscillations in the gate, suggesting a single dot with levels that are not split by exchange coupling or disorder. From the TMR measurement it is clear that tunneling onto the device preserves spin and there is an asymmetry in the source/drain tunneling rates, as seen in Figure 6.12(a).

Figure 6.13 shows Coulomb diamond data for SCF72 at $B = 0T$ and $-4T$; suppressed conductance levels are marked with dashed lines. Conductance peaks that mark ground state transitions between different dot occupation numbers (those that cross $V_{bias} = 0mV$) are suppressed as the applied field is increased. This can be

CHAPTER 6. FERROMAGNETIC CNTQD

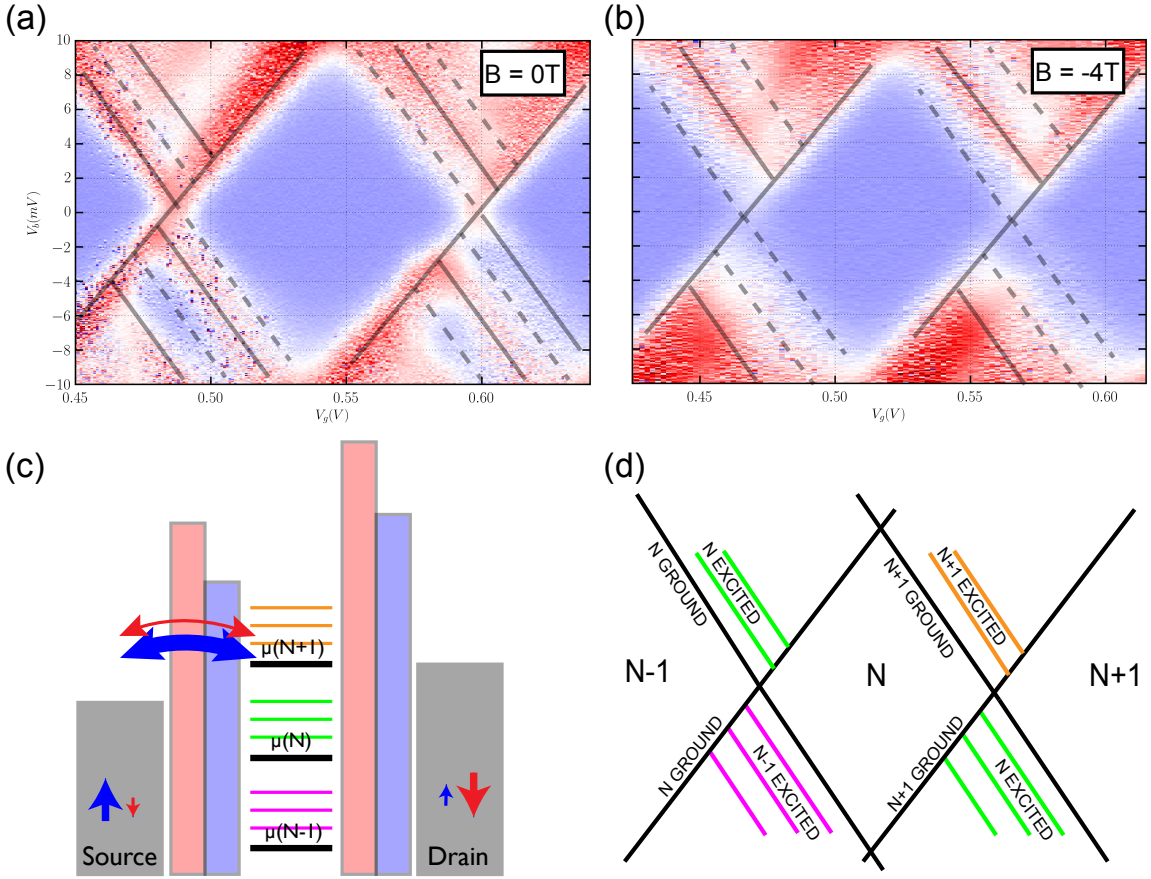


Figure 6.13: Conductance as a function of V_{gate} and V_{bias} for sample SCF72 at $B = 0\text{T}$ (a) and -4T (b). Solid lines trace conductance peaks. Dashed lines trace suppressed peaks. (c) Schematic of energies on the dot. (d) Sketch of energy levels as seen in the Coulomb diamond plots.

understood in light of the discussion in Section 6.2.2. Applying a strong magnetic field changes the spin ground state to one in which adjacent occupation numbers have spin levels differing by more than $\Delta S = 1/2$ as predicted by the constant interaction model. Looking at the excited states, it is clear that there is a similar change in which excited states are suppressed based on the change in lowest energy spin states.

The Zeeman splitting can be measured by measuring the change in excited state

CHAPTER 6. FERROMAGNETIC CNTQD

energies as the magnitude of the field is increased. At zero field, excited states are separated by $\Delta E = 1.8\text{meV}$. In a field of -4T, the levels are separated by $\Delta E = 2.0\text{meV}$. This is consistent with the Zeeman splitting energies previously measured in carbon nanotube quantum dots [92, 93]. This measurement does not show any splitting of degenerate levels. This suggests that the levels were not degenerate, or that some of the split levels do not participate in the conduction due to the same spin selection rules being discussed here.

6.3.1 Results and Discussion

Effects of spin selection rules have been observed in three samples. At least one of these samples, SCF72, is proven to be a clean, single quantum dot. This suggests that spin selection rules beyond the constant interaction model can be used to explain suppressed and negative differential conductance features in the Coulomb diamond data. Additional work must be done in modeling transport though a F-CNT-F dot to confirm that the features observed here can be fit using such a model.

6.4 Spectroscopy of a Magnetic Impurity

Coupling a nanoparticle to a carbon nanotube quantum dot makes it possible, through transport spectroscopy, to measure physical properties of nanoscale particles too small to contact using typical lithographic methods. Sample SCF96 shows such

CHAPTER 6. FERROMAGNETIC CNTQD

coupling to a magnetic impurity. The transport through the impurity was found to be tunable by varying the gate voltage and external magnetic field. The data are shown in Figure 6.14

Looking at the data it is clear that there are positive and negative differential conductance peaks that cut through the Coulomb blockaded regions of the conductance plot at positive bias in zero magnetic field. Both the positive and negative conductance peaks are suppressed at 2T.

6.4.1 Characteristic Size and Level Spacing

Figure 6.15 shows cuts through each of the three Coulomb diamonds where the resonance peaks are observed. Looking at plots at constant gate voltage, it is clear that the resonances have both positive and negative peaks in the conductance, with some background conductance superimposed due to the conductance through the nanotube quantum dot levels.

From the data in Figure 6.15 it is possible to derive the relevant energy scales of the impurity level. Positive and negative conductance peaks are split by 2meV. Adjacent positive peaks are separated by 5meV. This suggests that the impurity has at least 3 energy levels that are separated by 5meV. These three levels are spin split by 2meV, most likely because the impurity is ferromagnetic.

The charging energy for the impurity can be measured using the lever arm calculated in Table 6. Resonant tunneling through the impurity is observed for gate

CHAPTER 6. FERROMAGNETIC CNTQD

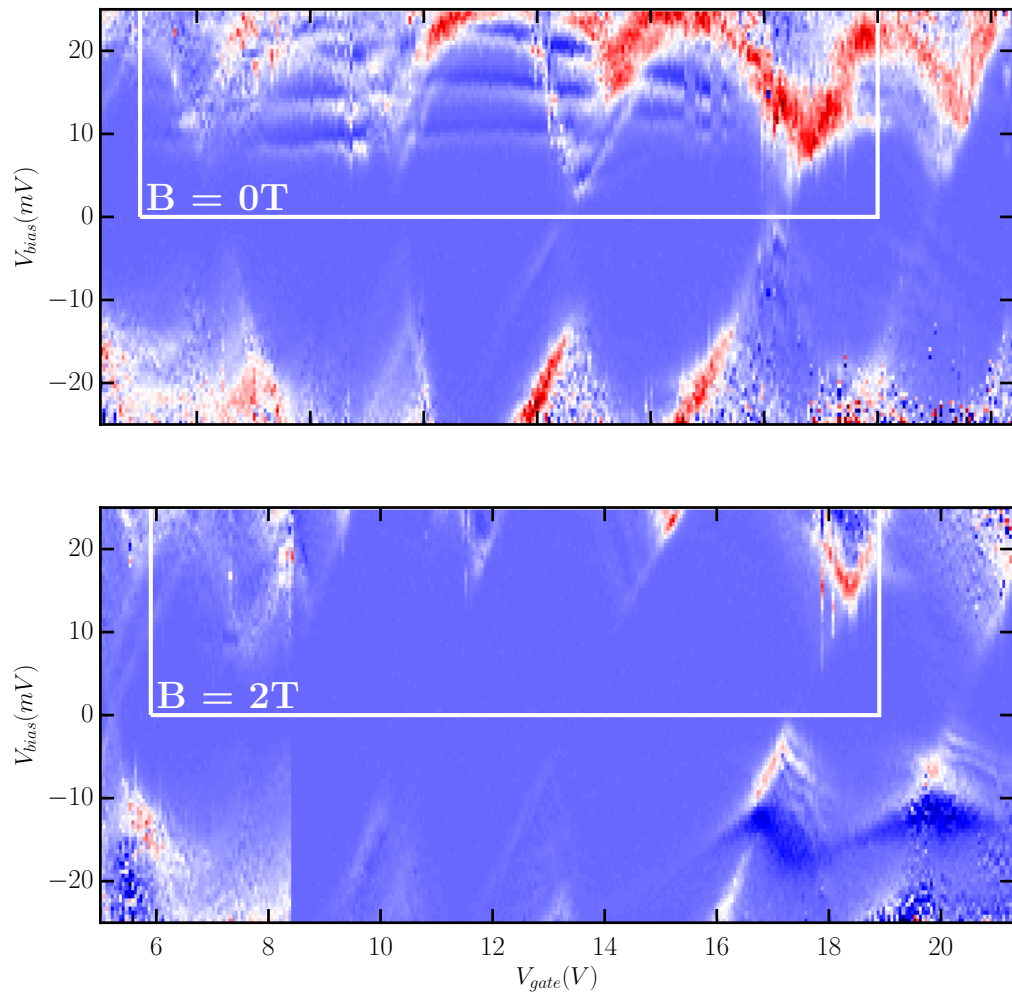


Figure 6.14: Top: Conductance as a function of V_{bias} and V_{gate} in zero field. Bottom: Conductance measured over the same portion of the quantum dot spectrum in a 2T magnetic field.

CHAPTER 6. FERROMAGNETIC CNTQD

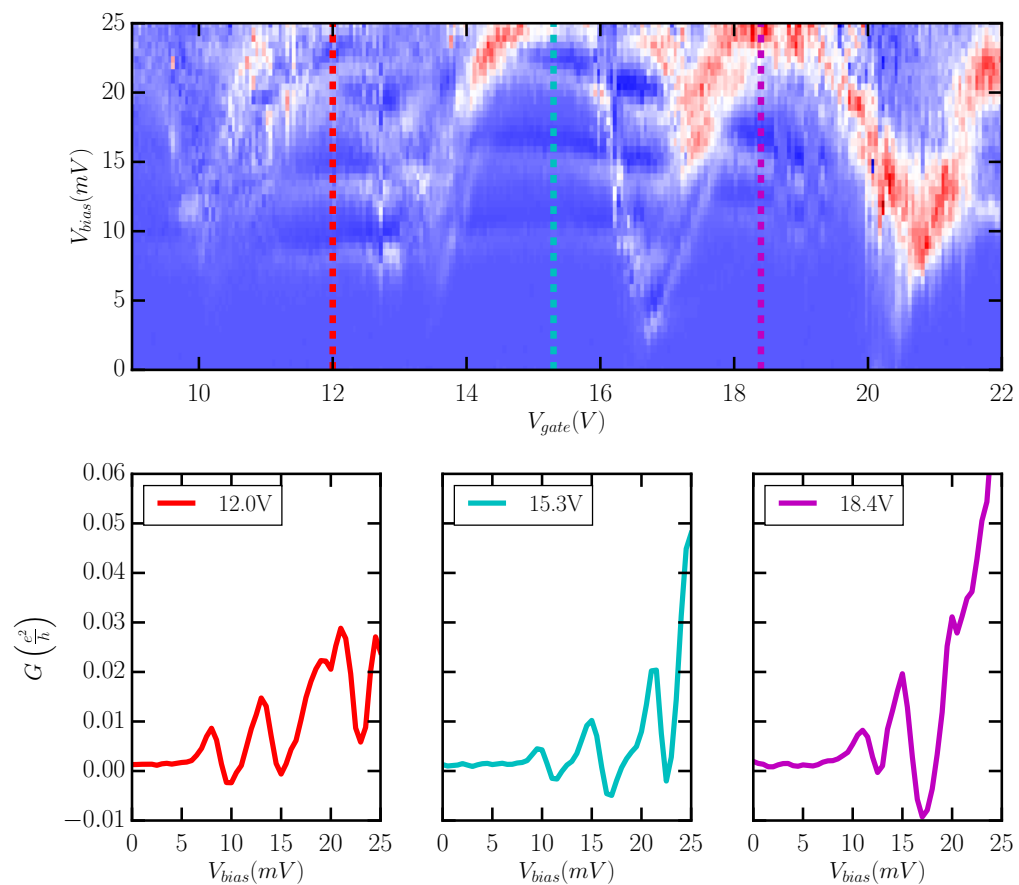


Figure 6.15: Top: Conductance as a function of V_{bias} and V_{gate} in zero field. Bottom: Conductance measured over the same portion of the quantum dot spectrum in a 2T magnetic field.

CHAPTER 6. FERROMAGNETIC CNTQD

voltages between 10 and 20V. With the lever arm of $\alpha_G = 0.006$ the charging energy can be estimated to be roughly 100meV, which corresponds to a capacitance of about $C_\Sigma = 0.8\text{aF}$.

The most likely origin of this impurity is a piece of magnetic contamination. The size of the impurity can be estimated in two ways. First, it can be estimated using the capacitance calculated above. Considering the impurity as a spherical metal shell gives $C_\Sigma \sim 4\pi\epsilon_0 r = 0.8\text{aF}$. With that, the radius is calculated to be $r = 7\text{nm}$. The size can also be estimated quantum mechanically from the level spacing, $\Delta E = 5\text{meV}$. Assuming the impurity is a 3D spherical well, the levels are $E_{n,l} = \frac{\hbar^2}{2ma^2} z_{n,l}^2$ where $z_{n,l}$ is the nth zero of the lth spherical Bessel function. For $l = 0$, the level spacing is $\Delta E = \frac{\pi\hbar^2}{2mr^2}$. Using the measured value $\Delta E = 5\text{meV}$ gives an estimate for the radius of $r = 5\text{nm}$. These two estimates are in good agreement and suggest an origin for the impurity. A 10nm diameter magnetic particle on the substrate perfectly describes the iron nanoparticles used in the nanotube catalyst.

6.4.2 Effects on CNT Quantum Dot Levels

Additional interactions between the dot and impurity levels can be seen at negative bias in the 2T magnetic field data. This region is highlighted in Figure 6.16.

There are two features to note in Figure 6.16. The first is the change in slope of the two Coulomb diamonds seen at negative bias. This is a clear indication that the conductance measured is not due to a single quantum dot as described by the

CHAPTER 6. FERROMAGNETIC CNTQD

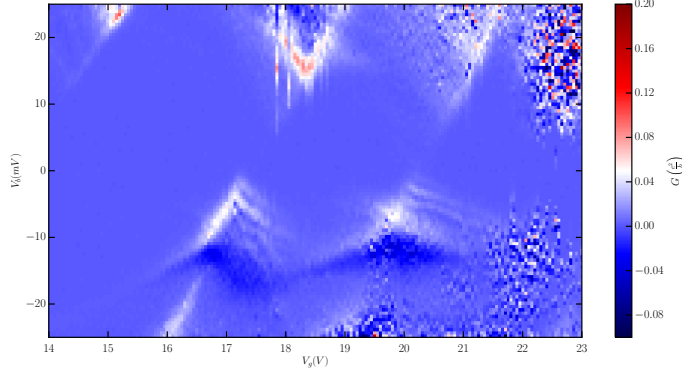


Figure 6.16: Conductance as a function of V_{bias} and V_{gate} at $B = 2T$ in sample SCF96. Note the difference in slope in the excited states of the two Coulomb diamonds seen at negative bias and the strong negative differential conductance.

constant interaction model. Additionally, note the strong negative differential conductance seen in these same diamonds. Both of these features suggest some coupling between the levels on the nanotube quantum dot and in the nearby magnetic impurity. A similar coupling has been observed previously between a magnetic impurity and vibrational modes in a suspended nanotube [94]. The exact nature of the coupling is not known, but it is likely that both of these observed features can be attributed to the presence of the magnetic impurity. The negative differential conductance in particular may fit with some existing models of hybridized levels in two quantum dots resulting negative differential conductance from spin blockade between the two dots as discussed in Section 6.2.1.

Chapter 7

Spin Transport in Tunable Ferromagnet/Superconductor Junction

In 1971, Tedrow and Meservey made their famous measurement of the spin polarization in a ferromagnetic nickel thin film [11]. This was done by creating a tunnel junction between the thin nickel film and a thin aluminum film. The density of states of the aluminum film was used as a probe into the spin polarization of the nickel film by measuring the conductance through the junction. Tedrow and Meservey later used this same technique to characterize a number of ferromagnetic materials [95]

The goal in this work was to replace the insulating barrier in the Meservey measurement with a carbon nanotube quantum dot. In doing so, it becomes possible to

CHAPTER 7. F-CNT-S

use the levels on the dot to further tune spin transport through the junction. Differential conductance measurements through such a F-CNT-S can be made to measure the ferromagnet polarization, exchange coupling in the carbon nanotube, and the spin-resolved density of states of the superconductor. The work presented in this chapter represents the first attempt to measure transport in this type of carbon nanotube quantum dot device.

7.1 Background

The results of the Tedrow and Meservey experiment can be described with a simple theory based on the density of states of the materials [5]. Figure 7.1(a) shows schematically the density of states on each side of the tunnel barrier in a non-zero magnetic field applied parallel to the thin films separated by an insulator. The ferromagnet has a larger number of spins aligned with its magnetization (and the applied field). In the superconducting film, the density of states is split due to Zeeman splitting in the applied magnetic field. The energy to add a spin up (aligned with the field) particle is lower than adding a spin down particle.

To begin, the tunneling current through a normal-insulator-superconductor junction can be written as follows:

$$I \sim N_n \int N_s(E)[f(E + eV) - f(E)]dE \quad (7.1)$$

CHAPTER 7. F-CNT-S

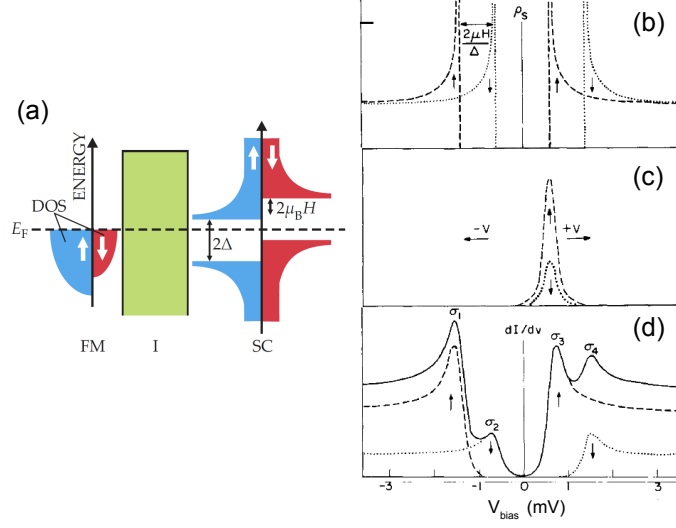


Figure 7.1: (a) Energy diagram showing the density of states of each material in the F-I-S junction. Figure adapted from [4]. (b) Superconducting density of states with Zeeman splitting. (c) Spin-dependent kernel used to calculate the tunneling current. (d) Differential conductance as measured through the junction. Different spin-resolved peaks are labeled σ_{1-4} . Figures (b)-(d) are adapted from [5].

Where N_n is the normal metal density of states which is independent of energy in 2D and $f(E)$ is the Fermi function. E is the Fermi level in the system and V is the applied bias voltage. The superconducting density of states N_s can be written in the BCS form [96]:

$$N_s(E) = \begin{cases} N_n(E) E \frac{e}{\sqrt{E^2 - \Delta^2}}, & |E| \geq \Delta, \\ 0, & |E| < \Delta. \end{cases} \quad (7.2)$$

Taking the derivative of Equation 7.1 gives the differential conductance for the NIS junction:

CHAPTER 7. F-CNT-S

$$\frac{dI}{dV} \sim N_n \int N_s(E) \left[\frac{df(E + eV)}{dV} \right] dE \quad (7.3)$$

In an applied magnetic field the spin up (parallel to applied field) and spin down (anti-parallel) contributions can be written separately.

$$\frac{dI}{dV} \sim N_n \int N_s(E + \mu H) \left[\frac{df(E + eV)}{dV} \right] dE + N_n \int N_s(E - \mu H) \left[\frac{df(E + eV)}{dV} \right] dE \quad (7.4)$$

Now that the expression for the differential conductance of an N-I-S junction is known, it is simple to infer the F-I-S results. Since the ferromagnet has a density of states that can be considered independent of the energy, like a normal metal in 2D, the only change is a factor to account for relative populations of spin up and spin down electrons.

$$\frac{dI}{dV} \sim N_n \int N_s(E + \mu H) \left[a \frac{df(E + eV)}{dV} \right] dE + N_n \int N_s(E - \mu H) \left[(1-a) \frac{df(E + eV)}{dV} \right] dE \quad (7.5)$$

Where a is the fraction of spin up electrons in the ferromagnet. Figure 7.1(b) shows the superconducting density of states in non-zero field and (b) shows the spin dependent kernel in the integrals in Equation 7.5. Finally, Figure 7.1(d) shows the resulting differential conductance through the F-I-S junction.

The peak heights seen in Figure 7.5(d), σ_{1-4} can be used to calculate the polarization.

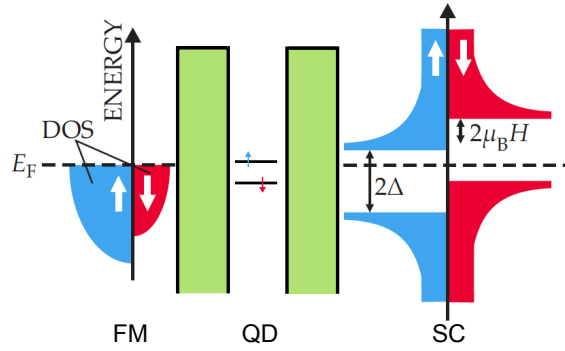


Figure 7.2: Energy diagram showing the density of states and energy levels in a F-QD-S junction. Figure adapted from [4].

$$P = 2a - 1 = \frac{(\sigma_4 - \sigma_2) - (\sigma_1 - \sigma_3)}{(\sigma_4 - \sigma_2) + (\sigma_1 - \sigma_3)} \quad (7.6)$$

Equation 7.6 is what Tedrow and Meserve derived to measure the spin polarization of a given ferromagnetic thin film using tunneling current through an F-I-S junction.

Now, it is important to consider what might be observed when replacing the tunnel junction with a carbon nanotube quantum dot. An energy diagram of the device can be seen in Figure 7.2.

The levels on the dot should be non-degenerate due to exchange coupling with the ferromagnetic lead. The exchange coupling magnitude is not known in carbon nanotubes and could be determined using the proposed devices. Such a measurement would be useful in discussing spin transport through ferromagnetically contacted nanotubes such as in Section 6.3. The magnitude of the conductance peaks sketched in Figure 7.1(d) will be modulated by bringing quantum dot levels with different spin

CHAPTER 7. F-CNT-S

polarizations in and out of resonance with the Fermi level on the magnetic and superconducting leads. Looking at how these conductance peaks evolve in the magnetic field at different gate voltages will give information about the exchange coupling between the nanotube and ferromagnet. A similar measurement has been made to confirm the ferromagnetic exchange coupling in InAs quantum dots [97]

Measurements of the differential conductance as a function of V_{bias} and applied field should show the conductance peaks sketched in Figure 7.1(d) move as a function of the applied field in the same was as observed by Tedrow and Meservey. If the spin texture of the resonant quantum dot level is known, this measurement will probe the density of states of the ferromagnet and superconductor materials.

7.2 Characteristics of Samples

Of the devices fabricated, two F-CNT-S devices yielded clean measurements at 4K, MT7 and SCFMH8. Basic properties of each device will be summarized here. These properties will be useful later in discussing the spin transport through each device.

MT7

Sample MT7 was one of the earliest samples made for this project and motivated a lot of my later work on fabrication and experimental setup. It was made using

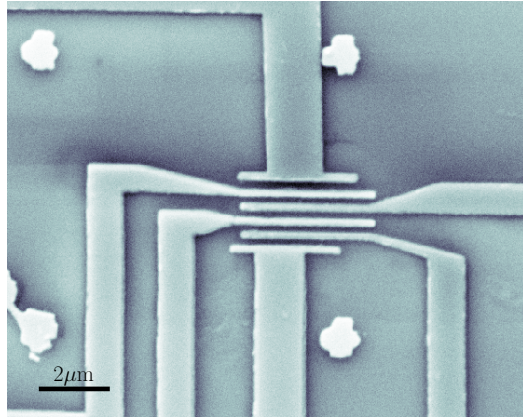


Figure 7.3: Scanning electron microscope image of sample MT7. The leads are alternating Co and Nb, starting with Co at the top. Each section of nanotube between two adjacent leads forms a 300nm long quantum dot. The nanotube is not visible because of the 30kV accelerating potential used to make the image.

dropcast nanotubes on a silicon substrate with sputtered cobalt (50nm) and niobium (60nm) leads.

The device is shown in Figure 7.3. Figure 7.4 shows the conductance as a function of V_{gate} measured at 4K. The inset of that figure shows some two-fold symmetry in the peaks. The spin degeneracy should be broken by the presence of the cobalt leads. The two-fold symmetry likely comes from orbital symmetry, which is assumed to not be broken by the magnetic contacts.

Coulomb blockade features were measured in this device both above and below the critical field of the niobium contacts, which is just under 1T. Figure 7.5 shows this data. Some important information about the nature of this quantum dot can be extracted from the data in Figure 7.5. In the normal state ($B=1T$), the energy level splitting is measured to be $\Delta E = 2.0\text{meV}$. This corresponds to a calculated quantum

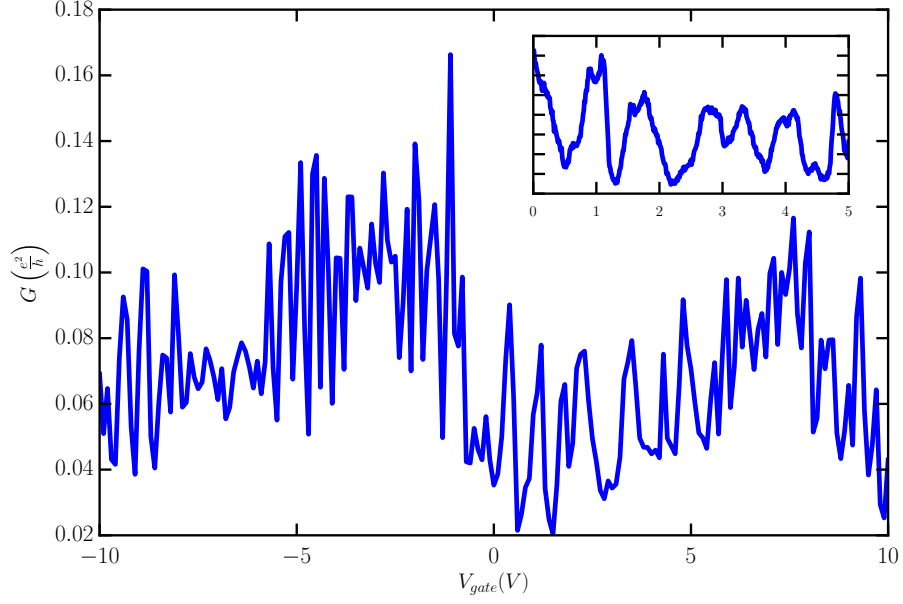


Figure 7.4: Conductance as a function of V_{gate} in MT7. The inset shows a region with clear two-fold symmetry in the addition energy.

dot size of 250nm, in good agreement with the image in Figure 7.3. The measured addition energy is about 2.5meV, giving a charging energy of 0.7meV and a total capacitance of 100aF and lever arm of $\alpha_G = 3.8$. This puts MT7 in a wildly different coupling regime than the substrate grown nanotubes used in the rest of this thesis.

In the top plot of Figure 7.5 the niobium lead is in the superconducting state. Due to the presence of the superconducting gap, the overall measured conductance is decreased and the coulomb diamonds no longer close at low bias. The splitting between diamond peaks gives a measure of the superconducting gap, $2\Delta = 3.5\text{meV}$. The expected gap can be calculated from BCS theory:

$$\Delta(T \rightarrow T_C) \approx 3.07k_B T_C \sqrt{1 - T/T_C} \quad (7.7)$$

CHAPTER 7. F-CNT-S

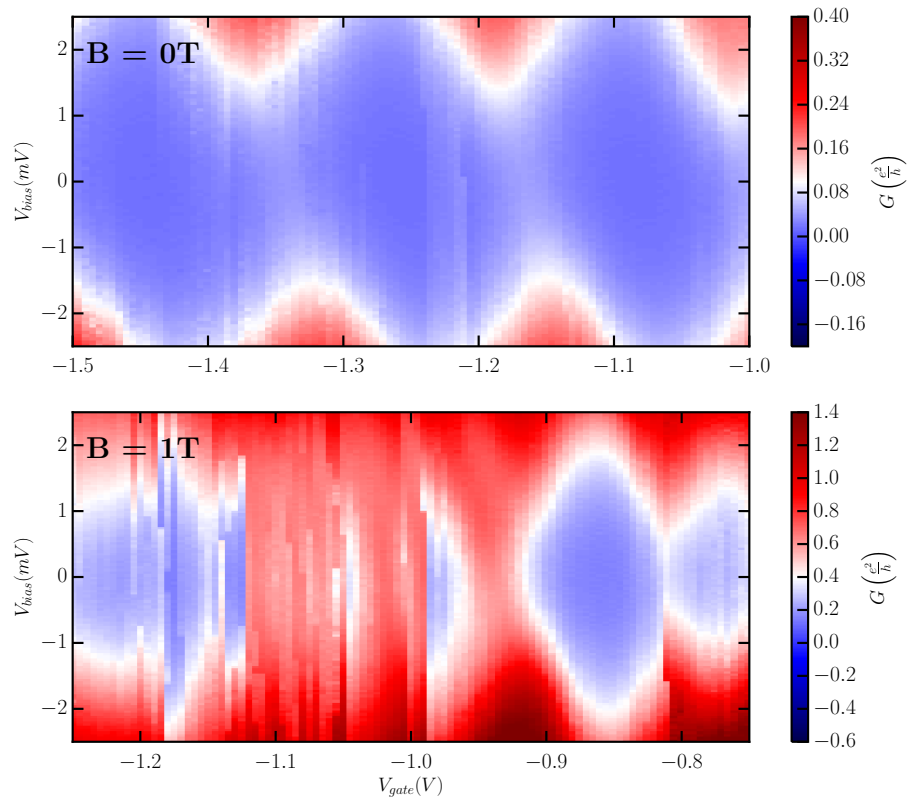


Figure 7.5: Conductance as a function of V_{bias} and V_{gate} in 0T (top) and 1T (bottom) magnetic field parallel to the leads.

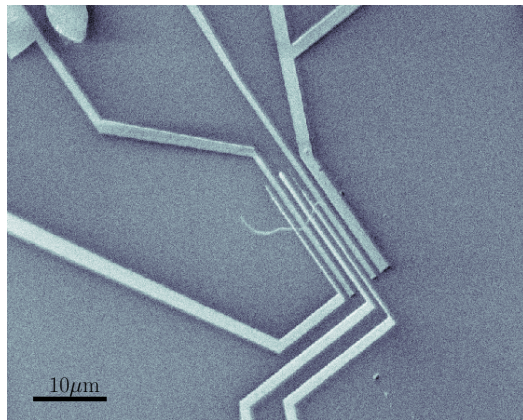


Figure 7.6: Scanning electron microscope image of sample scfmh8. The three wide leads are Nb, while the three narrow leads are Py. These leads are connected to bonding pads made with electron beam lithography and thermally evaporated Cr/Au layers.

Using this equation and the measured value of $T_C = 7\text{K}$, gives an expected gap of 1.2meV, which is in reasonably good agreement with the measured value, given the resolution of these measurements.

SCFMH8

Sample SCFMH8 was one of the last samples made for this work. Nanotubes were grown directly on the substrate with predefined Mo markers and contacted with thermally evaporated permalloy (40nm) and sputtered Ti/Nb (5nm/60nm). An image of the device can be seen in Figure 7.6.

As fabricated, the thermally evaporated permalloy leads had contact resistances in the $100\text{M}\Omega$ range. After fabrication, the samples were annealed at 325°C for 3

CHAPTER 7. F-CNT-S

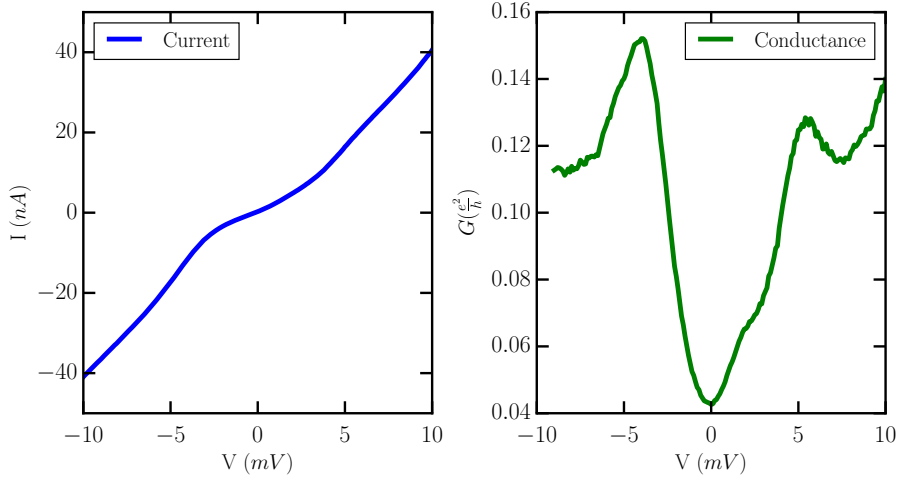


Figure 7.7: Current (left) and conductance (right) as a function of V_{bias} in sample SCFMH8.

hours in an Ar/H₂ atmosphere. After annealing, both Py-CNT-Py and Nb-CNT-Nb junctions were around 100kΩ. Tuning the back gate on this device was found to have no effect on the transport properties. It is possible that the high temperature growth or anneal damaged the gate oxide.

Figure 7.7 shows the current and conductance as a function of the bias voltage. The sample is clearly in the Coulomb Blockade regime, but the level spacings are difficult to determine. A two probe resistance measurement was made across a niobium wire fabricated on the same chip as SCFMH8. The critical field in this wire was found to be 2T.

7.3 Zeeman Splitting of Differential Conductance Peaks

In calculating Equation 7.5, a tunnel barrier with a height independent of energy was assumed. By replacing the tunnel barrier used in that model with a quantum dot, the assumption no longer holds. In order to capture the energy dependence of the quantum dot a term proportional to the density of states on the quantum dot must be added to the integral over the superconducting density of states. The data discussed in this section correspond to such a model.

Figure 7.8 shows the evolution of the differential conductance peaks in sample MT7 as a function of the magnetic field. Yellow dashed lines in the bottom plot serve as a guide to the eye for each of the differential conductance peaks.

Due to low resolution of the data it is difficult to make any fits to the dashed yellow lines tracing the conductance peaks in Figure 7.8. Similar data was taken for SCFMH8 and can be seen in Figure 7.9

To more easily discuss the differential conductance as a function of field, vertical cuts across the data in Figures 7.8 and 7.9 are shown in Figure 7.10

Figure 7.10 shows how the tunneling differential conductance evolves as a function of the magnetic field in each sample. Sample SCFMH8 shows very little movement of the peaks with the magnetic field. There are a number of reasons this might be the case. Most importantly, the splitting could be obscured by thermal noise in the

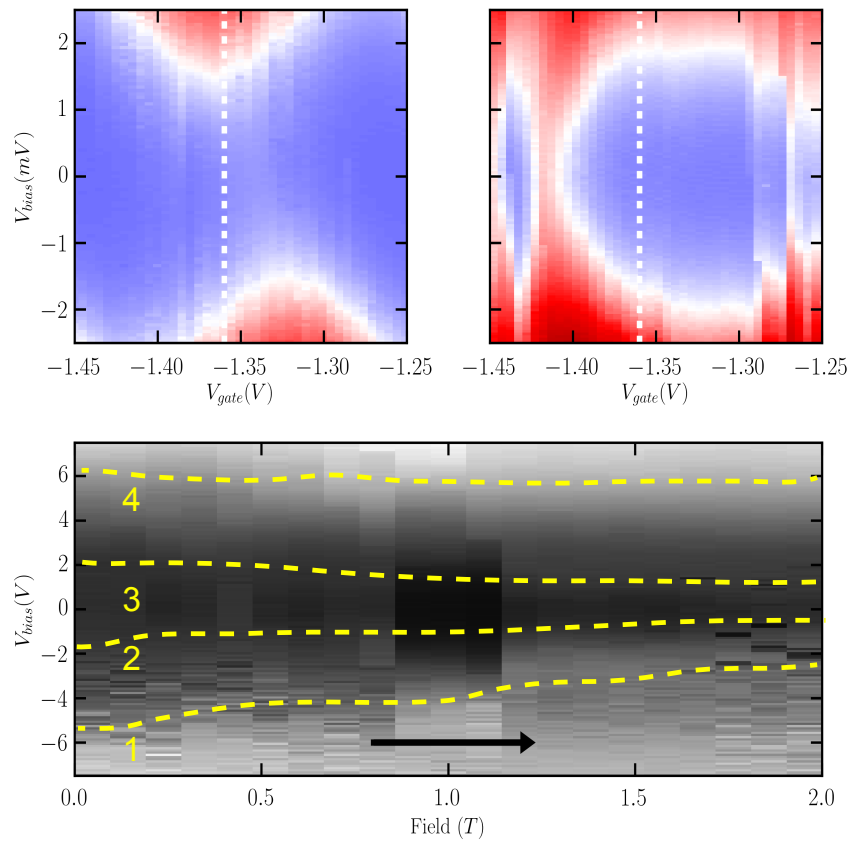


Figure 7.8: Top left: Coulomb diamonds in 0T. The white dashed line marks the gate voltage where the field sweep was taken. Top right: Coulomb diamonds in 2T parallel field. Bottom: Conductance as a function of V_{bias} and parallel magnetic field. Here V_{bias} was the fast sweep axis. Dashed lines represent approximate peak positions.

CHAPTER 7. F-CNT-S

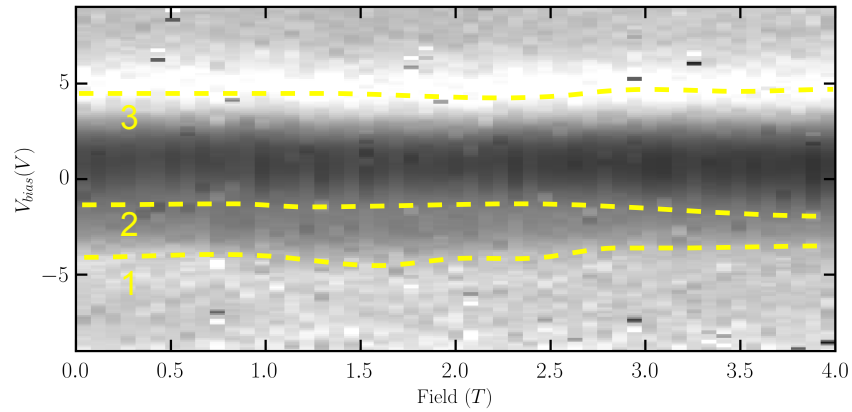


Figure 7.9: Conductance as a function of V_{bias} and parallel magnetic field in SCFMH8. V_{bias} was the fast sweep axis. Dashed lines represent approximate peak positions. Magnetic field sweep direction is from left to right.

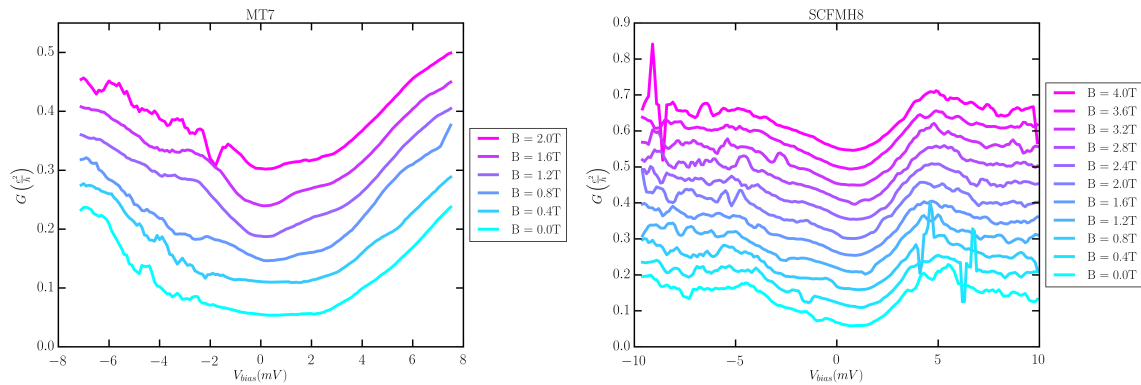


Figure 7.10: Conductance as a function of V_{bias} and parallel magnetic field in samples MT7 (left) and SCFMH8 (right). Conductance curves have been offset for clarity.

CHAPTER 7. F-CNT-S

system, which is on the order of $500\mu\text{eV}$. Zeeman splitting of opposite spin levels on a nanotube quantum dot has been observed in the past to be of the same order of magnitude [98]. This seem to be the most reasonable explanation. It is difficult to speculate any more on what splittings are expected from the Coulomb blockade features alone without the device being gate tunable. Looking closely at Figure 7.9 it is possible that there is some evidence of the superconducting gap closing in the outermost conductance peaks near $B = 2T$.

In Figures 7.10 and 7.8 it is clear that there is some field dependent movement of the conductance peaks in sample MT7. Again, it is important to remember a change in conductance at low bias is not solely due to the superconducting gap, but rather a combination of the gap and Coulomb blockade. From $B = 0\text{T}$ to 0.5T conductance peak 1 (labelled in Figure 7.8) shifts from $V_{bias} = -4.2\text{meV}$ to $V_{bias} = 3\text{meV}$. This agrees well with the closing of the calculated superconducting gap of 1.2meV . Similar features are observed in the other three conductance peaks. At fields above 0.5T , peaks 1-3 have a slight field dependance. Peaks 1 and 2 show positive slopes of 1.5 and 0.3 meV/T , respectively. Peak 3 has a slope of -0.1meV/T . Qualitatively this makes sense in terms of the Coulomb blockade. The magnitudes of the slopes are consistent with Zeeman splitting energies, $g\mu_BB$, in carbon nanotubes with a g-factor of 2. This also suggests that the levels are spin split due to exchange coupling with the ferromagnet, giving a hint at the magnitude of the coupling.

Further measurements to resolve these features at lower temperatures will be

necessary for a more quantitative analysis.

7.4 Hysteretic Switching of Quantum Dot Conductance in an External Field

After not observing any clear field dependence in the differential conductance of sample SCFMH8, additional measurements were performed. For these measurements the fast and slow scan axes were switched. Sweeping the magnetic field, at a fixed bias, while measuring current through the quantum dot revealed some interesting behavior. The full data set is seen in Figure 7.11.

There are three features to note in Figure 7.11. There are two changes in conductance, at 0.5T and 2.0T, apparent in each sweep. Based on the measured niobium critical field, it is obvious to associate the 2T change in conductance with the niobium leads transitioning to the normal state. The switch at 0.5T is 10-50 times larger than the expected coercive field for permalloy leads of this approximate size and shape [66,99]. Additionally, both of these switching events show a hysteresis with the magnetic field sweep direction.

The curves in Figure 7.11 can be compared to horizontal cuts across the data in Figure 7.9 to reveal the difference in the two measurements more clearly. A comparison of the two data sets is seen in Figure 7.12.

As a control, the same measurement seen in Figure 7.11, was made on a Nb-CNT-

CHAPTER 7. F-CNT-S

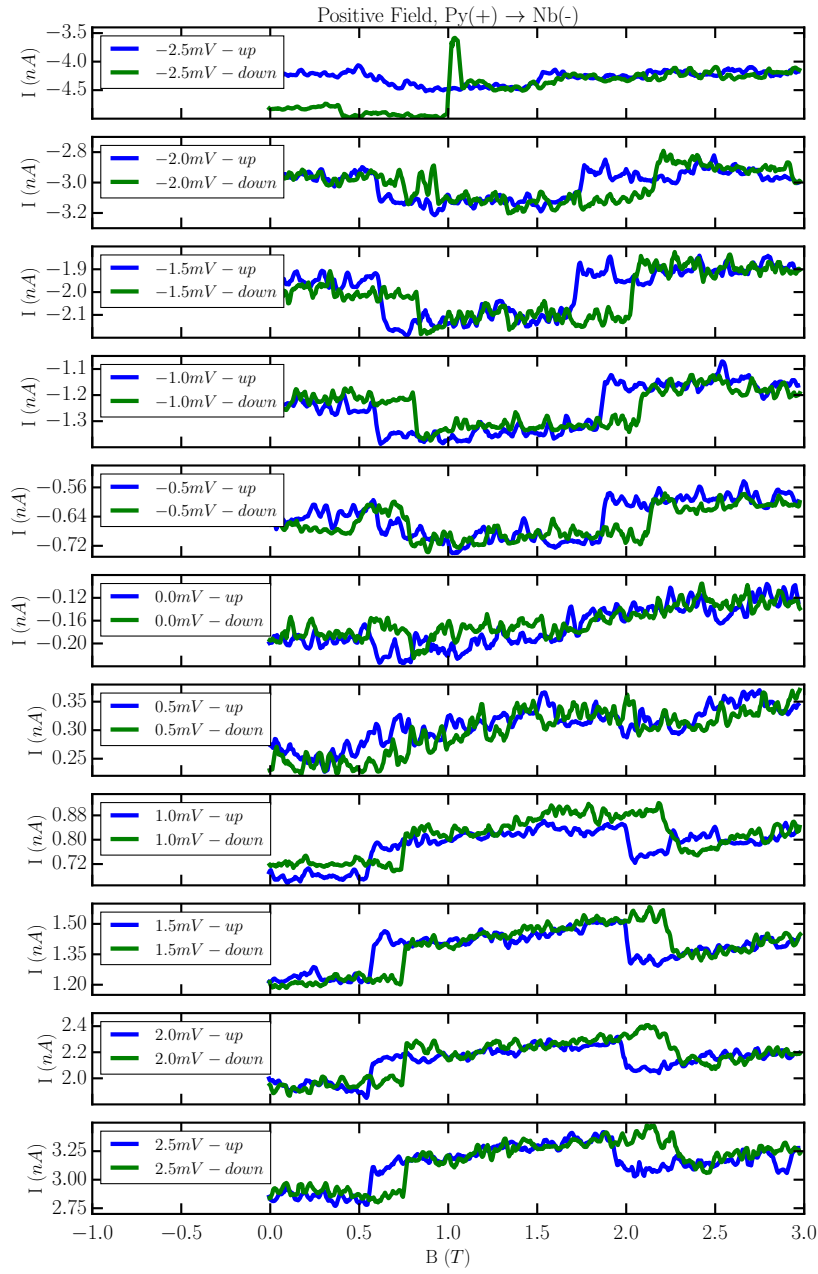


Figure 7.11: Current as a function of field measured at V_{bias} between -2.5 and 2.5mV. The same measurement was made from 0 to -3T with similar results. See Figure 7.17 for a summary of the switching behaviors at both field polarities.

CHAPTER 7. F-CNT-S

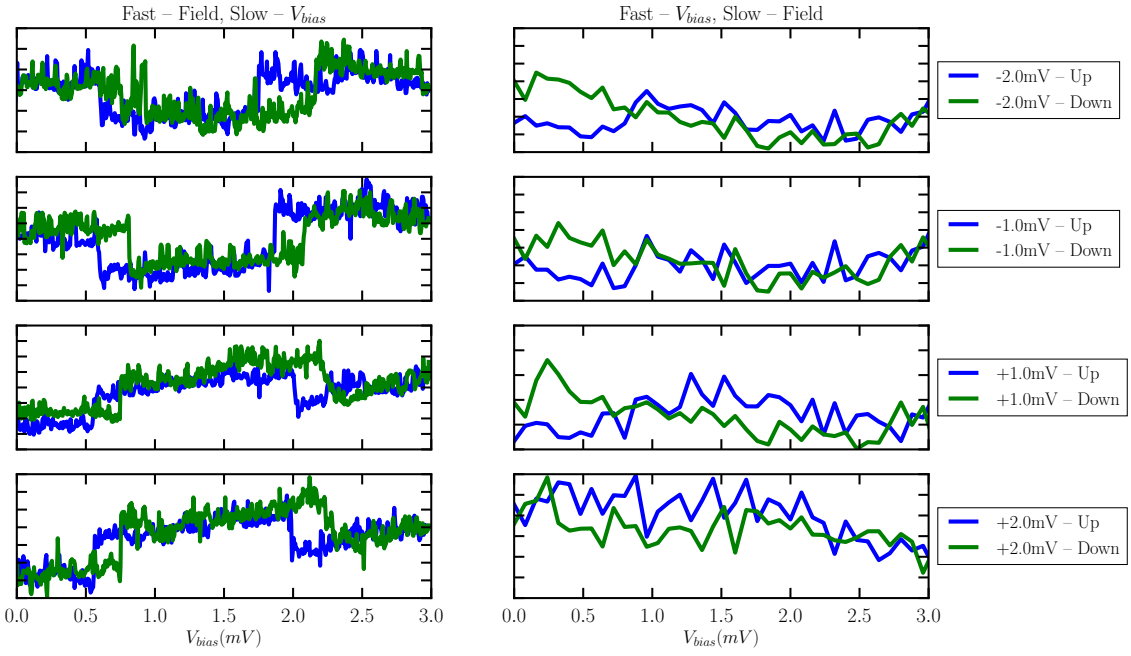


Figure 7.12: A comparison of the current versus field data with fast and slow sweep axes reversed.

Nb quantum dot on the same nanotube. A subset of those results are compared with the Py-CNT-Nb quantum dot in Figure 7.13.

Figure 7.13 shows clearly that the hysteresis is missing from the field sweep in the Nb-CNT-Nb quantum dot. The conductance change associated with the superconducting critical field is still seen at 2T in each measurement. The sweep at $V_{bias} = -1\text{mV}$ data shows the switching behavior at 0.5T remains in this quantum dot. The feature is not nearly as well-defined and the hysteresis is completely absent in this quantum dot. The full Nb-CNT-Nb dataset is plotted in Figure 7.14.

CHAPTER 7. F-CNT-S

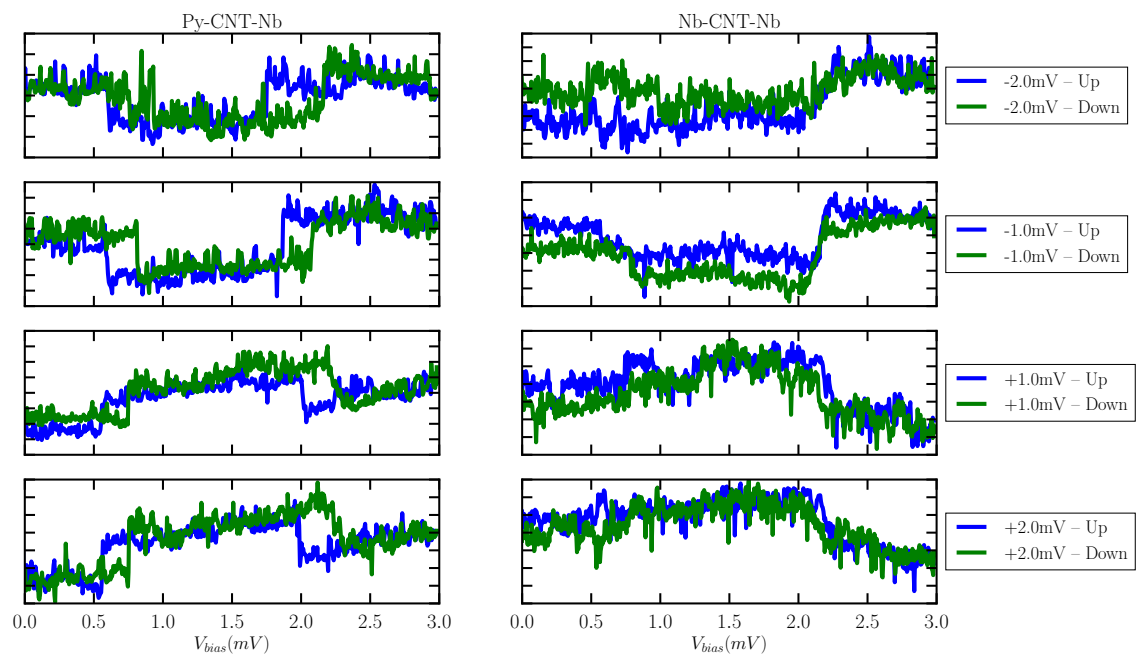


Figure 7.13: Left column shows current as a function of magnetic field for the Py-CNT-Nb quantum dot. Right column shows the same data for a Nb-CNT-Nb quantum dot on the same nanotube. Note the appearance of a conductance change at 0.5T in some of the Nb-CNT-Nb data with no hysteresis.

CHAPTER 7. F-CNT-S

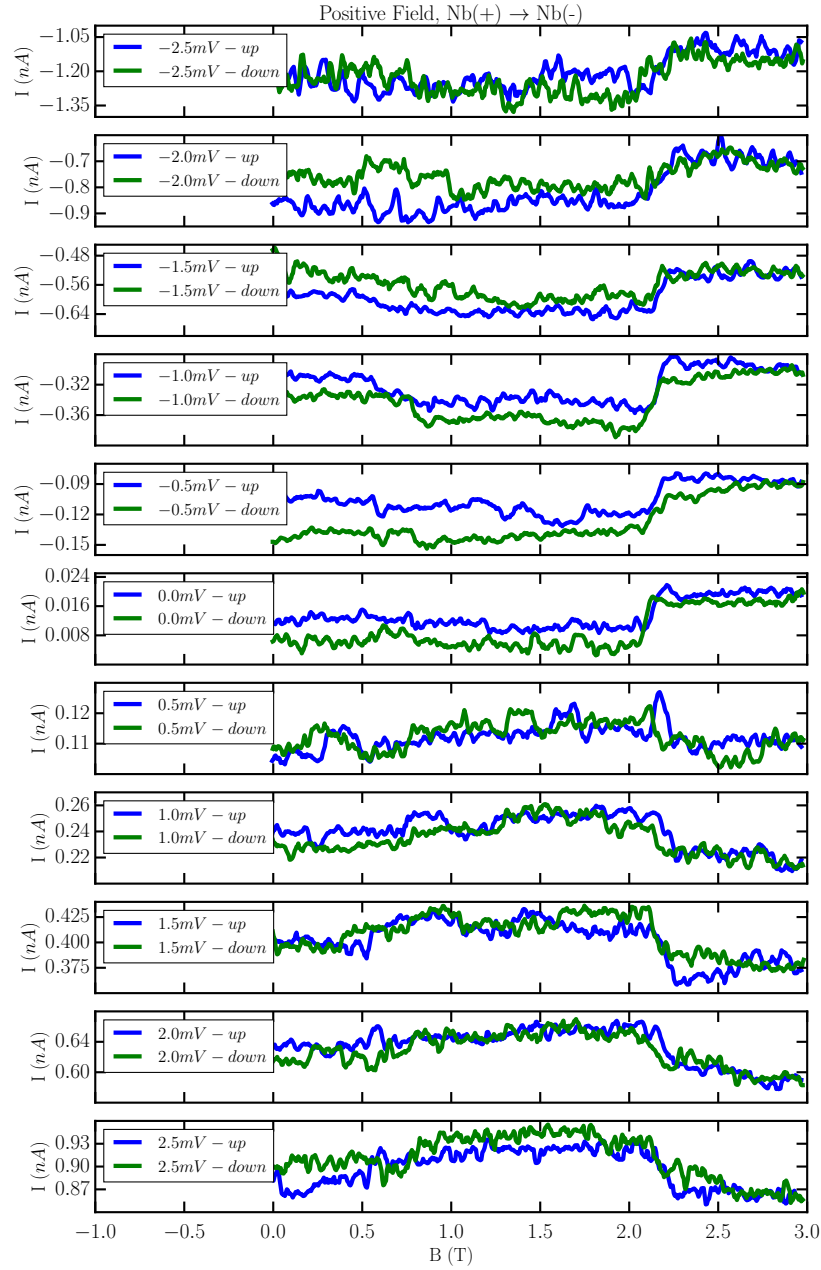


Figure 7.14: Current as a function of field measured at V_{bias} between -2.5 and 2.5mV for a Nb-CNT-Nb quantum dot.

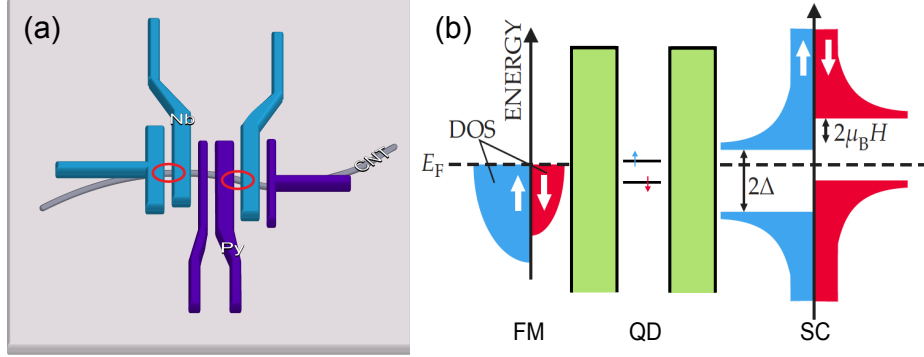


Figure 7.15: (a) A schematic of sample SCFMH8. Purple leads are Py, blue are Nb. The two quantum dots measured for Figure 7.11 and 7.14 are circled in red. (b) An energy level diagram representing the tunneling at $V_{bias} = 0$.

7.4.1 Discussion

A schematic of the full device with both measured quantum dots highlighted is shown in Figure 7.15(a).

It is difficult to determine the source of the hysteresis in these current versus field measurements. To begin, several possibilities can be ruled out. First, the effect cannot be due to the switching of the ferromagnetic lead magnetization. As mentioned above, the coercive field of Py is expected to be much smaller than 0.5T. Second, the field is swept repeatedly from 0 to 3T and back. There should be no switching of the magnetization unless the polarization of the field is changed.

We will rule out subgap transport phenomena, such as Kondo states [100–102], cotunneling [103], and Andreev reflection [104] due to the magnitude of the field and relatively high temperature. The change in conductance, at least at 0.5T, could be attributed to a level coming into resonance with the edge of the superconducting gap

CHAPTER 7. F-CNT-S

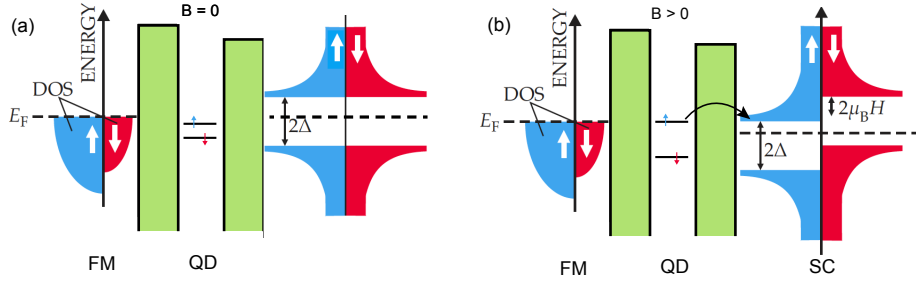


Figure 7.16: (a) An energy level diagram in zero field. (b) The same diagram with Zeeman splitting of the quantum dot levels and the superconducting density of states.

due to Zeeman splitting. A diagram of the process is seen in Figure 7.16.

There are a few reasons to rule out the situation in Figure 7.16. First, the conductance switching exists independent of the bias voltage. Second, there is no reason to expect the process depicted in Figure 7.16 to be hysteretic. Finally, it is unlikely for the Nb-CNT-Nb to have the same configuration of levels.

To investigate the bias dependence of the switching behavior, the field values at which the conductance switching occurs are plotted in Figure 7.17. Based on the data, it does not appear that the switching behavior depends on the bias. Both the switching positions and the width of the hysteresis appears to be constant as a function of V_{bias} . It is also interesting to note that the Nb-CNT-Nb switching fields correspond to those measured in the Py-CNT-Nb down sweep.

One final possibility is that the hysteresis is not due to any transport phenomena, but rather a thermodynamic effect due to the arrangement of leads on the substrate. Looking at the superconducting quantum dot that was used as a control, it is separated from the large ferromagnetic leads by nearly $1\mu\text{m}$. Conversely, the supercon-

CHAPTER 7. F-CNT-S

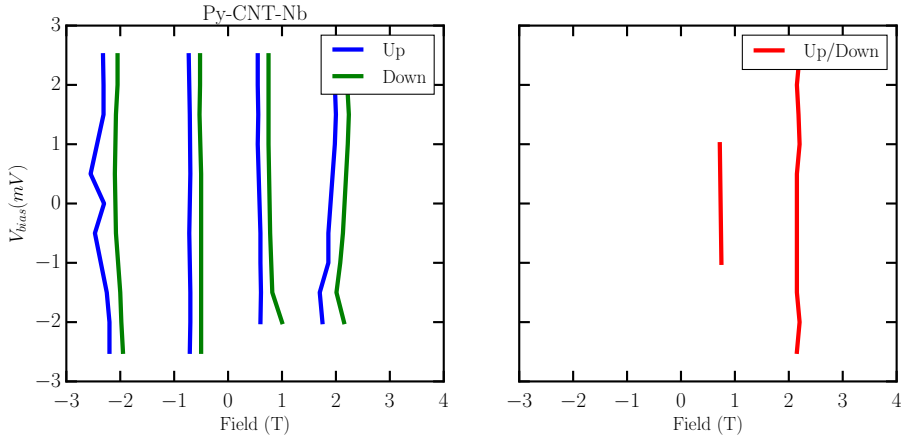


Figure 7.17: Position of the hysteretic switching events as a function of V_{bias} at positive and negative magnetic field values. Note, the field was not swept through 0. Positive field data was taken for all bias voltages, then negative field data. This is done to separate the feature at 0.5T from any effects related to the switching magnetization of the leads, as discussed in Section 6.1

ducting lead used in the F-CNT-S junctions is surrounded on both sides by larger ferromagnetic leads.

In light of this discussion, there is no clear physical picture for either the switching at 0.5T or the hysteresis observed at 0.5T and 2.0T. Future measurements looking at the behavior of this feature as a function of V_{gate} at lower temperatures should determine if the switching is a result Zeeman splitting of levels on the dot. If it is, the physical origin of the hysteresis may be very interesting. Additionally, different device geometries (ordering the ferromagnetic and superconducting leads differently) could eliminate the possibility of a thermodynamic switching in the superconducting lead, rather than a transport phenomena.

This chapter represents the first attempt at measuring spin-dependent transport

CHAPTER 7. F-CNT-S

properties through a F-CNT-S junction. The Zeeman splitting of conductance peaks and closing of the superconducting gap demonstrates that both superconductivity and spin non-degenerate quantum dot levels exist in the device. The measurement of hysteretic conductance splitting suggests the existence of new transport phenomena in this device that provides the basis for future work.

Chapter 8

Additional Carbon Nanotube Devices

8.1 NM-CNT-NM Quantum Dots

Palladium contacts to nanotubes, as discussed in Section 4.1.3, showed very low room temperature resistances of about $20\text{ k}\Omega$. It was thought that by using a metal that makes very good contacts, fabrication problems not dependent on contact material might be easier to pinpoint. A few of these samples were made and measured in our dunker at 4K.

The room temperature gate voltage behavior can be seen in Figure 8.1(a). This quantum dot was made on a small gap semiconducting nanotube. Many of the Pd contacted devices showed similar gate behavior; suggesting we grow a majority of small band gap semiconducting nanotubes, most likely due to the diameter of the catalyst particles used in nanotube growth.

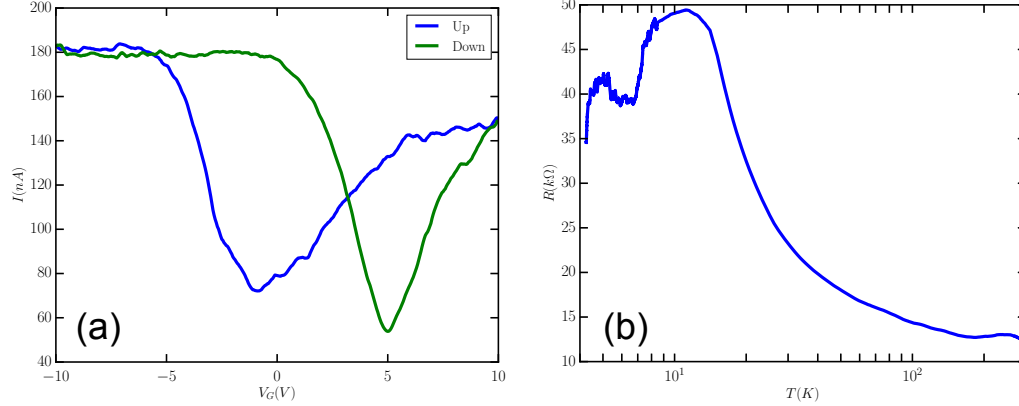


Figure 8.1: (a) Room temperature gate sweep of a palladium contacted quantum dot at positive bias voltage. (b) Resistances versus temperature curve for the same device. Coulomb blockade effects begin to dominate the transport below 10 K.

At low temperatures these devices showed weak Coulomb blockade behavior. Low temperature measurements of the device measured in Figure 8.1 are seen in Figure 8.2. The charging and excitation energies are consistent with other devices measured in this work. Figure 8.2(b) shows conductance peaks in the gate sweep have irregular spacing and no clear four fold symmetry. This suggests the quantum dot has impurities along its length causing more than one quantum dot to act in series along the nanotube [89]. Again, this is consistent with other devices measured and suggests defects in the nanotube growth or contamination on the substrate near the nanotube.

8.2 Locally Gated Quantum Dots

Due to the nature of the Schottky barriers between metals and carbon nanotubes, it can be difficult to tune the levels on a nanotube quantum dot without affecting

CHAPTER 8. ADDITIONAL DEVICES

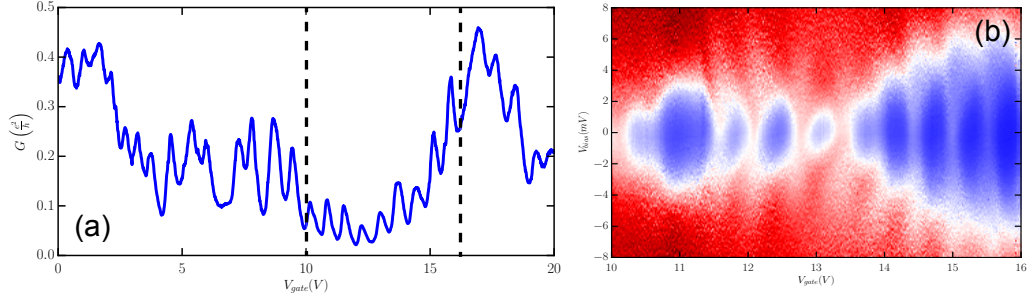


Figure 8.2: (a) Conductance as a function of V_{gate} in a Pd contacted nanotube quantum dot at 4K. (b) Conductance as a function of V_{bias} and V_{gate} taken in the region marked by dashed lines in (a).

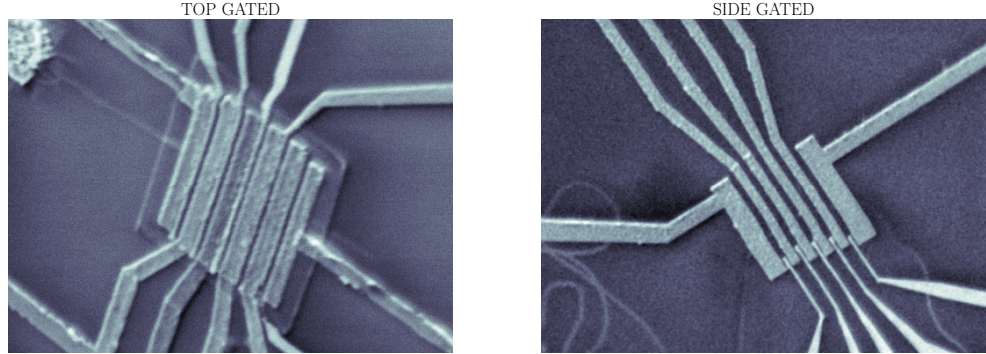


Figure 8.3: Two local gating techniques. Left: A top gated devices with a low temperature ALD grown Al_2O_3 layer separating the top gate from the underlaying nanotube. Right: a side gated devices with narrow Cr/Au leads positioned between the Co leads 200 nm from the nanotube.

the barrier height and charging energy of the dot [105, 106]. One solution to better control of the quantum dot is to add narrow local gates to the devices. This is most easily done by adding side gates or top gates. Figure 8.3 shows an example of each of these device geometries.

Contacting nanotubes with ferromagnetic and superconducting metals proved so difficult, adding an additional fabrication set to position local gates was deemed too

CHAPTER 8. ADDITIONAL DEVICES

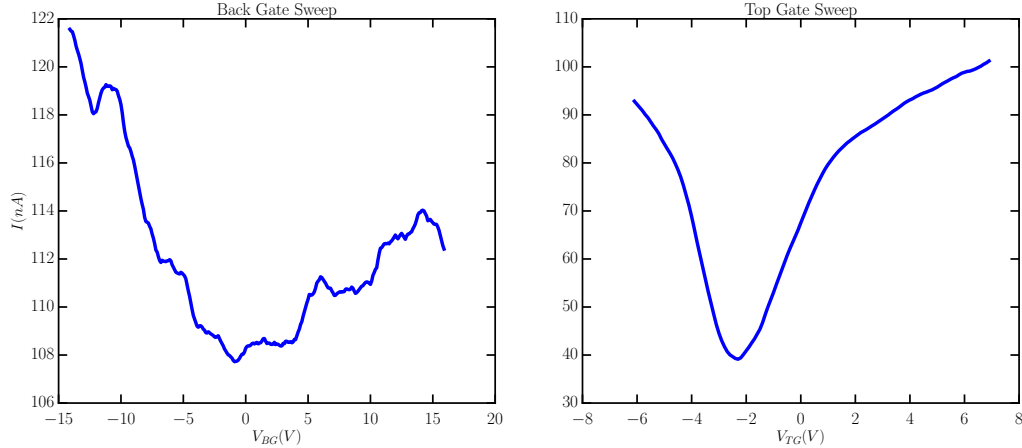


Figure 8.4: Left: Current as a function of V_{BG} . Right: Current as a function of V_{TG} . Even in this simple example it is clear that the local gates are much more effective at tuning the Fermi level on the carbon nanotube.

much of a risk in most cases. A few devices were measured toward the end of this thesis work. Typical room temperature and 4K data are seen in Figures 8.4 and 8.5.

Figure 8.5(top) shows how the resonant tunneling peaks behave as a function of both gates. The dashed white line across the plot is perpendicular to the path followed by the conductance peaks. By tuning the gates along this line, the tunnel barriers in the source and drain contacts can be held constant while the energy levels on the dot are varied relative to the Fermi level on the leads. A plot of the measured current along this detuning axis can be seen in the bottom of Figure 8.5.

CHAPTER 8. ADDITIONAL DEVICES

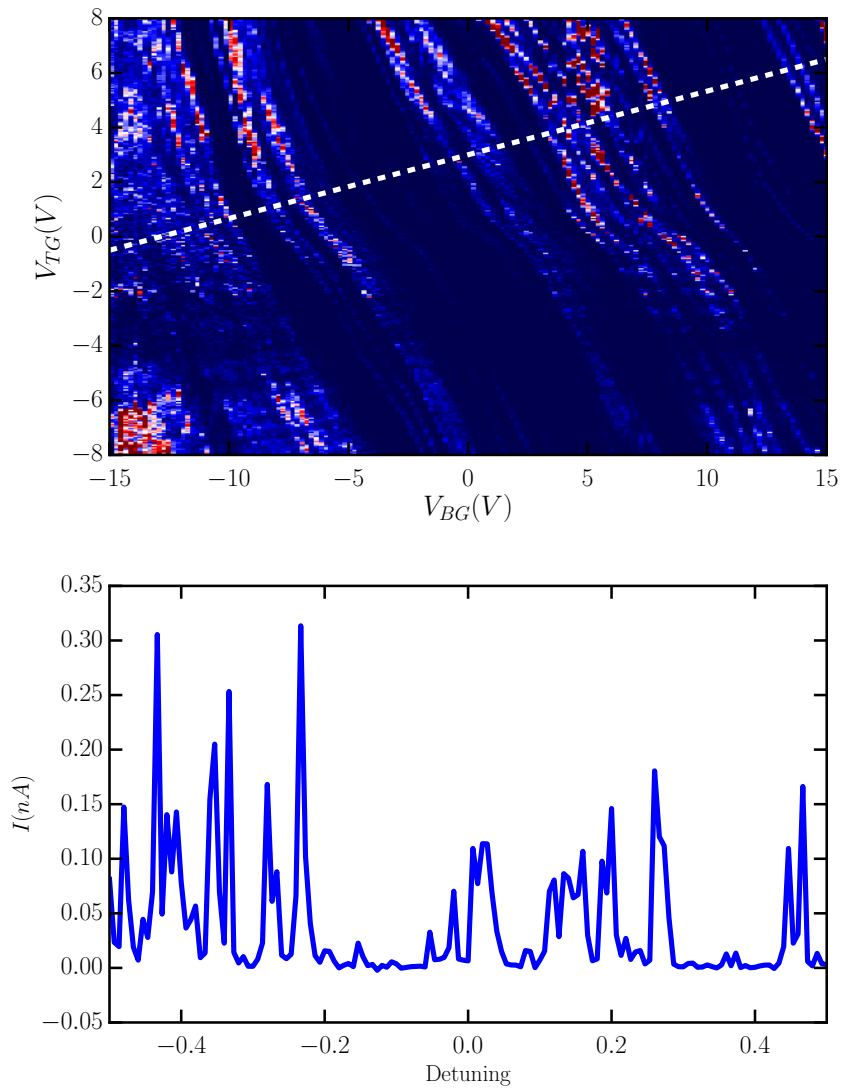


Figure 8.5: Top: Current as a function of V_{TG} and V_{BG} . Bottom: A cut across the plot demonstrating how both gates can be used together to keep the tunnel barrier height fixed while varying the Fermi level on the quantum dot.

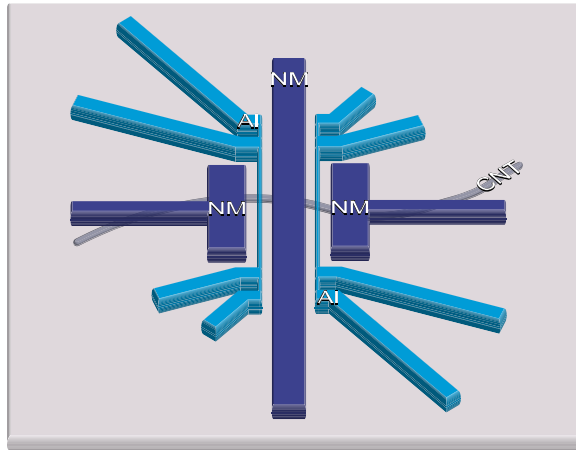


Figure 8.6: Schematic of a CNT tunnel probe under two narrow aluminum wires.

8.3 CNT Tunnel Probe into Aluminum Nanowires

Carbon nanotubes, because of their small diameter and high contact resistances with metals, make good candidates for tunnel probes into other mesoscopic systems. In this project, nanotubes were used in an attempt to probe the density of states of a quasi 1D aluminum wire. A schematic of the device being discussed can be seen in Figure 8.6

8.3.1 Background

Aluminum is a superconductor with a bulk transition temperature of 1.2K. When placed in a perpendicular magnetic field, thin films of aluminum allow magnetic

CHAPTER 8. ADDITIONAL DEVICES

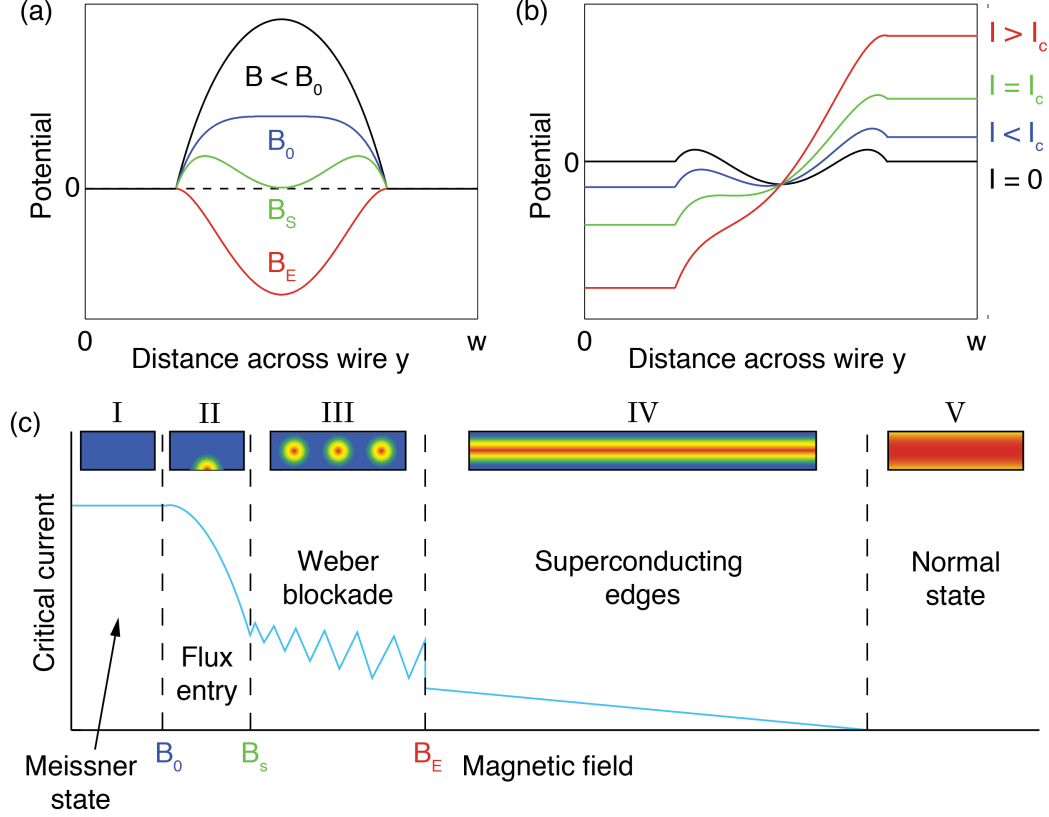


Figure 8.7: Figure taken from Ref [6]. (a) Potential seen by vortices along width of the aluminum nanowire as a function of applied perpendicular magnetic field. (b) Potential seen by vortices along width of the aluminum nanowire as a function of applied current. (c) Critical current as a function of applied perpendicular magnetic field. The Weber blockade region can be seen clearly in Region III.

vortices to pass through in the superconducting state. These vortices have a diameter on the order of the superconducting coherence length [96]. When the width of the aluminum film is made to be on the order of the coherence length, these vortices are forced to pass through the superconductor in a single line. This geometric confinement makes it possible to tune the number of vortices trapped in the nanowire by varying the applied magnetic field. This effect is called the Weber blockade [107].

Figure 8.7 is taken from our lab's publication on Weber blockade in aluminum

CHAPTER 8. ADDITIONAL DEVICES

nanowires [6]. In Figure 8.7(a) the potential seen by a vortex is plotted as a function of the distance across the wire. A similar plot is shown in Figure 8.7(b) Showing the potential across the wire as a function of the applied current. By tuning these parameters into Region III, as labelled in Figure 8.7(c), vortices will hop from the vacuum onto the nanowire one at a time. The varying number of vortices can be identified by changes in the critical current of the nanowire, as seen in Region III of Figure 8.7(c). This is analogous to the Coulomb blockade in quantum dots. In fact, if the critical current is plotted as a function of applied field, we find the data looks just like a Coulomb blockade plot, with the blockaded regions being replaced by regions of superconductivity containing a fixed number of vortices. This measurement can be seen in Figure 8.8.

Because the vortices repel one another, their spacing is dependent on the number of vortices contained along the length of the nanowire. If a nanotube is placed at a fixed position under the aluminum wire, the tunnel current will depend on whether or not a vortex is positioned above the nanotube. Thus, by measuring the differential conductance through the nanotube tunnel probe, the position of vortices in the wire can be mapped as a function of applied magnetic field.

8.3.2 Device and Measurement

Several of these tunnel probe devices were created by placing aluminum nanowires across palladium carbon nanotube quantum dots. The fact that these were quantum

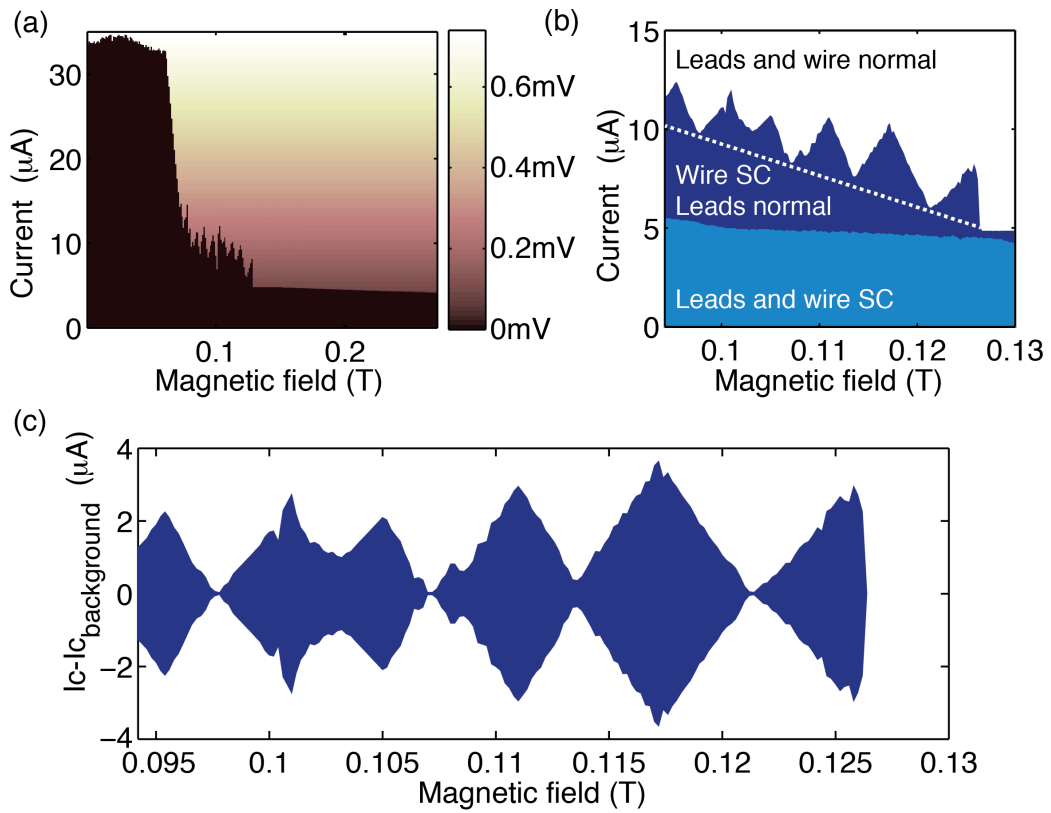


Figure 8.8: Figure taken from Ref [6]. (a) IV curves as a function of applied magnetic field. The Weber blockade region can be clearly seen around 100mT. (b) Close up of the Weber blockade region. (c) Weber blockade effect with superconducting regions containing a fixed number of vortices seen in blue.

CHAPTER 8. ADDITIONAL DEVICES

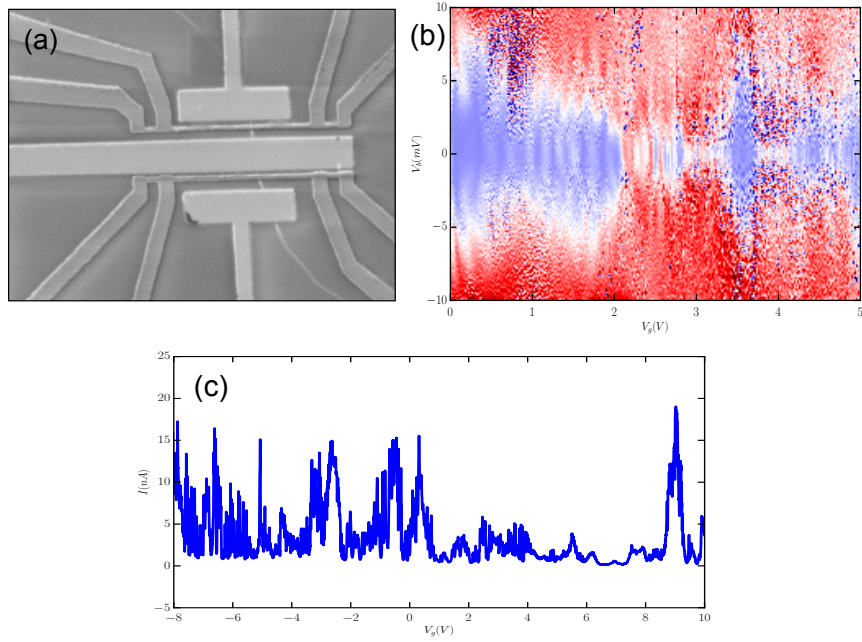


Figure 8.9: (a) SEM image of a typical aluminum wire tunnel probe device. The Pd leads connected to the nanotube form a quantum dot under the device. (b) Conductance through the nanotube quantum dot with aluminum nanowire on top. (c) Conductance as a function of back gate voltage through the same devices.

dots is not really important, but does provide a means of judging the quality of the nanotube portion of the devices. Typical measurements of Pd contacted nanotube quantum dots under aluminum nanowires are seen in Figure 8.9.

No useful measurements of the tunnel probe were made, mainly because of poor contact to the nanotube. The first few devices suffered from the Al-CNT resistances being larger than the input resistance of my current-to-voltage amplifier. This was improved in subsequent devices by adding thin titanium layers beneath the aluminum nanowire. However, later devices showed poor contact resistances between normal leads and nanotubes. With a little more time, I see no reason this project would not

yield the predicted results.

8.4 Majorana Ferimons in CNTs

For a time, around 2010, finding Majorana fermions in condensed matter systems was a source of much excitement. Naturally, this lead to attempts to create a Majorana mode in a carbon nanotube device. Below is a brief description of the project and a summary of the results.

8.4.1 Background

Majorana fermions, first predicted by Ettore Majorana in 1937 [108], can be thought of as charge-neutral particles that have the unique property of being their own anti-particle. Majorana first proposed these states as an explanation for neutrinos. Recently, much excitement has been generated by a number of papers proposing similar states may be created in solid state systems [109, 110]. This project focuses on measuring these states as they are predicted to exist in semiconductor-superconductor heterostructures.

Some basic insight can be gained from examining a toy model proposed by Kitaev [111]. By writing the Hamiltonian for a one-dimensional wire with N sites, a single spin component, and a superconducting gap, the model allows for the existence of Majorana modes within certain parts of the parameter space.

CHAPTER 8. ADDITIONAL DEVICES

$$H = \sum_{j=1}^N \left(-w \left(a_j^\dagger a_{j+1} + a_{j+1}^\dagger a_j \right) - \mu \left(a_j^\dagger a_j - \frac{1}{2} \right) + \Delta \left| e^{i\theta} a_j a_{j+1} + |\Delta| e^{-i\theta} a_{j+1}^\dagger a_j^\dagger \right| \right) \quad (8.1)$$

The Hamiltonian can be rewritten by splitting each fermion site into two half-fermion Majorana sites with the operators $c_{2j-1} = e^{i\frac{\theta}{2}} a_j + e^{-i\frac{\theta}{2}} a_j^\dagger$ and $c_{2j} = -i \left(e^{i\frac{\theta}{2}} a_j - ie^{-i\frac{\theta}{2}} a_j^\dagger \right)$. Considering the new Hamiltonian in two simple limits reveals two ground states. In the trivial case, $|\Delta| = w = 0$, $\mu < 0$, one finds a ground state with no unpaired Majorana modes.

$$H = -\mu \sum_{j=1}^N \left(a_j^\dagger a_j - \frac{1}{2} \right) = \frac{i}{2} \mu \sum_{j=1}^N c_{2j-1} c_{2j} \quad (8.2)$$

In the case of non-zero hopping and a non-zero superconducting gap, $|\Delta| = w > 0$, $\mu = 0$, one finds a ground state with coupling between Majorana operators on different sites. This leaves two unpaired Majorana modes at the ends of the wire (sites 1 and N).

$$H = 2w \sum_{j=1}^{N-1} \left(\tilde{a}_j^\dagger \tilde{a}_j - \frac{1}{2} \right) = iw \sum_{j=1}^N c_{2j} c_{2j+1} \quad (8.3)$$

The Majorana modes can also be shown to exist for ranges of μ , Δ , and w outside of the trivial cases discussed above.

8.4.2 Device and Measurement

The Kitaev model has three requirements. The model is specific to a one dimensional conductor, the conductor must have a superconducting gap, and the wire must support helical conduction modes (in which opposite spins are conducted in opposite directions). It may be possible to satisfy all of these conditions in a carbon nanotube device.

Kitaev's first condition is satisfied by the choice of carbon nanotubes as the conducting medium. Realizing the second condition in a nanotube device simply requires contacting the nanotube with a superconducting material, such as aluminum, which is most compatible with our fabrication techniques. Cooper pairing then becomes possible within the nanotube through proximity induced superconductivity [47, 48]. A summary of these conditions is seen in Figure 8.10.

It has recently been shown that carbon nanotubes may support helical conduction bands [112, 113]. When lattice curvature effects are calculated and some combination of external electric and magnetic fields applied the level splitting the carbon nanotube can be fixed such that helical bands exist for certain values of the chemical potential. Additionally, many measurements have been made confirming the spin-orbit coupling in carbon nanotubes [93, 114–116].

To detect the Majorana states, it should be possible to perform a simple tunneling experiment. The Majorana state is created and destroyed as a function of the applied fields (change level splitting) and gate (back) voltage applied to the semiconducting

CHAPTER 8. ADDITIONAL DEVICES

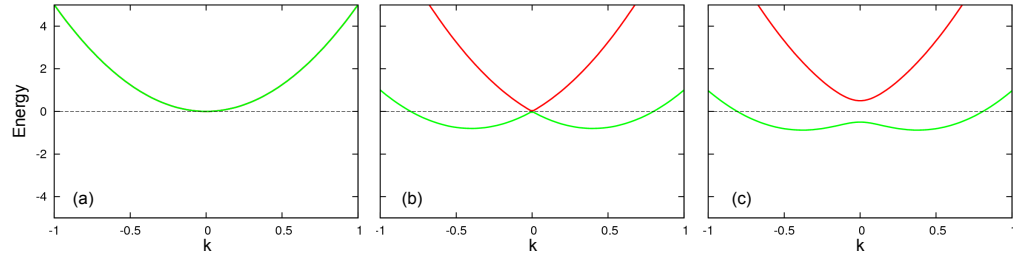


Figure 8.10: (a) Approximate band structure of a semiconductor. (b) Band splitting along the k -axis due to spin-orbit coupling. (c) Additional Zeeman splitting along the E -axis leads to individual, helical conduction bands.

wire (changes chemical potential). By adding an additional tunneling contact on top of the aluminum/CNT contact, the current through the tunneling contact and Al lead can be measured to determine the available conduction bands at the Al/CNT junction. With the creation of a Majorana state, a peak should be measured in the tunneling current at zero energy. Similar devices have been measured on InSb nanowires [117].

A typical device is seen in Figure 8.11. Several of these devices were measured at 250mK in an Oxford He3 cryostat. The devices did show superconducting quantum dot behavior, but none of the tunnel probes behaved as desired. The probes were either shorted to the leads or showed a resistance larger than the current amplifier input. An example of the data taken on one of these devices is seen in Figure 8.11

These devices were measured very early on in my thesis work. The low resolution data, and very long data acquisition times, are what motivated a lot of future work to improve the measurement technique. Unfortunately, no more data were taken for this project. Fabrication and measurement noise levels in our experiments never improved

CHAPTER 8. ADDITIONAL DEVICES

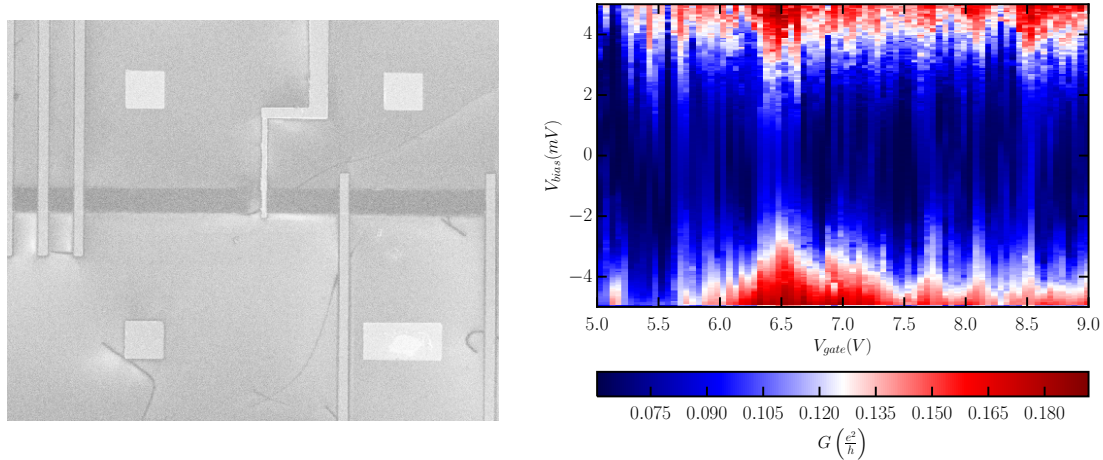


Figure 8.11: Left: A typical tunnel probe device with aluminum leads and a Cr/Au tunnel probe. Right: Data taken from a similar device with Niobium leads at 250mK.

to the levels required to make such a precise measurement. Future work on this topic is suggested in Chapter 9.

Chapter 9

Conclusion

Carbon nanotube devices have been widely discussed over the past two decades. Each year brings new publications discussing a wide variety of transport phenomena, applications, and fabrication techniques. This thesis adds to that pool by presenting a set of transport measurements on spin dependent tunneling process in F-CNT-F and F-CNT-S devices. Additionally, a large effort has been made to tabulate the success rates for various fabrication techniques tested. Despite the large volume of nanotube fabrication research currently available, there has been very little discussion of reproducibility and device yield.

CHAPTER 9. CONCLUSION

9.1 Fabrication of Nanotube Devices

Chapter 3 and Appendix A detail the methods used, and attempted, to produce carbon nanotube devices in our lab. An effort has been made to detail each fabrication method, as well as comment on those that were found to not be reproducible. Improvements to the fabrication, particularly in the area of nanotube imaging are presented. The imaging methods developed are intended to decrease the processing time required for each device and, as a result, decrease the risk of environmental contamination during imaging.

Chapter 4 extends the work in Chapter 3 and presents a detailed discussion of the device yield and contact resistances of devices produced as a function of materials and methods used. It is my hope that this analysis will help future researchers in producing devices with more consistent results and less wasted fabrication effort.

A few guidelines for device fabrication can be derived from the information in those two chapters (combined with information from the transport measurements in later chapters):

Drop cast nanotube samples have a few advantages over substrate growth methods. First, they are not prone to the types of gate leak problems that were frequently seen in substrate grown samples due to the high temperature growth process. Second, although it is more difficult to find a nanotube of sufficient length to make a device with drop casting, the devices made may show fewer growth defects. The sonication required to suspend nanotubes appears to preferentially break tubes at defects result-

CHAPTER 9. CONCLUSION

ing in a shorter average length, but with fewer defects in the long tubes that survive the process. Placing substrate grown tubes is a much more reliable process, with almost 100% of growth chips having nanotubes suitable for device fabrication. The process also does not require the handling of bulk carbon nanotube material which is difficult as well as hazardous. When combined with image processing techniques in Chapter 3, the device fabrication process is significantly faster. Because of the disorder measured in F-CNT-F devices, device lengths are best kept to less than 200nm if a single, defect-free quantum dot is desired in a substrate grown nanotube. It is difficult to compare the device yield due to a low number of drop cast samples having been made for this work.

Once nanotubes have located on the substrate, fabricating clean, low resistance contacts becomes the major challenge. My work has found that PMMA combined with low temperature IPA:H₂O development and over exposure of nanotube contact patterns produces the cleanest resist masks for contact deposition. Low-energy magnetron sputtering has proved to be the most reliable method for producing low-resistance nanotube contacts with normal metal, ferromagnetic, and superconducting materials. Control over the sample temperature may have a large effect on these results. Magnetron sputtering prevents samples from being exposed to free electron bombardment and keeps samples cool during deposition by avoiding high temperature melting of source materials. Future work may investigate this observation by testing thermal and electron beam evaporation with a temperature controlled sample stage

CHAPTER 9. CONCLUSION

to determine the optimum temperature range for deposition of nanotube contacts.

9.2 Ferromagnetic and Superconducting Device Measurements

Measurements on F-CNT-F devices show that it is possible to reproduce previously published results on gate-tunable tunnel magnetoresistance [83, 99]. In the same devices, evidence is present to show that the spin states can be probed through transport spectroscopy and manipulated by application of an external magnetic field. Finally, an argument has been made for F-CNT-F devices as probes into the spin dependent structure of magnetic impurities. Future work should focus on the evolution of the spin states in these quantum dots in the presence of a magnetic field. By measuring the evolution of the ground state transitions between different quantum dot occupation numbers the nature of the change in spin state discussed in Section 6.3 could be further probed.

A brief analysis of two F-CNT-S devices is presented in Chapter 7. These devices show evidence for proximity effect superconductivity in the nanotube, despite the presence of the ferromagnetic contact. Additionally, a discussion of magnetic field dependent conductance features is presented. This effect lacks a clear physical origin and should be further investigated by measurements with gate-tunable F-CNT-S junctions.

9.3 Future Work on Other Devices

Chapter 8 presents work done on additional carbon nanotube devices. The most promising avenue for future research is in the use of carbon nanotubes as tunnel probes into low-dimensional superconducting materials. This project was not completed due to time and equipment constraints, but shows great promise and sound theoretical footing.

The Majorana device discussed in Section 8.4 is very interesting from a theoretical standpoint. From the view of an experimentalist it is very difficult. The device was not pursued further in this work due to difficulties in fabricating the junctions as well as the noise limits of our experimental setup. Properly measuring the zero bias conductance peak predicted in the theory will require very low electron temperatures and accurate conductance measurements to make the results believable. A more realistic proposal might involve two tunable nanotube devices in a SQUID geometry in which the Majorana mode can be probed by measuring changes to the period in the critical current oscillations [118].

Appendix A

Fabrication Details

This appendix describes, in detail, each of the steps taken to create the carbon nanotube devices measured for this thesis. Some of the information is specific to the Markovic lab and Johns Hopkins University, but an effort has been made to make the discussion useful to anyone producing nanotube devices.

The devices measured in this thesis were all produced with the following recipe:

1. Use the mask aligner (A.1.2.2) to pattern large sputtered molybdenum (A.4.3)
leads or alignment markers on a silicon substrate
2. Pattern small catalyst islands (3.2) using electron beam lithography (A.3)
3. Grow nanotubes directly on substrate using chemical vapor deposition (3.2.2)
4. Locate nanotubes using a scanning electron microscope (3.3.4)
5. Design devices using vector graphics software (A.2)

APPENDIX A. FABRICATION DETAILS

6. Pattern devices using electron beam lithography (A.3) and thin film deposition (A.4)
7. Test device connectivity in the DC probe station (A.5.1)
8. Wire bond connected devices in a chip carrier for further testing (A.5.2)

For details on each of the steps see the sections referenced. The rest of this appendix discusses additional methods and contains some useful observations made over several years spent producing nanotube devices.

A.1 Wafer Preparation

Each nanotube device began with a highly doped silicon substrate capped with an insulating layer. The wafers used were chosen for their low temperature electrical properties and ease of use.

A.1.1 Selection and Cleaning

All of the devices discussed in this thesis were built on highly n-doped silicon wafers with SiO_2 capping layers. The wafers were purchased from Silicon Quest International. As ordered the wafers are 3 inches in diameter with a $<100>$ silicon face. This crystal alignment allowed the wafers to be easily cleaved along the crystal axes using only a diamond scribe. The wafers are heavily n-doped with phosphorus

APPENDIX A. FABRICATION DETAILS

giving them a resistivity of $10\text{-}20\,\Omega\text{ cm}$ down to the milliKelvin range. The oxide layers were 300 \AA of thermally grown SiO_2 and remained insulating at all measured temperatures.

Typically, wafers were cleaned by sonicating in acetone for 5 minutes, followed by an isopropanol rinse for 1 minute, and baking on a hot plate at 180°C for 1 minute. This procedure was usually enough to ready the surface for lithography. In cases where cleanliness had to be improved, piranha etch was used to clean the wafers.

Piranha etch is a mixture of 3:1 30% sulfuric acid to 30% hydrogen peroxide. It is important to be extremely careful with this wet etch as the solution is strongly exothermic. The wafers should be placed in the sulfuric acid, then the hydrogen peroxide is added slowly while stirring continuously. The solution will reach nearly 200°C within the first few minutes. After about 20 minutes, the solution should cool enough for the wafers to be removed. Surfaces cleaned in this way are free of organic and most metallic contaminants.

A.1.2 Optical Lithography

The first step in building the devices discussed in this thesis was to pattern the substrate using optical lithography. In this process the wafer is first coated in a UV sensitive polymer resist. The wafer is then partially exposed to UV light and developed, leaving a patterned polymer mask through which thin films can be deposited.

The resists used can be either positive or negative tone. For this work, MicroChem

APPENDIX A. FABRICATION DETAILS

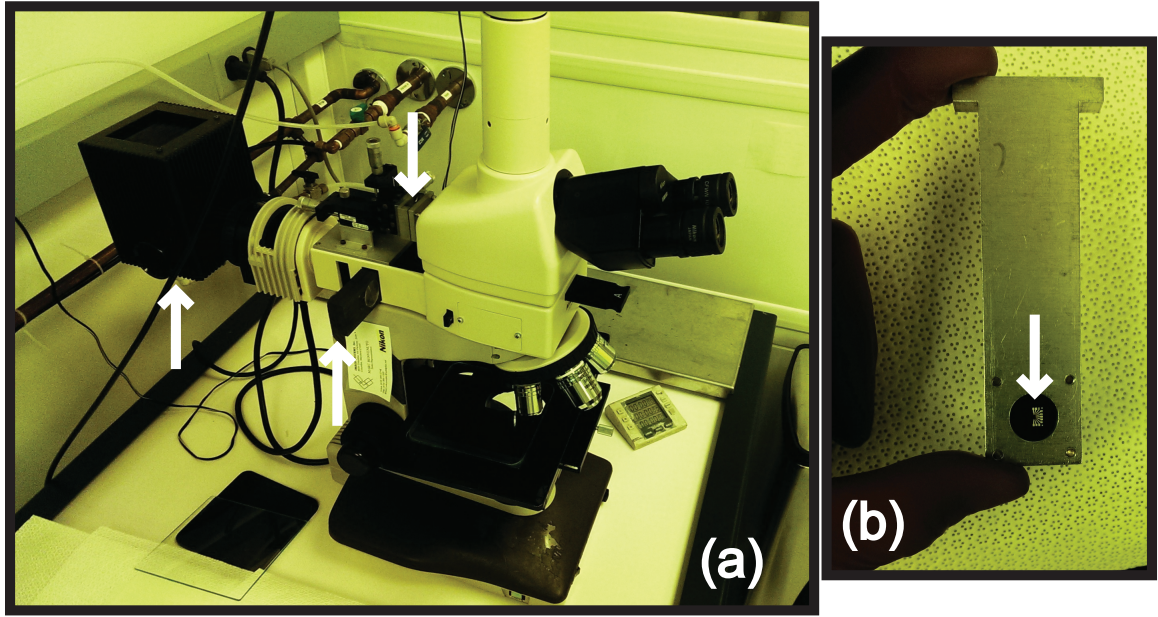


Figure A.1: Custom projection lithography setup in the JHU physics department cleanroom. (a) The arrows from left to right show the UV lamp, sliding UV filter, and mask holder. (b) A projection lithography mask and holder. The arrow shows the mask itself.

S1813 was used as a positive tone resist and Futurex NR9 was the negative tone resist. Exposure, baking, and development times were chosen according to the manufacturer's instructions.

A.1.2.1 Projection Lithography

Many of the devices produced in the Markovic lab have been patterned using the custom built projection lithography setup seen in Figure A.1. The setup was built around a Nikon optical microscope. The microscope has been fitted with a UV lamp, movable UV filtering, and a custom mask holder.

The masks were made using either a standard ink-jet printer or by a local printing

APPENDIX A. FABRICATION DETAILS

company for higher resolution. The sample is placed under the desired objective, which determines the size of the pattern projected onto the sample. The mask is then inserted into the holder and then focused and positioned using the micrometer drives. Exposure times are controlled by removing the UV filter from the light path.

This setup is useful for quickly producing a few samples at a time. Specifically, it is used for producing graphene and nanowire devices, which require careful positioning of the pattern over the nanostructure of interest. The resolution limit of this technique is about $2\text{ }\mu\text{m}$.

A.1.2.2 Mask Aligner

For production of many, identical devices, projection lithography as described in Section A.1.2.1 becomes extremely tedious. This problem was solved by use of a mask aligner.

First, a chromium on glass mask is made with the desired pattern in the actual size, as seen in Figure A.2. The mask is then loaded into the aligner and a substrate, coated with polymer resist, is mounted under it. Finally, the mask and substrate are pressed together and exposed to a UV light source. The resolution of the OAI mask aligner is about $1\text{ }\mu\text{m}$.

APPENDIX A. FABRICATION DETAILS

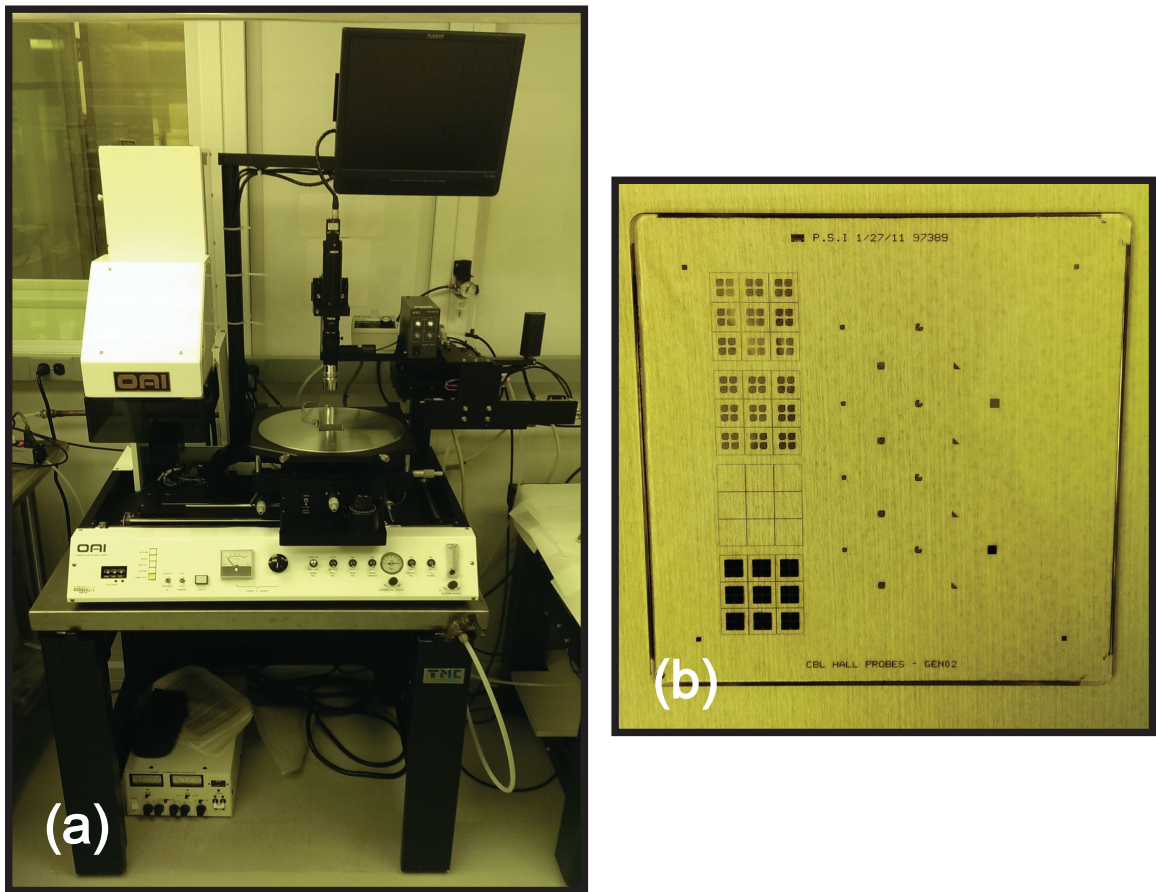


Figure A.2: OAI mask aligner in the JHU physics department cleanroom. (a) The mask aligner. (b) A typical 3" chromium on glass mask.

APPENDIX A. FABRICATION DETAILS

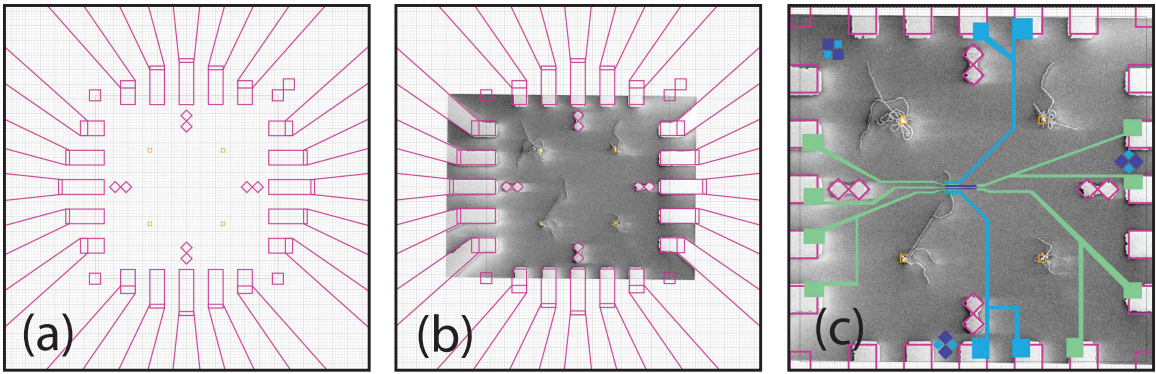


Figure A.3: Adobe Illustrator designs used for optical and electron beam lithography masks. (a) The pink outlines show the large molybdenum leads patterned with the mask aligner. Inside that pattern are the four $3\text{ }\mu\text{m}$ catalyst islands patterned with electron beam lithography. (b) An SEM micrograph of a sample after CVD growth fitted into the pattern. (c) A complete circuit design. In this case, the layers are normal metal (green), ferromagnet (purple), and superconductor (blue).

A.2 Device Design

Once the substrates are prepared, devices are designed one at a time using Adobe Illustrator. Any computer aided drafting (CAD) or vector graphics program would work just as well. The procedure is outlined in Figure A.3. Designing the devices is a simple process of aligning the image with the markers/leads patterned in the first lithography step, then designing the desired pattern of nanotube contacts and bonding pads. Some thought must be given to the size of the leads drawn. If the leads are too large, the write time for the electron beam lithography steps will be too long. Long write times are at risk for poor alignment due to stage drift in the SEM. It was found that keeping write times under 20 minutes yielded the best results. Additionally, one must be careful not to let any stray nanotubes short the device leads.

APPENDIX A. FABRICATION DETAILS



Figure A.4: Zeiss EVO50 SEM with Raith control computer and external beam blanker.

A.3 Electron Beam Lithography

Electron beam lithography is the process of creating masks by patterning a polymer resist by exposure to a focused beam of electrons. In the Johns Hopkins physics department the electron beam lithography setup is based around a Zeiss EVO50 scanning electron microscope. The microscope is controlled by Zeiss SmartSEM software. Attached to the microscope control computer by a serial port is a second computer running Elphy Quantum, electron beam lithography software from Raith. The Raith software can take control of the beam to write patterns based on GDSII drawings. The SEM setup is shown in Figure A.4.

The electron beam sensitive resist used in all of this work was polymethyl

APPENDIX A. FABRICATION DETAILS

Table A.1: Standard PMMA/MIBK recipe

EHT Voltage	30 keV
Beam Current	40 pA
Step Size	10 nm
Dose	300 $\mu\text{C cm}^{-2}$
Developer	1:3 MIBK:IPA
Development time	60s
Post-development	rinse 30s in IPA

methacrylate (PMMA) from MicroChem. PMMA is a polymer that, after baking on a hot plate, forms copolymer bonds that can be broken by exposure to a beam of electrons. Once these bonds are broken, the unbonded polymer can be washed away by a developer, leaving trenches in the PMMA wherever it was exposed to the electron beam. The patterned mask can later be removed by soaking in acetone.

A.3.1 Standard Recipe

This recipe, using room temperature methyl isobutyl ketone (MIBK) as a PMMA developer, is the simplest recipe to start with for almost any project requiring electron beam lithography. The relevant parameters are shown in Table A.1.

APPENDIX A. FABRICATION DETAILS

Table A.2: Cold developer recipe

EHT Voltage	30 keV
Beam Current	40 pA
Step Size	10 nm
Dose	1400 $\mu\text{C cm}^{-2}$
Developer	7:3 IPA:water at 0 °C
Development time	90s
Post-development	rinse 30s in water

A.3.2 Cold Development

It was discovered in 2004, that by lowering the development temperature and increasing the dose, the resolution of PMMA could be improved significantly [119]. This has been shown using MIBK:IPA as a developer as well as various mixtures of IPA and water [120–123]. The best results obtained in our lab were using IPA and water. The recipe is shown in Table A.2. The improved contrast can be attributed to the higher dose. By increasing the dose and decreasing the efficacy of the developer, the negative effects of backscattered electrons passing through the PMMA are diminished.

APPENDIX A. FABRICATION DETAILS

A.4 Thin Film Deposition

In this work, thin film deposition is used (along with polymer masks patterned with optical or electron beam lithography) to create circuits around carbon nanotubes. There are three main methods used; each method will be discussed along with a few materials typically deposited in that way.

A.4.1 Thermal Evaporation

Thermal evaporation is the simplest method of thin film deposition discussed here. The material to be evaporated is placed in a boat, typically made of tungsten, alumina, or both. Substrates for the film to be deposited on are located above the evaporation boat. Both the boat and the samples are placed in a high vacuum chamber. Once the chamber has reached around 1×10^{-7} Torr, current through the evaporation boat is increased until the material melts or begins to sublime. The deposited thickness and deposition rate are monitored using a quartz crystal monitor. Once the desired rate is reached, a shutter is opened to expose the sample to the evaporated material.

This type of evaporation is best used with materials that have a relatively low melting point ($\lesssim 1200^\circ\text{C}$). Two evaporators were used in this work, a 1970s Denton evaporator fitted with a newer Hewlett Packard power supply, and an early 2000s Torr thermal evaporator. The Torr chamber is kept free from magnetic materials in

APPENDIX A. FABRICATION DETAILS

Table A.3: Thermal evaporation materials

Au	alumina coated W crucible
Ti	long, narrow W boat
Cr	chrome plated W rod
Al	dimpled W boat
Co	alumina coated W crucible (does not last long)

hopes of limiting contamination of superconducting films. Some common materials and the boats we have found most useful are listed in Table A.3.

A.4.2 Electron Beam Evaporation

Electron beam evaporation uses a high energy (7.5 keV) beam of electrons to melt the source material. The electron gun sits under a crucible full of the source material. The electron beam generated is bent and rastered across the center of the crucible using a strong magnetic field. Substrates are placed above the crucible and as the material melts and evaporates it is deposited on the substrate.

This method of evaporation has two benefits over thermal evaporation. First, it can be used for materials with a higher melting point. In the case of the Sharon Vacuum electron beam evaporator used in this work, materials with melting points up to $\sim 1800^{\circ}\text{C}$ were successfully evaporated. Second, the evaporated films are typically

APPENDIX A. FABRICATION DETAILS

a little cleaner because the crucible, unlike thermal evaporation boats, does not have to be heated in order for the source material to melt.

Due to limited access to the evaporator, not many of the films discussed in this work were deposited with electron beam evaporation. However, we have successfully deposited Nb, Co, Ti, and Al films all from graphite crucibles. Graphite was chosen here because of its affordability. There are likely better choices of crucible available.

A.4.3 Sputtering

Magnetron sputtering is a great method to deposit an amorphous thin film of just about any material needed. The three-target sputtering chamber used in this work was custom built by Professor Chia-Ling Chien's group at Johns Hopkins.

To sputter a material, a target 1-2 inches in diameter is loaded onto a cathode at the bottom of a vacuum chamber. The substrate to be coated is placed above the target on the anode. Once the system is at high vacuum, argon gas (or any inert gas) is introduced to the chamber. An argon plasma is ignited between the cathode (target) and anode (sample). The strong electric potential and magnetic field from permanent magnets placed under the target focus the plasma in a ring pattern on the face of the target. Argon ions bombard the target and target atoms are ejected toward the substrate mounted above.

The benefit of sputtering, as mentioned above, is that almost any metal can be sputtered with a DC plasma (RF plasma is used for insulating materials). Due to

APPENDIX A. FABRICATION DETAILS



Figure A.5: The Markovic lab ALD reactor. Gas flow is from right to left.

the high energy of the argon ions and ejected target atoms, this method can damage some sensitive samples. There may be some evidence that this is the case with carbon nanotube samples. For this work, low energy plasma was used to keep the average energy of ejected target atoms around a few eV. This is about 10 times higher than the energies used in thermal and electron beam evaporation. Even if sputtering does introduce some damage to nanotube samples, it does not appear to be the primary source of disorder.

A.4.4 Atomic Layer Deposition

Atomic layer deposition (ALD) is a process in which thin, usually insulating, films are grown by reacting a series of gases. As a part of this work, we have constructed a homemade ALD reactor in the Markovic lab with the help of undergraduate student

APPENDIX A. FABRICATION DETAILS

Streit Cunningham. It uses the same Lindberg 1 inch tube furnace as the chemical vapor deposition setup.

Samples are loaded into a 1 inch quartz tube and placed in the furnace. The tube is evacuated to about 100 mTorr using a mechanical rough pump. A high purity N₂ flow is turned on and adjusted so the pressure in the chamber, with the pump still running, is 1000 mTorr. The N₂ flow will act as a carrier gas throughout the process. We have only tested the reactor for growth of Al₂O₃ layers. Two precursor gases are used in the growth of Al₂O₃, water vapor and trimethylaluminum (TMA). Once the quartz tube is evacuated and N₂ flow is set, the water vapor and TMA are alternately pulsed using computer controlled solenoid valves. Films grow one monolayer (1.1 Å) per pulse cycle. A typical recipe is as follows:

1. Evacuate tube to 100 mTorr with mechanical pump
2. Turn on N₂ flow such that the pressure reaches 1000 mTorr
3. Set furnace temperature to 130 °C
4. Pulse TMA for 1 second
5. Purge for 60 seconds
6. Pulse water for 1 second
7. Purge for 60 seconds
8. Repeat pulse/purge cycle until desired thickness has been reached

APPENDIX A. FABRICATION DETAILS

9. Cool furnace, turn off N₂ flow, turn off pump, remove sample

The goal with this recipe is to grow a quality insulating layer at a temperature low enough to be compatible with PMMA processing. This design is based on previous low temperature ALD growth by the George lab at the University of Colorado Boulder [124, 125].

A.4.5 Liftoff

When patterning a thin film using a polymer mask, such as PMMA or S1813, the final step after deposition of the film is to remove the mask. This process is called liftoff, as the excess metal is lifted off the substrate along with the dissolved polymer mask.

Typically, liftoff is very simple. The sample is soaked in acetone for 1-12 hours (depending on what else is going on in the lab), then rinsed in IPA for 30 seconds followed by a 30 second rinse in water.

To help remove any stubborn material, the sample can be sprayed with a bottle of acetone for a few seconds before rinsing in IPA. Some samples can also be placed in a beaker of acetone in a sonicator for a few seconds before rinsing in IPA. Sonication is not ideal for nanotube samples, as the process tends to break nanotubes off of the substrate and introduce defects in long tubes. An example of this can be seen in Figure A.6.

APPENDIX A. FABRICATION DETAILS

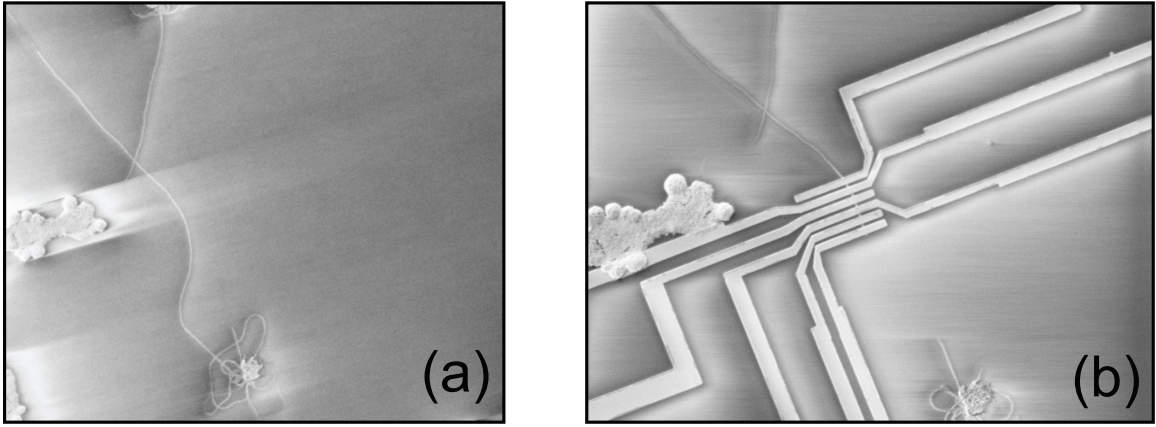


Figure A.6: (a) A substrate with catalyst islands and a few long nanotubes before patterning. (b) The same substrate after patterning and liftoff. Comparing the two images, it is clear that the use of sonication during liftoff has broken many of the nanotubes.

A.5 Room Temperature Testing

After devices have been fabricated, it is important to check the connectivity of the devices before spending the time to load samples into a cryostat.

A.5.1 Probe Station

The first step after fabrication is to test the resistance, and sometimes the gate behavior, of a device using a DC probe station. Our DC probe station was custom built for our lab and can be seen in Figure A.7.

The simplest and safest way found to check nanotube devices is to apply a small DC voltage (a few mV) between two of the large leads and measure the current with an ammeter. The measurements are done using a real-time LabView program. The bias is supplied by a National Instruments DAQ board through a 10^{-2} voltage divider.

APPENDIX A. FABRICATION DETAILS

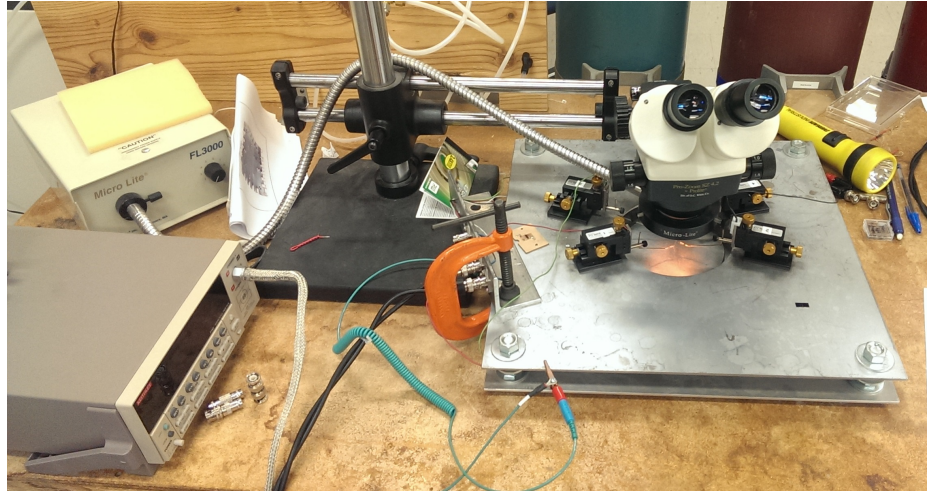


Figure A.7: The Markovic lab probe station. Four sharp probes are located under an optical microscope. Each can be connected to external sources and measurements using BNC connectors.

Current is measured by the same DAQ board by monitoring the output of an Ithaco 1211 current-to-voltage amplifier.

A.5.2 Wire Bonding

The final step in preparing devices for measurement is to wire bond the sample into a chip carrier. Each chip carrier is about 1×1 cm and fits into a standard socket on each of our cryostats. The wire bonder is used to connect the large leads/bonding pads on the sample to the chip carrier. Bonding pads have been successfully created with both optical and electron beam lithography. An old Kulicke and Soffa wire bonder in Chia-Ling Chien's lab was used for this work. It can be seen in Figure A.8a.

The wire bonder is used to connect a point on the chip carrier to a point on the

APPENDIX A. FABRICATION DETAILS

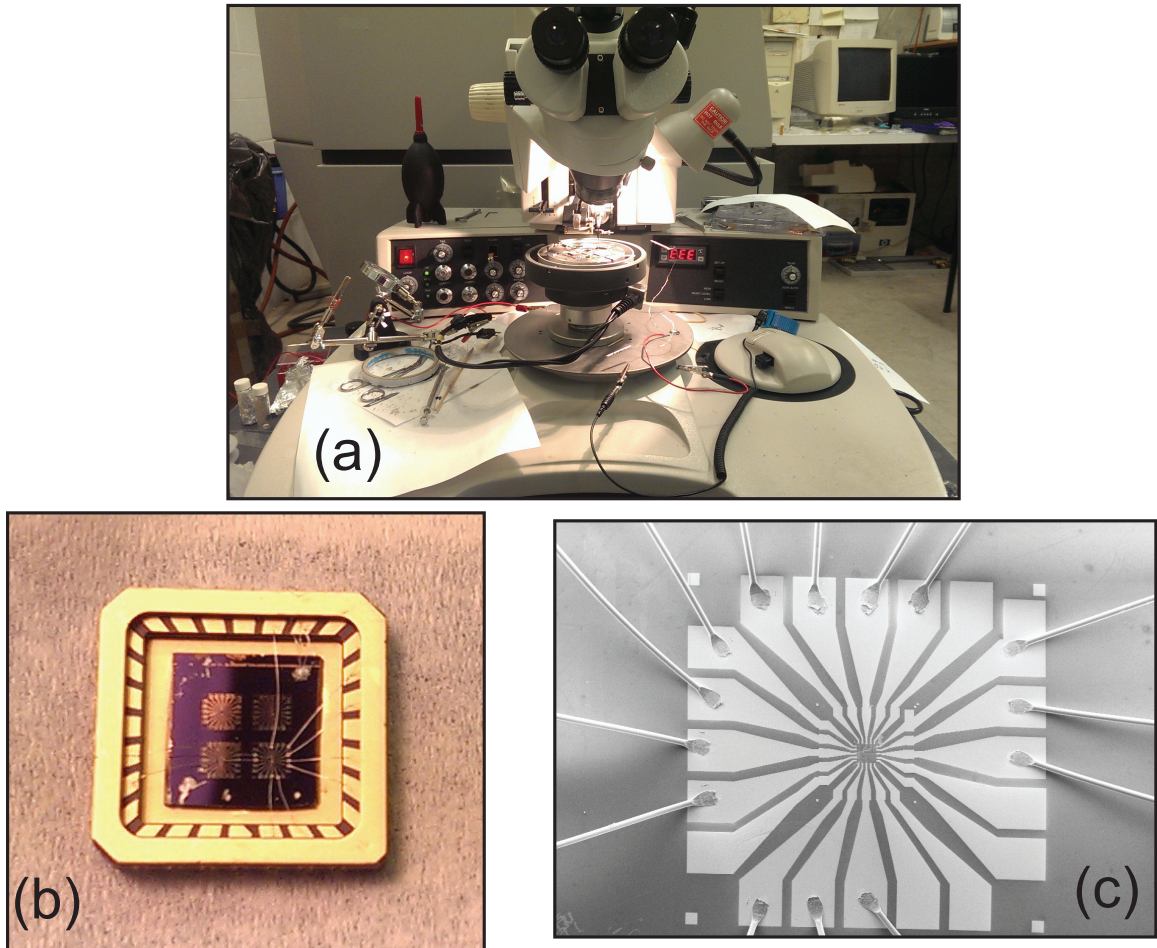


Figure A.8: (a) Kulicke and Soffa wire bonder. (b) An optical image of a completed device mounted in a chip carrier. (c) An SEM image detailing aluminum wires bonded to large gold leads.

APPENDIX A. FABRICATION DETAILS

sample with an aluminum or gold thread. The thread is first pressed by the wire bonder tip onto a bonding pad on the chip carrier. When the wire is in contact with the bonding pad the tip vibrates and presses down onto the sample to fix the wire into place. The tip can then be moved to contact one of the large optical lithography leads on the sample with the same wire. Once the second bond is made, the tip pulls away quickly to break the wire. The results of this process can be seen in Figures A.8b and c.

Appendix B

Details of Cryostat Operation

B.1 Oxford Kelvinox Dilution Refrigerator

The instructions below assume all of the gas handling lines have been leak checked and pumped out. The manual valves on the still/condenser lines should be open. It is also useful to monitor the still temperature with a resistance bridge while following these instructions.

Before opening dump

- Fill LN trap with liquid nitrogen. Stop when level is about 5 inches from top
- Slowly insert LHe trap into port on top of fridge.
- He recovery line should be connected at the large dewar exhaust port (this cools

APPENDIX B. CRYOSTAT OPERATION

the magnet leads).

- Check dump levels and cool LN trap
- Close all IGH valves.
- Cold trap 1 must be used for the initial cool down because only 12A is a needle valve
- Open green manual valves on the dump
- Switch on 3He rotary pump. Let the pump warm up for 20 minutes
- Open valve 9
- Wait a few moments, then record the reading on G2. This will be used later to be sure all of the mash has been pumped back out of the fridge. (762 ± 5 mbar)
- Close valve 9
- Open valve 1
- Open valve 13A. This will send some of the mash from behind the He3 pump into the LN trap. Wait for about 1 minute for LN boil off to slow.
- Open valve 12A to allow gas into the condenser line. Make sure P1 starts to rise. This proves there is no blockage in the fridge lines. G1 and G2 should drop to 30 while P1 remains at 1000.

APPENDIX B. CRYOSTAT OPERATION

Starting the 1K pot pump

- Make sure valves 1A, 2A, 4A, 5A are closed
- Start the 4He rotary pump
- Open valve 4A
- Open manual valve on the 1K pot line at the fridge
- Open needle valve to 100%. Wait for G3 to fill >300mbar.
- Close needle valve slowly until pressure in P2 drops to about 7.5 (from test values) Needle valve should be 10%
- Adjust needle valve until the 1K pot temperature stabilizes. It should be somewhere around 1.7K, maybe as low as 1.5K.

Condense mixture from storage dump

- Close valve 12A. Wait for needle valve
- Open valve 3 to connect still and condenser lines
- Open valve 9. G2 shows remaining pressure in dump (692mbar).
- Check that 13A is still open

APPENDIX B. CRYOSTAT OPERATION

- Slowly open 12A. Keep condenser pressure (G1) below 200mbar. This prevents excessive load on the 1K pot. P2 rises very quickly as 12A is opened. Keep an eye on the 1K pot temperature. Needle valve likely needs to be adjusted.
- Still temperature should drop to 1.2K
- When 12A is 100% open. Wait for G1<100mbar.
- Close valve 3. P1 still at 1000.

Starting circulation

- Close valve 9
- Open valve 14 to connect the dump to the still pumping line
- Begin pumping still by opening 6 slowly. Keep G2 between 100-200mbar. Once the mixing chamber is below 2K things speed up. Once 6 is open more than 18% it can be opened much faster.
- When 6 is fully open G1 and G2 should drop.
- After G1 and G2 stabilize most of the mixture should be condensed. (G1/G2 150 or lower)
- Close valve 14. Note: green manual valves on the dump should remain open during fridge operation

APPENDIX B. CRYOSTAT OPERATION

Going to base temperature

- Switch on roots pump. Watch 1K pot temp. All other temps should drop fast.
- Still should be $< 1.2\text{K}$ now. Mixing chamber and heat exchanger temperatures should follow still temperature
- When still line pressure (P1) is $<0.3\text{mbar}$ increase circulation rate by turning on still heater. See the test results for details.
- The lowest base temperature obtained in our lab was using a still heater power of 10mW.

With everything setup correctly, the fridge should remain at base temperature for a few weeks. LN traps should be switched and regenerated every few days, and all cryogen levels should be checked daily.

Removing Mixture

- Note: Do not remove LN or LHe traps before this process is complete
- Open valve 3 to equalize pressure in still and condenser lines
- Close valve 6
- Open valve 4
- Close 1K pot needle valve

APPENDIX B. CRYOSTAT OPERATION

- Close 4A
- Stop He4 pump
- Vent 1K pot with He gas from main bath (or gas tank connected to main bath port) by opening 1A (make sure main bath line is actually connected first)
- Increase still and mixing chamber heaters to maximum (20mW/200mW). This is very important. Otherwise the process takes more than a day.
- Close valves 4, 13A
- Open valve 9
- Slowly open valve 6 to pump mixture into dump
- Make sure 12A is open while moving mixture to dump
- When G1 is a few mbar, close valve 6, quick open valve 14 to let warm gas into the fridge, let G1 and G2 equalize, close valve 14, slowly open valve 6. (12A may need to be close for the pumping and flushing process to prevent warm gas from reaching the LN and causing excessive boil off.) This seemed to work best with the roots pump off.
- Repeat this pumping and flushing until G2 reaches its original value, $P1 < 0.1\text{mbar}$, and resistors show their 4.2K values

APPENDIX B. CRYOSTAT OPERATION

- When $G_2 =$ (pressure measured when the dump was first opened) and $P_1 < 0.1\text{mbar}$, close valves 4, 6, 9, 12A
- Open valve 6 all the way and wait for some time to be sure all of the mash has been pumped out of the fridge lines.
- In the end $G_1, P_1 = 0$ and $G_2 = (765 \pm 2)$
- Shut manual valves on fridge
- Close all valves on IGH
- Wait for valve 6 to fully close
- Shut green manual valves on dump
- Turn He3 pump off. G_2 may drop (to 600), but the mash is safely contained in the IGH and He3 pump.

LHe trap

- Before the LHe trap is warmed, close the manual speedivalve on the condenser line
- Open valve 1
- Monitor pressure at G1
- Start 1K pot pump

APPENDIX B. CRYOSTAT OPERATION

- Pull out cold trap from dewar
- Open valves 5A, 2A, 7, 2
- Heat trap gently
- Wait for G1 to drop back to 0
- Close 1, 2, 7, 2A, 5A

LN trap

- Open valve 12A
- Monitor G1 pressure
- Start 1K pot pump
- Pull out trap
- Pump trap by opening valves 5A, 2A, 7, 2
- Open 11A for faster pumping
- When G1 drops to zero close 11A, 12A, 2, 7, 2A, 5A.

Make sure all manual valves on the fridge are closed. Remove pumping lines.

Connect He gas source to vent port on sliding seal. Hoist fridge out of dewar. Cover dewar opening with blank plate.

APPENDIX B. CRYOSTAT OPERATION

B.2 RMC 3He Cryostat

Below are detailed instructions for cooling down the RMC 3He cryostat. To complete these instructions a turbo pump with backing pump, rough pump for the 1K pot line, a 4He gas tank, vacuum grease, and (optionally) a leak checker will be needed.

Setup

- Mount samples and check wiring
- Clean cone seal, grease and seat vacuum can then evacuate
- Leak check cone seal
- Add “thumbfull” of He4 exchange gas to IVC
- Purge the 1K pot pump line with 4He gas for at least 30 minutes at 1-5psi, then pressurize with 4He gas to 5 psi and close line

Cool Down

- Insert the cryostat into the cold dewar by clamping down the sliding seal and lowering very slowly into the LHe bath
- Once the temperature reaches 10K on the 3He pot, pump out the exchange gas with a turbo pump

APPENDIX B. CRYOSTAT OPERATION

Cooling to Base Temperature

- Connect the rotary pump to the 1K pot pumping line
- Turn on the pump, wait for pressure in line to drop, slowly open the valve to pump on the 1K pot.
- Wait for the pressure to stabilize
- Turn on the sorb heater to 500mW
- Wait for the 3He pot temperature to stabilize at 1.2-1.5K. **NOTE** If this takes longer than 10-20 minutes, lower the sorb heater power to 50mW
- Once the 3He pot temperature reaches about 1.2K, wait 30-40 minutes for the 3He to condense. At this point the sorb heater should be set to 50mW.
- Turn off the sorb heater power.
- Turn on the switch heater for 1 minute at 10mW. This is to cool the sorb more quickly by releasing some exchange gas from the charcoal sorb.
- Turn the switch heater down to 1mW (may need to be adjusted from 0-1mW depending on base temperature behavior)
- Wait for the 3He sorb temperature to reach its based temperature (250-300mK)

A diagram of this process can be seen in Figure B.1.

APPENDIX B. CRYOSTAT OPERATION

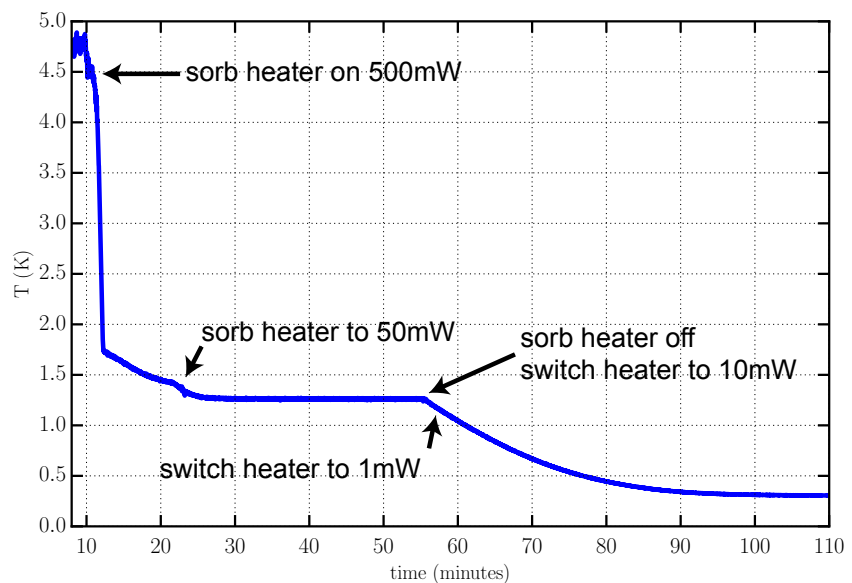


Figure B.1: 3He pot temperature versus time for the RMC 3He cryostat.

Bibliography

- [1] M. Buitelaar, J. Fransson, a. Cantone, C. Smith, D. Anderson, G. Jones, a. Ardashov, a. Khlobystov, a. Watt, K. Porfyrakis, and G. Briggs, “Pauli spin blockade in carbon nanotube double quantum dots,” *Physical Review B*, vol. 77, no. 24, p. 245439, Jun. 2008. [Online]. Available: <http://link.aps.org/doi/10.1103/PhysRevB.77.245439>
- [2] D. Weinmann, W. Häusler, W. Pfaff, B. Kramer, and U. Weiss, “Spin Blockade in Non-linear Transport through Quantum Dots,” *Europhysics Letters (EPL)*, vol. 26, no. 6, pp. 467–472, 1994.
- [3] D. Weinmann, W. Häusler, and B. Kramer, “Spin Blockades in Linear and Nonlinear Transport through Quantum Dots Dietmar,” *Physical Review Letters*, vol. 74, no. 6, pp. 984–987, 1995.
- [4] J. Moodera, G. Miao, and T. Santos, “Frontiers in spin-polarized tunneling,” *Physics Today*, vol. 63, p. 46, 2010. [Online]. Available: <http://link.aip.org/link/abstract/PHTOAD/v63/i4/p46/s1>

BIBLIOGRAPHY

- [5] R. Meservey and P. Tedrow, “Spin-polarized electron tunneling,” *Physics Reports*, vol. 238, no. 4, pp. 173–243, 1994.
- [6] T. Morgan-Wall, B. Leith, N. Hartman, a. Rahman, and N. Marković, “Measurement of Critical Currents of Superconducting Aluminum Nanowires in External Magnetic Fields: Evidence for a Weber Blockade,” *Physical Review Letters*, vol. 114, no. 7, p. 077002, 2015. [Online]. Available: <http://link.aps.org/doi/10.1103/PhysRevLett.114.077002>
- [7] D. C. Ralph, C. T. Black, and M. Tinkham, “Gate-Voltage Studies of Discrete Electronic States in Al Nanoparticles,” *Physical Review Letters*, vol. 78, no. 21, 1997. [Online]. Available: <http://arxiv.org/abs/cond-mat/9701081>
- [8] D. Davidović and M. Tinkham, “Coulomb blockade and discrete energy levels in Au nanoparticles,” *Applied Physics Letters*, vol. 73, no. 26, pp. 3959–3961, 1998.
- [9] P. L. McEuen, E. B. Foxman, J. Kinaret, U. Meirav, M. a. Kastner, N. S. Wingreen, and S. J. Wind, “Self-consistent addition spectrum of a Coulomb island in the quantum Hall regime,” *Physical Review B*, vol. 45, no. 19, pp. 11 419–11 422, 1992.
- [10] O. Klein, C. d. C. Chamon, D. Tang, D. Abusch-Magder, U. Meirav, X.-G. Wen, and M. Kastner, “Exchange Effects in an Artificial Atom at High Magnetic Fields,” *Physical Review Letters*, vol. 74, no. 5, 1995.

BIBLIOGRAPHY

- [11] P. M. Tedrow and R. Meservey, “Spin-Dependent Tunneling into Ferromagnetic Nickel,” *Physical Review Letters*, vol. 26, no. 4, Oct. 1971. [Online]. Available: <http://www.ncbi.nlm.nih.gov/pubmed/21971032>
- [12] T. Ihn, *Electronic Quantum Transport in Mesoscopic Semiconductor Structures*. New York: Springer-Verlag, 2004, vol. 192.
- [13] P. R. Wallace, “The Band Theory of Graphite,” *Physical Review*, 1947.
- [14] G. W. Semenoff, “Condensed matter simulation of a three-dimensional anomaly,” *Physical Review Letters*, vol. 55, no. 26, pp. 2449–2452, 1984.
- [15] K. S. Novoselov, A. K. Geim, S. Morozov, D. Jiang, Y. Zhang, S. Dubonos, I. V. Grigorieva, and A. A. Firsov, “Electric Field Effect in Atomically Thin Carbon Films,” *Science*, vol. 306, 2004. [Online]. Available: <http://arxiv.org/ftp/cond-mat/papers/0410/0410550.pdf>
- [16] K. S. Novoselov, D. Jiang, F. Schedin, T. J. Booth, V. V. Khotkevich, S. V. Morozov, and a. K. Geim, “Two-dimensional atomic crystals.” *Proceedings of the National Academy of Sciences of the United States of America*, vol. 102, no. 30, pp. 10 451–10 453, 2005.
- [17] A. Javey and J. Kong, *Carbon Nanotube Electronics*. Springer, 2009.
- [18] J.-C. Charlier and S. Roche, “Electronic and transport properties of

BIBLIOGRAPHY

- nanotubes,” *Reviews of Modern Physics*, vol. 79, no. 2, pp. 677–732, May 2007. [Online]. Available: <http://link.aps.org/doi/10.1103/RevModPhys.79.677>
- [19] H. Ibach and H. Lüth, *Solid-state physics: An introduction to principles of materials science.* Springer, 2010.
- [20] R. Saito, M. S. Dresselhaus, and D. G. Dresselhaus, *Physical Properties of Carbon Nanotubes.* London: Imperial College Press, 1998.
- [21] G. G. Samsonidze, a. R. Saito, D. a. Jorio, E. M. a. Pimenta, E. a. G. Souza Filho, F. a. Grüneis, D. G. Dresselhaus, and M. S. Dresselhaus, “The Concept of Cutting Lines in Carbon Nanotube Science,” *Journal of Nanoscience and Nanotechnology*, vol. 3, no. 6, pp. 431–458, Dec. 2003. [Online]. Available: <http://www.ingentaselect.com/rpsv/cgi-bin/cgi?ini=xref&body=linker&reqdoi=10.1166/jnn.2003.231>
- [22] J.-S. Jeong and H.-W. Lee, “Curvature-enhanced spin-orbit coupling in a carbon nanotube,” *Physical Review B*, vol. 80, no. 7, p. 075409, Aug. 2009. [Online]. Available: <http://link.aps.org/doi/10.1103/PhysRevB.80.075409>
- [23] L. P. Kouwenhoven, D. Austing, and S. Tarucha, “Few-electron quantum dots,” *Reports on Progress in Physics*, vol. 64, no. 6, pp. 701–736, May 2001.
- [24] D. H. Cobden and J. Nygård, “Shell filling in closed single-wall carbon

BIBLIOGRAPHY

- nanotube quantum dots,” *Physical review letters*, vol. 89, no. 4, p. 46803, 2002. [Online]. Available: <http://link.aps.org/doi/10.1103/PhysRevLett.89.046803>
- [25] C. C. Wu, C. H. Liu, and Z. Zhong, “One-step direct transfer of pristine single-walled carbon nanotubes for functional nanoelectronics.” *Nano letters*, vol. 10, no. 3, pp. 1032–6, Mar. 2010. [Online]. Available: <http://www.ncbi.nlm.nih.gov/pubmed/20108926>
- [26] F. Pei, E. a. Laird, G. a. Steele, and L. P. Kouwenhoven, “Valley-spin blockade and spin resonance in carbon nanotubes.” *Nature nanotechnology*, vol. 7, no. 10, pp. 630–4, Oct. 2012. [Online]. Available: <http://www.ncbi.nlm.nih.gov/pubmed/23001302>
- [27] J. Kong, “Chemical vapor deposition of methane for single-walled carbon nanotubes,” *Chemical Physics Letters*, vol. 292, no. 4-6, pp. 567–574, Aug. 1998. [Online]. Available: <http://linkinghub.elsevier.com/retrieve/pii/S0009261498007453>
- [28] J. Kong, H. T. Soh, A. M. Cassell, C. F. Quate, and H. Dai, “Synthesis of individual single-walled carbon nanotubes on patterned silicon wafers,” *Nature*, vol. 395, no. 3, pp. 878–881, 1998.
- [29] H. M. Aurich, “Carbon Nanotube Spin-Valve with Optimized Ferromagnetic Contacts,” Ph.D. dissertation, University of Basel, 2012.

BIBLIOGRAPHY

- [30] L. L. Ouellette, "CHEMICAL AND BIOLOGICAL SENSING WITH CARBON NANOTUBES IN SOLUTION," Ph.D. dissertation, Cornell University, 2008.
- [31] B. H. Hong, J. Y. Lee, T. Beetz, Y. Zhu, P. Kim, and K. S. Kim, "Quasi-continuous growth of ultralong carbon nanotube arrays." *Journal of the American Chemical Society*, vol. 127, no. 44, pp. 15 336–7, Nov. 2005. [Online]. Available: <http://www.ncbi.nlm.nih.gov/pubmed/16262374>
- [32] M. J. Biercuk, N. Mason, and C. M. Marcus, "Local Gating of Carbon Nanotubes," *Nano Letters*, vol. 4, no. 1, pp. 1–4, Jan. 2004. [Online]. Available: <http://pubs.acs.org/doi/abs/10.1021/nl034696g>
- [33] S. J. Kang, C. Kocabas, T. Ozel, M. Shim, N. Pimparkar, M. a. Alam, S. V. Rotkin, and J. a. Rogers, "High-performance electronics using dense, perfectly aligned arrays of single-walled carbon nanotubes." *Nature nanotechnology*, vol. 2, no. 4, pp. 230–6, Apr. 2007. [Online]. Available: <http://www.ncbi.nlm.nih.gov/pubmed/18654268>
- [34] T. L. Dirks, "Tunneling Spectroscopy of Carbon Nanostructures: A Romance in Many Dimensions," Ph.D. dissertation, University of Illinois at Urbana-Champaign, 2010.
- [35] S. Huang, X. Cai, and J. Liu, "Growth of millimeter-long and horizontally aligned single-walled carbon nanotubes on flat substrates." *Journal of the*

BIBLIOGRAPHY

- American Chemical Society*, vol. 125, no. 19, pp. 5636–7, May 2003. [Online]. Available: <http://www.ncbi.nlm.nih.gov/pubmed/12733894>
- [36] S. Huang, M. Woodson, R. Smalley, and J. Liu, “Growth Mechanism of Oriented Long Single Walled Carbon Nanotubes Using â€œFast-Heatingâ€ Chemical Vapor Deposition Process,” *Nano Letters*, vol. 4, no. 6, pp. 1025–1028, Jun. 2004. [Online]. Available: <http://pubs.acs.org/doi/abs/10.1021/nl049691d>
- [37] R. Zhang, Y. Zhang, Q. Zhang, H. Xie, W. Qian, and F. Wei, “Growth of Half-Meter Long Carbon,” *ACS nano*, vol. 7, no. 7, pp. 6156–6161, 2013.
- [38] M. Bockrath, N. Markovic, A. Shepard, M. Tinkham, L. Gurevich, L. P. Kouwenhoven, M. W. Wu, and L. L. Sohn, “Scanned Conductance Microscopy of Carbon Nanotubes and λ -DNA,” *Nano Letters*, vol. 2, no. 3, pp. 187–190, Mar. 2002. [Online]. Available: <http://pubs.acs.org/doi/abs/10.1021/nl0100724>
- [39] T. S. Jespersen and J. Nygård, “Mapping of individual carbon nanotubes in polymer/nanotube composites using electrostatic force microscopy,” *Applied Physics Letters*, vol. 90, no. 18, p. 183108, 2007. [Online]. Available: <http://scitation.aip.org/content/aip/journal/apl/90/18/10.1063/1.2734920>
- [40] T. Brintlinger, Y.-F. Chen, T. Durkop, E. Cobas, M. S. Fuhrer, J. D. Barry, and J. Melngailis, “Rapid imaging of nanotubes on insulating substrates,” *Applied Physics Letters*, vol. 81, no. 13, p. 2454, 2002. [Online]. Available: <http://scitation.aip.org/content/aip/journal/apl/81/13/10.1063/1.1509113>

BIBLIOGRAPHY

- [41] S. Chaudhuri, S. Chatterjee, N. Katz, M. Nelson, and M. Goldbaum, “Detection of blood vessels in retinal images using two-dimensional matched filters.” *IEEE transactions on medical imaging*, vol. 8, no. 3, pp. 263–9, Jan. 1989. [Online]. Available: <http://www.ncbi.nlm.nih.gov/pubmed/18230524>
- [42] A. d. J. G. J. TeresaE. and Zamudio, D. Oscar, and Alarcón, “Frequency Filter Bank for Enhancing Carbon Nanotube Images,” in *Human-Inspired Computing and Its Applications*. Springer International Publishing, 2014, ch. Frequency, pp. 316–326. [Online]. Available: http://link.springer.com/10.1007/978-3-319-13647-9_29
- [43] A. Javey, J. Guo, Q. Wang, M. Lundstrom, and H. Dai, “Ballistic carbon nanotube field-effect transistors.” *Nature*, vol. 424, no. 6949, pp. 654–657, 2003.
- [44] Y. Song and S. J. Kang, “Improvement of contact resistance between carbon nanotubes and metal electrodes for high performance electronics,” *Journal of Vacuum Science & Technology B: Microelectronics and Nanometer Structures*, vol. 29, no. 1, p. 011011, 2011. [Online]. Available: <http://scitation.aip.org/content/avs/journal/jvstb/29/1/10.1116/1.3520436>
- [45] A. A. Kane, K. Loutherback, B. R. Goldsmith, and P. G. Collins, “High temperature resistance of small diameter , metallic single-walled carbon nanotube devices,” *Applied Physics Letters*, vol. 083506, no. 2008, pp. 2006–2009, 2008.

BIBLIOGRAPHY

- [46] H. O. H. Churchill, “Quantum Dots in Gated Nanowires and Nanotubes,” Ph.D. dissertation, Harvard University, 2012.
- [47] A. Y. Kasumov, R. Deblock, M. Kociak, B. Reulet, H. Bouchiat, I. I. Khodos, Y. B. Gorbatov, V. T. Volkov, C. Journet, and M. Burghard, “Supercurrents Through Single-Walled Carbon Nanotubes,” *Science*, vol. 284, pp. 1508–1511, 1999.
- [48] P. Jarillo-Herrero, J. a. van Dam, and L. P. Kouwenhoven, “Quantum supercurrent transistors in carbon nanotubes.” *Nature*, vol. 439, no. 7079, pp. 953–956, 2006.
- [49] S. Jejurikar, D. Casterman, P. B. Pillai, O. Petrenko, M. M. De Souza, a. Tahraoui, C. Durkan, and W. I. Milne, “Anomalous n-type electrical behaviour of Pd-contacted CNTFET fabricated on small-diameter nanotube.” *Nanotechnology*, vol. 21, no. 21, p. 215202, 2010.
- [50] I. Maximov, A. A. Zakharov, T. Holmqvist, L. Montelius, and I. Lindau, “Investigation of polymethylmethacrylate resist residues using photoelectron microscopy,” *Journal of Vacuum Science & Technology B*, vol. 1139, no. 2002, pp. 16–20, 2009.
- [51] D. S. Macintyre, O. Ignatova, S. Thoms, and I. G. Thayne, “Resist residues and transistor gate fabrication,” *Journal of Vacuum Science & Technology B: Microelectronics and Nanometer Structures*, vol. 27, no. 6, p. 2597, 2009.

BIBLIOGRAPHY

- [Online]. Available: <http://scitation.aip.org/content/avs/journal/jvstb/27/6/10.1116/1.3243176>
- [52] H. Eisenmann, “PROXECCO™Proximity effect correction by convolution,” *Journal of Vacuum Science & Technology B: Microelectronics and Nanometer Structures*, vol. 11, no. 6, p. 2741, Nov. 1993. [Online]. Available: <http://scitation.aip.org/content/avs/journal/jvstb/11/6/10.1116/1.586594>
- [53] J. P. Stirnimann and M. L. Rieger, “Fast proximity correction with zone sampling,” *SPIE*, vol. 2197, no. 503, 1994.
- [54] E. Soe, B. K. Choi, and O. Kim, “Determination of proximity effect parameters and the shape bias parameter in electron beam lithography,” *Microelectronic Engineering*, vol. 53, no. 1, pp. 305–308, 2000.
- [55] M. Osawa, K. Takahashi, M. Sato, H. Arimoto, K. Ogino, H. Hoshino, and Y. Machida, “Proximity effect correction using pattern shape modification and area density map for electron-beam projection lithography,” *Journal of Vacuum Science & Technology B*, vol. 19, no. 6, p. 2483, 2001.
- [56] A. G. F. Garcia, M. Neumann, J. R. Williams, K. Watanabe, T. Taniguchi, and D. Goldhaber-gordon, “Effective Cleaning of Hexagonal Boron Nitride for Graphene Devices,” *Nano letters*, pp. 2–7, 2012.
- [57] J.-O. Lee, C. Park, J.-J. Kim, J. Kim, J. W. Park, and K.-H. Yoo,

BIBLIOGRAPHY

- “Formation of low-resistance ohmic contacts between carbon nanotube and metal electrodes by a rapid thermal annealing method,” *Journal of Physics D: Applied Physics*, vol. 33, no. 16, pp. 1953–1956, Aug. 2000. [Online]. Available: <http://stacks.iop.org/0022-3727/33/i=16/a=303?key=crossref.274b26ec505668f5940bad9f1bf01c73>
- [58] A. a. Kane, T. Sheps, E. T. Branigan, V. A. Apkarian, M. H. Cheng, J. C. Hemminger, S. R. Hunt, and P. G. Collins, “Graphitic electrical contacts to metallic single-walled carbon nanotubes using Pt electrodes.” *Nano letters*, vol. 9, no. 10, pp. 3586–91, Oct. 2009. [Online]. Available: <http://www.ncbi.nlm.nih.gov/pubmed/19754066>
- [59] P. Stokes and S. I. Khondaker, “Evaluating Defects in Solution-Processed Carbon Nanotube Devices via Low-Temperature Transport Spectroscopy,” *ACS Nano*, vol. 4, no. 5, pp. 2659–2666, 2010.
- [60] V. Derycke, R. Martel, J. Appenzeller, and P. Avouris, “Controlling doping and carrier injection in carbon nanotube transistors,” *Applied Physics Letters*, vol. 80, no. 15, pp. 2773–2775, 2002.
- [61] W. Kim, A. Javey, O. Vermesh, Q. Wang, Y. Li, and H. Dai, “Hysteresis Caused by Water Molecules in Carbon Nanotube Field-Effect Transistors,” *Nano Letters*, vol. 3, no. 2, pp. 193–198, Feb. 2003. [Online]. Available: <http://pubs.acs.org/doi/abs/10.1021/nl0259232>

BIBLIOGRAPHY

- [62] a. Pirkle, J. Chan, a. Venugopal, D. Hinojos, C. W. Magnuson, S. McDonnell, L. Colombo, E. M. Vogel, R. S. Ruoff, and R. M. Wallace, “The effect of chemical residues on the physical and electrical properties of chemical vapor deposited graphene transferred to SiO₂,” *Applied Physics Letters*, vol. 99, no. 12, pp. 31–34, 2011.
- [63] J. Chan, A. Venugopal, A. Pirkle, S. McDonnell, D. Hinojos, C. W. Magnuson, R. S. Ruoff, L. Colombo, R. M. Wallace, and E. M. Vogel, “Reducing extrinsic performance-limiting factors in graphene grown by chemical vapor deposition,” *ACS Nano*, vol. 6, no. 4, pp. 3224–3229, 2012.
- [64] Z. Cheng, Q. Zhou, C. Wang, Q. Li, C. Wang, and Y. Fang, “Toward Intrinsic Graphene Surfaces : A Systematic Study on,” *Nano letters*, vol. 11, no. 2, pp. 767–771, 2011. [Online]. Available: <http://dx.doi.org/10.1021/nl103977d>
- [65] J. Gramich, A. Baumgartner, M. Muoth, and C. Hierold, “Fork stamping of pristine carbon nanotubes onto ferromagnetic contacts for spin-valve devices,” *arXiv*, vol. 1, no. c, pp. 1–7, 2015.
- [66] D. Preusche, S. Schmidmeier, E. Pallecchi, C. Dietrich, a. K. Hüttel, J. Zweck, and C. Strunk, “Characterization of ferromagnetic contacts to carbon nanotubes,” *Journal of Applied Physics*, vol. 106, no. 8, pp. 1–9, 2009.
- [67] H. Maki, M. Suzuki, and K. Ishibashi, “Local change of carbon nanotube-metal contacts by current flow through electrodes,” *Japanese Journal of Applied Physics*

BIBLIOGRAPHY

- Physics, Part 1: Regular Papers and Short Notes and Review Papers*, vol. 43, no. 4 B, pp. 2027–2030, 2004.
- [68] Y. Woo, G. S. Duesberg, and S. Roth, “Reduced contact resistance between an individual single-walled carbon nanotube and a metal electrode by a local point annealing,” *Nanotechnology*, vol. 18, no. 9, p. 095203, 2007.
- [69] L. Dong, S. Youkey, J. Bush, J. Jiao, V. M. Dubin, and R. V. Chebiam, “Effects of local Joule heating on the reduction of contact resistance between carbon nanotubes and metal electrodes Effects of local Joule heating on the reduction of contact resistance between carbon nanotubes and metal electrodes,” *Journal of Applied Physics*, vol. 101, 2007.
- [70] F. Liu, K. L. Wang, D. Zhang, and C. Zhou, “Random telegraph signals and noise behaviors in carbon nanotube transistors,” *Applied Physics Letters*, vol. 89, no. 24, p. 243101, 2006. [Online]. Available: <http://scitation.aip.org/content/aip/journal/apl/89/24/10.1063/1.2402224>
- [71] V. a. Sydoruk, K. Goß, C. Meyer, M. V. Petrychuk, B. a. Danilchenko, P. Weber, C. Stampfer, J. Li, and S. a. Vitusevich, “Low-frequency noise in individual carbon nanotube field-effect transistors with top, side and back gate configurations: effect of gamma irradiation.” *Nanotechnology*, vol. 25, no. 3, p. 035703, Jan. 2014. [Online]. Available: <http://www.ncbi.nlm.nih.gov/pubmed/24345726>

BIBLIOGRAPHY

- [72] P. Collins, M. Fuhrer, and a. Zettl, “1/F Noise in Carbon Nanotubes,” *Applied Physics Letters*, vol. 76, no. 7, pp. 894–896, 2000. [Online]. Available: <http://link.aip.org/link/APPLAB/v76/i7/p894/s1&Agg=doi>
- [73] M. Ishigami, J. H. Chen, E. D. Williams, D. Tobias, Y. F. Chen, and M. S. Fuhrer, “Hooge’s constant for carbon nanotube field effect transistors,” *Applied Physics Letters*, vol. 88, no. 20, pp. 2004–2007, 2006.
- [74] F. Hooge, “1/ES Noise Is No Surface Effect,” *Physics Letters A*, vol. 29, no. 3, pp. 139–140, 1969.
- [75] D. Tobias, M. Ishigami, A. Tselev, P. Barbara, E. Williams, C. Lobb, and M. Fuhrer, “Origins of 1/Lf noise in individual semiconducting carbon nanotube field-effect transistors,” *Physical Review B*, vol. 77, no. 3, pp. 1–4, 2008.
- [76] S. W. Jung, T. Fujisawa, Y. Hirayama, and Y. H. Jeong, “Background charge fluctuation in a GaAs quantum dot device,” *Applied Physics Letters*, vol. 85, no. 5, pp. 768–770, 2004.
- [77] X.-X. Song, H.-O. Li, J. You, T.-Y. Han, G. Cao, T. Tu, M. Xiao, G.-C. Guo, H.-W. Jiang, and G.-P. Guo, “Suspending Effect on Low-Frequency Charge Noise in Graphene Quantum Dot,” *Scientific Reports*, vol. 5, p. 8142, 2015. [Online]. Available: <http://www.nature.com/doifinder/10.1038/srep08142>
- [78] G. Gotz, G. A. Steele, W.-j. Vos, and L. P. Kouwenhoven, “Real Time Electron

BIBLIOGRAPHY

- Tunneling and Pulse Spectroscopy in Carbon Nanotube Quantum Dots,” *Nano Lett*, vol. 8, no. 11, pp. 4039–4042, 2008.
- [79] C. A. Merchant and N. Markovic, “Current and shot noise measurements in a carbon nanotube-based spin diode (invited),” *Journal of Applied Physics*, vol. 105, no. 7, p. 07C711, 2009. [Online]. Available: <http://link.aip.org/link/JAPIAU/v105/i7/p07C711/s1&Agg=doi>
- [80] N. H. Balshaw, *Practical Cryogenics: an introduction to laboratory cryogenics*. Oxford Instruments, 2001, no. 01865.
- [81] M. Julliere, “Tunneling between ferromagnetic films,” *Physics Letters A*, vol. 54, no. 3, pp. 225–226, 1975.
- [82] E. Tsymbal, a. Sokolov, I. Sabirianov, and B. Doudin, “Resonant Inversion of Tunneling Magnetoresistance,” *Physical Review Letters*, vol. 90, no. 18, pp. 16–19, May 2003. [Online]. Available: <http://link.aps.org/doi/10.1103/PhysRevLett.90.186602>
- [83] S. Sahoo, T. Kontos, J. Furer, C. Hoffmann, M. Gräber, A. Cottet, and C. Schönenberger, “Electric field control of spin transport,” *Nature Physics*, vol. 1, no. 2, pp. 99–102, Oct. 2005. [Online]. Available: <http://www.nature.com/doifinder/10.1038/nphys149>
- [84] R. Thamankar, S. Niyogi, B. Y. Yoo, Y. W. Rheem, N. V. Myung, R. C. Had-

BIBLIOGRAPHY

- don, and R. K. Kawakami, “Spin-polarized transport in magnetically assembled carbon nanotube spin valves,” *Applied Physics Letters*, vol. 89, no. 3, pp. 7–10, 2006.
- [85] A. H. Morrish, *The Physical Principles of Magnetism*. New York: Wiley, 1983.
- [86] M. T. Johnson, P. J. H. Bloemen, F. J. a. D. Broeder, and J. J. D. Vries, “Magnetic anisotropy in metallic multilayers,” *Reports on Progress in Physics*, vol. 59, no. 11, pp. 1409–1458, 1999.
- [87] S. Maekawa, U. Gafvert, G. Ag, and G. G. G. T. G. J. Pb, “Electron tunneling between ferromagnetic films,” *Magnetics, IEEE Transactions on*, vol. 18, no. 2, pp. 707–708, 1982.
- [88] P. L. McEuen, M. Bockrath, D. H. Cobden, Y.-G. Yoon, and S. G. Louie, “Disorder, pseudospins, and backscattering in carbon nanotubes,” *Physical Review Letters*, vol. 83, no. 24, 1999. [Online]. Available: <http://arxiv.org/abs/cond-mat/9906055>
- [89] M. Bockrath, W. Liang, D. Bozovic, J. H. Hafner, C. M. Lieber, M. Tinkham, and H. Park, “Resonant electron scattering by defects in single-walled carbon nanotubes.” *Science (New York, N.Y.)*, vol. 291, no. 5502, pp. 283–285, 2001.
- [90] N. Mason, M. J. Biercuk, and C. M. Marcus, “Local gate control of a carbon

BIBLIOGRAPHY

- nanotube double quantum dot.” *Science (New York, N.Y.)*, vol. 303, no. 5658, pp. 655–658, 2004.
- [91] H. Jorgensen, “Experimental Quantum Transport in Carbon Nanotubes: Josephson Quantum Dot Junctions and Double Quantum Dots,” Ph.D. dissertation, University of Copenhagen, 2007.
- [92] D. H. Cobden, M. Bockrath, P. L. McEuen, A. G. Rinzlet, and R. E. Smalley, “Spin Splitting and Even-Odd Effects in Carbon Nanotubes,” *Physical Review Letters*, vol. 81, no. 3, pp. 681–684, Jul. 1998. [Online]. Available: <http://link.aps.org/doi/10.1103/PhysRevLett.81.681>
- [93] R. a. Lai, H. O. H. Churchill, and C. M. Marcus, “ $\langle \rangle$ -Tensor Control in Bent Carbon Nanotube Quantum Dots,” *Physical Review B*, vol. 89, no. 12, p. 121303, Mar. 2014. [Online]. Available: <http://link.aps.org/doi/10.1103/PhysRevB.89.121303>
- [94] M. Ganzhorn, S. Klyatskaya, M. Ruben, and W. Wernsdorfer, “Strong spin-phonon coupling between a single-molecule magnet and a carbon nanotube nanoelectromechanical system.” *Nature nanotechnology*, vol. 8, no. 3, pp. 165–9, Mar. 2013. [Online]. Available: <http://www.ncbi.nlm.nih.gov/pubmed/23377456>

BIBLIOGRAPHY

- [95] P. Tedrow and R. Meservey, “Spin Polarization of Electrons Tunneling from Films of Fe, Co, Ni, and Gd,” *Physical Review B*, vol. 7, no. 1, 1973.
- [96] M. Tinkham, *Introduction to Superconductivity*. New York: McGraw-Hill Inc., 1996.
- [97] L. Hofstetter, a. Geresdi, M. Aagesen, J. Nygård, C. Schönenberger, and S. Csonka, “Ferromagnetic proximity effect in a ferromagnet-quantum-dot-superconductor device,” *Physical Review Letters*, vol. 104, no. 24, pp. 1–4, 2010.
- [98] S. J. Tans, M. H. Devoret, H. Dai, A. Thess, R. E. Smalley, L. J. Geerligs, and C. Dekker, “Individual single-wall carbon nanotubes as quantum wires,” *Nature*, vol. 386, pp. 474–477, 1997.
- [99] H. Aurich, a. Baumgartner, F. Freitag, a. Eichler, J. Trbovic, and C. Schönenberger, “Permalloy-based carbon nanotube spin-valve,” *Applied Physics Letters*, vol. 97, no. 15, p. 153116, 2010. [Online]. Available: <http://scitation.aip.org/content/aip/journal/apl/97/15/10.1063/1.3502600>
- [100] J. Nygård, D. H. Cobden, and P. E. Lindelof, “Kondo physics in carbon nanotubes.” *Nature*, vol. 408, no. 6810, pp. 342–346, 2000.
- [101] K. Grove-Rasmussen, H. I. Jørgensen, and P. E. Lindelof, “Kondo resonance enhanced supercurrent in single wall carbon nanotube Josephson junctions,” *New Journal of Physics*, vol. 9, no. 5, pp. 124–124, May

BIBLIOGRAPHY

2007. [Online]. Available: <http://stacks.iop.org/1367-2630/9/i=5/a=124?key=crossref.4113dacbcade89643c981907c68af9ce>
- [102] P. Jarillo-Herrero, J. Kong, H. Van Der Zant, C. Dekker, L. Kouwenhoven, S. De Franceschi, and T. V. Superfluid, “Orbital Kondo effect in carbon nanotubes,” *Nature*, vol. 434, no. 7032, pp. 484–488, 2005. [Online]. Available: <http://www.nature.com/nature/journal/v434/n7032/full/nature03422.html> \ delimiter"026E30F\\$nhttp://www.nature.com/nature/journal/v434/n7032/extref/nature03422-s3.doc
- [103] W. Liang, M. Bockrath, and H. Park, “Shell Filling and Exchange Coupling in Metallic Single-Walled Carbon Nanotubes,” *Physical Review Letters*, vol. 88, no. 12, pp. 1–4, Mar. 2002. [Online]. Available: <http://link.aps.org/doi/10.1103/PhysRevLett.88.126801>
- [104] J.-D. Pillet, C. H. L. Quay, P. Morfin, C. Bena, a. L. Yeyati, and P. Joyez, “Andreev bound states in supercurrent-carrying carbon nanotubes revealed,” *Nature Physics*, vol. 6, no. 12, pp. 965–969, Nov. 2010. [Online]. Available: <http://www.nature.com/doifinder/10.1038/nphys1811>
- [105] W. Schottky, “Halbleitertheorie der Sperrsicht,” *Naturwissenschaften*, vol. 26, no. 8, p. 938, 1938.
- [106] J. Svensson and E. E. B. Campbell, “Schottky barriers in carbon nanotube-metal contacts,” *Journal of Applied Physics*, vol. 110, no. 11, 2011.

BIBLIOGRAPHY

- [107] D. Pekker, G. Refael, and P. M. Goldbart, “Weber blockade theory of Magnetoresistance oscillations in superconducting strips,” *Physical Review Letters*, vol. 107, no. 1, pp. 2–5, 2011.
- [108] E. Majorana, “Teoria simmetrica dell’ $\bar{\text{e}}\text{lettrone}$ e del positrone,” *Il Nuovo Cimento*, vol. 14, no. 4, pp. 171–184, 1937.
- [109] R. M. Lutchyn, J. D. Sau, and S. Das Sarma, “Majorana Fermions and a Topological Phase Transition in Semiconductor-Superconductor Heterostructures,” *Physical Review Letters*, vol. 105, no. 7, pp. 1–4, Aug. 2010. [Online]. Available: <http://link.aps.org/doi/10.1103/PhysRevLett.105.077001>
- [110] J. Alicea, “Majorana fermions in a tunable semiconductor device,” *Physical Review B*, vol. 81, no. 12, pp. 1–10, Mar. 2010. [Online]. Available: <http://link.aps.org/doi/10.1103/PhysRevB.81.125318>
- [111] A. Y. Kitaev, “Unpaired Majorana fermions in quantum wires,” *Physics-Uspekhi*, vol. 44, p. 131, 2001. [Online]. Available: <http://iopscience.iop.org/1063-7869/44/10S/S29/>
- [112] J. Klinovaja, M. Schmidt, B. Braunecker, and D. Loss, “Helical Modes in Carbon Nanotubes Generated by Strong Electric Fields,” *Physical Review Letters*, vol. 106, no. 15, pp. 1–4, Apr. 2011. [Online]. Available: <http://link.aps.org/doi/10.1103/PhysRevLett.106.156809>

BIBLIOGRAPHY

- [113] J. Klinovaja, M. J. Schmidt, B. Braunecker, and D. Loss, “Carbon nanotubes in electric and magnetic fields,” *Physical Review B*, vol. 085452, no. June, pp. 1–22, 2011. [Online]. Available: <http://arxiv.org/abs/1106.3332>
- [114] F. Kuemmeth, S. Ilani, D. C. Ralph, and P. L. McEuen, “Coupling of spin and orbital motion of electrons in carbon nanotubes.” *Nature*, vol. 452, no. 7186, pp. 448–52, Mar. 2008. [Online]. Available: <http://www.ncbi.nlm.nih.gov/pubmed/18368113>
- [115] T. S. Jespersen, “Gate-dependent spin–orbit coupling in multielectron carbon nanotubes,” *Nature Physics*, vol. 7, no. 4, pp. 348–353, 2011. [Online]. Available: <http://dx.doi.org/10.1038/nphys880>
- [116] G. Steele, F. Pei, E. Laird, J. Jol, H. Meerwaldt, and L. Kouwenhoven, “Large spin-orbit coupling in carbon nanotubes,” *Nature Communications*, vol. 4, p. 1573, 2013. [Online]. Available: <http://www.nature.com/doifinder/10.1038/ncomms2584>
- [117] V. Mourik, K. Zuo, S. M. Frolov, S. R. Plissard, E. P. a. M. Bakkers, and L. P. Kouwenhoven, “Signatures of Majorana Fermions in Hybrid Superconductor-Semiconductor Nanowire Devices,” *Science*, vol. 336, p. 1003, 2012.
- [118] Z. Wang, Q.-F. Liang, D.-X. Yao, and X. Hu, “Viewing Majorana Bound States by Rabi Oscillations,” *Scientific Reports*, vol. 5, p. 11686, 2015. [Online]. Available: <http://www.nature.com/doifinder/10.1038/srep11686>

BIBLIOGRAPHY

- [119] W. W. Hu, K. Sarveswaran, M. Lieberman, and G. H. Bernstein, “Sub-10 nm electron beam lithography using cold development of poly(methylmethacrylate),” *Journal of Vacuum Science & Technology B: Microelectronics and Nanometer Structures*, vol. 22, no. 4, p. 1711, 2004. [Online]. Available: <http://scitation.aip.org/content/avs/journal/jvstb/22/4/10.1116/1.1763897>
- [120] B. Cord, J. Lutkenhaus, and K. K. Berggren, “Optimal temperature for development of poly(methylmethacrylate),” *Journal of Vacuum Science & Technology B: Microelectronics and Nanometer Structures*, vol. 25, no. 6, p. 2013, 2007. [Online]. Available: <http://link.aip.org/link/JVTBD9/v25/i6/p2013/s1&Agg=doi>
- [121] S. Yasin, D. Hasko, and H. Ahmed, “Comparison of MIBK/IPA and water/IPA as PMMA developers for electron beam nanolithography,” *Microelectronic Engineering*, vol. 61-62, pp. 745–753, Jul. 2002. [Online]. Available: <http://linkinghub.elsevier.com/retrieve/pii/S0167931702004689>
- [122] M. J. Rooks, E. Kratschmer, R. Viswanathan, J. Katine, R. E. Fontana, and S. a. MacDonald, “Low stress development of poly(methylmethacrylate) for high aspect ratio structures,” *Journal of Vacuum Science & Technology B: Microelectronics and Nanometer Structures*, vol. 20, no. 6, p. 2937, 2002.

BIBLIOGRAPHY

- [Online]. Available: <http://scitation.aip.org/content/avs/journal/jvstb/20/6/10.1116/1.1524971>
- [123] K. Koshelev, M. Ali Mohammad, T. Fito, K. L. Westra, S. K. Dew, and M. Stepanova, “Comparison between ZEP and PMMA resists for nanoscale electron beam lithography experimentally and by numerical modeling,” *Journal of Vacuum Science & Technology B: Microelectronics and Nanometer Structures*, vol. 29, no. 6, p. 06F306, 2011. [Online]. Available: <http://scitation.aip.org/content/avs/journal/jvstb/29/6/10.1116/1.3640794>
- [124] J. W. Elam, M. D. Groner, and S. M. George, “Viscous flow reactor with quartz crystal microbalance for thin film growth by atomic layer deposition,” *Review of Scientific Instruments*, vol. 73, no. 8, p. 2981, 2002. [Online]. Available: <http://scitation.aip.org/content/aip/journal/rsi/73/8/10.1063/1.1490410>
- [125] M. D. Groner, F. H. Fabreguette, J. W. Elam, and S. M. George, “Low-Temperature Al₂O₃ Atomic Layer Deposition,” *Chemistry of Materials*, no. 16, pp. 639–645, 2003.

Vita

Nikolaus George Hartman was born June 8, 1985 in Harrisburg, Pennsylvania. In 2003, he graduated from Central Dauphin High School. Nik received a Bachelors of Science degree in Physics from the University of Pittsburgh in 2007. After briefly working in healthcare technology at the ECRI Institute in Philadelphia, Nik started his PhD at Johns Hopkins University in 2008, joining the Markovic lab in 2009. Nik received his PhD in August 2015. He will continue his work in quantum transport as a post-doctoral fellow at the University of British Columbia in October 2015.